DOCTORAL THESIS

A moment of weakness: The anomalous geomagnetic field in the Ediacaran period

Author:
Daniele A. THALLNER

Supervisors:
Andrew J. BIGGIN
Mimi J. HILL

Examiners:
Richard HOLME
Claire I.O. NICHOLS

Thesis submitted in accordance with the requirements of the University of Liverpool for the degree of Doctor of Philosophy

in the

DEEP research group
Department of Earth, Ocean and Ecological Sciences

February 1, 2022

Declaration of Authorship

I, Daniele A. THALLNER, declare that this thesis titled, "A moment of weakness: The anomalous geomagnetic field in the Ediacaran period" and the work presented in it are my own. I confirm that:

- This work was done wholly or mainly while in candidature for a research degree at this University.
- Where any part of this thesis has previously been submitted for a degree or any other qualification at this University or any other institution, this has been clearly stated.
- Where I have consulted the published work of others, this is always clearly attributed.
- Where I have quoted from the work of others, the source is always given. With the exception of such quotations, this thesis is entirely my own work.
- I have acknowledged all main sources of help.
- Where the thesis is based on work done by myself jointly with others, I have made clear exactly what was done by others and what I have contributed myself.

Signed:

Date:

"Burn the land and boil the sea, you can't take the sky from me!"

Sonny Rhodes - Ballad of Serenity

UNIVERSITY OF LIVERPOOL

Abstract

School of Environmental Sciences
Department of Earth, Ocean and Ecological Sciences

Doctor of Philosophy

A moment of weakness: The anomalous geomagnetic field in the Ediacaran period

by Daniele A. THALLNER

Long-term variations in geomagnetic field behaviour can contain essential information on deep Earth processes. A major topic of debate has been the age of the onset of Earth's inner core nucleation, as uncertainty in the value of thermal conductivity of the core allows for a wide range in age estimates. Recently, an inner core age in the late Ediacaran period (635-538 Ma) has been inferred from an ultra-weak palaeointensity estimate at 565 Ma. Palaeomagnetic investigations using rocks from this time are known to give anomalous results and show ambiguous apparent polar wander paths in a hyper-reversing field. To date, a full characterisation of the geomagnetic field at that time has been prevented by a lack of field strength estimates. The studies presented in this thesis add 27 new and reliable field strength estimates between 0.31 ± 0.11 and 2.25 ± 0.39 $\times 10^{22}$ Am^2 to the record. These exceptionally weak estimates were obtained from rocks of the Grenville dykes (Canada), the Skinner Cove Formation (Newfoundland) and the Volyn traps (Ukraine). These cover the time period between 550 - 600 Ma and suggest that the geomagnetic field has been remarkably weak over a much longer time period than previously seen from palaeointensity data and starts to increase in strength at the Ediacaran-Cambrian transition, as suggested by less chaotic palaeomagnetic directions. These results could correspond to considerably lower field strengths predicted by geodynamo simulations for fields with low dipolarity before the onset of inner core nucleation. However, the context of these extremely weak palaeointensities is still unclear, as field strengths are still mostly unexplored for the time periods that surround the Ediacaran, highlighting the ubiquitous need for additional high quality palaeointensity data. New estimates of VGP dispersion and dipole moment variance for the Ediacaran were calculated using filtered data from the literature combined with the new data from this thesis. These estimates, although based on a low number of data, suggest enhanced palaeosecular variation in the Ediacaran compared to other time periods. With the high reversal frequencies, the field might have been in a transitional state throughout the Ediacaran and none of the currently available geodynamo model solutions was able to capture the full range of the unique Ediacaran field behaviour.

Contents

Declaration of Authorship iii

Abstract vii

Acknowledgements xix

1 Introduction and Background 1

1.1 Objectives and thesis overview . . . 1

1.2 In GAD we trust - Basics of rock- and palaeomagnetism . . . 3

1.2.1 Basic definitions . . . 4

1.2.2 Origin of the geomagnetic field and secular variation . . . 5

1.2.3 Magnetic properties of solid materials . . . 7

Diamagnetism and Paramagnetism . . . 7

Ferromagnetism . . . 7

Magnetic domains . . . 8

1.2.4 Types of remanent magnetisation . . . 9

Thermoremanent magnetisation . . . 10

Isothermal remanent magnetisation . . . 11

Chemical remanent magnetisation . . . 11

Viscous remanent magnetisation . . . 11

Anhysteretic remanent magnetisation . . . 12

Other remanent magnetisations . . . 12

1.2.5 Magnetic minerals . . . 12

Titanomagnetite . . . 12

Titanohematite . . . 14

Titanomaghemite . . . 14

Fe-oxyhydroxides and Fe-sulfides . . . 15

1.3 May the FORC be with you – Rock magnetism and palaeo-directions . . . 15

1.3.1 Hysteresis . . . 16

1.3.2 Susceptibility and thermomagnetic curves . . . 18

1.3.3 Magnetic anisotropy . . . 19

1.3.4 Demagnetisation . . . 19
1.4 To intensity and beyond - Introduction to palaeointensity determination 21
1.4.1 The Thellier method . . . 23
1.4.2 The microwave method . . . 25
1.4.3 The Wilson method . . . 26
1.4.4 The Shaw method . . . 27
1.4.5 The calibrated pseudo-Thellier method . . . 29
1.4.6 The Multispecimen Protocol method . . . 30
1.4.7 Quantifying reliability of palaeointensity estimates - Q_{PI} . . . 31
1.5 DEEP impact - Determining Earth Evolution from Palaeomagnetism . . . 32
1.5.1 Palaeomagnetic statistics and field models . . . 33
1.5.2 Numerical geodynamo simulations . . . 37
1.5.3 Quality of Paleomagnetic Modeling criteria Q_{PM} . . . 40
1.6 The Ediacaran Period . . . 41
1.6.1 Definition and historical background . . . 41
1.6.2 Life and climate . . . 42
1.6.3 Palaeogeography and the geomagnetic field . . . 44

2 A palaeointensity study of the Grenville Dykes, Canada 47
2.1 Introduction . . . 49
2.2 Materials and methods . . . 50
2.2.1 Sample material . . . 50
2.2.2 Methods . . . 52
2.3 Results . . . 55
2.4 Discussion . . . 61
2.5 Conclusions . . . 68

3 A palaeointensity study of the Skinner Cove Fm, Newfoundland 69
3.1 Introduction . . . 70
3.2 Samples and Methods . . . 72
3.3 Results . . . 75
3.4 Discussion . . . 83
3.5 Conclusion . . . 88

4 A palaeointensity study of the Volyn Traps, Ukraine 89
4.1 Introduction . . . 91
4.2 General geology . . . 92
4.3 Ages of rocks . . . 94
4.4 Palaeomagnetic sampling and methods . . . 95
4.5 Results . . . 98

4.5.1 Palaeomagnetic directions from quarry samples . . . 98
4.5.2 Palaeomagnetic results from borehole core samples . . . 100
4.5.3 Magnetic properties . . . 105
4.5.4 Palaeointensity results . . . 108
4.6 Discussion . . . 114
4.7 Conclusion . . . 117

5 Characterisation of the Ediacaran geomagnetic field 119
5.1 Introduction . . . 119
5.2 Sources of data . . . 124
5.3 VGP dispersion and latitude dependence of published dispersion estimates . . . 126
5.4 Towards a coherently filtered dataset . . . 128
5.5 Treatment of outliers . . . 130
5.6 Results and discussion . . . 133
5.6.1 An observation-based model for Ediacaran PSV . . . 133
5.6.2 Comparison to numerical geodynamo model results . . . 137
5.7 Conclusions . . . 146

6 Conclusions 147
6.1 Summary of results . . . 147
6.2 Implications and future work . . . 149

References 153

A Grenville Dykes supplementary data 187
A.1 Supplementary Tables . . . 188
A.2 Supplementary Figures . . . 193

B Skinner Cove supplementary data 201
B.1 Supplementary Tables . . . 202
B.2 Supplementary Figures . . . 207

C Volyn Traps supplementary data 215
C.1 Supplementary Tables . . . 216
C.2 Supplementary Figures . . . 227

D PSV analysis supplementary data 229
D.1 Supplementary Tables . . . 229

List of Figures

1.1 Magnetic domain structures . . . 9
1.2 Ternary diagram of titanium- and iron oxides . . . 13
1.3 Analysis of hysteresis data . . . 17
1.4 Schematic examples of demagnetisation experiments . . . 20
1.5 Schematic example of an Arai plot . . . 24
1.6 Example of analysis plots for a DHT-Shaw experiment . . . 28
1.7 The DEEP approach . . . 33
1.8 Mega-/microfossil zonation in the upper Ediacaran system . . . 43
1.9 Estimated plate velocities of Laurentia, Baltica and Amazonia . . . 46

2.1 Geographic distribution of the Grenville Dykes . . . 51
2.2 Rock magnetic results of Grenville Dyke basalts . . . 56
2.3 Thellier experiment results of the Grenville Dykes . . . 58
2.4 Shaw experiment results of the Grenville Dykes . . . 59
2.5 Example of multimethod results for a French River dyke sample . . . 65
2.6 Virtual dipole moments throughout the Ediacaran . . . 67

3.1 Geographic location and geological map of the Skinner cove formation . . . 73
3.2 Rock magnetic results of the Skinner cove formation . . . 76
3.3 Scanning electron microscopy of rocks of the Skinner cove formation . . . 77
3.4 Thellier experiment results of the Skinner cove formation . . . 80
3.5 Comparison of intensity results from different methods . . . 82
3.6 Virtual dipole moments in the Cambrian and Ediacaran . . . 86

4.1 Schematic map of the Volyn Large Igneous Province (VBP) . . . 93
4.2 Paleomagnetic directions from the Berestovets and Basaltovoe quarries . . . 100
4.3 Paleomagnetic results from the core CK3 . . . 102
4.4 Stratigraphy and magnetic inclination of ChRM from core samples . . . 104
4.5 Rock magnetic data of the Volyn Traps . . . 106
4.6 Scanning electron microscope images . . . 108
4.7 Palaeointensity results and magnetic properties of Volyn basalts . . . 109

4.8 Virtual and palaeomagnetic dipole moments of the Ediacaran and Cambrian . . . 116

5.1 PSV of published Ediacaran data . . . 127
5.2 Influence of data filters on model G fits . . . 129
5.3 Tests of a modified variable cutoff . . . 132
5.4 Model A and model G parameters as well as VDM distribution from Ediacaran data . . . 134
5.5 Statistical estimates for directional PSV and variability of dipole moments of 12 geodynamo simulations . . . 139
5.6 Statistical field models for solutions of geodynamo simulations . . . 142
5.7 Statistical field models for solutions of LEDA010 . . . 143
5.8 Dipole variance of Ediacaran observational data in comparison to numerical geodynamo simulation outputs . . . 145

6.1 Virtual dipole moments between 700 Ma and present day . . . 151

A.1 Rock magnetic measurements - Grenville Dykes . . . 193
A.2 Elemental composition maps for Fe and Ti from BSE analysis . . . 197
A.3 VGP dispersion of the Grenville Dykes . . . 199

B.1 Rock magnetic measurements - Skinner Cove . . . 207
B.2 Elemental composition maps - Skinner Cove . . . 212
B.3 Stereographic projection of Skinner Cove A and B site mean directions . . . 214

C.1 Rock magnetic parameters - Rafalovka and Policy-2 . . . 227

List of Tables

1.1 Conversion of standard units 5

2.1 Palaeointensity results of the Grenville Dykes 60

3.1 Selection criteria for Skinner Cove Fm palaeointensity experiments . . . 74
3.2 Palaeointensity results of the Skinner cove Formation 79
3.3 Q_{PI} scores of Skinner Cove intensities 84

4.1 Selection criteria for Volyn Traps palaeointensity experiments 97
4.2 Site-mean palaeomagnetic directions and statistical parameters for the Volyn Traps 99
4.3 Paleomagnetic directions and poles for basalts of the Ratne suite 101
4.4 Palaeointensity results of the Volyn Traps 113

5.1 Summary of filtered Ediacaran PSV data 136

A.1 Thellier results and critical SPD values, Grenville Dykes 188
A.2 Shaw results and critical values, Grenville Dykes 190
A.3 Pseudo-Thellier results and critical values, Grenville Dykes 191
A.4 Comparison of different sets of selection criteria 192
A.5 List of Q_{PI} criteria 193

B.1 Microwave Thellier results and critical SPD values, Skinner Cove 202
B.2 Thermal Thellier results and critical SPD values, Skinner Cove 203
B.3 DHT Shaw results and critical SPD values, Skinner Cove 204
B.4 Pseudo-Thellier results and critical SPD values, Skinner Cove 205
B.5 Paleomagnetic site mean results for the Skinner Cove Formation 206

C.1 Mean paleomagnetic directions (Ratne Formation) 216
C.2 Thermal Thellier results and critical SPD values, Volyn Traps 217
C.3 Microwave Thellier results and critical SPD values, Volyn Traps 220
C.4 Wilson results and critical SPD values, Volyn Traps 221
C.5 DHT-Shaw results and critical SPD values, Volyn Traps 223

C.6 pseudo-Thellier results and critical SPD values, Volyn Traps 224

D.1 Palaeomagnetic data of final selection for PSV analysis 229
D.2 Numerical geodynamo simulations and control parameters 232

List of Abbreviations

AC	**A**lternating **C**urrent
AF	**A**lternating **F**ield
AMS	**A**nisotropy (of) **M**agnetic **S**usceptibility
ARM	**A**nhysteretic **R**emanent **M**agnetisation
APWP	**A**pparent **P**olar **W**ander **P**ath
BDS	**B**ulk **D**omain **S**tability
BSE	**B**ack**s**catter **E**lectron (image)
ChRM	**C**haracteristic **R**emanent **M**agnetisation
CMB	**C**ore **M**antle **B**oundary
CRM	**C**chemical **R**emanent **M**agnetisation
DC	**D**irect **C**urrent
Dec	**D**eclination
(C)DRAT	(**C**umulative) **D**ifference **R**atio
DRM	**D**etrital **R**emanent **M**agnetisation
FMR	**F**erri**m**agnetic **R**esonance
FORC	**F**irst **O**rder **R**eversal **C**urve
FRAC	**F**raction
Ga	Billion (**G**iga) years **a**go
GAD	**G**eocentric **A**xial **D**ipole
Inc	**I**nclination
IRM	**I**sothermal **R**emanent **M**agnetisation
Ma	Million (**M**ega) years **a**go
MAD	**M**aximum **A**ngular **D**eviation
MD	**M**ulti**d**omain
MHD	**M**agneto**h**ydro**d**ynamics
MW	**M**icro**w**ave
NRM	**N**atural **R**emanent **M**agnetisation
PSV	**P**alaeo**s**secular **V**ariation
PSD	**P**seudo**s**ingle **D**omain
$\mathbf{Q_{PI}}$	**Q**uality (of) **P**alaeo**i**ntensity (estimates)
$\mathbf{Q_{PM}}$	**Q**uality (of) **P**alaeomagnetic **M**odeling (criteria)

SD	**S**ingle**d**omain
SEM	**S**canning **E**lectron **M**icroscope
SP	**S**uper**p**aramagnetic
SPD	**S**tandard **P**alaeointensity **D**efinitions
TAF	**T**ime **A**veraged **F**ield
TCRM	**T**hermo**c**hemical **R**emanent **M**agnetisation
TD	**T**hermal **D**emagnetisation
TM	**T**itano **M**agnetite
(II)TPW	**I**nertial **I**nterchange **T**rue **P**olar **W**ander
(p)TRM	(partial) **T**hermo **R**emanent **M**agnetisation
TVRM	**T**hermo**v**iscous **R**emanent **M**agnetisation
V(A)DM	**V**irtual (**A**xial) **D**ipole **P**oment
VFTB	**V**ariable **F**ield **T**ranslation **B**alance
VGP	**V**irtual **G**eomagnetic **P**ole
VRM	**V**iscous **R**emanent **M**agnetisation

Acknowledgements

I thank my supervisors Andy Biggin and Mimi Hill. Fun fact: historically, the German term for 'PhD supervisor' has been 'Doktorvater'. For obvious reasons, this term is not as commonly used any more nowadays, which probably won't stop me from bringing it up from time to time :). But seriously, I thank Andy for giving me this amazing opportunity and jump-starting my scientific journey with his guidance, support, patience and ability to find (or make) time for advice whenever the state of the project looked less than promising. Thanks to Mimi as well for all the helpful discussions and support. I am also grateful for Greig Paterson's invaluable support and mentorship within and outside the PhD project. It may be well hidden most of the time, but I have actually learned an awful lot from Andy and Greig about how to navigate the academic world; I definitely owe you a pint or two. I must also thank Elisabeth Schnepp, Robert Scholger and Roman Leonhardt for introducing me to palaeomagnetism during my undergraduate degree.

There were many people who made sure that it was never boring to work in the lab and should be acknowledged. I thank Elliot Hurst for fixing all the equipment that I have broken and for encouraging me to hide the word 'cabbage' somewhere in this thesis. I also appreciate Ben, Courtney, Domenico, Louise, Michael, and Richard for keeping the lab exciting every day. Special thanks go out to Annique for all her help, for adventurous field trips and for sharing my semi-healthy lunch habits. I could not leave out Simon, who provided numerous eloquent expressions for me to add to my vocabulary and to use in the bumf you are about to read. Last, but not least, I thank Yael for her persistent (and futile) attempts to convince me that there is a life outside of work.

Funding for this PhD was provided by the Leverhulme Trust through Andy Biggin's grant RL-2016-080.
The studies presented in Chapters 2 - 4 would not have been possible without the assistance of my collaborators. I thank Henry Halls, Phil McCausland, as well as Valentina Shcherbakova, Valery Shcherbakov, Vladimir Bakhmutov and their groups at GO Borok IPE RAS and the Institute of Geophysics of the National Academy of Sciences of Ukraine for their help during fieldwork and all the great work that was put into these studies.

I definitely need to thank my close friends back home in Austria - Elisa, Flo, Julius, Kattl, Max, Poschi, Stoffl, Tinsch, Vero and the rest of the 'ÖH-Heim Haufen'. They somehow managed to keep me sane(ish) during the course of the pandemic.
Finally, I thank my family for their continued patience, support and encouragement throughout this process.

Chapter 1

Introduction and Background

1.1 Objectives and thesis overview

Earth's geomagnetic field has been shielding the planet's atmosphere and surface from solar radiation for more than 3.5 billion years (Biggin et al., 2011; Tarduno et al., 2015). It is generated by dynamo processes in Earth's liquid outer core, and as it stretches out into space, it represents a unique opportunity to observe deep Earth processes on the planet's surface, where these observations can be preserved in the rock record throughout geological time (e.g., Sprain et al., 2019). Observations of long-term variations of the field, caused by variations in the magnetohydrodynamic processes in the core, allow palaeomagnetism to provide insight into the state of Earth's core over geological times whereas direct geophysical observations of the core are limited to snapshots of its present-day state (Gerya, 2019). The search for links between palaeomagnetic signatures and changes in core conditions is fuelled by the continued development of numerical geodynamo models that have been successful in producing Earth-like models of the field (e.g., Christensen et al., 2010; Meduri et al., 2021). Long term trends and variations of the geomagnetic field have been connected to interactions between layers of the planet because some features of the field, such as the variability of its reversal frequency, have been observed to occur on similar timescales as the convective overturn of the mantle (e.g., Biggin et al., 2012; McFadden and Merrill, 1984). A strong impact on the palaeomagnetic signature is expected from the onset of inner core nucleation. This marks the transition from a thermally driven geodynamo to a geodynamo powered by chemical convection (e.g., Aubert et al., 2009; Labrosse and Macouin, 2003). This is of special interest for the study of the thermal evolution of the planet because different estimates for the core's thermal conductivity have led to a wide range of possible ages for the core (e.g., Hsieh et al., 2020; Starchenko, 2017; Zhang et al., 2020). The observation of an increase in geomagnetic field strength has led to the proposal of a Mesoproterozoic age for the inner core nucleation (1 - 1.5 Ga; Biggin et al., 2015). Recently, a much younger age ($\sim$565 Ma) of the inner core has

been inferred from measurements of ultra-low field strengths (Bono et al., 2019). This age falls at the end of the Ediacaran period (635 - 538 Ma), which is a time period of special interest for the studies of Earth's evolution due to the extreme climatic and tectonic changes (e.g., Evans, 2013; Li et al., 2013) as well as the first observations of life in form of large, architecturally complex organisms (e.g., Meert et al., 2016; Xiao and Narbonne, 2020).

Palaeomagnetic observations from that time are highly controversial and have been puzzling palaeomagnetists since the last century (e.g., Halls et al., 2015; Kirschvink et al., 1997; McCausland et al., 2011; Meert, 2014). They suggest ambiguous apparent polar wander paths that have led to various interpretations for palaeogeographic reconstructions with especially large impacts on the individual drifting history of the continents Laurentia and Baltica after the final break-up of the supercontinent Rodinia (e.g., Li et al., 2013; Robert et al., 2021). However, a standard interpretation of the incompatible palaeomagnetic directions would suggest extreme and physically implausible plate velocities (Tsai & Stevenson, 2007). Alternative interpretations have been proposed that include large-scale processes such as inertial interchange true polar wander (Kirschvink et al., 1997; Robert et al., 2017). Several studies have also suggested that the geomagnetic field in the Ediacaran behaved radically different than the modern field and represented an unstable transitional field (e.g., Halls et al., 2015) with extreme reversal frequencies (Bazhenov et al., 2016; Levashova et al., 2021) and/or extended periods of time spent in an equatorial dipole configuration (Abrajevitch & Van der Voo, 2010).

A full characterisation of the Ediacaran field requires an excellent distribution of full-vector palaeomagnetic observations, but with the exception of one estimate of ultra-low field intensity (Bono et al., 2019), the field strength throughout the Ediacaran is completely unknown and represents a large data gap for the assessment of long-term behaviour of the geomagnetic field at this critical time of the planet's evolution (e.g., Driscoll, 2016). The main objective of this thesis is the determination of global field strengths throughout the Ediacaran to address this information gap. Our rationale is that by measuring the field strength and its variability, we can use this new information together with the already available directional palaeomagnetic data to develop statistical field models that describe the Ediacaran field and can be used to constrain the search for geodynamo simulations that produce a similar field. If such geodynamo simulations could be found, then those might be able to provide useful predictions about the state of the geodynamo and the deep Earth properties at that time.

This first chapter introduces the basic concepts and background of this thesis, starting with the fundamentals of palaeomagnetism, followed by short introductions to

rock magnetic methods, the basic theory of palaeointensity determinations, and an overview of the Ediacaran period including its definition, life, climate and palaeogeography. The second chapter is the first step towards a better definition of the Ediacaran geomagnetic field and presents palaeointensity results from a multi-method palaeointensity study performed on rocks of the Grenville Dykes (Canada, 580 - 598 Ma). These results represent the first field strength estimates for the mid-Ediacaran and were measured to gain insight into the long-term field behaviour in the Ediacaran. In the third chapter, we shift our focus to the Ediacaran-Cambrian transition and measure the field strength recorded in volcanic rocks of the Skinner Cove formation (Newfoundland, 551 Ma) to compare these results to predictions from geodynamo simulations. Chapters 2 and 3 both look at rocks from a similar area on the continent of Laurentia. In Chapter 4, we present palaeointensity results from Baltica measured on rocks of the Volyn Basalt Province (Ukraine, 560 - 580 Ma) to see if the weak field period was a global phenomenon and or a 'local´ Laurentian anomaly. Finally, Chapter 5 records the attempt to characterise the Ediacaran field in terms of statistical parameters and use solutions from numerical geodynamo models to link deep Earth processes to the anomalous geomagnetic field.

1.2 In GAD we trust - Basics of rock- and palaeomagnetism

Earth's geomagnetic field has shielded and protected the planet's surface and atmosphere from solar wind radiation for almost 4 billion years (Tarduno et al., 2014). The desire to understand this field and its variations is rooted in its importance for navigation as well as for the study of Earth's evolution, as it is one of the most direct ways of observing the dynamics of our planet's core. From early Chinese 'compasses´ (Lowrie & Fichtner, 2020) to ESA's swarm satellite data, our ability to measure the geomagnetic field has come a long way, but no matter how extensive these observations are, they can only give us a snapshot of information about the field in its present state. To fully understand the geomagnetic field, and to be able to use it to study the evolution of our planet, detailed knowledge about the field's origin and evolution throughout time is essential. However, records of direct measurements of the field only exist for the last $\sim$400 years. The study of the geomagnetic field and its variations in earlier times and on longer time scales relies on indirect measurements of the field and is the basis for the science of palaeomagnetism. This section will introduce the basic definitions and concepts of palaeomagnetic research, that are used throughout this thesis. More in-depth knowledge of the topics in this section can be found in general palaeo- and rockmagnetic textbooks such as Butler (1992), Dunlop and Özdemir (1997) or Tauxe (2010).

1.2.1 Basic definitions

From the pioneering works of H.C. Ørsted and A.M. Ampere in the early 19^{th} century, we know that electric (circulatory) currents produce magnetic fields and can define the smallest unit of magnetic 'charge´ – the magnetic (dipole) moment (m) – as the product of an electrical current (i) and the area (A) enclosed by a current loop. The magnetic (force-) field (H) itself is a vector field defined as the force applied on a moving charge. At any point in space, a magnetic field can be represented by a vector with direction and magnitude. The density of magnetic field lines – the magnetic induction (B) – can be used as an estimate of the strength of a magnetic field. In vacuum, the relationship between magnetic induction and the magnetic field is defined as $B = {}_0H$, where ${}_0$ is the permeability of free space ($4\pi \times 10^{-7}$ Hm^{-1}). A magnetic moment placed in a magnetic field experiences an aligning torque of $\Gamma = mB$ and the potential energy of alignment (magnetostatic energy, $E_m = -mBcos\theta$) is at a minimum when the angle θ between m and B is zero. A magnetic moment will therefore align with the magnetic field if it is free to rotate. On a sub-atomic scale (conveniently ignoring quantum mechanics and electron spins), a magnetic moment can be generated by the circulating current from the orbital motion of electrons around the nucleus. For any material, the vector sum of individual atomic dipole moments can be normalised by volume or mass to give the magnetisation (or magnetic intensity) of a material. Placed in a magnetic field H, a material may acquire an induced magnetisation of $M_i = \chi * H$, where χ is the dimensionless bulk magnetic susceptibility of a material, describing the 'magnetisability´ of a substance (Butler, 1992). In addition to induced magnetisations, some materials may also produce magnetic moments without being exposed to an external magnetic field. Several processes (see section 1.2.4) can cause these spontaneous magnetic moments to become fixed in a coordinated way and preserve a record of a past magnetic field as remanent magnetisation $\mathrm{M_r}$ (Tauxe, 2010). In palaeomagnetism, the remanent magnetisation of igneous and sedimentary rocks (as well as baked archaeological material) can be used to determine Earth's ancient geomagnetic field.

At any point on the planet's surface, the geomagnetic field can be measured as a vector with a radial (vertical) component B_v and tangential (horizontal) components, that can be broken into the geographic north and geographic east components B_n and B_e, respectively. These components are defined as

$$B_v = B * \sin(I), B_n = B * \cos(I) * \cos(D), B_e = B * \cos(I) * \sin(D) \tag{1.1}$$

Parameter	SI unit	c.g.s. unit	conversion
Magnetic dipole moment	Am^2	emu	1 Am^2 = 10^3 emu
Magnetisation (volume)	Am^{-1}	emu/cm^3	1 A/m = 10^{-3} emu/cm^3
Magnetisation (mass)	$Am^{-1}kg^{-1}$	emu g^{-1}	1 Am^2/kg = 1 emu/g
Magnetic field (H)	Am^{-1}	oe	1 Am^{-1} = 4 π $\times 10^{-3}$ oe
Magnetic induction (B)	T	G	1 T = 10^4 G
Susceptibility (volume)	-	emu $cm^{-3}oe^{-1}$	1 = 4 π emu $cm^{-3}oe^{-1}$

TABLE 1.1: Conversion between SI and c.g.s. system units of common parameters used throughout this thesis. After Butler (1992) and Tauxe (2010).

where B is the magnitude, I is the inclination, defined as the angle from a horizontal plane with values of -90° $\leq I \leq$ 90° (positive values are defined as 'downward´), and D is the declination, defined as the angle between the horizontal component and geographic north with values of 0° $\leq D \leq$ 360° (positive values defined as clockwise from North). The direction of B is fully described by declination and inclination. If all components are known, then the strength of B is given by

$$B = \sqrt{B_v^2 + B_n^2 + B_e^2}. \tag{1.2}$$

A major source of errors and confusion on the field of palaeomagnetism lies in the 'choice´ of unit systems. This thesis follows the recommended use of the Système International (SI). However, the older c.g.s. system is still used by a considerable fraction of measurement equipment, and raw measurement data in the supplementary datasets of this thesis may therefore be in c.g.s. units. A list of conversions between SI and c.g.s. units for the most common parameters in magnetism is given in Table 1.1.

1.2.2 Origin of the geomagnetic field and secular variation

Observations of the geomagnetic field comprise contributions from internal and external sources. Both contributions are variable in time, but these variations differ significantly in their range of time scales, allowing for these contributions to be separated. Using spherical harmonics to fit surface harmonics to measurement data, Carl Friedrich Gauss proved that the majority of the field measured at the surface was of internal origin (Garland, 1979). His best fit was consistent and almost identical with the prediction of a magnetic field from a magnetised sphere or a dipole at the centre of the sphere that was tilted at an angle of approximately 11° to Earth's rotational axis. In

the modern understanding, more than 90% of the main field at Earth's surface is generated by dynamo processes in the planet's liquid outer core (Korte & Mandea, 2019). Slow changes of this 'core field´ with time (secular variation), seen as changes of direction, magnitude and polarity of the surface field, cover time scales from several months to tens of millions of years (Wicht & Sanchez, 2019). Gauss' spherical harmonics are still used as one of the most convenient tools to describe the geomagnetic field variations. At any point outside of the magnetic source, the magnetic field can be determined from the gradient of a scalar potential field. For the field from internal sources, this potential equation can be written as

$$\Psi = \frac{a}{\mu_0} \sum_{l=1}^{\infty} \sum_{m=0}^{l} \left(\frac{a}{r}\right)^{l+1} P_l^m(\cos\theta)(g_l^m \cos m\phi + h_l^m \sin m\phi) \tag{1.3}$$

where a is Earth's radius (a = 6371 $\times 10^6$m), r is the radial distance, θ is the colatitude, and ϕ is the longitude (Merrill et al., 1998). The coefficients g_m^l and h_m^l are the Gauss coefficients of degree l and order m in units of nT, and P_m^l are partially normalised Schmid polynomials of cos(θ) (Tauxe, 2010). The terms in this equation represent equivalent sources at the planet's centre with the three terms of degree l = 1 representing the (geocentric) dipole field and terms of higher degrees representing the nondipole field (l = 2: geocentric quadrupole, l = 3 geocentric octupole, etc). Equation 1.3 also shows that the magnetic potential due to a dipole falls off as r^{-2}, whereas the potential due to a quadrupole falls off as r^{-3}, the potential due to an octupole as r^{-4}, and so on. The relative contributions of the higher degree terms are therefore much higher at the core-mantle boundary (CMB) than on the surface, where the field is dipole dominated and the relative contribution of the nondipole field is estimated to be in the order of 10 - 20% (Korte & Mandea, 2019). These relative contributions are however subject to change as part of secular variation. For the present-day field, the decay of the axial dipole (g_0^1) is (in addition to the westward drift of the field) one of the most striking features of secular variation (Jackson & Finlay, 2015).

If the geomagnetic field – and therefore secular variation – is averaged over a sufficient amount of time (> 10^4 - 10^5 yrs; Tauxe, 2010), then the resulting time-averaged field (TAF) can be approximated by a geocentric axial dipole (GAD) field (Hospers, 1954). This idealised field can be fully described by the g_0^1 term. It shows no longitudinal variation (declination is always zero) and the inclination varies as a function of latitude λ, given by the 'dipole equation´

$$\tan I = 2 \tan \lambda, \tag{1.4}$$

allowing latitudes to be calculated from the inclinations of a GAD field – a fundamental observation for tectonic reconstructions (e.g., Creer et al., 1954). The determination of the structure of Earth's TAF and the (palaeo) secular variation on discrete time intervals over geologic time scales becomes less trivial for ancient times as measurement data is not as readily available. This has been the focus of numerous studies (e.g., Johnson and McFadden, 2015; Johnson and Constable, 1996; McElhinny and McFadden, 1997) and the basic concepts will be introduced in section 1.5.1.

1.2.3 Magnetic properties of solid materials

There are different fundamental types of magnetic behaviour of materials that define how magnetisation is acquired in response to an applied external field.

Diamagnetism and Paramagnetism

Due to the gyroscopic effect of the Lorentz force, experienced by electrons moving in a magnetic field, electron orbits precess about the direction of the applied field, which produces a negative induced moment (Dunlop & Özdemir, 1997). This 'diamagnetic´ response is experienced by all materials and leads to the acquisition of a small induced magnetisation that is antiparallel to the applied field and changes linearly with the strength of the applied field. Diamagnetic materials are defined as materials that comprise only atoms without atomic magnetic moments. The magnetic susceptibility of diamagnetic materials (e.g., most non-iron bearing minerals) is small, negative and temperature independent.

'Paramagnetic´ materials contain atoms with (non-interacting) permanent atomic magnetic moments that experience a partial alignment of these moments in response to the application of a magnetic field. In absence of an applied magnetic field, vibrations of the crystal lattice due to thermal energy (at temperatures > 0 K) cause the atomic magnetic moments to oscillate rapidly and in random orientations, resulting in a net magnetisation of zero. In an applied field, the induced magnetisation is small, parallel, and linearly dependent on the applied field. The magnetic susceptibility of paramagnetic materials (e.g., iron-sulphides, silicates) are 10 – 100 times larger than the ones of diamagnetic materials (Dunlop & Özdemir, 1997) and show a temperature dependence observed as a decrease of susceptibility with increasing temperature.

Ferromagnetism

Ferromagnetism is a property of matter that is composed of atoms with permanent atomic magnetic moments, which are strongly interacting, as electron spins of neighbouring electrons are coupled by exchange forces. Depending on the crystal structure,

the exchange energy is at a minimum at parallel or antiparallel alignments of spins. In contrast to dia- and paramagnetic materials, ferromagnetic materials can acquire a remanent magnetisation in an applied field. Due to the strong interactions of atomic magnetic moments, the magnetisation of a ferromagnetic material from an applied field can be several orders of magnitude larger than the magnetisation of a paramagnetic material in the same field, up to the saturation magnetisation, above which an increase of the applied field no longer results in an increase of magnetisation. These interactions are temperature dependent and become weaker with increasing temperature, up to the material-specific Curie temperature T_c. Above this critical temperature, the thermal energy is so high, that spins are no longer interacting and the ferromagnetic material is paramagnetic. In some materials with multiple magnetic sublattices in their crystal structure, the coupling of atomic magnetic moments can be parallel within and antiparallel between the sublattice layers. In a strict sense, these materials are not ferromagnetic (Butler, 1992). If the application of an external field results in an equal number of parallel and antiparallel atomic magnetic moments and the resulting net magnetisation is zero, then the material is called antiferromagnetic. If the numbers of resulting parallel and antiparallel moments is unequal and the net magnetisation is not zero, then the material is referred to as 'ferrimagnetic´.

Magnetic domains

The magnetisation of ferromagnetic particles is controlled by the particles' desire to achieve a minimum-energy state. In a uniformly magnetised particle (Figure 1.1a), atomic magnetic moments cancel out internally but lead to a large magnetostatic energy stored in the internal and external fields associated with the distribution of surface poles (Dunlop & Özdemir, 1997). Depending on the size (and shape) of the particle, it can be energetically favourable to form magnetic domains separated by domain walls, resulting in a multidomain (MD) grain (Figure 1.1b - d). For small particles below the critical grain size, referred to as single-domain (SD) particles, the decrease in magnetostatic energy from the subdivision of a single domain to two domains is smaller than the energy required for the formation of a domain wall. SD particles that are sufficiently small, so that the thermal energy exceeds the energy required to rotate the magnetic moment, are in a 'thermally activated´ state, act paramagnetically, and are referred to as superparamagnetic (SP). Both SD and MD particles can preserve remanent magnetisations, but show different magnetic properties and behaviour. This can affect studies of the ancient field strength because the theory of remanence acquisition and methods of palaeointensity determination are based on the theoretical

behaviour of SD particles (see section 1.4). However, there is no sharp boundary between SD and MD particles. Instead, particles in the interval of grain sizes with unclear domain structure and SD-like behaviour are called pseudo-single-domain (PSD), that are assumed to be able to preserve remanent magnetisations as well as SD particles (e.g., Nagy et al., 2017). PSD particles show more complex magnetic structures that act to minimise the energies of atomic dipole interactions. These structures have been studied using micromagnetic modelling (Williams & Dunlop, 1989) that showed two possible (meta)stable domain states for cubic grains in sizes between 0.01 - 1.0 µm: the flower state, there the magnetic moments roughly follow the shape of a double cone and 'flower out´ at the grain surface, and the vortex state where the magnetic moments curl around a centre axis (Williams & Wright, 1998).

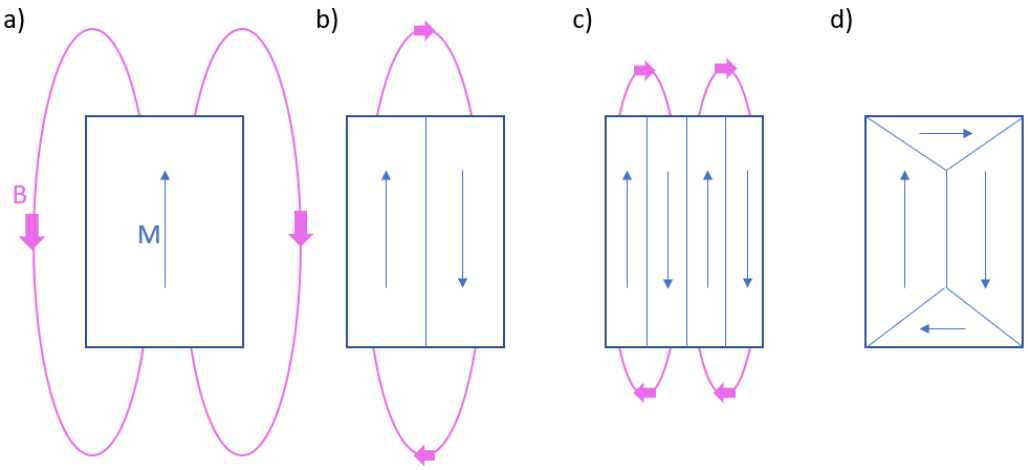

FIGURE 1.1: Cross section through magnetised grains with different domain structures; a) single domain (SD) particle, b) two-domain particle, c) multidomain (MD) particle, d) two-domain particle forming closure domains. Redrawn from Dunlop and Özdemir (1997).

1.2.4 Types of remanent magnetisation

The magnetisation of in situ rocks in nature is the vector sum of induced and remanent magnetisations. The acquisition of induced magnetisation has important applications for exploration geophysics. However, this process is reversible. The induced magnetisation decays rapidly if the external field is removed and this magnetisation can therefore not hold a record of a past external field, which limits its use for palaeomagnetism. In contrast, the remanent magnetisation remains after the magnetising field is removed and holds a record about the strength and direction of the external field. The ratio between remanent and induced magnetisation is given by the Königsberger ratio (Königsberger, 1936) $Q = M_r / M_i$. In general, rocks with higher values of Q tend to be

better recorders, which can be useful for pre-selection of studied rocks (e.g., Di Chiara et al., 2021; Schnepp et al., 2020a). Remanent magnetisations that have been acquired in nature and/or before laboratory treatment are referred to as natural remanent magnetisation (NRM). Natural remanent magnetisations that are acquired during the formation of a rock, and therefore hold a record of the geomagnetic field at the time of rock formation, are termed primary NRMs. In addition, secondary NRMs can be acquired by processes after rock formation. In ancient rocks, primary and secondary magnetisations coexist and the total NRM represents the vector sum of $NRM_{primary}$ and $NRM_{secondary}$. There are several different processes that can lead to the acquisition of a remanent magnetisation; those relevant to this thesis are outlined below.

Thermoremanent magnetisation

When magnetic grains are cooled to ambient temperature from a temperature above their Curie temperature T_c, while being exposed to a (weak) external field, they acquire a thermoremanent magnetisation (TRM). The basic theory of this process, resulting from the studies of Louis Néel (Néel, 1949, 1955), deals with magnetic stability of an assemblage of non-interacting SD grains. In essence, thermal excitations will cause an initial magnetisation to decay gradually (and exponentially) over time, as the orientations of magnetic moments of individual grains randomise in absence of an external field. The time it takes for an initial magnetisation to decay to a value of 1/e of the initial magnetisation was defined by Néel as the characteristic relaxation time τ, given by

$$\tau = \frac{1}{C}\exp(E_b/kT) = \frac{1}{C}\exp\left(\frac{vh_c j_s}{2kT}\right), \tag{1.5}$$

where C is the frequency factor ($\sim 10^8$ s^{-1}; Butler, 1992), E_b is the blocking energy, defined by the product of the volume v, the microscopic coercive force h_c and the saturation magnetisation J_s of the SD grain. kT is the thermal energy from the product of Boltzmann constant k and temperature T. The relaxation time depends on the ratio of blocking energy ($v*h_c*j_s$), representing the energy barrier for the rotation of the magnetisation, to the thermal energy, and has therefore a strong temperature dependence (Butler, 1992; Dunlop & Özdemir, 1997). In addition to the temperature dependence, the coercive force in this equation is strongly controlled by shape anisotropy and magnetocrystalline anisotropy, and relaxation times vary for different mineralogies, grain sizes and shapes. The temperature at which the relaxation time becomes longer than a critical relaxation time is the blocking temperature T_b. Natural bulk rock samples generally comprise a range of shapes, sizes and mineralogies of their magnetic grains, and show therefore a range of blocking temperatures as different grains gradually 'block

in ´ their TRMs during cooling from T_c. The TRM that is acquired in a specific blocking temperature interval during cooling is called partial thermoremanent magnetisation (pTRM). The law of additivity (Thellier, 1938) states, that the vector sum of all pTRMs between T_c and ambient temperature equals the value of the total TRM.

Isothermal remanent magnetisation

All processes that lead to the acquisition of a remanent magnetisation without a change of temperature can be combined under the umbrella term of isothermal remanent magnetisation (IRM). By definition, all processes introduced in this sub-section (other than (p)TRMs) are IRMs. In practice, an IRM refers to the remanent magnetisation due to a strong external field applied over a short period of time. In nature, IRMs can occur as secondary NRMs due to lightning strikes (Butler, 1992).

Chemical remanent magnetisation

Chemical processes such as the growth of new magnetic minerals, or chemical and structural changes of pre-existing grains, can lead to the acquisition of a chemical remanent magnetisation (CRM) at constant temperature T_{CRM}. If this process occurs during the initial cooling of the rock formation, then the resulting magnetisation is referred to as thermochemical remanent magnetisation (TCRM). In this case, the TCRM would be considered a primary magnetisation. In nature, CRMs and TCRMs can also be acquired at some point after the initial cooling of the rock as secondary NRMs (Shcherbakov et al., 2019). The process of CRM acquisition is, in principle, similar to the acquisition of a TRM, and equation 1.5 can be used for the determination of relaxation times. Instead of changes in temperature (and temperature dependent changes of j_s and h_c), the grain volume v increases as new magnetic grains are formed until the 'blocking volume´ is reached, at which the relaxation time increases significantly (Dunlop & Özdemir, 1997).

Viscous remanent magnetisation

A remanent magnetisation that is acquired gradually due to long exposure to weak magnetic fields is referred to as viscous remanent magnetisation (VRM) if the magnetisation is acquired at ambient temperatures, and as thermoviscous remanent magnetisation (TVRM) for the acquisition at an elevated temperature between Tc and ambient temperature. In nature, VRMs and TVRMs occur as secondary NRMs, usually due to exposure to Earth's geomagnetic field over long time periods, and are generally treated as noise in palaeomagnetic experiments (Butler, 1992).

Anhysteretic remanent magnetisation

The acquisition of an anhysteretic remanent magnetisation (ARM) occurs by superimposing the weak direct current (DC) field with an initially strong alternating field (AF) with gradually decreasing magnitude. An ARM in direction of the weak bias field is locked in when the grain's microscopic coercive force exceeds the strength of the oscillating AF field. During the progressive decay of the AF field, the ARM is imparted in grains with gradually decreasing coercive forces. ARM acquisitions differ from the acquisition of TRMs due to differences in grain size dependencies for remanence magnitudes. The remanence acquired from the same external field can be much higher for a TRM than for an ARM (Tanaka & Komuro, 2009; Yu, 2010).

Other remanent magnetisations

Other types of remanent magnetisations have little to no importance in this specific thesis. However, at least one other type should be mentioned as it is very common in nature: detrital remanent magnetisation (DRM). DRMs are acquired through alignment of magnetised particles with the ambient field during deposition of sediments. These magnetisations can be affected by physical and chemical processes during deposition and compaction. A DRM is locked in when dewatering and consolidation prevents any motion of the (magnetised) sedimentary particles. The strength of a DRM shows a linear dependence on the the strength of the ambient field at the time of sedimentation. Because the conditions of DRM acquisition cannot be reproduced in a laboratory, however, absolute values of the ancient field strength cannot be recovered from a DRM. Instead, rocks carrying a DRM are used to determine relative field strengths (see section 1.4, Tauxe et al., 1995).

1.2.5 Magnetic minerals

There are numerous magnetic phases that can carry remanent magnetisations in natural rocks. The most important magnetic minerals in Earth's crust are the iron and titanium oxides shown in the ternary diagram in Figure 1.2. This section provides a short description of the main magnetic minerals that are relevant for palaeomagnetic studies of igneous rocks.

Titanomagnetite

One of the primary crystallising phases in igneous rocks (1 - 5 vol%, Butler, 1992) are the opaque and cubic minerals of the titanomagnetite series (TMx%, $Fe_{3-x}Ti_xO_4$, $0 \leq x \leq 1$) between the end-members magnetite (TM0, Fe_3O_4) and ulvöspinel (TM100,

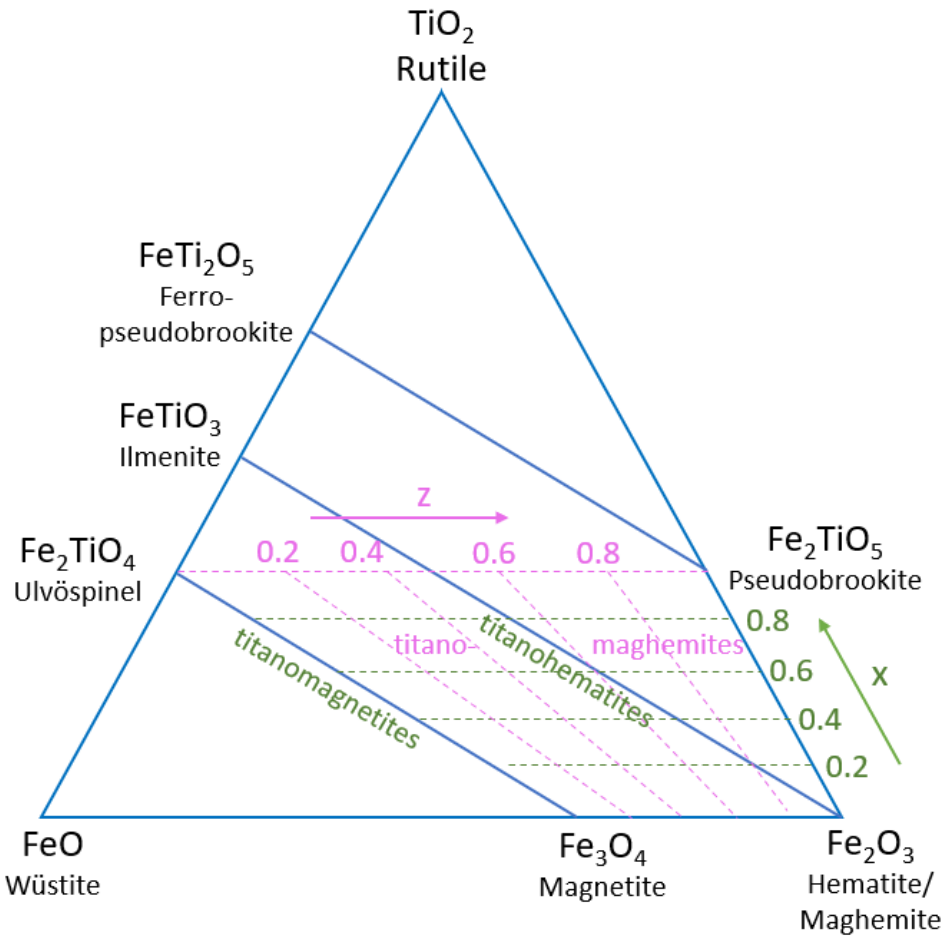

FIGURE 1.2: Ternary diagram of titanium- and iron oxides. X indicates the titanium concentration for the solid solution series of titanohematites. Z shows direction and grades of oxidation. For details see text. Redrawn after Dunlop and Özdemir (1997).

Fe_2TiO_4). The compositional parameter x gives the mol fraction of Ti that is replacing Fe by substituting $2Fe^{3+}$ for Ti^{4+} + Fe^{2+}. The complete solid solution series for all compositions of TM is formed at temperatures > 600°C. Single phase minerals of intermediate TM compositions at ambient temperatures are only preserved if the melt is cooled rapidly, as slower cooling would result in exsolution intergrowth structures of near-magnetite and near ulvöspinel phases. The general abundance of oxygen in basaltic melts leads to a high-temperature oxidation of titanomagnetites and magnetite-ulvöspinel phase intergrowths therefore rarely occur in nature. Instead, this oxy-exsolution results in intergrowths of near-ilmenite and near-magnetite phases (Dunlop & Özdemir, 1997).

Titanomagnetites have an inverse spinel crystal structure of $(A)[B]_2O_4$, where the Fe

cations in the A and B sublattices are distributed as $(Fe^{+3})_A[Fe^{3+},Fe^{2+}]_BO_4{}^{-2}$, which results in an uneven distribution of antiparallel magnetic moments, and makes titanomagnetites ferrimagnetic. Because of their filled electron orbital, Ti^{4+} cations do not have an atomic magnetic moment. Rock magnetic parameters of titanomagnetites are therefore highly dependent on their composition and saturation magnetisation as well as Curie temperatures decrease almost linearly with increasing Ti content from the initial values of M_s = 480 kA/m (at 23°C) and T_c = 580°C for pure magnetite (Dunlop & Özdemir, 1997; Lattard et al., 2006). Both M_s and T_c can be lowered further through substitution of minor amounts of Al^{3+}, Mg^{2+} and Mn^{2+} into the crystal structure, which is often the case for natural titanomagnetites (Özdemir & Moskowitz, 1992).

Titanohematite

The opaque, rhombohedral minerals of the titanohematite series ($Fe_{2-x}Ti_xO_3$, $0 \leq x \leq 1$) show rock magnetic properties that differ substantially from the titanomagnetites. The end member hematite (αFe_2O_3) is a canted antiferromagnetic mineral, where slightly canted antiparallel magnetic moments of the Fe^{3+} cations in the A and B sublattices result in a weak spontaneous magnetisation. Hematite is defined by a low saturation magnetisation of M_s = 2.5 kA/m (at 23°C) and a high Curie temperature of T_c = 675°C (Dunlop & Özdemir, 1997). Similar to the titanomagnetite series, titanohematites have a complete solid solution series at high temperatures and the degree of exsolution depends on the cooling history. In contrast to the linear decrease of T_c with increasing Ti-content, the saturation magnetisation of titanomagnetites has a non-linear dependence on composition. For compositions of $x < 0.45$, the substitution of Ti^{4+} cations for Fe^{3+} cations results in an equal distribution of Ti and Fe cations in the cation layers and the low saturation magnetisation as well as the canted antiferromagnetic behaviour remain approximately constant (Butler, 1992). For higher Ti contents of $x \geq 0.45$, Fe and Ti cations are distributed unequally and titanomagnetites in this compositional range are ferrimagnetic. In the compositional range around $0.5 \leq x \leq 0.7$ of rapidly cooled single phase titanomagnetites, microscopic exsolutions into ferrimagnetic high-Ti phases and canted antiferromagnetic low-Ti phases can lead to self-reversed thermoremanent magnetisations (Dunlop & Özdemir, 1997).

Titanomaghemite

The process of low-temperature ($\leq$ 200°C) oxidation of (titano)magnetites, which commonly occurs during weathering of rocks, is indicated by the horizontal lines in Figure 1.2, where increasing degrees of oxidation are indicated by the values of the oxidation parameter z ($0 \leq z \leq 1$). The final product of fully oxidised TM0 is maghemite

(γFe_2O_3), which is a chemical equivalent of hematite, but has the spinel crystal structure of magnetite. During the oxidation process, the valence state of two thirds of the available Fe^{2+} changes to Fe^{3+}, while one third of the original Fe^{2+} is removed by diffusion (Butler, 1992), which mainly happens at the crystal surface. The removal of Fe^{2+} cations in maghemite leads to a decreased saturation magnetisation of M_s = 380 kA/m and a smaller unit cell edge of a = 8.337 Å compared to magnetite (M_s = 480 kA/m, a = 8.396 Å; Dunlop and Özdemir, 1997). The cubic maghemite is a metastable mineral that inverts to the rhombohedral hematite upon heating to temperatures above 250°C. The Curie temperature of maghemite is difficult to measure, because it generally lies above the inversion temperature, but it is estimated to be between 590°C and 675°C (Dunlop & Özdemir, 1997). Titanomaghemites from the low-temperature oxidation of titanomagnetites show similar behaviour, where unit cell edge and saturation magnetisation decrease, and Curie temperatures increase with increasing z. Low-temperature oxidation is a slow process and maghemites generally carry a remanence in form of a (secondary) CRM.

Fe-oxyhydroxides and Fe-sulfides

Neither Fe-oxyhydroxides nor iron sulfides have a major impact in this thesis, but are mentioned as they commonly occur as weathering products of igneous rocks. Goethite (αFeOOH) is the most relevant oxyhydroxide and can be the result of alteration of pyrite (FeS_2). It is orthorhombic, antiferromagnetic, and converts to hematite through dehydration or heating (Butler, 1992). Iron sulfides occur in a range of compositions as FeS_{1+x} ($0 \leq x \leq 1$). For additional details on magnetic minerals, the reader is referred to Dunlop and Özdemir (1997).

1.3 May the FORC be with you – Rock magnetism and palaeo-directions

Since the days of Königsberger (1938), Thellier (1938), Néel (1949) and Nagata (1953, 1943), the field of rock magnetism has evolved to widespread usage in various fields of Earth and planetary science studies (e.g., Greve et al., 2021; Li and Kodama, 2016; Nagy et al., 2017; Tikoo et al., 2014; Yang et al., 2020). During palaeointensity analysis, rock magnetic data is mainly used to determine the type and domain state of the magnetic carriers in order to answer the essential question: are the rocks carrying a stable, primary (thermo)remanence? This section briefly introduces the theoretical background of those rock magnetic methods that are widely used in palaeointensity studies. Detailed information about the used equipment and experimental setup for

the palaeointensity studies, presented in Chapters 2 - 4, will be given in the 'method´ section of each chapter.

1.3.1 Hysteresis

Magnetic hysteresis describes the irreversible magnetisation process of ferromagnetic materials in external fields due to the energy that is spent either on (a) displacing domain walls to enlarge domains with magnetic moments, oriented in the direction of the applied field at the expense of domains with differently oriented moments, (b) on the nucleation of new favourably oriented domains, or (c) on the rotation of domains if no unfavourably oriented domains exist (Dunlop & Özdemir, 1997). The energy spent is similar for external fields of equal strengths in opposite directions and proportional to an area that is enclosed by a closed loop that describes the acquisition of magnetisation of the material in response to the external field (Dunlop & Özdemir, 2007).

The measurement of a hysteresis loop is started by applying a large field B to a sample. If the material was not previously subjected to a magnetising field, then it will acquire a magnetisation following the initial curve in Figure 1.3a. If at any point the external field is removed, the magnetisation of the material will not return to zero, as a remanent magnetisation M_r will be preserved and the magnetisation follows the curve of the minor loop to B = 0. If the applied field is large enough, then the material will reach its saturation magnetisation M_s. Further increases to the strength of B will not result in an additional increase in magnetisation. The remanent magnetisation that is preserved after removing a saturating field is the saturation remanence M_{rs}. To force the magnetisation to zero, the external field has to be applied in the opposite (negative) direction with a strength equal to the (bulk) coercive force B_c. A remanent magnetisation of zero after removal of the external field can be achieved by applying a negative field equal to the remanent coercive force B_{cr}. After the applied field is increased in negative direction to reach saturation, it is applied in positive direction again to complete the loop, which is (in its idealised and noise corrected form) inversely rotational symmetric about the origin (Jackson & Solheid, 2010; Paterson et al., 2018).

Hysteresis parameters are typically displayed in the Day diagram (Day et al., 1977), by plotting the ratios of M_{rs}/M_s and B_{cr}/B_c. In a Day diagram, lines of constant ratios divide the measured data into areas representing the grain sizes and domain states of the magnetic carrier (Figure 1.3b). The hysteresis of a magnetic particle depends on its size, shape, domain state, mineralogy as well as its state of stress (Roerts et al., 2018; Tauxe et al., 2002). Natural samples are rarely a simple assemblage of homogeneous

magnetic carriers and the measured hysteresis parameters are therefore only indicative of the bulk average properties of the sample. Additional variables, such as mineral stochiometry, surface oxidation, thermal relaxation, mixing, and measurement issues, introduce additional ambiguities into the Day diagram and it is not recommended to use the Day diagram for domain state analysis on its own (Roerts et al., 2018).

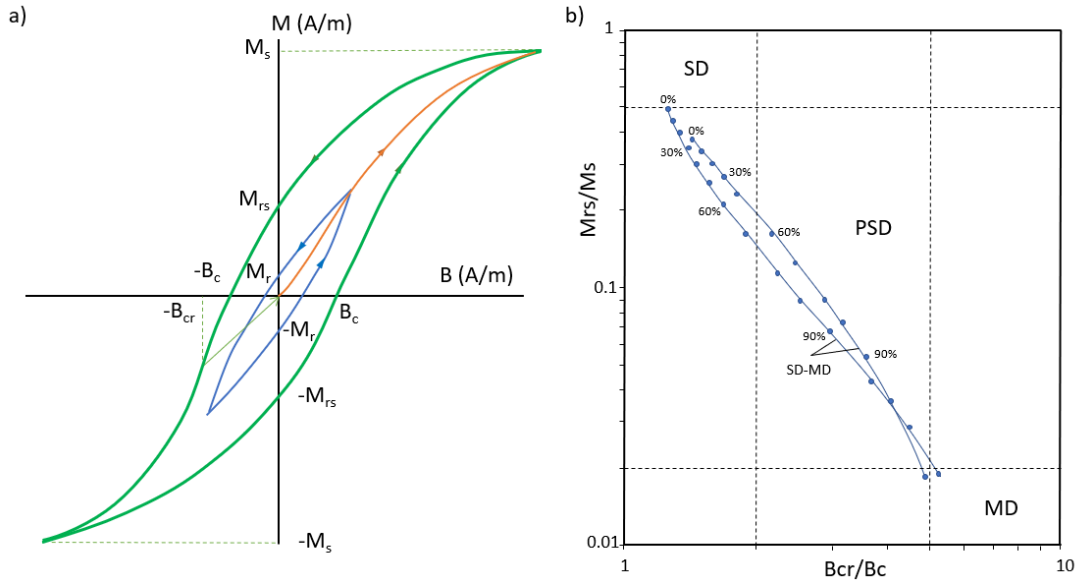

FIGURE 1.3: a) Schematic hysteresis loop showing the main hysteresis parameters. The initial curve is shown in orange. Blue and green represent minor and major loops, respectively. Redrawn from (Dunlop & Özdemir, 2007). b) Day (1977) plot showing mixing curves for single domain and multidomain particles (SD - MD) of magnetite based on Dunlop (2002). Percentages indicate the fraction of MD particles.

Theoretical curves for mixtures of grains with different domain states, shown in Figure 1.3b for the mixture of SD and MD magnetite (Dunlop, 2002), indicate that the qualitative interpretation of hysteresis parameters in the Day plot can be rather complex and more effort is being put into finding ways of unmixing mineral phases during hysteresis analysis (e.g., Fabian, 2003; Leonhardt, 2006). These processes are aided by increasingly powerful possibilities of simulating complex magnetic domain structures and creating numerical micromagnetic models of magnetic recorders (e.g., Conbhuí et al., 2018; Nagy et al., 2017; Williams et al., 2010). Nevertheless, bulk average hysteresis parameters have been used to predict the stability of remanence by characterising a trend of bulk domain stability (BDS) to pre-select specimens with high values of BDS that promise higher success chance for palaeointensity experiments (Paterson et al., 2017).

Diagrams of first-order reversal curves (FORC) are a different approach to presenting

hysteresis data (e.g., Harrison and Feinberg, 2008; Hejda and Zelinka, 1990; Pike et al., 1999). Before a FORC is measured, a sample is saturated by a strong positive field, after which the external field is decreased to a specific value B_a of a reversed field. The magnetisation of the sample as function of an increasing field B_b between the point B_a and positive saturation is measured as one FORC. This process is repeated for multiple different reversal fields, where the values of B_a and B_b are chosen to cover a regular grid, so that a large number of FORCs sample the whole area enclosed by the major hysteresis loop. The resulting FORC diagram is a contour plot of the mixed second derivative of the magnetisation $M(B_a,B_b)$ with respect to B_a and B_b. The FORC distribution at any point is calculated by a least squares fit to $M(B_a,B_b)$ or a locally weighted regression smoothing technique where the number of points included in the fit is controlled by the smoothing factor SF (Harrison & Feinberg, 2008; Pike et al., 1999).

1.3.2 Susceptibility and thermomagnetic curves

The temperature dependence of saturation magnetisation and bulk susceptibility is often measured in order to identify the mineralogy of different magnetic phases in a natural sample by determining their Curie temperatures. To measure a 'strong-field thermomagnetic´ curve of temperature dependent magnetisation $M_s(t)$, a specimen is placed in a strong (> 100 mT) and constant external field, and the specimen's magnetisation is measured while the temperature is increased (and decreased). The Curie temperatures can be determined at major drops of M_s and are approximated by the analysis software by identifying the maximum concave curvature of the smoothed data curve either through calculation of the second derivative (Leonhardt, 2006), or by finding the intersection of the two tangents (Gromme et al., 1969). The analysis of curves of temperature dependent susceptibilities $\kappa(t)$ generally follows a similar approach. However, the physical justification for the use of the same methods to determine Curie temperatures from $M_s(t)$ and $\kappa(t)$ curves has been questioned (e.g., Petrovský and Kapička, 2006) and alternative methods have been proposed (e.g., Curie temperature from Hopkinson peak; Wehland et al., 2005). Curves of $M_s(t)$ and $\kappa(t)$ are measured during heating and cooling of the specimen and the similarity of the heating and cooling curves can give additional essential information about the thermal stability of the magnetic grains. Differences between heating and cooling curves can be an indicator that magnetic grains have been created, destroyed, or converted to a different phase during the heating process. To pinpoint the approximate temperature at which these alterations occur, $M_s(t)$ and $\kappa(t)$ curves can be measured in several

heating-cooling cycles to progressively increased maximum temperatures. Measurements of susceptibility versus temperature are commonly conducted in an Argon environment to discourage oxidation processes during heating.

1.3.3 Magnetic anisotropy

Rocks show magnetic anisotropy if their induced and/or remanent magnetisation direction differs from the direction of the magnetising field (Butler, 1992). Two important types of magnetic anisotropy are anisotropy of magnetic susceptibility (AMS) and anisotropy of remanent magnetisation. AMS can be measured rapidly by measuring the susceptibility of a specimen in several (≥ 6) directions to obtain a magnetic susceptibility ellipsoid, which is defined by the three perpendicular directions of maximum (K1), intermediate (K2), and minimum (K3) susceptibility. AMS is often connected to shape and orientation of magnetic grains and measurements of AMS have wide applications from sedimentology to structural geology (e.g., Yang et al., 2020). Rocks with strong AMS are likely to show a strong anisotropy of remanent magnetisation, making them inaccurate magnetic recorders. However, AMS and remanence anisotropy are not always closely related, as AMS measures the anisotropy of all available magnetic particles, irrespective of their actual contribution to the remanent magnetisation. The anisotropy of remanent magnetisation is obtained by imparting and measuring ARMs in six directions. The resulting ARM tensor can be used to apply anisotropy corrections to palaeomagnetic and palaeointensity results, a procedure that is slowly becoming the standard for analysis of materials where higher grades of anisotropy are expected (e.g., Schnepp et al., 2020b).

1.3.4 Demagnetisation

Demagnetisation is the process of unblocking magnetic moments in a material in order to remove a remanent magnetisation by randomising the orientations of magnetic moments of a sample. Thermal demagnetisation follows the Néel (1955) theory of TRM acquisition described in section 1.2.4. A bulk sample is heated from ambient temperature to a temperature T_{demag} ($< T_c$), causing all magnetic grains with blocking temperatures $T_b \leq T_{demag}$ to unblock and randomise their magnetisations. If the sample is subsequently cooled back down to ambient temperature in absence of an external field, then these magnetic grains retain the randomised magnetisations, the remanent magnetisation carried by magnetic grains with $T_b \leq T_{demag}$ is erased, and the sample is 'partially demagnetised´. Higher values of T_{demag} will cause particles in a larger range of blocking temperatures to demagnetise, until the sample is fully demagnetised when T_{demag} exceeds the maximum Curie temperature of any magnetic carrier in the bulk sample (Figure 1.4a).

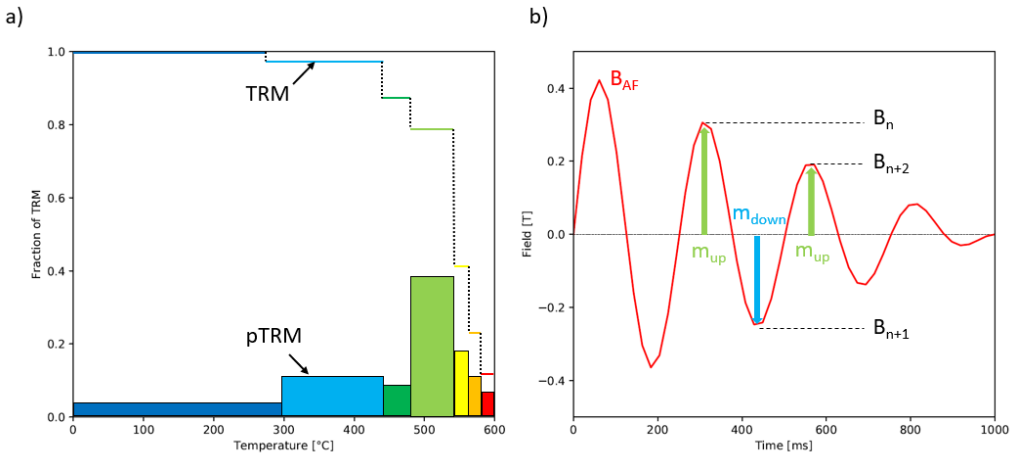

FIGURE 1.4: a) Schematic distribution of pTRMs and blocking temperatures that are removed during thermal demagnetisation. The total TRM at every temperature T is the sum of all pTRMs with $T_b \geq T$; b) Alternating Field demagnetisation: magnetic moments align with the alternating field (red) and block in arbitrary 'up´ (green) and 'down´ (blue) orientation so that the moments with coercivities $B_C \leq B_{AF}$ cancel out. Redrawn after Butler (1992).

Physically, the thermal energy applied to the sample causes lattice vibrations (phonons) that transfer energy to the magnetic system by creating spin waves (magnons) that affect the precession of magnetic moments and decrease their alignment. With increasing energy, more magnons are created until the magnetic moments are fully randomised at T_c (Gubbins & Herrero-Bervera, 2007; Néel, 1949). During microwave demagnetisations, magnons are created directly using ferrimagnetic resonance (FMR), where microwave photons decay into magnon pairs with half the frequency of the photon and opposite momentums (parallel pumping; Walton et al., 1992, 1993). In this process, the bulk sample is only heated by the dielectric loss and the phonons that are excited by the created magnons, resulting in considerably lower temperatures of the bulk sample (∼150 - 200°C; Hill and Shaw, 2000) compared to a conventional thermal demagnetisation. The application of microwave demagnetisation significantly increases the speed of the demagnetisation process and decreases the chances of thermochemical alterations in the bulk sample (Hill & Shaw, 1999; Walton et al., 1993). Dielectric heating and the generation of magnons are both frequency dependent. A balance between efficient generation of magnons and dielectric heating not being dominant was found for small (3 - 5 mm) samples in a cylindrical resonance chamber around 14.8 GHz (Suttie et al., 2010).

The procedure of alternating-field (AF) demagnetisation is, in essence, an ARM acquisition in an external field of B = 0. During AF demagnetisation (Figure 1.4b), the

sample is exposed to an alternating field, where the amplitude linearly decays from a peak value (B_{AF}) to zero. The alternating field can be represented in a time series as a sinusoidal wave with the amplitude B_n linearly decreasing at each cycle. If a sample is exposed to such a field, then, for each cycle, all magnetic moments with coercive forces of $B_n \leq B_c \leq B_{n+1}$ align with the oscillating field leading to an equal distribution of all magnetic moments with $B_c \leq B_{AF}$ in two directions and therefore demagnetising this coercivity range of a sample. This process is generally repeated for all three Cartesian axes of a sample. Alternatively, a sample can also be demagnetised while tumbling so that all three axes are affected simultaneously by the AF field.

All types of demagnetisation experiments are typically done in multiple steps where the magnetisation of a sample is repeatedly measured after demagnetisation with progressively increasing temperatures, microwave powers or AF peak fields, so that principle component analysis (PCA; Kirschvink, 1980) can be used to analyse multicomponent NRMs and their respective directions in a specimen coordinate system. To determine the direction of the ancient field, these NRM directions have to be rotated into a geographic coordinate system, using the in-situ orientation of the sampled/measured material.

1.4 To intensity and beyond - Introduction to palaeointensity determination

The geomagnetic field on Earth's surface at any point in time is defined by the full vector information of direction and intensity. The directional information can easily be obtained from PCA of stepwise demagnetisation data, but to be able to determine the strength of an ancient geomagnetic field, several assumptions have to be made. The theoretical foundation for palaeointensity determination lies in the proportionality of a (thermo)remanent magnetisation to the strength of the magnetising field (Néel, 1949, 1955). For an NRM of a rock, this can be expressed as $M_{NRM} = \alpha_{anc} * B_{anc}$, where α_{anc} is a proportionality constant. Similarly, a thermoremanent magnetisation imparted in a laboratory follows $M_{lab} = \alpha_{lab} * B_{lab}$. If the assemblage of magnetic carriers in the rock does not change, then it is assumed that α_{anc} equals α_{lab} and the two equations can be rearranged to

$$B_{anc} = \frac{M_{NRM}}{M_{lab}} * B_{lab}. \tag{1.6}$$

The used laboratory field B_{lab} is a known quantity and both M_{NRM} and M_{lab} can be measured to determine the strength of the ancient field B_{anc}. Following this simple

relationship, a palaeointensity could be determined simply from the measurement of the NRM of a sample as well as a measurement of its magnetisation after fully replacing the NRM with a laboratory induced magnetisation (e.g., by heating the sample to a temperature above its T_c in a known laboratory field B_{lab}). This total thermoremanent magnetisation (TTRM) method can be used for quick test measurements (e.g., Bono et al., 2019), but is not viewed as a reliable method to obtain palaeointensity estimates. This is because the equality of the ancient and laboratory proportionality constants cannot be verified and because it only works for a single component NRM which is uncommon in ancient rocks. To obtain reliable absolute palaeointensities, the TRM of a rock has to be viewed as a spectrum of partial TRMs, which allows to make three further assumptions that are known as Thellier's laws (Thellier, 1938; Thellier & Thellier, 1959).

As introduced in section 1.2.4, a pTRM is the remanent magnetisation that is acquired by cooling through two temperatures T_1 and T_2 (T_1,$T_2 \leq T_c$) in an external field. The 'law of additivity´ states that the sum of all pTRMs is equal to the total TRM of the rock. In addition, the direction and intensity of each pTRM of a temperature range T_1 - T_2 are fully independent of any other pTRM acquired in any temperature interval that does not overlap with the range T_1 - T_2. This is known as the 'law of independence´. For the laws of additivity and independence to be possible, the blocking and unblocking temperatures have to be identical, which is stated in the 'law of reciprocity´.

These assumptions form the theoretical basis for the determination of palaeointensities. However, they only hold true for an assemblage of small, non-interacting SD particles, since magnetostatic interactions between pTRMs of different blocking temperature ranges would break at least the laws of independence and additivity (Dunlop & Özdemir, 1997). For larger particles in the PSD/MD range, as well as for elongated SD particles, it has been shown that even the basic assumption of a linear relation between field strength and remanence acquisition can fail at relatively weak magnetising fields in the range of Earth's field strength (Dunlop & Argyle, 1997; Selkin et al., 2007). Other factors that influence a remanence acquisition, such as remanence anisotropy (e.g., Aitken, 1988), cooling rates (e.g., Halgedahl et al., 1980), or thermochemical alteration during heating experiments (e.g., Coe, 1967) further complicate the simplicity of palaeointensity determination as implied by equation 1.6. The search for a way of using the above assumptions to determine palaeointensities, while at the same time being able to detect (and sometimes adjust for) non-ideal effects, has led to a range of different methods that are presently used for the determination of palaeointensities. This section briefly outlines the theoretical backgrounds of the most common methods that were utilised in the studies presented in Chapters 2 - 4. The specific experimental setup and used equipment for each of these studies will be given in the 'method´

sections of Chapters 2 - 4.

1.4.1 The Thellier method

Factors that lead to an inequality of the proportionality constants α_{anc} and α_{lab}, such as multicomponent NRMs or chemical alterations during laboratory heating, affect different blocking temperature ranges of the sample. Viscous overprints and chemical alterations during heating are often found at low and high blocking temperatures, respectively. In an effort to detect such effects during palaeointensity determination, a method was developed that employed a stepwise replacement of natural pTRMs with laboratory pTRMs at progressively increasing blocking temperature ranges (Koenigsberger, 1938; Thellier, 1938; Thellier & Thellier, 1959). This method is sometimes referred to as 'Königsberger-Thellier-Thellier (KTT) technique´ (Tauxe & Yamazaki, 2015), but commonly known simply as 'Thellier technique´ or 'Thellier method´. The vast majority of palaeointensities (77.4%) that have been measured in the past and are collected in the PINT database (v2015.05; Biggin et al., 2015), have been determined with the Thellier method (or one of its variants). In the original form of the Thellier method, a sample was heated (and cooled) in a laboratory field twice for each progressively increasing temperature step (T_i). The magnetisation was measured after each of these in-field (I) steps and the orientation of the sample was reversed for the second heating, so that the remaining magnetisation and gained magnetisation at each temperature could be determined from vector subtraction. The resulting values of $NRM_{remaining}$ and $pTRM_{gained}$ are commonly plotted against each other in an 'Arai plot´ (Nagata et al., 1963) as shown in Figure 1.5. In an idealised experiment, the plotted results would show a linear relationship between $NRM_{remaining}$ and $pTRM_{gained}$ where the slope of a best-fit line represents the ratio of M_{NRM}/M_{lab} and can be used together with the known laboratory field strength to determine the palaeointensity using equation 1.6.

After magnetic shielding was improved and became more readily available, several variants of the original Thellier (OT or II) protocol emerged, that replaced one of the I-steps with a zero-field (Z) step. In these variants, the Z-step is either measured before the I-step (ZI or Coe protocol; Coe, 1967), after the I-step (IZ or Aitken protocol;Aitken, 1988), or in alternating order (IZZI protocol; Tauxe and Staudigel, 2004; Yu and Tauxe, 2005) at each temperature step. For each of these protocols, the I step of a temperature T_i (or both I steps in the OT protocol) can be repeated at a lower temperature $T_{i\text{-}x}$ as a so-called 'pTRM check´, to ensure that the rock's capacity to acquire a magnetisation has not changed for the blocking temperature range of T_i - $T_{i\text{-}x}$ and that equation 1.6 is still valid.

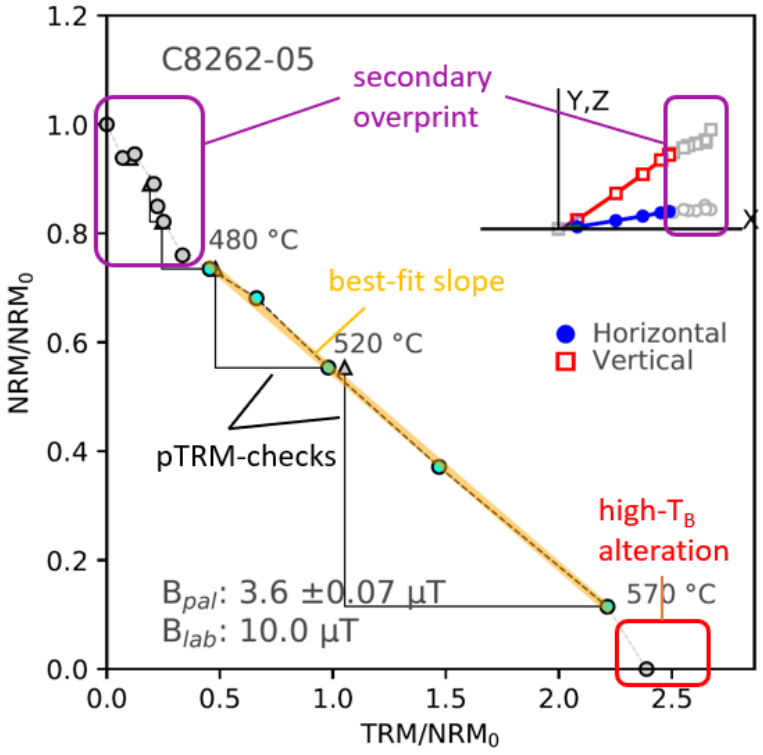

FIGURE 1.5: Schematic example of an Arai plot (Nagata et al., 1963) for the analysis of Thellier-style experiments. Associated directions are shown in a Zijderveld (1967) plot (top right). The best fit slope (yellow) for the calculation of B_{anc} (B_{pal}) was determined from the selected points (cyan) representing the primary magnetisation. Highlighted areas in the low and high blocking temperature areas indicate a (viscous) overprint from a stronger ambient field and laboratory induced thermal alteration, respectively.

In a qualitative analysis of an Arai plot, non-linear portions of data represent non-ideal effects that can bias or prevent the determination of palaeointensities. With the exception of multicomponent NRMs and chemical alterations during heating, the causes for such non-linear Arai plots are still poorly understood but most likely represent violations of the law of reciprocity (Tauxe et al., 2020). This is often the case for, but not limited to, rocks that contain larger PSD or MD particles. Non-ideal effects that are linked to 'MD behaviour´ lead to curved, 'sagging´, and/or 'zig-zagging´ Arai plots, and can result in inaccurate palaeointensity results, which often underestimate the ancient field strength when the high temperature portion of the curve is used to fit the slope (e.g., Cromwell et al., 2015; Krása et al., 2003; Paterson et al., 2015; Smirnov et al., 2017). In these cases, the violation of the law of reciprocity is seen when the demagnetisation of a sample in a blocking temperature range does not fully remove a pTRM given to the sample in the same blocking temperature range. The part of the pTRM that is not demagnetised is referred to as 'pTRM tail´ and can be detected

with 'pTRM tail checks´, where the Z-step at a given temperature is repeated after the I-step of the same temperature (Riisager & Riisager, 2001). A method to statistically correct palaeointensity biases from non-linear Arai plots has recently been proposed (Cych et al., 2021), but at the moment it is still common practice to reject results from non-linear Arai plots. The numerical basis for the quantitative detection and rejection of biased intensity results lies in statistical quantities, that are compiled in the Standard Paleointensity Definitions (SPD v1.1, Paterson et al., 2014) and can be combined to sets of 'selection criteria´ (e.g., Biggin et al., 2007a; Kissel and Laj, 2004; Leonhardt et al., 2004a; Paterson et al., 2015) that define a maximum threshold of non-ideal effects for an unbiased result. However, to date, little to no consensus exist on which set of selection criteria to use (see section 2.4).

The large number of heating steps required for a Thellier experiment is one of the major disadvantages of the method, as it makes this technique time-consuming. Also, each consecutive heating step presents an additional chance to introduce thermochemical alterations in the sample. In addition, excellent temperature control is required to ensure that the same temperatures can be reproduced for each of the double heating temperature steps. In order to offset these disadvantages, Kono and Ueno (1977) introduced a single-heating variant of the Thellier technique. This protocol determined the values of NRM remaining and pTRM gained from vector subtraction of a single I-step at each temperature in the blocking temperature range of the primary magnetisation, where the direction of the laboratory field is chosen perpendicular to the ChRM of the sample. With this so-called 'perpendicular protocol´ variant of the technique, a full experiment could be conducted in half the time. However, a lack of pTRM checks reduces this method's ability to produce reliable palaeointensity estimates (Grappone et al., 2020).

1.4.2 The microwave method

In an effort to reduce laboratory alteration, a step towards less time-consuming experiments was made with the microwave palaeointensity method. In principle, the microwave method is an exact copy of the conventional Thellier technique with the difference that it applies microwave demagnetisation and remagnetisation (Walton et al., 1992, 1993; see section 1.3.4) instead of conventional heating and cooling in an electric oven. It significantly reduces the duration of an experiment, as every heating-cooling step can be completed in tens of seconds instead of tens of minutes. In addition, the direct excitation of magnons prevents excessive heating of the bulk sample and temperatures rarely exceed 200°C (Gratton et al., 2005; Hill & Shaw, 2000), reducing thermochemical alteration of the rock.

Palaeointensity experiments conducted with a first generation 8.2 GHz microwave system (Hill & Shaw, 1999, 2000; Shaw et al., 1996) struggled with the accurate reproduction of 'heating temperatures´ (e.g., Böhnel et al., 2003; Tauxe and Yamazaki, 2015), as defined by the absorbed power integral from used microwave power and exposure time. This prevented the use of double heating protocols and microwave palaeointensity determinations were restricted to the use of the single heating perpendicular protocol (Hill & Shaw, 2007). Improvements to the reproducibility of internal temperature steps in the latest generation 14 GHz microwave system (Hill et al., 2008; Suttie et al., 2010), that is presently available and utilised only at University of Liverpool's Geomagnetism Laboratory, enable the use of double-heating Thellier protocols (Grappone et al., 2019, 2020; Gratton et al., 2007). Analysis of microwave Thellier data is conducted in an identical manner to conventional Thellier data and the method therefore inherits all issues and ambiguities related to nonlinear Arai plots from the conventional Thellier techniques (Tauxe & Yamazaki, 2015).

Since the first application of the microwave technique, concerns about differences between the processes of thermal and microwave blocking and unblocking of remanences have been raised (e.g., Le Goff and Gallet, 2004), as such differences could prevent palaeointensity determination. Even though reliable palaeointensities have been successfully recovered in many studies using the microwave method (e.g., Greve et al., 2017; Hawkins et al., 2019; Hill et al., 2002, 2008; Shcherbakova et al., 2017; Suttie et al., 2010), puzzling differences in absolute palaeointensity estimates between (perpendicular protocol) microwave and conventional (OT protocol) Thellier experiments on Hawaiian lava flows (Biggin, 2010; Grappone et al., 2019; Gratton et al., 2005; Teanby et al., 2002) reduced trust in the reliability of the microwave method. Recently, Grappone et al. (2020) found the source of these differences in the inability of the used microwave and thermal Thellier protocols to detect non-ideal MD-like behaviour.

Even though the microwave method is mainly used for Thellier-type experiments, promising results have been gained when the microwave method was applied to reduce the time- and material-consumption of other palaeointensity techniques (e.g., Yamamoto and Shaw, 2008).

1.4.3 The Wilson method

A less utilised way to compare the NRM with a laboratory induced TRM is the so-called 'Wilson method´ (Muxworthy, 2010; Wilson, 1961). In this method, measurements are taken during the continuous thermal demagnetisation of the NRM of the

sample. After cooling in a known laboratory field from a temperature above T_c, another continuous thermal demagnetisation curve is measured where this TRM is removed. The palaeointensity is then determined from the comparison of these two curves.

An obvious advantage of using the Wilson method lies in the continuous measurements at temperature during the two demagnetisations, which make it an exceptionally fast way of determining an absolute palaeointensity. Since a full TRM is acquired by the sample during cooling from T_c instead of a series of pTRMs, the resulting palaeointensity is not biased by pTRM tails and is said to be independent of magnetic domain states (Muxworthy, 2010). However, to reach T_c of the magnetic carriers in a rock, it is generally necessary to heat the sample to high temperatures, which favours the occurrence of chemical alteration, which can then be seen in different shapes of the two demagnetisation curves. Without the possibility of confirming that different curve shapes are caused by chemical alteration during the second heating without the first heating being affected, it is not possible to use the magnetic information of a blocking temperature range below the alteration temperature to determine a palaeointensity. If such a chemical alteration occurred only in the first heating step and did not continue in the second, then it would not be detectable at all by differently shaped demagnetisation curves, and a biased palaeointensity result could be accepted.

1.4.4 The Shaw method

The comparison of NRM/TRM_{lab} ratios for different sections of a rock's coercivity spectrum forms the basis of the 'Shaw technique´ (Shaw, 1975; van Zijl et al., 1962). Similar to a Wilson experiment, the specimen is given a full TRM by heating it once to a temperature above T_c in a known field, but in this case, the demagnetisation curves are gained from AF demagnetisation for both the original NRM (step NRM0) and the laboratory induced TRM (step TRM1). Since a full TRM is demagnetised for the second curve, possible chemical alterations during the heating step would lead to the rejection of data from the whole coercivity spectrum. As an improvement, Rolph and Shaw (1985) introduced an 'ARM correction´ to account for small chemical alterations during heating. For this, the sample is given a full ARM which is then AF demagnetised. This is done before and after the heating step, so that the ratio of M_{ARM} before heating (step ARM0) to M_{ARM} after heating (step ARM1) can be used to correct TRM1 to values of TRM1* using TRM1* = TRM1 $\times$ ARM0/ARM1. However, this correction is only effective for small degrees of alteration where the ratio of TRM/ARM acquisition is not greatly influenced by changes of grain size, or changes in the blocking temperature/coercivity spectra (Dunlop & Argyle, 1997; Kono, 1985; Tanaka & Komuro, 2009).

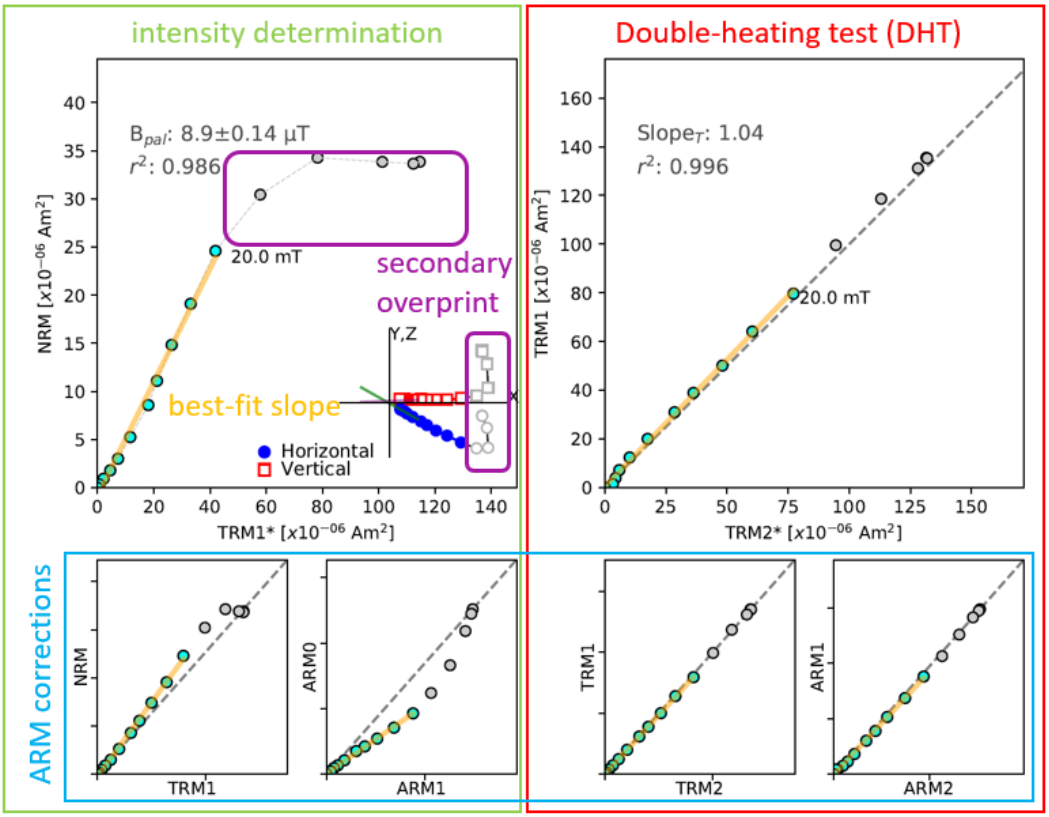

FIGURE 1.6: Example of analysis plots for a DHT-Shaw experiment. Left (green) and right (red) columns show the best fit lines (yellow) to the selected coercivity range of primary magnetisation (cyan) and the associated ARM corrections (blue) for the first and second heating, respectively. Palaeointensities are determined from the plot of $NRM_{remaining}$ versus ARM corrected $TRM_{remaining}$ (top left). Secondary overprints are seen in a change of the Zijderveld plots of the AF demagnetisation of NRM.

To confirm that this correction is valid, a second ARM correction can be done after imparting a second full TRM by heating the sample to a temperature above its T_c (Figure 1.6; Tsunakawa and Shaw, 1994). If the ARM correction in this 'double-heating test´ (DHT) is valid, then the theoretical slope between TRM1 and the ARM-corrected TRM2* would be 1. To encourage a similar degree of alteration to occur in the first and second heating steps, the sample is kept at maximum temperature for a longer time in the second step. There is, however, no consensus about how to define 'longer´ in this case (Lloyd et al., 2021b and references therein). The effectiveness of the DHT was confirmed by Tanaka and Komuro (2009) who concluded that the Shaw method should not be attempted without the double heating test.

The presently used iteration of this method often includes a pre-measurement step

of low-temperature demagnetisation (LTD; Yamamoto et al., 2003) to remove parts of the remanence that are held by MD particles, which could bias the resulting palaeointensity. However, concerns have been raised that LTD can remove some of the low coercivity fraction of magnetisation carried in SD grains as well (Carter-Stiglitz et al., 2006; Tauxe & Yamazaki, 2015). In addition, LTD treatment significantly increases the duration of an experiment. Studies utilising the LTD-DHT-Shaw protocol (e.g., Lloyd et al., 2021a; Yamamoto et al., 2007a), or a DHT-Shaw protocol without LTD treatment (e.g., Kitahara et al., 2018), have demonstrated similar palaeointensity results and success rates compared to thermal and microwave Thellier results.

Changes in the coercivity/blocking temperature spectra during heating, that can be caused by MD particles and/or alteration, can lead to small non-linearity of the analysed plot of NRM0-TRM1* (Tanaka & Komuro, 2009). Tanaka and Komuro, 2009 suggested that linearity of the NRM-TRM1* plot should be considered during analysis of Shaw results. As an objective way of doing this, Lloyd et al. (2021b) introduced the application of the curvature parameter (Paterson, 2011) as an additional rejection criterion for analysis of Shaw-type experiments.

1.4.5 The calibrated pseudo-Thellier method

A method that completely avoids heating steps is the so-called 'pseudo-Thellier´ technique that uses an induced ARM_{lab} instead of a TRM_{lab} (e.g., Tauxe et al., 1995). In the pseudo-Thellier protocol, stepwise AF demagnetisation is used to remove a sample's NRM. After this demagnetisation, the sample is subjected to a stepwise acquisition of an ARM which is subsequently demagnetised as well. For analysis, $NRM_{remaining}$ can be plotted against ARM_{gained} at every AF level in a 'pseudo-Arai plot´ to get a slope of B_{anc}/B_{lab}. Since B_{anc} and B_{lab} are different types of remanences, equation 1.6 can only be used to gain relative palaeointensity values (e.g., Béguin et al., 2019; Tauxe et al., 1995). In order to obtain absolute palaeointensities, the results have to be calibrated to account for the ratio of different remanence acquisition efficiencies between TRMs and ARMs. In such a 'calibrated pseudo-Thellier´ experiment, an absolute palaeointensity is determined using $B_{anc} = b * B_{lab}/c$, where b is the absolute value of the slope of $NRM_{remaining}/ARM_{gained}$ and c is the calibration factor (Paterson et al., 2016). The calibration factor has been determined from comparison of experimental pseudo-Thellier palaeointensity results from historical or archaeological sample material with the expected field strengths according to the international geomagnetic reference field (IGRF; de Groot et al., 2013; Paterson et al., 2016; Yu, 2010). Each study reports slightly different calibration factors, none of which result in a zero intercept for the ratio of B_{anc}/B_{IGRF}. The reason for this is unknown (Paterson et al., 2016), but suspected to lie in a non-linearity of the calibration in the weak-field range (de Groot et al., 2013). The

most recent iteration of the calibration factor was defined by Paterson et al. (2016) as c = 0.0820 ± 0.0207. The large uncertainty of this factor directly propagates to a large uncertainty of every palaeointensity result gained from this method.

The TRM/ARM ratio is grain size dependent (e.g., Levi and Merrill, 1976; Yu, 2010; Yu et al., 2003), and the calibration factor is not linear for all grain size distributions (de Groot et al., 2013). The AF field strength that is required to demagnetise half of the imparted ARM ($B_{1/2ARM}$) is often used as a selection criterion to screen out specimens with non-ideal grain size distributions (Béguin et al., 2019; de Groot et al., 2013). In addition, Paterson et al. (2016) looked at changes in the ratio of ARM_{left} to ARM_{gained}, where non-linearity can suggest a violation of the law of reciprocity. With the issues and the uncertainty related to the calibration factor, it is presently not recommended to use the calibrated pseudo-Thellier technique as a standalone method for the determination of absolute palaeointensities (Paterson et al., 2016). In the following chapters, pseudo-Thellier results have been given supportive meaning – experiments were conducted, but the resulting absolute palaeointensities were not used to calculate a mean palaeointensity with the results from the other methods.

1.4.6 The Multispecimen Protocol method

Another family of methods that reduce the number of required heating steps for palaeointensity determination is the 'multispecimen procedure´ where a set of sister specimens with the same cooling history is exposed to a low number of heating steps that can then be analysed like a standard Thellier experiment in a composite Arai plot (Hoffman & Biggin, 2005; Hoffman et al., 1989). By reducing the maximum temperatures as well as the number of heating steps, both the experiment time and the risk of alteration for each sister specimen is reduced. However, experimental difficulties and a focus on a lower blocking temperature range can lead to overestimates of the ancient field gained from this method (Tauxe & Yamazaki, 2015). Another method following the idea of using multiple specimens was introduced by Dekkers and Böhnel (2006). This 'multispecimen parallel differential pTRM method´ (MSP-DB) was based on the idea that replacing a natural pTRM of a specimen with a laboratory pTRM, that is imparted parallel to the direction of the natural pTRM, will result in a higher total magnetisation if the laboratory field is stronger than the ancient field, or a lower total magnetisation if $B_{lab} < B_{anc}$. This method departs from the typical Thellier-approach of intensity determination, as each sister specimen is only heated to a single temperature that can be chose freely to be within the blocking temperature range of the primary NRM but below the temperature, at which alteration occurs. For each sister specimen, a different laboratory field is used, so that the ancient field strength can be calculated as the field strength where the removed $pTRM_{anc}$ would be equal to the imparted

$pTRM_{lab}$. With only a single heating step, this method was unable to the detect pTRM tails and chemical alterations, and generally struggled with multi-component NRMs. The latest iteration of this method is the 'domain state corrected multispecimen protocol´ (MSP-DSC) method, which uses four heating steps for each sister specimen (Fabian & Leonhardt, 2010). Here, the first two steps are used to impart a laboratory field parallel (step 1) and antiparallel (step 2) to a specimen's ChRM to determine the change in magnetisation due to the replaced pTRM, which leads to the same results as the MSP-DB technique. In the third step, the specimen is heated in zero-field and cooled with an applied field to determine the specimen's domain state from the size of the pTRM tails (Shcherbakov et al., 2001), seen from differences in blocking and unblocking temperatures (e.g., Krása et al., 2003; Leonhardt et al., 2004b). Data from this step is then used to apply a 'domain-state-correction´ to each specimen (Fabian & Leonhardt, 2010). The fourth step repeats step 1 to detect chemical alterations.

The introduced alteration check increases the reliability of MSP-DSC results compared to the results of MSP-DB experiments, but chemical alterations during the first heating step are still not detectable. Nevertheless, multiple studies have reported equivalent palaeointensities from MSP-DSC and thermal Thellier experiments (e.g., de Groot et al., 2013; Monster et al., 2015; Schnepp et al., 2020b). However, 'multispecimen´ methods require more sample material than other intensity methods and struggle with multicomponent/high blocking temperature NRMs as well as highly heterogeneous sample collections. They are therefore generally applied in palaeointensity studies of younger rocks. The sample collections, described and used in Chapters 2 – 4, comprise small numbers of heterogeneous rocks with multicomponent NRMs (Halls et al., 2015; McCausland & Hodych, 1998; Shcherbakova et al., 2020). This method was therefore not deemed suitable and therefore was not applied for palaeointensity determination in the studies described in this thesis.

1.4.7 Quantifying reliability of palaeointensity estimates - Q_{PI}

In order to assess the reliability of palaeointensity estimates, Biggin and Paterson (2014) introduced a set of qualitative reliability criteria (Q_{PI}). In its current form, this set consists of 10 criteria (Bono et al., 2021). For each site-mean palaeointensity estimate, these criteria assess the reliability of the associated age estimate (QAGE) and palaeomagnetic direction (QDIR), statistical robustness (QSTAT), thermoremanent origin of magnetisation (QTRM) and whether the palaeointensity averages results from more than one lithology (QLITH). Additional criteria assess the conducted intensity experiments in terms of possible biases due to thermochemical alteration

(QALT), non-ideal domain states (QMD), or non-linear TRM, cooling rate and anisotropy effects (QACN), and if different techniques have been used to increase the robustness of results (QTECH). One final criterion assesses if the specimen-level data is published following the FAIR (findable, accessible, interoperable and reusable; Wilkinson et al., 2016) principles (QMAG). Each criterion can either score 0 (fail) or 1 (pass), leading to a summarised Q_{PI} value 0 - 10. Q_{PI} values for palaeointensity estimates published before 2019 are available in the most recent update (v8.0.0) of the PINT database (Bono et al., 2021).

There are different ways that Q_{PI} criteria have been scored and applied in palaeointensity studies. The majority of studies (e.g., Hawkins et al., 2019; Shcherbakova et al., 2017) treat all criteria as equally relevant. Other studies (e.g., Kulakov et al., 2019) use a system of prioritised Q_{PI} criteria, where some criteria, such as QAGE and QTRM, were considered to be more important than others for the reliability of results. A thorough discussion of the importance and applications of different Q_{PI} criteria in published studies can be found in Bono et al. (2021). The main goal of Q_{PI}, however, is to serve as a guideline for best practice in palaeointensity determination. If these are followed, then palaeointensity estimates, especially from archaeological material, have repeatedly demonstrated to be able to reflect the recorded field (e.g., Schnepp et al., 2020a). With consistent treatment of errors, such palaeointensity results have shown to be within 12 - 15 % of the historical field strength, even without the rejection of outliers (Suttie et al., 2011).

1.5 DEEP impact - Determining Earth Evolution from Palaeomagnetism

The interactions between different layers in Earth's interior are responsible for a wide range of planetary processes, such as plate tectonics, volcanism, and the geodynamo. The study of such interactions and their formation and evolution throughout the planet's history is confronted with a major challenge, posed by the limitations of geological and geophysical observations. Geophysical observations of Earth's internal structure can give detailed information across all layers, which are, however, limited to showing a snapshot of the present-day state. In contrast, the geological record preserved in rocks covers a wide range of Earth's history, but only holds information of the uppermost layers of the planet (e.g., Gerya, 2019).

The gap of information about Earth's deep interior throughout geological time can be covered by observations of the geomagnetic field, which has been generated in the planet's outer core for the last $\sim$3.5 billion years (Biggin et al., 2015; Tarduno et al., 2010)

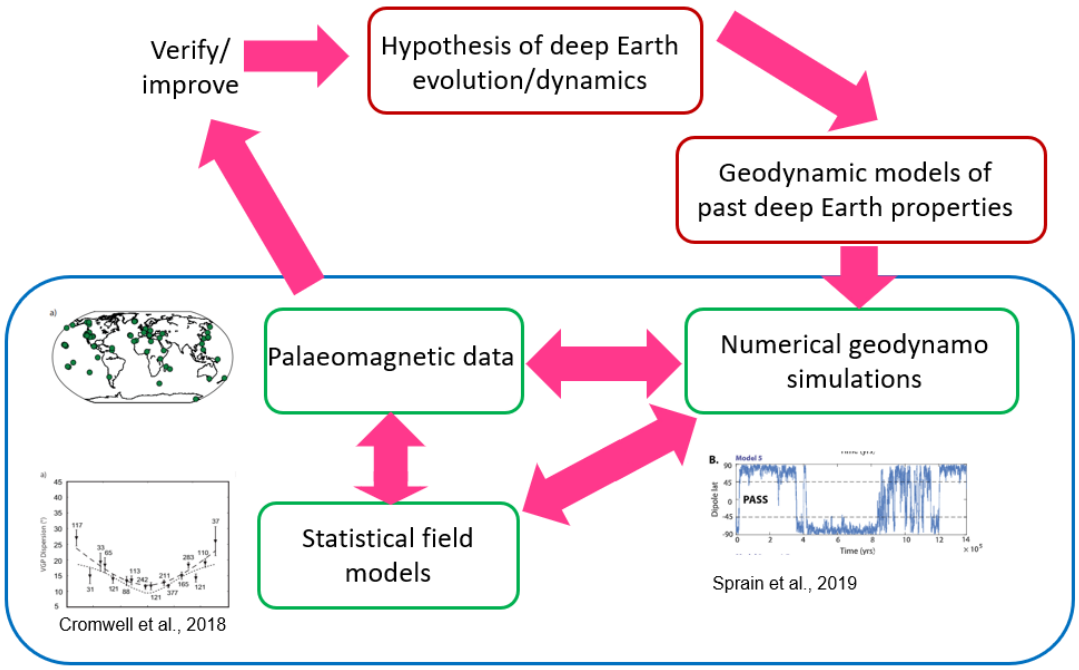

FIGURE 1.7: Flow chart of the DEEP approach, where deep Earth evolution is determined from predictions of numerical dynamo simulations, statistical field models and palaeomagnetic measurements. Redrawn after Biggin et al. (2017).

or longer (Tarduno et al., 2015) and is preserved in the geological record on the surface. Long-term (> 10 million years; Sprain et al., 2019) variations of the geomagnetic field are caused by persistent changes in the magnetohydrodynamic processes in the outer core which might be directly influenced by changes in core-mantle boundary (CMB) conditions (e.g., Aubert et al., 2010). Using the palaeomagnetic record to study the evolution of deep Earth processes requires a statistical characterisation of magnetic field variations in time, as well as an understanding of how these changes can be tied to changes in Earth's deep interior (Sprain et al., 2019).

This section gives a short introduction to the pillars of the DEEP approach (Figure 1.7; Biggin et al., 2017) where statistical field models, that describe the time-averaged field captured in palaeomagnetic data, are used to constrain numerical geodynamo simulations, which can give predictions of geomagnetic field variations tied to geodynamic models of past deep Earth properties.

1.5.1 Palaeomagnetic statistics and field models

The timescales of long-term variation and structure of the geomagnetic field, that can give valuable information about changes in the geodynamo related to deep Earth

physical processes, exceed the timescales for which direct measurements of the field are available, and data from palaeo-/archaeomagnetic records have to be used. With increasing age, these records show a decrease in resolution of spatial and temporal distribution as well as an increase of uncertainties (e.g., Korte and Constable, 2011), so that statistical models are required to describe the time averaged field for a specific time interval using the spherical harmonic representation, introduced in section 1.2.2.

These statistical models assess variability of the field (as seen in PSV) in terms of the field's departure from the first-order approximation of GAD in its normal (present) or reversed configuration (Johnson & McFadden, 2015). To be able to use compilations of palaeomagnetic data from different (palaeo-)localities, measurements of direction and intensity of the field (typically reported for individual sites as Dec, Inc, F, see section 1.2.1) are generally transformed to their respective virtual geomagnetic poles (VGPs) and virtual (axial) dipole moments (V(A)DM). A VDM represents the moment of a theoretical geocentric dipole that would result in the observed field strength (Smith, 1967) and normalises the variation of the field strength with latitude due to its dipole source. It is defined as

$$VDM = \frac{4\pi r^3}{\mu_0} B_{anc} (1 + 3\cos^2 \theta_m)^{-1/2}, \tag{1.7}$$

where θ is the (palaeo-)colatitude, that can be calculated from the measured inclination using the dipole equation (equation 1.4). This equation follows the assumption that the field strength is purely associated to a dipole source and treats nondipolar contributions as part of the dipole field, which leads to an overestimation of the true dipole moment (TDM; Korte and Constable, 2005).

Under the assumption of a geocentric dipole field, a (palaeo)magnetic pole position, defined as the projection of the negative end of the dipole onto the surface (Butler, 1992), can be calculated from (palaeo)magnetic directions using spherical trigonometry. A VGP is defined as a pole position determined from a single observation of a field direction, such as a palaeomagnetic site mean direction, and represents a spot reading of the field at the time of the acquisition of magnetisation. The average of several site-mean VGPs from sites that have been magnetised over time periods > 10^4 years (Merrill & McFadden, 2003), calculated using Fisher (1953) statistics, is the palaeomagnetic pole which coincides with Earth's rotational axis (according to the GAD hypothesis). Differences between the palaeomagnetic pole and its VGPs (and therefore departures from GAD) can be attributed to nondipole contributions, recorded in the instantaneous spot readings of each VGP. Thus, the average of a set of directions from N sites, that have been magnetised over a long enough time period, can describe the

TAF (where the offset from GAD can be seen as an 'inclination anomaly´; Tauxe and Kent, 2004), whereas its variance (dispersion) provides an estimate of PSV (Johnson & McFadden, 2015). This is only possible using (primary) site-mean directions from fast-cooled (igneous) units, because secular variation is already averaged out in sites of slow-cooled rocks or sedimentary bodies.

The dispersion of VGPs can be calculated using

$$S^2 = \frac{1}{N-1}\sum_{i=1}^{N}\Delta_i^2, \tag{1.8}$$

where S is the scatter, N is the number of VGPs, and Δ_i is the angular distance between the i^{th} VGP and the mean pole (Cox, 1970). Random orientation/measurement errors, that are completely unrelated to PSV, can be assessed as the scatter at the site level (within-site scatter S_W), that can be approximated from site-mean Fisher statistics, using

$$S_W = \frac{81}{\sqrt{K}}; K = k(\frac{1}{8}(5 + 18\sin^2\lambda + 9\sin^4\lambda))^{-1}, \tag{1.9}$$

where λ is the palaeolatitude, and k and K are the precision parameters of a Fisherian (Fisher, 1953) distribution of within-site directions in directional and pole-space, respectively (Biggin et al., 2008).

If S_W is considered in the calculation of the total scatter, then the so-called 'between-site scatter´ S_B (the angular dispersion of VGPs due to PSV) can be calculated via

$$S_B = \sqrt{\frac{1}{N-1}\sum_{i=1}^{N}(\Delta_i^2 - \frac{S_{Wi}^2}{n_i})}, \tag{1.10}$$

where n_i is the number of samples at the i^{th} site (Biggin et al., 2008).

VGPs from transitional data (e.g., during excursions or around reversals), show large deviations from the palaeomagnetic poles predicted by GAD and it is common practice to exclude such VGPs from PSV studies that assess PSV in relation to stable polarity periods (e.g., Johnson and McFadden, 2015; Quidelleur et al., 1994). There is no clear definition of what counts as 'transitional´. Often, a maximum angular distance to the palaeomagnetic pole is defined as 'cutoff´, that is used to screen out transitional VGPs. This cutoff is then either defined as a fixed angle (e.g., 45°; McElhinny and McFadden, 1997), or a variable cutoff, determined through an iterative process, where

the VGP with the largest angular distance is removed at every iteration until no VGPs outside the cutoff remain. The cutoff angle at each iteration is then calculated as

$$cutoff = 1.8 * (\sum_{i=1}^{N} \frac{\Delta_i^2}{N-1})^{1/2} + 5 \tag{1.11}$$

(Vandamme, 1994).

From the earliest studies of angular dispersions (e.g., Cox, 1962; Creer, 1962), it quickly became obvious that angular dispersions are a function of (palaeo)latitude, and that the scatter of palaeomagnetic directions decreases with increasing latitudes, which can be seen as an increase of dispersion with increasing latitude in VGP space. Early global PSV models either attributed PSV to a variation of the direction of the dipole ('dipole wobble´, e.g., model A; Irving and Ward, 1964), or tried to use the latitudinal variability in VGP space to discriminate between latitude invariant dipole wobble and non dipole variations (e.g., model C; Cox (1962); model D, Cox (1970); model F, McFadden and McElhinny, 1984). Based on present-day data of the field, and taking into consideration spherical harmonic descriptions of the field, McFadden et al. (1988) developed model G, that modelled the latitudinal variance of dispersion according to the different variance contributions of the "dipole family" and the "quadrupole family". The function of dispersion is given as

$$S = \sqrt{(A\lambda)^2 + B^2}, \tag{1.12}$$

where λ is the (palaeo)latitude and A and B are constant parameters that describe the contributions from the dipole and quadrupole families, respectively. In the context of spherical harmonics, the parameter A describes the contribution from the equatorially antisymmetric (l-m odd) family of Gauss coefficients, whereas parameter B accounts for the equatorially symmetric (l-m even) Gauss coefficients. Since model G is based on observations of present-day field data, it provides the best fits for the predicted latitudinal variance of dispersion in g_0^1 dominated fields (McFadden et al., 1988). Although the possibility of a complete separation of symmetric and antisymmetric families has been questioned (e.g., Doubrovine et al., 2019), model G is widely used for straightforward comparison of VGP dispersion between different VGP studies (e.g., Biggin et al., 2008; Cromwell et al., 2018; Veikkolainen and Pesonen, 2014).

To give a complete description of a model field and allow for the determination of direction and intensity of the modelled field at any point on the globe in a time series, a description of the TAF has to be presented as sets of Gauss coefficients with statistical properties. This is done by models that describe PSV as statistical variability of each Gaussian coefficient. This family of models, introduced by Constable and Parker

(1988), assume that the variation of Gauss coefficients is described by a giant Gaussian process (GGP) and treat each coefficient as normally, independently and identically distributed. The first GGP model (CP88; Constable and Parker, 1988) based these distributions on the spatial power spectrum of the present-day field, and assigned zero means to all nondipole terms (with the exception of the axial quadrupole g_0^2). As a result, CP88 was not able to reproduce the observed latitudinal variation of VGP dispersion (Johnson & McFadden, 2015). First descendants of CP88 improved predictions by adding anisotropy to the variability in the Gauss coefficients (e.g., CJ98; Constable and Johnson, 1999), or changing the relative variances of symmetric and antisymmetric terms (QC96; Quidelleur and Courtillot, 1996). In a further improvement, later models removed the separate treatment of variance of the axial dipole and introduced a scaling term for the dipole family by fitting the model to both directional and intensity data (TK03; Tauxe and Kent, 2004). Since these models fail to simultaneously reproduce field strengths and VGP dispersions, when compared to palaeomagnetic data from the last 10 million years, the separate treatment of the variance of the axial dipole has recently re-emerged in the model BB18 (Bono et al., 2020).

1.5.2 Numerical geodynamo simulations

The geomagnetic field is generated by dynamo processes in Earth's liquid outer core where a convective circulation of an electrically conducting fluid is driven by thermal and/or compositional buoyancy forces. A pre-existing magnetic field induces electric currents in the moving fluid, which in turn generate a magnetic field. If the generated field is strong enough that no external field is necessary for the induction process, then the dynamo is 'self-sustained´. Modern numerical simulations of such magnetohydrodynamic (MHD) processes are built on the works of Glatzmaier and Roberts (1995) and Kageyama and Sato (1995). Since then, numerous numerical geodynamo models have been published, that are more or less able to reproduce properties of the geomagnetic field (see section 1.5.3; Sprain et al., 2019). Numerical geodynamo models consider a spherical shell, representing Earth's outer core, that is filled with an electrically conducting fluid of constant density, which is convecting and rotating rapidly about a vertical axis. Numerically, this is done by considering a basic set of equations, comprising the Navier-Stokes equation, the induction equation, a transport equation for temperature or composition, the flow continuity equation and the magnetic continuity equation (e.g., Wicht et al., 2015). These equations are generally used in nondimensional form (e.g., Wicht and Sanchez, 2019) where the fundamental length scale is defined by the spherical shell thickness $D = r_o - r_i$ (with r_o and r_i giving the outer and inner core radii, respectively), time is scaled by the viscous diffusion time D^2/ν (with ν being the kinematic viscosity) and temperature is scaled by ΔT

(Christensen & Wicht, 2015). In combination with a scaling of the magnetic induction, this leads to the following set of dimensionless equations (e.g., Christensen and Wicht, 2015), that are solved in a frame of reference co-rotating with the outer boundary. The momentum equation

$$E(\frac{\partial u}{\partial t} + u \cdot \nabla u) + 2\hat{z} \times u + \nabla \Pi = E\nabla^2 u + Ra\frac{r}{r_o}T + \frac{1}{Pm}(\nabla \times B) \times B \tag{1.13}$$

describes the evolution of the flow velocity u in terms of pressure forces, Coriolis force, buoyancy and Lorentz forces, where the unit vector $\hat{z}$ describes the direction of the rotation axis. The temperature equation

$$\frac{\partial T}{\partial t} + u\nabla T = \frac{1}{Pr}\nabla^2 T + \varepsilon \tag{1.14}$$

describes the evolution of temperature perturbations, where ε is the volumetric heating rate. These equations are complemented by the induction equation

$$\frac{\partial B}{\partial t} - \nabla \times (u \times B) = \frac{1}{Pm}\nabla^2 B \tag{1.15}$$

as well as the flow and magnetic continuity equations

$$\nabla \cdot u = 0, \nabla \cdot B = 0, \tag{1.16}$$

which ensure that the flow follows the Boussinesq approximation and the field is divergence free. These equations are controlled by four dimensionless parameters: The Ekman number

$$E = \frac{\nu}{\Omega D^2}$$

is a measure for the ratio of viscous forces to Coriolis forces. The modified Rayleigh number

$$Ra = \frac{\alpha g_o \Delta T D}{\nu \Omega}$$

describes the fluid regime, where α is the thermal diffusivity and g_o is the gravity at the outer boundary (assuming gravity to be a linear function of the radius r). The modified Rayleigh number is connected to the classical Rayleigh number for convection in a

non-rotating plane layer via Ra = RE/Pr. The onset of convection is defined by the critical Rayleigh number Ra_c. The Prandtl number

$$Pr = \frac{\nu}{\kappa}$$

and magnetic Prandtl number

$$Pm = \frac{\nu}{\lambda}$$

are ratios of kinematic viscosity ν to thermal diffusivity κ and magnetic diffusivity λ, respectively (Braginsky & Roberts, 1995; Wicht & Sanchez, 2019).

To be able to solve the equations of the dynamo problem, several boundary conditions have to be defined for the CMB as well as the inner core boundary (ICB). Either rigid or free slip boundary conditions are used for the flow, where the radial flow components are forced to vanish at both the ICB and CMB, and the horizontal components are forced to match the rotation of the boundary (= zero in a co-rotating reference frame) for the rigid boundary condition, whereas the viscous shear stresses are forced to zero instead in the free-slip condition (Christensen & Wicht, 2015).

For thermally driven models, boundary conditions are assumed to be either fixed temperature or fixed heat flux conditions. The heat flux and its lateral (and temporal) variations (e.g., Aubert et al., 2009; Olson and Christensen, 2006) at the CMB are controlled by mantle convection processes, making fixed heat flux the preferred boundary condition for the outer boundary. For the compositional component, a vanishing flux is set as the outer boundary condition, assuming that light elements effectively do not penetrate the CMB (e.g., Wicht and Sanchez, 2019). The appropriate boundary conditions at the (growing) inner core are less clear, as the flux depends on the local cooling rate, which is dependent on convection and therefore varies with time (Braginsky & Roberts, 1995; Wicht et al., 2015). The magnetic boundary conditions consider the electrical conductivity contrasts at the boundaries. Due to its low electrical conductivity, the mantle is generally treated as an electrical insulator so that the magnetic field at the CMB matches a potential field, and the boundary condition can be set for the individual contributions of the spherical harmonic field (Christensen & Wicht, 2015). The same can be applied at the ICB, assuming an electrically insulating inner core. In the more realistic case, where the inner core has the same electrical conductivity as the outer core, the induction equation has to be solved for the inner core field, which the outer core field has to match at the ICB (Wicht et al., 2015). However, only minor

differences have been observed when a conducting inner core was used instead of an insulating inner core (Wicht, 2005).

Due to limitations in computational power, non-dimensional numbers like the Ekman number or the magnetic Prandtl number still differ by several orders of magnitude in numerical models from their geophysical estimates for Earth (e.g., Aubert et al., 2017). Nevertheless, numerical dynamo models have been successful in reproducing the main features of Earth's geomagnetic field, including polarity reversals (e.g., Christensen and Wicht, 2015; Glatzmaier and Roberts, 1995) and secular variation similar to historical observations (e.g., Aubert et al., 2013; Davies et al., 2008; Gubbins et al., 2007).

1.5.3 Quality of Paleomagnetic Modeling criteria Q_{PM}

In order to use the solutions of geodynamo simulations to make predictions about magnetic field behaviour (e.g., Biggin et al., 2020) and long-term temporal variations of the field related to changes in the boundary conditions (reflecting the evolution of Earth's deep interior), criteria have been introduced to assess how well a numerical dynamo simulation reproduces an Earth-like geomagnetic field (e.g., Amit et al., 2015; Christensen et al., 2010; Davies and Constable, 2014). These criteria used observations of the field for the past 100 kyrs to define an 'Earth-like´ field, and therefore assume that the modern secular variation is representative for the long-term field behaviour, which may not be the case (Johnson & McFadden, 2015). To be able to assess whether the solutions of geodynamo models can reproduce long-term (> 0.1 - 10 Myr) secular variation, the Quality of Palaeomagnetic Modelling (Q_{PM}) criteria were introduced by Sprain et al. (2019). These calculate a non-parametric misfit between simulated and palaeomagnetic data (ΔQ_{PMi}) and assign a binary score for each criterion (Q_{PM}). Q_{PM} comprises five criteria. Three criteria are based on PSV behaviour. Two of those use a model G (McFadden et al., 1988) fit to assess PSV in terms of equatorial VGP dispersion (VGPa) and latitudinal variability of VGP dispersion (VGPb). The third gives an estimate of the variability of field strength (VDMvar), calculated by the ratio of the interquartile range of a distribution of VDMs to the median of the distribution. The criterion IncAnom is based on TAF behaviour and assesses the inclination anomaly compared to the predicted inclination in a GAD field (Tauxe & Kent, 2004). The last criterion (Rev) is met if the simulation produces Earth-like polarity reversals, as shown by examples in Sprain et al. (2019). For each criterion, a ΔQ_{PMi} misfit is calculated as the ratio of the absolute distance between the median values for Earth data and simulated data to the total distance covered by the uncertainty bounds that lie between Earth data and simulated data. If the misfit of a criterion is ≤ 1, then the Q_{PM} score for

that criterion is set to 1. The total misfit and total Q_{PM} score are calculated from the sum of all individual misfits and scores, respectively.

1.6 The Ediacaran Period

The Ediacaran period at the end of the Precambrian is a complex time of extreme climatic changes and continental break-ups that directly predated the Cambrian period. This section introduces the Ediacaran period as the temporal setting for the work described in this thesis.

1.6.1 Definition and historical background

Named after the Ediacara Hills of southern Australia, the Ediacaran period in its current definition is one of the most recent additions to the geologic time scale. It is the longest of all stratigraphically defined geological periods, with a duration of 97 million years between 635 and 538 Ma (Knoll et al., 2006; Xiao & Narbonne, 2020). The need for a chronostratigraphic section predating the Cambrian slowly arose after the idea of the 'Lipalian Interval´ (Walcott, 1914) of global erosion, to explain the lack of ancestors for the diverse groups of (shelly) fossils that appeared at the base of the Cambrian (Darwin, 1859), was contradicted by the existence of regional lithostratigraphic sections that conformably underlie Cambrian sections, such as the 'Sinian´ (China; Grabau, 1922; Lee, 1924), the 'Marinoan´ (Australia; Mawson and Sprigg, 1959), and the 'Vendian´ (Russia/Ukraine; Sokolov, 1952). Imprints of large, soft-bodied animal-like fossils in Precambrian sections (Ford, 1958) eventually led to the recognition of a global 'Ediacara Fauna´ (Glaessner, 1959), the proposition of an 'Ediacarien´ chronostratigraphic interval (Termier & Termier, 1960), and the formal proposition of the 'Ediacaran system´ (Jenkins, 1981). The final definition of the Global Boundary Stratotype Section and Point (GSSP) representing the base of the Ediacaran was found after 15 years by the 'Working Group on the Terminal Proterozoic Period´, launched by the International Commission on Stratigraphy in 1989, and ratified by the Subcommission on Ediacaran stratigraphy in 2004 (Knoll et al., 2006). The Ediacaran GSSP was defined in the Enorma Creek section in South Australia, at the base of the cap carbonate of the Nuccaleena Formation on top of the Cryogenian glacial and glacio-marine sediments of the Elatina Formation (Xiao & Narbonne, 2020). The base of the Ediacaran is constrained by radiometric dates to be around 635 Ma. The GSSP is not dated directly, but the Cryogenian Ediacaran boundary is radiometrically defined to be between the top of the Cryogenian Nantuo Formation (634.57 ± 0.88 Ma; Zhou et al., 2019) and the base of the Ediacaran cap dolostone (635.23 ± 0.57 Ma; Condon et al., 2005). The end of the Ediacaran, and therefore the boundary between Proterozoic and

Phanerozoic, was defined in 1992 (Landing, 1994) after a similarly long process (the interested reader is referred to the summary in Geyer and Landing (2017)) as the base of the Cambrian GSSP at the Fortune Head section, Newfoundland (Narbonne et al., 1987), with an age of about 538.8 Ma (Linnemann et al., 2019; Peng et al., 2020). A final decision on whether to divide the Ediacaran into 'Upper´ and 'Lower´ Series, or into 'Upper´, 'Middle´, and 'Lower´ Series, has not yet been made (Canfield et al., 2020; Wang et al., 2017; Xiao & Narbonne, 2020).

1.6.2 Life and climate

Ediacara-type macrofossils, often found well preserved as centimetre to metre sized imprints at the bottom of event horizons, are the first abundant, large and architecturally complex organisms on Earth (Xiao & Narbonne, 2020). With a few older (Hofmann et al., 1990) and younger (Jensen et al., 1998) exceptions, Ediacara-type fossils are restricted to be indicative for the upper half of the Ediacaran. Ediacara-type macrofossils and trace fossils are also common in shallow- and deep-water siliciclastics, allowing a global correlation of the upper part of the Ediacaran system (Narbonne et al., 2014). The macrofossils are divided into three assemblages suitable for biostratigraphy (Figure 1.8), that each show major diversity changes and evolutionary innovations in terms of complexity, segmentation, or calcification: the Avalon, White Sea and Nama assemblages (Droser et al., 2017; Waggoner, 2003; Xiao & Narbonne, 2020).

The oldest Ediacara-type fossils are included in the Avalon assemblage, which has only been found in deep-water deposits and comprises mainly fossils of decimetre- to metre-scale constructions built from branched centimetre-scale modules. These fossils have not been found in shallow-water deposits of equivalent ages, which is seen as an indicator that early complex macroscopic life has originated in deep-sea environments (e.g., Narbonne et al., 2014). The highest taxonomic diversity can be found in the White Sea assemblage (e.g., Droser et al., 2017), that includes the first abundant animal burrows and is dominated by unbranched and subhorizontal burrows (Gehling & Droser, 2018). The final phase of Ediacaran biota before its decline near the Ediacaran-Cambrian boundary is represented by the Nama assemblage, that comprises some non biomineralised ribbon-shaped or tubular fossils, but also includes the first appearance of the earliest skeletal animal fossils (Xiao and Narbonne, 2020 and references therein).

The lower part of the Ediacaran is represented by 50 - 1000 µm large, morphologically complex and taxonomically diverse acanthomorphic acritarchs (organic-walled microfossils covered in spines; Chen and Liu, 1986). Five assemblage zones of these microfossils have been recognised in Australia, most of which are characterised by large

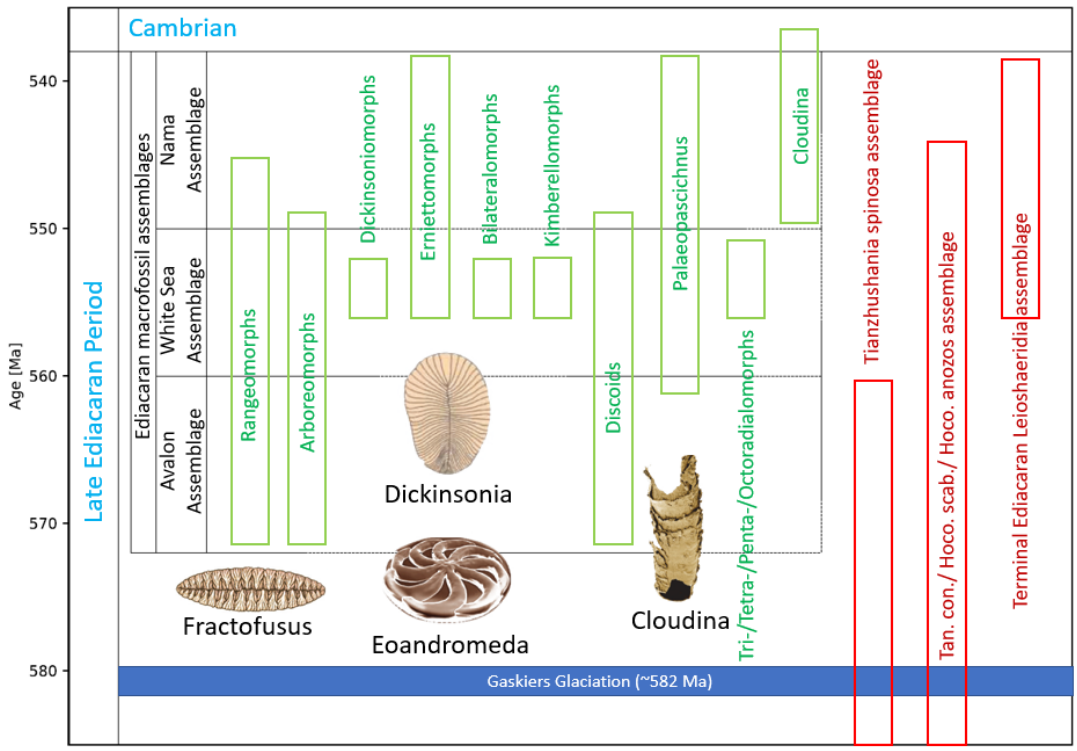

FIGURE 1.8: Mega-/microfossil zonation in the upper Ediacaran system. Green bars represent Ediacara-type macrofossils, red bars show microfossil assemblages. Redrawn from Xiao and Narbonne (2020).

acantomorphs, but it is still unclear if these zones are recognisable in areas outside of Australia (Xiao & Narbonne, 2020). Other groups of Ediacaran microfossils, such as embryo-like, tubular, and multicellular algal fossils, as well as coccoidal and filamentous cyanobacteria, show only limited global distributions or long stratigraphic ranges, limiting their significance for biostratigraphy (e.g., Xiao et al., 2014; Zhang et al., 1998).

Compared to the preceding Cryogenian, glacial deposits are relatively rare in the Ediacaran sedimentary record, with 13 glacial deposits on eight palaeocontinents (Hoffman & Li, 2009). The most prominent and best-known Ediacaran glacial deposit is the 250 m thick deep-water glaciomarine deposit of the Gaskiers Formation in Newfoundland, dated between 580.90 ± 0.4 and 579.88 ± 0.44 Ma (Eyles & Eyles, 1989; Pu et al., 2016). Deposits of the Marinoan glaciation at the beginning of the Ediacaran at 635 Ma have been found on most major continents. Due to the distribution of glacial deposits from the Marinoan and Gaskiers glaciations, covering palaeolatitudes from > 70° to the (palaeo)equator, these glaciations have been interpreted as 'Snowball Earth´ events (Hoffman et al., 1998; Li et al., 2013).

The chemical evolution of Ediacaran oceans is characterised by several excursions of negative $\delta^{13}C_{carb}$ values in the Ediacaran carbon isotope record. Prominent excursions are seen at the base (e.g., Knoll et al., 2006) and the top (Basal Cambrian Carbon Isotope Excursion (BCCIE); Zhu et al., 2006) of the Ediacaran as well as in the so-called 'Shuram´ excursion (Burns & Matter, 1993) with unclear origin, complexity, age and duration (Xiao & Narbonne, 2020). Sulphur isotopes show strong geographic and stratigraphic variations that have been interpreted as a low-sulphate ocean (Halverson & Hurtgen, 2007) which can develop ferruginous deep waters when combined with a low-oxygen atmosphere (Xiao & Narbonne, 2020). However, trace metal isotopes and concentrations indicate three or more deep-water oxygenation events throughout the Ediacaran (e.g., Sahoo et al., 2016; Zhang et al., 2019).

1.6.3 Palaeogeography and the geomagnetic field

The Ediacaran palaeogeography is a highly controversial and speculative topic, where numerous alternative plate configurations have been proposed because of the ambiguity, varying quality, scattered distribution, and/or general scarcity of palaeomagnetic constraints (e.g., Li et al., 2008; McCausland et al., 2011; Meert, 2014; Pisarevsky et al., 2008). The main source of confusion lies in palaeomagnetic data from multiple continents, that result in two distinct (and equally reliable) groups of palaeomagnetic poles of similar age that are separated by large (∼90°) angles and lead to contradicting interpretations (e.g., Abrajevitch and Van der Voo, 2010). A short summary of the associated controversy will be presented in the introduction of Chapter 2 of this thesis. Additional, more comprehensive summaries can be found in in Abrajevitch and Van der Voo (2010) and Robert et al. (2021).

Competing explanations for the puzzling palaeomagnetic pole configuration are:

(a) some of the poles represent secondary magnetisations (e.g., Bono and Tarduno, 2015; Hodych et al., 2004),

(b) the geomagnetic field in the Ediacaran departed multiple times from a GAD field and was then dominated by an equatorial dipole (Abrajevitch & Van der Voo, 2010),

(c) poles from both groups are primary and consistent with a GAD field and the resulting unrealistically high plate motion velocities are explained by multiple episodes of (inertial interchange) true polar wander (IITPW, e.g., Evans, 2003; Kirschvink et al., 1997; Robert et al., 2017), and

(d) the field was unstable and rapidly reversing, and the palaeomagnetic record represents readings of a transitional field (e.g., Halls et al., 2015).

Option (a) suggesting remagnetisation is not implausible but struggles to explain directions from both groups that are supported by field tests. An equatorial dipole (option b) would have to reoccur at the same longitudinal position in order to not disappear in the time averaged field. Numerical geodynamo simulations of a stable equatorial dipole predict the geomagnetic field drifting as prograde-propagading waves (Aubert & Wicht, 2004). Option (d) of a transitional field could be supported by estimates of an exceptionally weak field strength (Bono et al., 2019) and extreme reversal frequencies that have been reported for some parts of the upper Ediacaran (Bazhenov et al., 2016; Levashova et al., 2021). These studies also suggest a stable, (axial) dipole dominated field even though VGP dispersions are rather high. A bistability between equatorial and axial dipole states has been suggested by numerical geodynamo simulations for rapidly reversing fields (Gissinger et al., 2012), suggesting that the explanation of an equatorial dipole field and the explanation of a transitional field (options b and d) might be different observations of the same mechanism. A main issue of option (c) is that the proposed Ediacaran true polar wander events would exceed geophysical limitations (Tsai & Stevenson, 2007). However, palaeomagnetic records of transitional and/or non-GAD-like fields are of limited use for continental reconstructions which instead use geological constraints and are palaeomagnetically based on exclusion of poles due to various reasons, or multiple (II)TPW events (Figure 1.9).

The stage for Ediacaran palaeogeography is set by the breakup of the supercontinent Rodinia around 750 - 720 Ma (Li et al., 2013). At the beginning of the Ediacaran around 635 Ma, this breakup was in its final phase where all continents, other than Siberia and Baltica (and possibly Amazonia; Pisarevsky et al., 2008; Robert et al., 2021), had already separated from Laurentia and started to form East- and West Gondwanaland at high and low (southern) latitudes, respectively, until ∼580 Ma (Li et al., 2019). With the exception of North China, that was later attached in the mid- to late Cambrian (McKenzie et al., 2011), the assembly of Gondwanaland on the southern hemisphere was complete at 540 Ma (Li et al., 2013).

The breakup and individual drifting histories of Laurentia and Baltica probably started with the emplacement of the Central Iapetus Magmatic Province (CIMP) around ∼615 Ma with Laurentia at low latitudes (Robert et al., 2021). At the end of the Ediacaran around 540 Ma, Laurentia and Baltica were isolated at low and mid-latitudes, respectively (Li et al., 2013; McCausland et al., 2011; Robert et al., 2021). The individual drifting histories and the opening of the Iapetus Ocean is still mostly open for debate because the ambiguous palaeomagnetic data allow two scenarios, where Laurentia either stayed at low latitudes throughout the Ediacaran, or moved to a high latitude position around 590 Ma, as shown by the models in Pisarevsky et al. (2008) and Robert et al. (2021). The high-latitude Laurentia model seems to be the preferred option (e.g.,

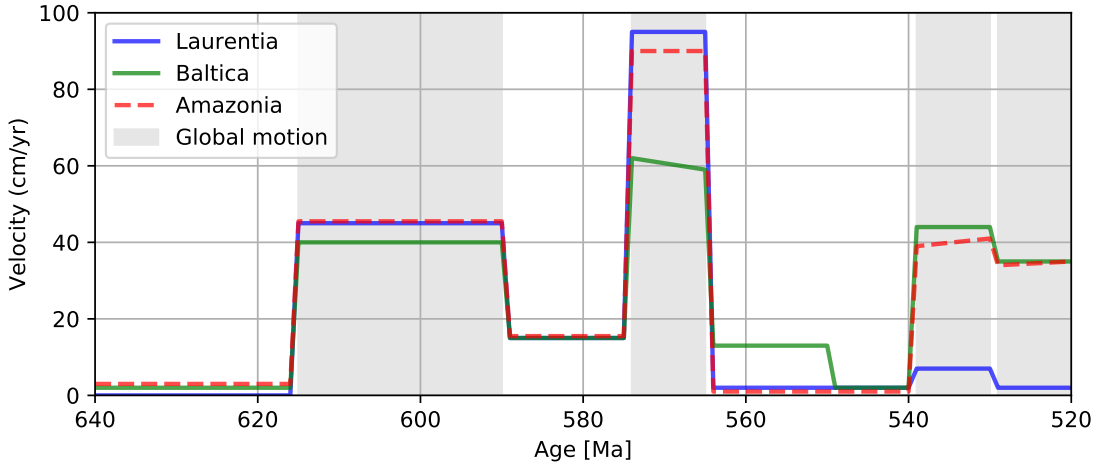

FIGURE 1.9: Estimated plate velocities of Laurentia (blue), Baltica (green) and Amazonia (red), showing extreme plate velocities (in a palaeomagnetic reference frame), when plate motions are constrained by palaeomagnetic methods based on a GAD-like field. Grey areas show time periods where global events like IITPW are required to explain the plate velocities. Redrawn from Robert et al. (2021).

Bono and Tarduno, 2015; Li et al., 2013; Robert et al., 2021). This model does however rely on multiple TPW events to explain the high ($\leq$~90 cm/year) plate velocities (Figure 1.9).

It seems unlikely that better constrained palaeogeographic models will be found without a better characterisation of the geomagnetic field. The following chapters represent the first step towards a field characterisation based on both directional and field strength behaviour.

Chapter 2

A palaeointensity study of the Grenville Dykes, Canada

Thesis context

The anomalous geomagnetic field in the Ediacaran is captured best in the palaeomagnetic records of Laurentia (McCausland et al., 2007), Baltica (Meert, 2014), and West Gondwana (Robert et al., 2017). It can be explained by following the time series of palaeomagnetic directions of Laurentia, which oscillate between steep and shallow directional components between 600 and 550 Ma (Abrajevitch & Van der Voo, 2010). Shallow components recorded in the Long Range dykes (615 Ma, Hodych et al., 2004; Murthy et al., 1992), the Johnnie Formation (555 Ma, Van Alstine and Gillett, 1979), and the Skinner Cove Formation (551 Ma, McCausland and Hodych, 1998) place Laurentia at low latitudes at the beginning and the end of the Ediacaran, where it remained throughout the Cambrian, as suggested from Cambrian palaeomagnetic data and the presence of warm-water archaeocyathan reefs (McCausland et al., 2007 and references therein). Steep components measured in the Grenville dykes (590 Ma, Murthy, 1971), the Callander complex (577 Ma, Symons and Chiasson, 1991), the Catoctin Basalts (572 Ma, Meert et al., 1994), and the Sept-Îles intrusion (565 Ma, Tanczyk et al., 1987) point to a high-latitude position of Laurentia in the mid-Ediacaran. In a GAD-like field, this would however require implausibly high (Tsai & Stevenson, 2007) plate motion velocities for the transitions between high and low latitudes. To add to the complexity, and imply stronger contributions of a highly variable nonaxial dipole field, both steep and shallow (primary) components were observed at the Grenville Dykes, the Catoctin Basalts, and the Sept-Îles intrusion.

More recent studies, utilising palaeomagnetic measurements of magnetic inclusions in single silicate crystals, concluded that the steep component of the Sept-Îles intrusion represents a secondary remanence (Bono & Tarduno, 2015) and the primary shallow

component recorded a stable magnetic field that was an order of magnitude weaker than the present-day field (Bono et al., 2019). In contrast, a second palaeomagnetic study of the Grenville dykes confirmed the presence of primary steep and shallow components at that locality (Halls et al., 2015), suggesting a transitional field at that time. Palaeointensities were not measured, but the presence of a weak field had been inferred from the anomalous directions and high reversal frequencies (e.g., Meert et al., 2016).

In this chapter, we build on the study of Halls et al. (2015) and examine the palaeointensities, recorded in the Grenville dykes, to reveal the first field strength estimates for the mid-Ediacaran. This will allow us to directly compare the absolute intensities and magnetisation behaviour of the directional components. If both steep and shallow components are primary, then this additional information could enable the distinction between a GAD-like field and alternative field configurations (e.g., Abrajevitch and Van der Voo, 2010) for a 20 myr time-window in the mid-Ediacaran.

This chapter is published as Thallner, D., Biggin, A., Halls, H. (2021), An extended period of extremely weak geomagnetic field suggested by palaeointensities from the Ediacaran Grenville dykes (SE Canada), *Earth and Planetary Science Letters*, 586.
In this study, I measured and analysed all rock samples, and wrote the publication together with Andy Biggin and Henry Halls.

Abstract

Long-term variations of the geomagnetic field, observed in the palaeomagnetic record, have the potential to shed much light on the evolution of Earth's deep interior. With a geomagnetic field characterised by anomalous directions and ultra-low intensities, the Ediacaran period (635 - 538 Ma) is a time of special interest. Steep and shallow directions, leading to virtual geomagnetic poles (VGPs) separated by angles of up to 90° and very close in age could have recorded a geomagnetic field switching between axial and equatorial dipole-dominated states. Alternatively, the field may simply have been highly nondipolar and subject to rapid reversals. Palaeointensity determinations of units that record the anomalous directions could potentially help to discriminate between morphologies but the spatial and temporal distribution of palaeomagnetic data require improvement. Here we present new palaeointensities from 6 dykes from the western end of the Grenville Dyke swarm that recorded directionally anomalous geomagnetic fields around ∼585 Ma. Results from double-heating Thellier experiments failed to satisfy the used selection criteria, but successful microwave Thellier, Shaw and pseudo-Thellier experiments lead to palaeointensities that show field strength values of 2.9 ± 2.2 μT and corresponding virtual dipole moments of 0.3 - 1.7 x10^{22}

Am^2. These field strengths are an order of magnitude weaker than the present-day field. VGPs grouping in two distinct clusters with almost identical angular dispersions of VGPs (S_B = 18.5° and 18.9°) may argue for the presence of an equatorial dipole. In contrast, the palaeointensities associated with the steep and shallow components are indistinguishable. Although based on a low number of results, this observation, together with the overall very large VGP dispersion may rather support that the Grenville Dykes have recorded enhanced secular variation linked to a highly unstable and rapidly reversing field.

2.1 Introduction

Extreme climatic changes in the late Neoproterozoic (Evans and Raub, 2011) and tectonic activity between the final breakup of Rodinia and the assembly of Gondwana have made the Ediacaran period (635 - 538 Ma, Xiao and Narbonne, 2020) a prime target for palaeomagnetic and geodynamic research. During this period, the individual drifting histories of Laurentia and Baltica remain mysterious (Li et al., 2013) although both their positions are relatively well constrained around the beginning and the end of the Ediacaran at ∼615 Ma and from ∼550 Ma (Meert, 2014). Anomalous directional data in palaeomagnetic datasets leading to ambiguous apparent polar wander paths (APWP) throughout the Ediacaran and parts of the Cambrian have puzzled palaeomagnetists for decades. These APWPs were based on almost orthogonal steep and shallow primary directional components that are extremely close in age and would require unprecedented continental plate velocities to occur in the framework of a geocentric axial dipole field. First attempts to explain this issue led to the proposition of inertial interchange true polar wander (IITPW) events (Kirschvink et al., 1997) – a hypothesis that was met with resistance in parts of the palaeomagnetic community (Torsvik, 1998) and was later labelled as geodynamically implausible (Tsai and Stevenson, 2007). Subsequent studies of APWPs for Laurentia (Hodych et al., 2004) and Australia (Schmidt and Williams, 2010) did not confirm the proposed IITPW and more attention was given to the possibility of an anomalous behaviour of the geomagnetic field itself. In this case, the steep and shallow directions have been interpreted as being caused by the geomagnetic field flipping between an axial and an equatorial dipole field configuration (Abrajevitch and Van der Voo, 2010) or as showing an intermediary state of an axial dipole field during continuous reversals (Halls et al., 2015). Numerical geodynamo simulations have suggested that the occurrence of a protracted equatorial dipole field may be possible during the reversal of an axial dipole field (Aubert and Wicht, 2004; Gissinger et al., 2012) with significant differences between the intensities of the axial and equatorial field states. Questioning the primary

nature of anomalous directions, new studies revisited sites that recorded these directions. Analysis of single domain particles in single silicate crystals of the Sept Îles Complex showed that only the shallow components were recorded in single domain carriers and did not confirm the primary nature of the steep component, eliminating the need of IITPW to explain these directions (Bono and Tarduno, 2015). In contrast, new palaeomagnetic analysis of the Grenville Dykes confirmed the existence of several directional components (Halls et al., 2015). The two polarities recorded in the Sept Îles complex and the complex magnetisations of the Grenville Dykes pointed to an unstable and rapidly reversing field as explanation for the anomalous data (Bono and Tarduno, 2015; Halls et al., 2015). The overall paucity of spatial and temporal coverage of palaeomagnetic data in the Ediacaran still impedes a definitive characterisation of the geomagnetic field (Meert, 2014) and new contributions of complex palaeomagnetic signals, that prefer interpretations with the IITPW hypothesis (Robert et al., 2017), may also be compatible with a more complex field geometry during a period of rapid reversals. Studies of magnetostratigraphic data from the late Ediacaran and the early Cambrian (Bazhenov et al., 2016; Levashova et al., 2021), resulting in reversal frequencies of more than 20 reversals/Myr, claim that the field might have been in a hyperactive state at that time. Due to the correlation between reversal frequency and dipole field strength (Kulakov et al., 2019; Tarduno and Cottrell, 2005; Tauxe et al., 2013) the dipole field strength in the Ediacaran is expected to be low. First palaeointensity studies of Ediacaran rocks from Canada (Bono et al., 2019) and Ukraine (Shcherbakova et al., 2020) show ultra-low virtual dipole moments (VDM) that are an order of magnitude weaker than dipole moments in the Phanerozoic. To date, similarly low dipole moments have only been found in the Devonian (Hawkins et al., 2019; Shcherbakova et al., 2017) and the Jurassic (Kulakov et al., 2019; Tauxe et al., 2013). Information about reversals and palaeointensities is critical to delineate the anomalous field behaviour in the Ediacaran. However, no estimates for the strength of the geomagnetic field exist for the early-mid Ediacaran before 580 Ma. Here we report multi-method palaeointensity measurements performed on mid-Ediacaran age units showing both steep and shallow directions to look for differences that could help explain the directional observations of that time.

2.2 Materials and methods

2.2.1 Sample material

The samples from dykes within the Grenville province used in this study were collected in Halls et al. (2015) and were taken preferentially from chilled margins. Several dykes were sampled at multiple sites over distances of up to 150 km across and along

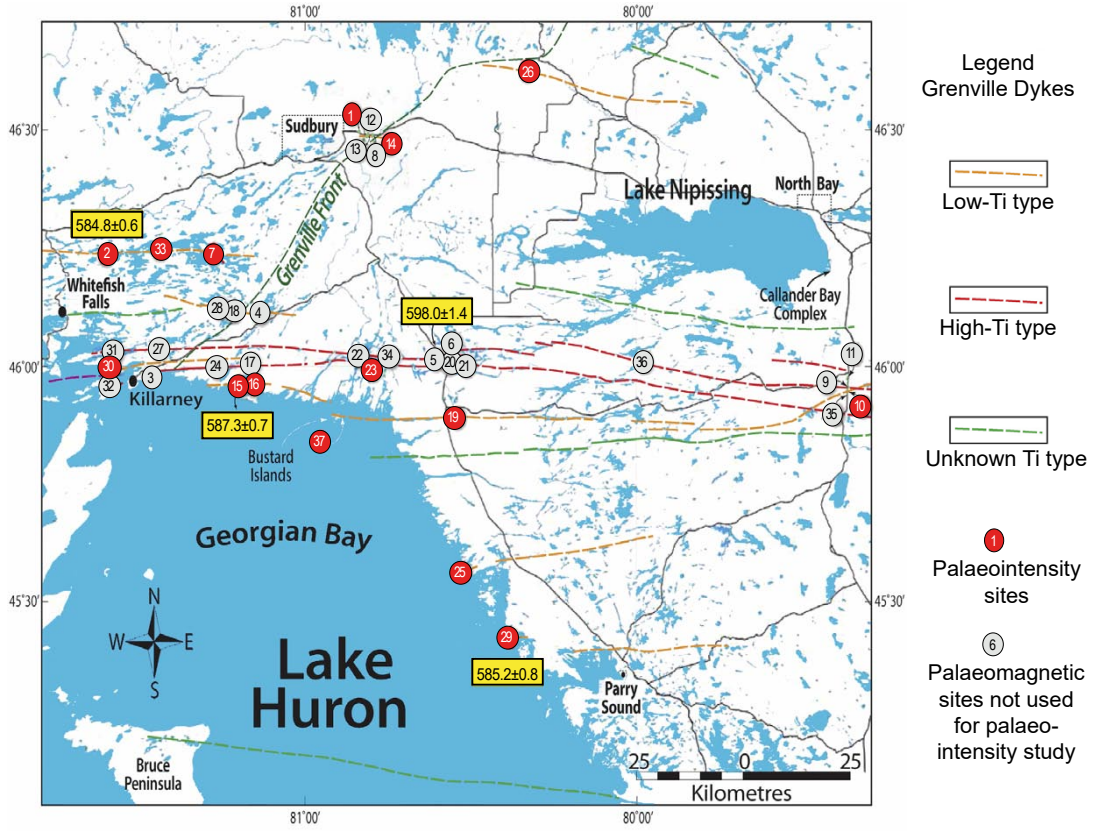

FIGURE 2.1: Map of southeast Ontario, showing the Grenville dykes and locations of sites studied in Halls et al. (2015) and sites selected for this palaeointensity study; from Halls et al. (2015).

the dyke strike. Analysis of geochemical composition helped with longitudinal correlation of the dykes. Samples were selected for intensity determination if sister-samples from the same site showed a stable component of characteristic remanent magnetisation (ChRM) in the previous study, which was the case for 99 samples from 15 sites within nine dykes (Figure 2.1). Following the naming convention used in Halls et al. (2015), the five dykes analysed in this study were: Coniston dyke (sites GD02, GD33), French River dyke (GD23), Key River dyke (GD10, GD15, GD16, GD19, GD37) and Sand Bay dyke (GD29). Additionally, four sites from other dykes in the area associated with the dyke swarm (GD07, GD25, GD26, GD30) were also analysed. U-Pb ages exist for Sand Bay dyke (585.2 ± 0.8 Ma), Augusta Lake dyke (584.8 ± 0.6 Ma), Key River dyke (587.3 ± 0.7 Ma) and French River dyke (598.0 ± 1.4 Ma) (Halls et al., 2015).

Differences in chemical composition between the individual dykes suggest single intrusion events at different development stages of the magma chamber (Halls et al., 2015). The directional results in Halls et al. (2015) show four components resulting

in antipodal steep and shallow directions close to directions of older studies of the Grenville dykes (e.g., Hyodo and Dunlop, 1993). Positive contact (Halls et al., 2015) and reversal tests (Hyodo and Dunlop, 1993) support the primary nature of the steep direction. This comprises the steep up component B (D: 131.2°, I: -70.9°, α_{95}: 11.3°) that can be seen in sites of the Key River dyke (Halls et al., 2015) and the approximately antipolar component E, seen in one site of the French River dyke (D: 294°, I: 74.1°, α_{95}: 5.1°), and indistinguishable from the primary direction of the 585.9 Ma Mattawa dyke (D: 298°, I: 72°, α_{95}: 7°; Hyodo and Dunlop, 1993). The shallow component from the almost antipolar components C and D can also be observed continuously in sites of the same dyke and component D differs significantly from the regional overprint recorded in the close-by Whitestone anorthosite (Ueno et al., 1975). Because of an inconclusive contact test, it cannot be excluded that the shallow component was remagnetised (Halls et al., 2015). In this study, we nevertheless analysed samples from sites that recorded both steep and shallow components.

2.2.2 Methods

All measurements were carried out at University of Liverpool's Geomagnetism Laboratory. To assess the rocks' suitability for palaeointensity determination, at least two specimens per site were selected for rock magnetic measurements. Measurements of isothermal remanent magnetisation, hysteresis loop parameters and thermomagnetic curves were done on a Variable Field Translation Balance using both crushed specimens and cylinder specimens with a diameter of 5 mm. Hysteresis loop parameters were processed and analysed in HystLab (Paterson et al., 2018). Temperature dependent susceptibilities were measured on an AGICO MFK-1A Kappabridge using crushed specimens heated in air to 700°C. To monitor thermochemical alterations in more detail, the same measurements were also performed in incremental heating and cooling cycles in temperature steps of 100°C between 150°C and 650°C. Scanning electron microscope (SEM) images were taken with a Hitachi TM3000 tabletop microscope and analysed with Quantax70.

The magnetic viscosity of 59 specimens was determined by measuring their remanent magnetisation after being stored for three weeks in different orientations without shielding from the ambient field (Prévot, 1981). For this experiment, the specimens were stored on a rack in the laboratory with their z axis parallel to the field lines of the geomagnetic field for the first duration and antiparallel to the field lines for the second duration. The remanent magnetisations were measured on an AGICO-JR6 spinner magnetometer.

A multi-method approach was used to measure palaeointensities in an effort to strengthen the quality of our determinations by demonstrating consistent results obtained from fundamentally different methods (de Groot et al., 2013). Here we used thermal and microwave Thellier, pseudo-Thellier and double-heating Shaw methods. Microwave Thellier palaeointensity experiments were performed on the high frequency (14 GHz) microwave system and SQUID magnetometer (Suttie et al., 2010). This instrument uses unoriented cylinder specimens with a 5 mm diameter. These were drilled from the available 1" cylinders, which allowed for 5 to 15 sub-specimens to be drilled from one standard cylinder specimen. This allowed for a large number of fast palaeointensity experiments (∼90 minutes/specimen) to be done despite the low amount of available sample material. Specimens are subjected to microwave treatment with incrementally increasing power and/or duration in a range between 20 W·s and 500 W·s. The succession of zero-field and in-field steps for the experiments followed the IZZI protocol (Tauxe and Staudigel, 2004). Checks of reproducibility of partial thermoremanent magnetisations (pTRM) were done after every other I-Z-pair, resulting in 4 - 5 pTRM-checks per specimen. To detect multidomain effects, the laboratory field was applied in angles of 45° - 90° to the ChRM of the specimen (Yu and Tauxe, 2005). The laboratory field itself was varied between 3 and 30 µT between experiments to detect possible field dependencies of the results.

Thermal Thellier experiments were undertaken using the IZZI protocol with pTRM checks in vacuum, using an MMTD80 oven with a bias field of 10 µT in the temperature range of 100°C - 550°C. Magnetisations of the specimens were measured on an AGICO-JR6 spinner magnetometer after applying a 2 mT alternating field (AF) demagnetisation step before every measurement using an AGICO-LDA5 AF demagnetiser to ensure no spurious magnetisations affected the specimen.

In addition to the microwave and thermal Thellier experiments, that are both based on the same method and therefore potentially prone to being biased by non-ideal carrier effects in similar fashions (e.g., sagging of Arai plots due to MD grains; Smirnov et al., 2017), the double-heating Shaw method (Tsunakawa and Shaw, 1994) used AF demagnetisations and acquisitions of anhysteretic remanent magnetisations (ARM). These experiments were carried out on a 2G-RAPID superconducting rock magnetometer system in incremental steps of 2 - 10 mT up to a peak AF-field of 100 mT. ARMs were given at peak AF field in bias fields of 57.9 µT or 81.2 µT. The specimens were given a full TRM twice by heating them to 610° or 650°C in bias fields of 5 µT or 10 µT to be able to apply an ARM correction (Rolph and Shaw, 1985).

The pseudo-Thellier method (de Groot et al., 2013; Paterson et al., 2016) was performed on the automatic 2G-RAPID system with the same AF levels as used in the

Shaw method. This was done to have results that avoided heating the specimen at all during palaeointensity determination. Absolute intensity values were calculated using the generalised calibration from Paterson et al. (2016). Since different pseudo-Thellier calibrations are disagreeing in the expected weak field range (de Groot et al., 2013; Paterson et al., 2016), the pseudo-Thellier results were only used for comparison with the measurements made using other methods. For the purpose of this experiment, bias fields of 11.4 µT and 81.2 µT were used for the ARM acquisition and, in some cases, Shaw and pseudo-Thellier experiments were run as a combined experiment, where the ARM acquisition steps were performed instead of the single ARM magnetisation at peak AF field in standard Shaw experiments.

For thermal and microwave Thellier experiments, the selection criteria followed the Standard Palaeointensity Definition (SPD, Paterson et al., 2014) and were modified from the SELCRIT2 criteria (Biggin et al., 2007a). The criteria of $N \geq 4$, $FRAC \geq 0.35$, $\beta \leq 0.1$, $q \geq 1$, $MAD \leq 15°$, $\alpha \leq 15°$, $DRAT \leq 10\%$ and $CDRAT \leq 10\%$ were used together with a curvature factor if the best-fit line (Paterson, 2011) of $|k'| \leq 0.27$.

The selection criteria used for the Shaw method were similar to those set out by Yamamoto et al. (2010): number of consecutive data points $N \geq 5$, correlation coefficients of the linear parts of the NRM - TRM1* diagram and the TRM1 - TRM2* diagram of $r^2_N \geq 0.995$ and $r^2_T \geq 0.995$, the fraction of used NRM $f \geq 0.2$ and the slope of the linear part of the TRM1 - TRM2* diagram $0.95 \leq slope_T \leq 1.05$. In addition, the selected part of the NRM must appear linear and convergent on the orthographic plot of the NRM demagnetisation with $|k'| \leq 0.27$ and with α and MAD values $\leq 10°$.

The SPD selection criteria used for pseudo-Thellier experiments were slightly relaxed from Paterson et al. (2016) and applied to a convergent part of NRM in the orthographic plot: $N \geq 6$, $f \geq 0.3$, $\beta \leq 0.1$, $r^2 \geq 0.990$, $f_{resid} \geq 0.15$, $\alpha \leq 10°$, $MAD \leq 10°$, $|k'| \leq 0.27$ and $0.85 \leq |b_{AA}| \leq 1.15$.

Results that passed all criteria were classified as 'A'. Because the selection criteria used in this study for the numerical handling of Arai plot data as a qualifier were stricter than the ones used in other intensity studies of similarly aged rocks (Bono et al., 2019; Shcherbakova et al., 2020), we introduced relaxed values in certain specific cases based on the criteria used by Shcherbakova et al. (2020). Results that used relaxed criteria were classified as 'B'. Limits for relaxed selection criteria were: $FRAC \geq 0.25$, $DRAT \geq 15\%$, $CDRAT \geq 15\%$ and $|k'| \geq 0.48$ for microwave and thermal Thellier experiments and $r^2_N \geq 0.990$ and $r^2_T \geq 0.990$ for Shaw experiments. Microwave Thellier, thermal Thellier and pseudo-Thellier results were analysed with paleointensity.org (Béguin et al., 2020). If multiple fits passed selection criteria, then the fit with the highest number of included points and lowest curvature was chosen.

2.3 Results

Thermomagnetic curves and susceptibility versus temperature curves measured on samples from different dykes showed quite diverse behaviour (Supplementary Figure B.1). Most specimens showed one or two Curie temperatures between 550°C and 580°C. Heating curves for specimens from the French River and Key River dykes as well as specimens from sites GD25 and GD26 also had noticeable Hopkinson-like peaks, often indicating the presence of single-domain (SD) or pseudo-single-domain (PSD) magnetic phases. Apart from small alterations around 400°C, heating and cooling curves of cyclic experiments were reversible up to 550°C. Considerable alterations occurred in the temperature range between 550°C and 650°C and features such as Hopkinson like peaks were not visible in the final cooling curve of the last cycle. Exceptions related to higher levels of weathering were measurements on specimens from site GD01 with a Curie temperature of 470°C and from sites GD07 and GD30, where susceptibilities were about two orders of magnitude weaker. Accordingly, no palaeointensity estimates were obtained from these sites. The susceptibility curves of specimens from Coniston, French River and Sand Bay dykes showed a small 'toe' with another Curie temperature up to 610 - 620°C, possibly suggesting the presence of a small fraction of maghemite or titanohematite. Backscattered electron imaging (Figure 2.2a - c) shows relatively coarse (∼30 - 200 µm) (Ti-)magnetite grains with sharp edges as well as small dendritic (< ∼40 µm) (Ti-)magnetite grains (e.g., Figure 2.2a, b), indicating rapid cooling of the rocks. Energy dispersive spectroscopy elemental composition mapping of larger grains shows structures of full and partial exsolutions with lamellae of titanium-rich ilmenite and titanium-poor magnetite (Figure 2.2c, Supplementary Figure B.2). The preservation of high-temperature textures and lack of low-temperature oxidation structures suggest that the grains are carriers of a primary TRM. For some samples it cannot be ruled out that the oxy-exsolution continued to temperatures lower than the Curie temperatures. Thermochemical remanences (TCRM) from such processes have been connected to underestimates of Thellier data (Smirnov and Tarduno, 2005). More recently, a study on rocks with artificially induced TCRMs found contrasting results showing only small effects on their resulting palaeointensities (Shcherbakov et al., 2019).

Hysteresis parameters (Figure 2.2d - f) fall in two clusters on the Day et al. (1977) plot with one large cluster in the "PSD" area and several data points at lower ratios of magnetic remanence to saturation magnetisation (M_{rs}/M_s) and higher ratios of remanent coercivity to coercivity (B_{cr}/B_c) indicating a mixture of magnetic domain types with both single-domain and multidomain grains. However, all samples show reasonably high bulk domain stability (Paterson et al., 2017) with positive values between 0.08

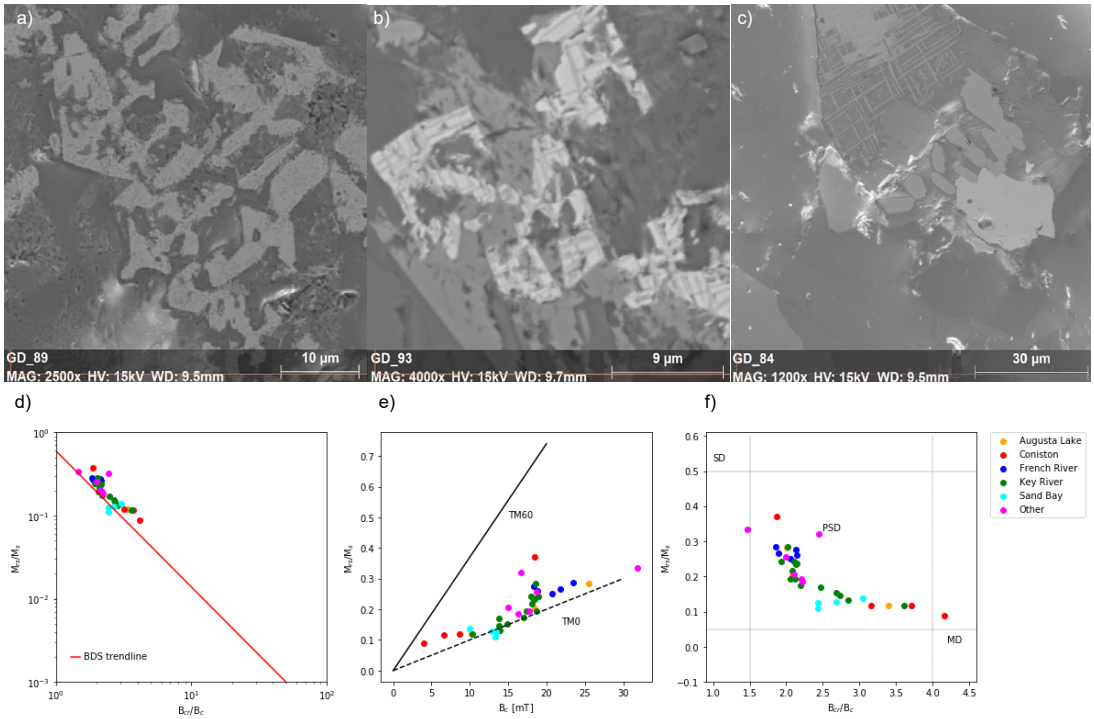

FIGURE 2.2: SEM backscatter images: (a) GD23, (b) GD29, examples of dendritic TM grains, (c) GD02, coarse Tm grain, showing magnetite-ilmenite exsolution. (d) frequencies of viscosity indexes of all sites, (e) Hysteresis parameters and (f) Day plot of representative samples of each site.

and 0.63 (Figure 2.2d) implying that the rocks may give good palaeointensity results. Hysteresis loops of weathered samples (sites GD07, GD30) show large paramagnetic contributions, probably carried by clays. Comparison of hysteresis parameters with the theoretical predictions for titanomagnetites $Fe_{3-x}Ti_xO_4$ with x = 0 (TM0) and x = 0.6 (TM60) (Wang and Van der Voo, 2004) shows that most specimens plot close to the TM0 line. This includes results from the French River dyke, which showed a substantially higher TiO_2 content in the geochemical analysis of the sites in Halls et al. (2015). In contrast, specimens from the low-Ti-type Coniston dyke (Halls et al., 2015) plot further away from the TM0 and closer to the TM60 line.

Fractions of viscous remanent magnetisations (VRM) of specimens from the different sites, acquired after 3 weeks in the ambient field, did not show any differences at the dyke level. The average viscosity index (v) for all sites was 14.4% (median = 9.6%, σ = 14.9%). This mean viscosity index includes v values of up to 80% from sites GD07 and GD30. Specimens from those sites had very low magnetisations and the viscosity index was mostly calculated from noise. Specimens with v values of > 30% were not

used for intensity determination. We note that low palaeointensities will naturally produce weak NRMs (on account of Thellier's law of linearity; Thellier, 1941) which will then be more radically affected by a VRM acquired in the strong present-day field.

Microwave demagnetisation experiments were performed on 29 specimens to determine their response to microwave treatments. These measurements showed that it was possible to demagnetise specimens from all sites with microwave treatment. However, specimens from the weathered sites GD07 and GD30 as well as host rock specimens from site GD29 were too weakly magnetised to be measured on the microwave system. In total, palaeointensity measurement was attempted on 204 specimens of the Grenville dykes. Of these, 127 used microwave-IZZI, 20 used thermal-IZZI, and 57 used Shaw and/or pseudo-Thellier experiments (Table 2.1). A relatively small number of thermal Thellier experiments were attempted because these were inefficient in terms of the amount of material used, the time taken to perform, and the degree of alteration produced by repeated heatings in air. In any case, the microwave Thellier approach has been shown to give equivalent, or better, results in many studies when the same protocols were followed (Biggin et al., 2007b; Grappone et al., 2019, 2020).

In the relatively small number of thermal Thellier experiments, specimens universally showed non-ideal behaviour and did not pass selection criteria. These mostly produced chaotic Arai and orthographic plots (Figure 2.3e) and the experiment was stopped at 550°C. Strong 'zig-zagging' and high β values together with high curvature values suggest strong MD behaviour over the full temperature range that was seen in all experiments. In contrast, for about half of the specimens pTRM checks passed the criteria up to the highest temperature steps.

The majority of Arai plots from all Thellier experiments (75%) and of passing Thellier results (94%) showed two slopes. Similar to the results of other studies yielding extremely low palaeointensities (Hawkins et al., 2019; Shcherbakova et al., 2020), the sharp bend between the high- and low-temperature/power slopes usually coincided with the junction between ChRM and secondary components in the associated Zijderveld plots (Figure 2.3a, c), but this was not clearly visible for all results (Figure 2.3b, Figure 2.5a - d). For results that do not show a clear directional change (Figure 2.3b) it can be difficult to ascertain whether a two-sloped Arai plot is due to large palaeointensity differences between ChRM and overprint or due to a sagging of the slope caused by MD grains. Here, zig-zagging and curvature were used as prime criteria to detect and reject results biased by MD behaviour. Of the accepted microwave Thellier results, 6 passed as A and 19 as B result. For all B results, DRAT, CDRAT or curvature had to be relaxed. About 10% of the results that were not accepted failed only one

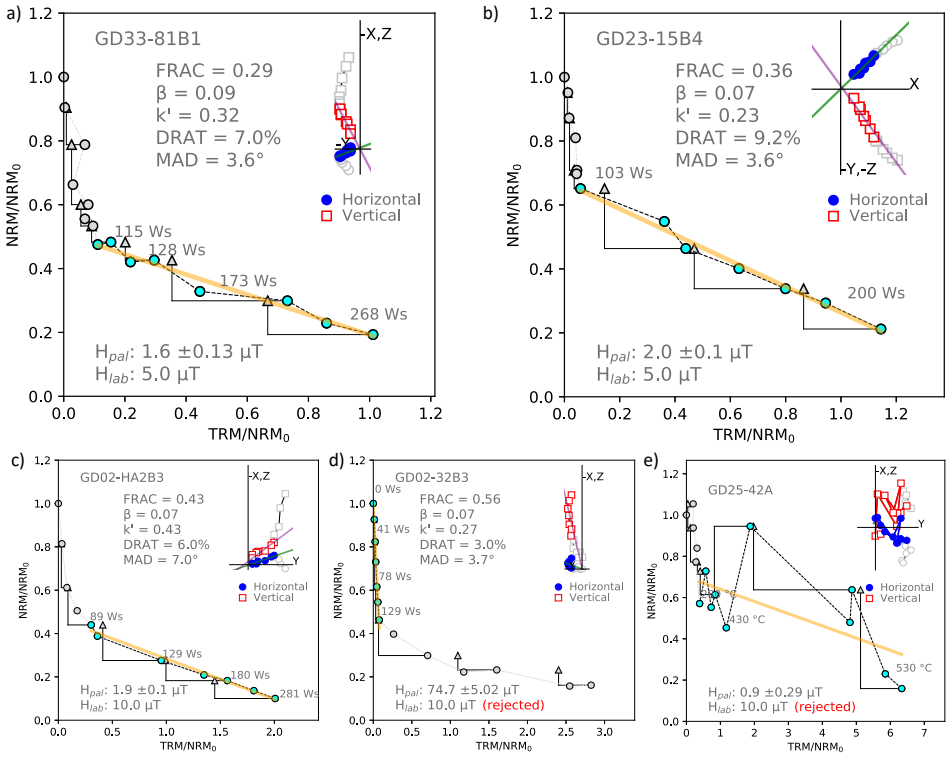

FIGURE 2.3: Arai plots of Thellier experiment results. a)-d) show microwave experiments, e) shows a result of a thermal Thellier experiment. For more details, readers are referred to section 2.3 of the text.

of the selection criteria. All other rejected results failed more than one selection criterion (e.g., Figure 2.3e). The most commonly failed criteria were β (57% of results), FRAC (56%), DRAT/CDRAT (48/52%) and k' (30%). The high failure rate due to β, k' and DRAT/CDRAT shows that MD effects and mineral alterations during heatings were both primary issues in the results of thermal and microwave experiments. Six low-temperature/power slopes (5%) would pass the selection criteria, but it is clearly visible in the orthographic plot that the selected fraction is not the ChRM (Figure 2.3d). One outlier intensity from a high-power slope of 26.7 μT passed the selection criteria (GD19-43B1) but was rejected as unreliable because the standard deviation of possible intensities from the high-power slope of sister specimens of this sample was larger than the mean intensity.

Of the 12 accepted Shaw results, 7 passed as A and 5 as B results. For all 7 B results, the correlation coefficient of the best fit line in the NRM-TRM1* plot r_N^2 was relaxed to $r_N^2 \geq 0.990$ (Figure 2.4a). Results not passing r_N^2, k' and/or $slope_T$ was the main reason for unsuccessful experiments. Multidomain effects in Shaw experiments can cause biased ARM corrections and often lead to non-linear Shaw plots (Tanaka & Komuro,

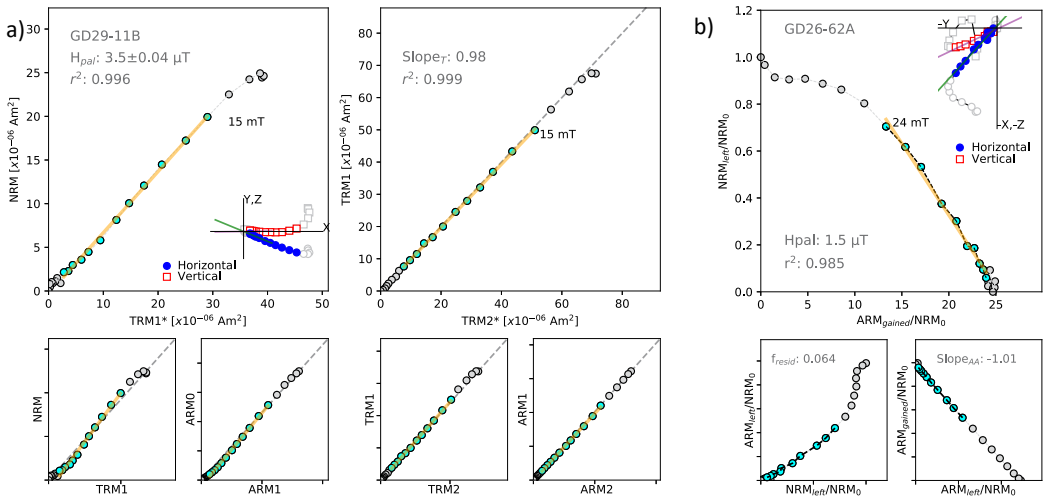

FIGURE 2.4: a) Representative example of a successful Shaw experiment: left column shows the orthogonal plot of the demagnetisation of NRM (top) and absolute values of magnetisation during AF demagnetisations of NRM, ARM0 and TRM1 (bottom). middle and right columns show results from first and second laboratory heating, respectively; b) example of a successful pseudo-Thellier experiment: pseudo-Arai plot with orthogonal projection, demag-demag plot (NRM vs ARM) and ARM-ARM plot (acquisition vs. demagnetisation).

2009). Here, rejected results with correlation coefficients of $r_N^2 \leq 0.95$ also showed high curvatures while in turn, linearity of Shaw plots was high ($|k'| = 0.1 \pm 0.05$) for results that passed as A or B (Figure 2.5e). Validity of ARM corrections is checked in the double heating method and four results with linear Shaw plots were rejected because a failed ARM correction was detected in the plot of the TRM of the first heating versus the ARM corrected TRM of the second heating. Specimens showed a wide range of coercivities with an average median destructive field MDF = 19.2 ± 9.6 mT. Eight specimens were too weakly magnetised to generate ChRMs during demagnetisation. Secondary magnetisations that accounted for NRM fractions of up to 80% were usually removed by AF fields of less than 40 mT. Similar to the AF demagnetisation experiments in Halls et al. (2015) that successfully generated reliable directions and passed field tests, the remaining fraction of primary NRM was sufficiently large in the Shaw experiments such that only ∼20% of specimens failed the FRAC criterion. The directions gained from analysis of the demagnetisation of NRM were used together with directions from Halls et al. (2015) to recalculate site-mean directions for determinations of VDMs (Table 2.1).

Dyke	Site	Age [Ma]	Directions					Intensities [μT]						pThel [μT]	VDM [10^{22} Am^2]		Q_{PI}
			N/n	Dec	Inc	α_{95}	k	N/n_{PI}	N/n_{TH}	N/n_{MW}	N/n_S	PI	Std	PI	VDM	Std	
Augusta	GD2	584 ± 0.6	*10/9**	*120.5*	*20.0*	*7.7*	*46*	13/2	1/0	9/1	3/1	2.1	0.04	-	-	-	
Lake	GD33		*8/6**	*134.0*	*38.2*	*10.7*	*40*	17/5	1/0	14/5	2/0	2.6	0.62	1.9	-	-	8
	Mean		*18/15**	*125.6*	*30.2*	*7.3*	*28*	30/7	2/0	23/6	5/1	2.4	0.23	1.9	0.52	0.05	
Coniston	GD01		*5/3*	*115.5*	*17.1*	*32.4*	*16*	5/0	1/0	3/0	1/0	-	-	-	-	-	
	GD14		*13/3*	*95.5*	*23.8*	*26.3*	*13*	6/1	1/0	2/1	3/0	7.6	-	-	-	-	6
	Mean		*13/3*	*95.5*	*23.8*	*26.3*	*13*	6/1	1/0	2/1	3/0	7.6	-	-	1.66	x	
French River	GD23	598 ± 1.4	*6/3*	*133.9*	*31.3*	*7.4*	*280*	24/13	2/0	20/12	1.8	0.67	-	0.42	0.16	7	
Key River	GD10	587 ± 1.4	10/9	137.7	-75.8	6.7	61	14/0	1/0	9/0	4/0	-	-	-	-	-	
	GD15		5/5	140.9	-66.8	6.7	130	14/1	1/0	10/1	3/0	5.6	-	-	-	-	
	GD16		6/6	166.7	-86.7	12.5	21	11/1	1/0	7/1	3/0	4.3	-	1.3	-	-	9
	GD19		9/5	100.6	-56.2	11.9	42	12/0	1/0	8/0	3/0	-	-	-	-	-	
	GD37		9/8*	145.7	-68.2	4.2	30	7/3	1/0	2/0	4/3	5.3	1.57	3.1	-	-	
	Mean		10/19	146.2	-73.4	8.2	12	58/5	5/0	36/2	17/3	5.1	0.56	2.2	0.78	0.09	
Sand Bay	GD29	585 ± 0.8	*9/9**	*297.7*	*-38.3*	*5.2*	*97*	43/7	6/0	26/3	11/4	3.7	0.69	4.1	0.82	0.15	8
Other	GD07		*7/6*	*134.8*	*1.2*	*11.2*	*37*	3/0	0/0	0/0	3/0	-	-	-	-	-	
Grenville	GD25		*9/9**	*138.9*	*15.1*	*8.7*	*36*	15/2	1/0	10/1	4/1	6.8	5.82	-	1.71	1.43	7
Dykes	GD26		*9/6**	*129.9*	*-20.2*	*10.8*	*39*	8/2	1/0	4/0	3/2	1.4	0.40	1.5	0.34	0.10	6
	GD30		10/6	139.0	-67.3	8.4	64	5/0	1/0	3/0	1/0	-	-	-	-	-	

TABLE 2.1: Summary of palaeointensity results of the Grenville dykes: Dyke/Site: dyke/site name, Ages and directional information from Halls et al. (2015) (* directions recalculated using ChRMs from Shaw/pseudo-Thellier data, directions of sites in italics are not supported by field tests), N/nPI: total/ successful number of results (MW: microwave Thellier, TH: thermal Thellier, S: Shaw), PI/pThel: palaeointensity/pseudo-Thellier results in μT, VDM: virtual dipole moment, Q_{PI} values of sites.

From the 28 pseudo-Thellier experiments, 5 specimen results passed selection criteria and were accepted. Results from successful pseudo-Thellier experiments, which involve no laboratory heating whatsoever, showed good agreement with the site-mean values calculated from microwave and Shaw results (Table 2.1). Pseudo-Thellier results from sites GD33, GD29 and GD26 and associated site-means calculated using other methods agree within uncertainty. For sites GD26 and GD37 that show a larger difference (> 1 µT) between intensities from pseudo-Thellier experiments and intensities from other methods, the palaeointensities from pseudo-Thellier experiments are lower than the palaeointensities from the other methods. Most unsuccessful pseudo-Thellier experiments failed due to a high curvature of the selected line segment in the demag-demag plot (Figure 2.4b) suggesting that NRM and ARM (de)magnetisations behave differently in these specimens and a palaeointensity calculated from these would be unreliable (Figure 2.5f).

Combining A and B results, 25 results of the microwave-Thellier experiments (20% success rate) and 12 results of the Shaw experiments (24%) passed the used selection criteria. None of the thermal-Thellier experiments passed selection criteria, leading to an overall success rate of 18% for Shaw and Thellier-type experiments. Palaeointensity estimates were averaged for each dyke as separate spot readings of the field strength (Table 2.1). The resulting intensity values range from 1.4 µT to 7.6 µT, and yielded VDMs of 0.3 - 1.7 $\times 10^{22}$ Am^2. Five pseudo-Thellier results passed selection criteria as well and gave intensity values between 1.1 µT and 4.1 µT. All intensity results with critical values are listed in Supplementary Tables A.1 - A.3 and measurement data of all experiments are available on the MagIC database (www2.earthref.org/MagIC).

2.4 Discussion

The geomagnetic field in the Ediacaran is characterised by ambiguous field directions that impede APW curves. Recently, it has been stated that the time averaged dipole field strength is uniquely low in the Ediacaran which is seen in both single-crystal (Bono et al., 2019) and whole-rock studies (Shcherbakova et al., 2020). We expand these intensity data with the whole-rock palaeointensities of the Grenville dykes with VDMs of 0.76 ± 0.5 $\times 10^{22}$Am^2.

Due to the low number of available samples and non-ideal behaviour during thermal-Thellier experiments, microwave experiments were preferred as the small sample size allowed for a high number of experiments with sub-specimens. To account for a possible method-bias of the MW results, a number of thermal-Thellier, Shaw and pseudo-Thellier experiments were conducted as well. All methods suffered from low success rates that made it hard to compare the different methods on the site level. Where such

a comparison was possible, the results from different methods differed by less than 1 µT, similar to the overall variability on the dyke level. From this, a method related systematic bias seems unlikely. Furthermore, results from Thellier and Shaw experiments are also supported by the results of the pseudo-Thellier experiments. Figure 2.5 shows a range of rejected and accepted results that show consistent palaeointensities from all methods for sister specimens from a sample of the French River dyke.

To confirm that the intensity results are not biased by the choice of selection criteria, other commonly used sets of selection criteria were used to re-analyse all Thellier-type results (Supplementary Table A.4). All sets show only small differences in the range of ∼1 µT and agree well with the results of the Shaw experiments. Results from combined A and B results only differ from pure A results by 0.2 µT and are well inside the standard deviation of A results, while the number of accepted results almost doubled.

The two-slope behaviour, seen in most Arai plots of Thellier experiments in this study, has been recognised in other studies of basalts with low palaeointensities as well (e.g., Hawkins et al., 2019). Similar behaviour is often ascribed to MD behaviour (Riisager & Riisager, 2001; Smirnov et al., 2017) and/or alteration of magnetic minerals during heating steps of the experiments (Kissel & Laj, 2004) as well as to instabilities of aged thermoremanence (Shaar & Tauxe, 2015). Thermochemical alteration during the heatings was very common in the experiments of this study and results that were affected by alteration, as seen from pTRM checks, were rejected. Curved or zig-zagging Arai plots, caused by MD behaviour and/or instability of TRM, were excluded if the curvature or β criteria were not met. Hawkins et al. (2019) argued that the two-slope behaviour without a corresponding directional change in their study was attributed to strong thermal or thermoviscous overprints of similar direction. This is also the case in our study, but here a directional change is often observable at the bend between the two slopes in the Arai plots as well. Therefore, the slope of the high unblocking temperature ranges, that also carried the ChRM in Halls et al. (2015), were selected in the Arai plots to calculate palaeointensities.

While all steps were taken to detect and reject results biased by MD behaviour, the ambiguity of sagging and two-sloped Arai plots may cause doubt over whether every single biased result was rejected, especially since MD effects were one of the main issues leading to low success rates. The high agreement of results from different methods, however, confers confidence that the accepted mean results were not substantially biased. It is noted that even if palaeointensity errors due to non-ideal carriers were as large as 25% (Smirnov et al., 2017; Tanaka & Komuro, 2009), these would produce a very small absolute bias in the results of this study.

The overall quality of accepted palaeointensity results was assessed by the application of Q_{PI} criteria (Biggin & Paterson, 2014) for each dyke (Supplementary Table A.5).

The AGE criterion was met by all dykes as the dyke swarm was radiometrically dated in Halls et al. (2015). Augusta Lake dyke, Key River dyke and Sand Bay dyke met the STAT criterion. The French River dyke has more than the required 5 individual intensity estimates, but the estimate had a dispersion (stdev/mean) $\leq$ 25% (Paterson et al., 2010), which is often the case for ultra-low palaeointensity results (e.g., Shcherbakova et al., 2020). Other units yielded less than the 5 successful individual palaeointensity results needed to meet the STAT criterion.

Mostly fresh looking titanomagnetite grains with high-temperature oxy-exsolution structures and rapidly cooled dendritic magnetite grains without signs of low temperature oxidations as seen from SEM suggest that the magnetisation is a primary TRM. However, concerns can be raised about the validity of the magnetisation itself due to the anomalous nature of the palaeodirections (Halls et al., 2015). This is especially the case for sites associated with the shallow directional component, where the possibility of a remagnetisation event cannot be completely dismissed due to inconsistent results of a baked contact test (Robert et al., 2017). Our rock magnetic data imply a similar range of magnetic mineralogy for samples from sites of either directional component and no systematic differences could be seen that would support a remagnetisation of the shallow component. Halls et al. (2015) argued that these shallow directions are also primary because they are almost antipodal and can be followed continuously along the dyke. Palaeointensity estimates, irrespective of the associated directions were similar and extremely low and the angular dispersions of VGPs show almost identical behaviour of steep and shallow components. On the basis of the combined microscopic and palaeomagnetic evidence for samples of both directional components, we chose to award the TRM criterion to all units.

The use of pTRM checks and the application of the IZZI protocol with β and k' criteria as well as the double heating checks of the Shaw experiments enabled the exclusion of all estimates that could be significantly biased by thermochemical alteration or MD behaviour during the experiments. Therefore, all sites passed both the ALT and MD criteria. Following the standard palaeointensity definitions (SPDv1.1; Paterson et al., 2014), the angle between the laboratory field and the last pTRM check of the Thellier experiments was calculated as $\gamma = 3.2° \pm 1.2°$, showing that the results were not majorly influenced by anisotropy effects. Systematic bias of estimates due to non-linear TRM behaviour was avoided by using different laboratory TRM fields between 3 µT and 30 µT and ARM fields between 10 µT and 81.2 µT. The similarity of results between the Shaw method with cooling times of $\sim$1 h and the microwave Thellier

method with cooling times of < 1 min exclude a cooling rate bias. Therefore, the ACN criterion was given to all units.

Four different methods were used to determine palaeointensities. To pass the TECH criterion, the palaeointensity estimate of a unit has to comprise results from at least two different methods which was the case for 5 units. The rejection of all thermal-Thellier results remains troubling as systematic differences between results from thermal and microwave experiments were found in previous studies (Biggin, 2010). Instead of the different demagnetisation methods causing the discrepancies, the bulk of differences has recently been attributed to the failure to detect non-ideal behaviour (Grappone et al., 2020). Grappone et al. (2020) suggested that the use of appropriate protocols in both methods could reduce the differences in results. This is supported by the results of Shcherbakova et al. (2020) where thermal and microwave experiments using IZZI and Coe protocols produced agreement in Ediacaran-aged rocks. Good agreement of results between the microwave and Shaw/pseudo-Thellier methods in this study gave additional confidence in the reliability of the accepted intensity determinations. The criterion LITH was only awarded to Key river dyke since site GD37 combines results from both the dyke and baked host rocks. All measurement data are available on the MagIC database, awarding the MAG criterion to all units.

Summing up the Q_{PI} criteria results in scores of 6 - 9 indicating that the accepted palaeointensity estimates, despite being low in number and lacking accepted thermal Thellier results, are of high technical quality. A higher number of accepted results would allow the palaeointensities associated with the steep B and shallow C+D directions found in Halls et al. (2015) to be compared. Assuming a high-latitude of Laurentia around ~590 Ma, the palaeointensities of the shallow component – if recording an equatorial dipole field state – might be expected to be much lower than the intensities of the steep component. The number of accepted intensities is insufficient for significant comparison of the two components, but the average site-mean palaeointensities of all sites with shallow directions (3.7 ± 2.3 µT) and sites with steep directions (5.0 ± 0.5 µT) are within error at one standard deviation. This similarity of the ultra-low palaeointensities of the two components may be a hint that the Grenville Dykes have recorded a highly unstable field as proposed in Halls et al. (2015). In contrast, the high and almost identical values for angular dispersions (Supplementary Figure B.3) of two distinct groups of VGPs around the mean VGPs of the steep (S_B = 18.5°) and the shallow component (S_B = 18.9°) look consistent with the existence of an equatorial dipole. However, some caution is advised when taking the dispersions at face value. Recent studies of VGP scatter required a minimum of N = 9 sites (Doubrovine et al., 2019).

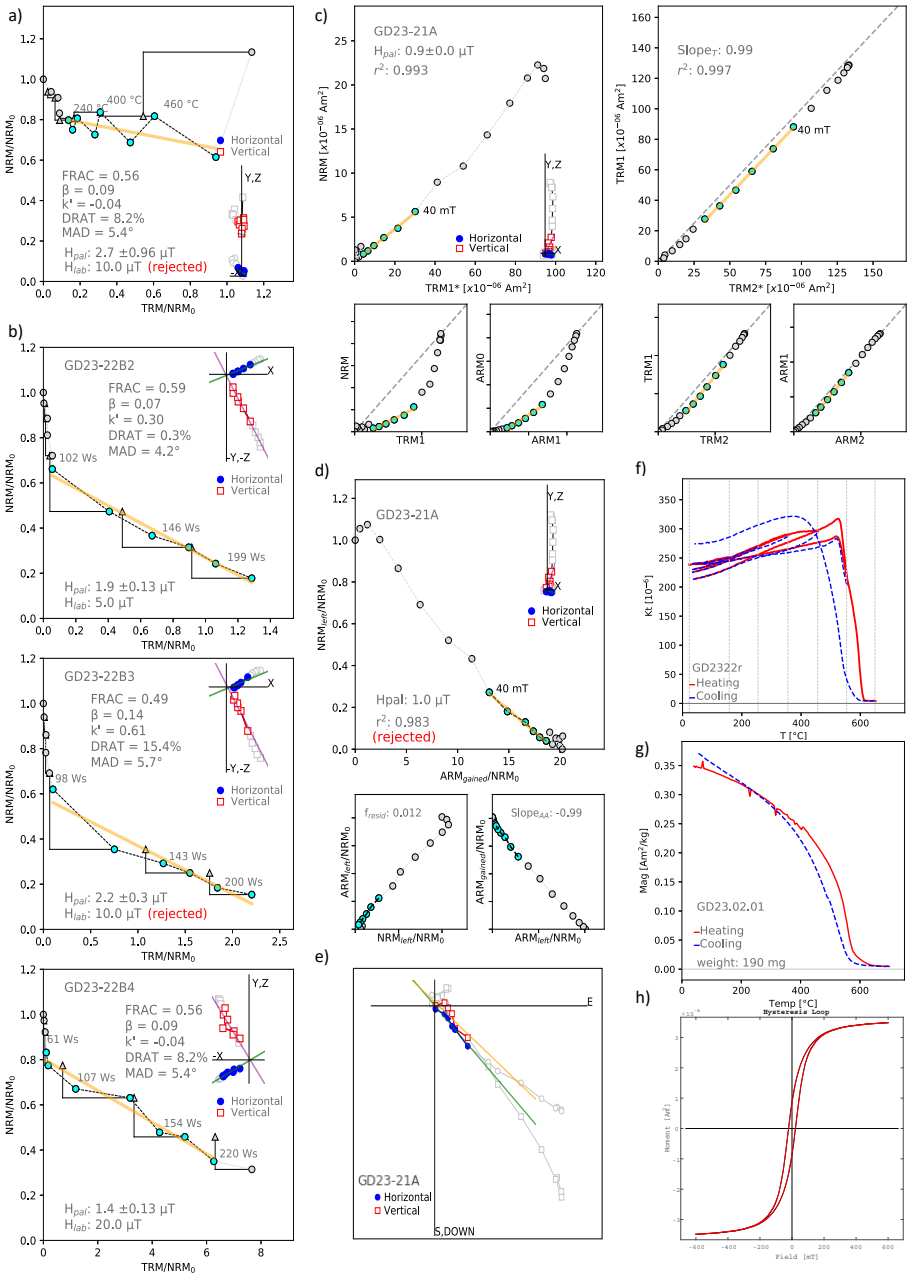

FIGURE 2.5: Compilation of results for sister specimens of sample GD23-2, all orthogonal plots for intensity experiments are shown in specimen coordinates: a) Arai plot of thermal Thellier experiment, measurement points are shown up to a temperature of 510°C; b) Arai plots of microwave Thellier experiments; c) result of Shaw experiment; d) result of pseudo-Thellier experiment; e) Zijderveld plot in geographic coordinates; f) cyclic heatings of temperature dependent susceptibility in 100°C increments up to 650°C; g) thermomagnetic curve up to 700°C; j) temperature dependent susceptibility between 40 and 700°C; h) Hysteresis loop, analysed in HystLab (Paterson et al., 2018). Critical values of shown intensity experiments are listed in Supplementary Tables A.1 - A.4.

After the exclusion of lower quality directions from sites with n $\leq$ 4 or k $\leq$ 30 in the calculations, this requirement was only met by the shallow component (N = 11), but not by the steep (N = 7). The dispersion values seem reasonable for the time period with comparable values for Laurentia showing a wide range between S_B = 13.5° (McCausland & Hodych, 1998; Veikkolainen & Pesonen, 2014) and S = ∼26° (Bono et al., 2019). If the two groups of VGPs were interpreted as one group, showing a transitional field, then the resulting VGP dispersion would be S_B = ∼33° at low latitude. This would be an extremely high value but the current lack of constraints on the Ediacaran field means that it is not implausible.

With the exception of sites GD14 where only one single intensity was accepted and GD25, where a single high (7.6 and 12.6 µT) microwave result leads to high VDMs of ∼1.7 ×10^{22}Am^2, the mean VDMs of 0.6 ± 0.2 ×10^{22}Am^2 are comparable to the single-crystal results of the Sept Îles (∼0.7 ×10^{22}Am^2, Bono et al., 2019) and the whole-rock results of the Volyn Traps (0.9 ± 0.2 ×10^{22}Am^2, Shcherbakova et al., 2020). The palaeointensities, coming from dykes with ages that span ∼15 million years, could suggest that a sustained geomagnetic field with these extremely low intensities extended back at least until 600 Ma with intensities being an order of magnitude weaker than the strength of the present-day field (Figure 2.6). Palaeointensities this low have been reported for Earth before, but were generally not attributed to a sustained field. The PINT database (Biggin et al., 2015) contains 6 site-mean estimates with $H_{pal} \leq$ 5 µT or VDM $\leq$ 0.5 ×10^{22}Am^2, N > 1 and reliable experiment types (excluding single-heating Shaw and total TRM experiments) that can be roughly divided into two groups. The first group comprises entries with mid-Miocene or younger ages that show the ultra-low intensity values in single basalt flows from Iceland (Lawley, 1970) and the Canary Islands (Brown et al., 2009; Leonhardt & Soffel, 2002) that are all connected to the short-term drop of dipole moments during polarity transitions interrupting a much stronger sustained field. The palaeointensities with Mesoproterozoic to Archaean ages from the second group are either (a) extremely low due to fractions of chemical remanent magnetisation (Yoshihara & Hamano, 2004), (b) would not satisfy any modern sets of selection criteria (Ueno, 1995), or (c) are only seen as spot reading of the field in a single dyke showing an anomalously low intensity (Smirnov & Tarduno, 2005) in a population of dykes with higher palaeointensities (Halls et al., 2004). Non-Ediacaran weak sustained fields as in the Jurassic (∼2.8 ± 0.9 ×10^{22}Am^2, Tauxe et al., 2013) or the Devonian (∼1.1 ± 0.5 ×10^{22}Am^2, Hawkins et al., 2019) are all stronger. However, a field strength behaviour, similar to the one in the Ediacaran, can be observed in the Upper Devonian around ∼370 Ma, where site-mean palaeointensities as low as 2.4 µT (0.4 ×10^{22}Am^2) have been reported in a weak time-averaged field as well (Hawkins et al., 2019).

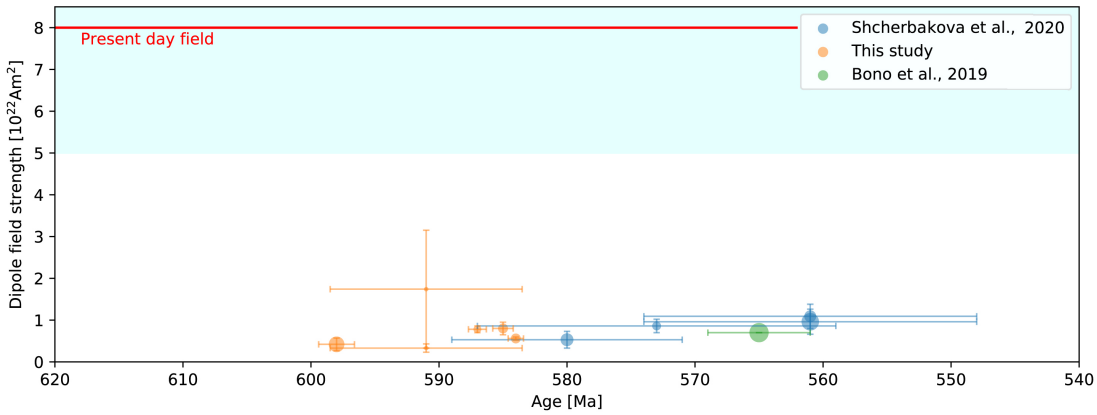

FIGURE 2.6: Virtual dipole moments of the Grenville dykes plotted versus age in with virtual dipole moments of the Baltican Volyn traps (Shcherbakova et al., 2020) and the palaeomagnetic dipole moment of the Sept Îles (Bono et al., 2019) in comparison to the present-day field strength. Marker sizes correspond to number of individual intensity estimates N used in the average. Plotted are mean values with N > 1. Error bars show estimated age errors and one standard deviation of dipole moments.

The similarity of the weak palaeointensities in this study with those seen during reversals and excursions further strengthens the hypothesis of an unstable/transitional and possibly hyperactive field throughout the Ediacaran. Similar to the palaeointensities for the later Ediacaran (Shcherbakova et al., 2020) the possibility that all of our spot readings of the field sample reversals or excursions in a hyper-reversing Ediacaran field and miss periods of stronger fields cannot be dismissed. Consistency of directional results do not necessarily contradict the intensities belonging to a reversal (e.g., Prevot et al., 1985). However, to date there have been no reports of any stronger fields throughout the Ediacaran and the ultra-low intensities seen in the spot readings of this study and Shcherbakova et al. (2020) agree with estimates of time-averaged intensities in Bono et al. (2019) (Figure 2.6). To confirm that a sustained weak field does indeed extend back to the mid-Ediacaran – or further – a better data coverage and time-averaged palaeointensities will be required.

These ultra-low Ediacaran intensities are consistent with the predicted weak-field state of the geodynamo before the onset of inner core growth (Bono et al., 2019; Driscoll, 2016). Under this scenario, the dynamo was operating marginally, powered by thermal convection due to heat loss at the core-mantle-boundary alone and the field was diminished. Subsequently, the inner core nucleated providing additional convective power from the release of light elements and latent heat of crystallisation. An entirely different cause of a massively diminished dipole moment in the Ediacaran, perhaps related to a reconfigured convective pattern in the core, perhaps related to an unusual core-mantle heat flow pattern, cannot be ruled out, however. That the measured

palaeointensities are similar in magnitude to ground measurements of a local crustal field of Mars (Johnson et al., 2020), a planet which is suspected to have been without a core dynamo for 4.1 billion years, raises profound questions concerning measurement limits and the history of the geodynamo.

2.5 Conclusions

We report new palaeointensities from six dykes at the western end of the Grenville dyke swarm. Success rates of palaeointensity experiments were substantially lowered by the rejection of all samples where thermochemical alteration during laboratory heating or MD behaviour were suspected. Detection of MD behaviour was especially important as non-ideal magnetic carriers were present in the studied rocks and MD behaviour would lead to an underestimate of palaeointensities. The application of strict selection criteria resulted in the rejection of all thermal-Thellier results. The resulting site mean ($N \geq 3$) palaeointensity values and standard deviations ($\pm$ 1 σ) from Shaw and microwave-Thellier experiments range between 1.4 $\pm$ 0.4 µT - 6.8 $\pm$ 5.8 µT (0.33 $\pm$ 0.1 $\times 10^{22} Am^2$ – 1.71 $\pm$ 1.4 $\times 10^{22} Am^2$). These estimates agree well with results from other palaeointensity studies from this time period (Figure 2.6) and suggest that the Ediacaran field might have been weak over a longer time frame than previously seen from palaeointensity data. This opens up questions about what geodynamo regimes could sustain such weak fields over longer time periods. The behaviour of VGPs with almost identical angular dispersion around two clusters argues for the presence of an equatorial dipole field. In contrast, the consistency of presented ultra-low intensities along dykes for both directional components supports the idea of an unstable and/or transitional field in the Ediacaran. The presented data are another argument for the Ediacaran field behaving strangely but at this point, a more precise definition is elusive. Measurements from the early to mid-Ediacaran are still scarce and a better coverage of spot readings of palaeointensity, time averaged palaeointensities and magnetostratigraphic data would be immensely useful to better characterise the geomagnetic field in the Ediacaran.

Chapter 3

A palaeointensity study of the Skinner Cove Fm, Newfoundland

Thesis context

In the previous chapter, the measured palaeointensities of the Grenville dykes revealed some of the weakest field strengths ever measured and suggested the presence of an extended period of extremely weak geomagnetic field, which had previously been inferred from the high reversal frequencies in the Ediacaran (e.g., Bazhenov et al., 2016; Meert et al., 2016) and the inverse correlation between reversal frequency and dipole moment strength (e.g., Biggin et al., 2012; Tauxe et al., 2013). However, similarly high reversal frequencies have been reported for the late Ediacaran (Levashova et al., 2021) and the Early Cambrian (Gallet et al., 2019). Following the relation between dipole moment strength and reversal frequency, this would imply that the weak Ediacaran field extends into the Cambrian. This contradicts the expected rise in field strength and decrease in reversal frequency after a late Ediacaran onset of inner core nucleation (e.g., Bono et al., 2019; Driscoll, 2016).

In this chapter, we take a closer look at the geomagnetic field at the end of the Ediacaran and measure the palaeointensities of the Skinner Cove formation, which has recorded the youngest Ediacaran palaeopole for Laurentia (McCausland & Hodych, 1998) and has been key in placing Laurentia at low latitudes before the transition to the Cambrian period (Hodych et al., 2004; Li et al., 2013; Robert et al., 2021). This will allow us to expand the record of Ediacaran field strengths towards the Cambrian, and explore the field behaviour at a (possibly) critical time of Earth's core evolution.

This chapter is published as Thallner D., Biggin A.J., McCausland P.J., Fu, R. (2021), New palaeointensities from the Skinner Cove Formation, Newfoundland, suggest a changing state of the geomagnetic field at the Ediacaran-Cambrian transition, *Journal of Geophysical Research: Solid Earth*, 126.

In this study, I conducted all rock magnetic and palaeointenity experiments. Measurements of magnetic maps on the quantum diamond microscope were performed by Roger Fu at Harvard University. I also analysed all results and wrote the publication together with Andy Biggin, Phil McCausland and Roger Fu.

Abstract

The geomagnetic field in the Ediacaran period appears to be characterised by anomalous directions, high reversal frequencies and ultra-low field strength. At the Ediacaran - Cambrian transition, apparent polar wander paths become less controversial, but hyper-reversing fields with reversal frequencies similar to earlier in the Ediacaran have been reported until the mid-Cambrian. To understand the long-term behaviour of the magnetic field during this transitional interval, information about the field strength is vital but currently lacking. In order to improve the intensity record at that time, samples of volcanic rocks from the 550 Ma Skinner Cove Formation, western Newfoundland, have been used for palaeointensity determination. This multi-method palaeointensity study, utilising thermal and microwave Thellier as well as double-heating Shaw and pseudo-Thellier experiments produces palaeointensity estimates of 2.6 - 10.3 µT, corresponding to virtual dipole moments of 0.65 - 2.25 $\times 10^{22}$ Am^2. Analyses using SEM and rock magnetic measurements, as well as a positive intraformational conglomerate test suggest that the remanence is primary. These intensity estimates are higher than earlier Ediacaran intensities and could point to the geomagnetic field entering into a stronger, more dipole-dominated state at the Ediacaran-Cambrian boundary.

3.1 Introduction

Information about long-term variations of geomagnetic field behaviour, derived from palaeomagnetic data, may be vital to gain insight to the evolution of the deep Earth interior over geological timescales (Sprain et al., 2018). Numerical geodynamo simulations used to tie the geomagnetic field behaviour to changes in the Earth's core and mantle rely on high quality palaeomagnetic data and their interpretations. However, scarce and/or ambiguous palaeomagnetic data lead to controversial and highly discussed interpretations of the field behaviour in time periods like the Ediacaran (e.g., Robert et al., 2017) or the Devonian (Torsvik et al., 2012).

A recent rise in interest for the Ediacaran period (635-538 Ma, Xiao and Narbonne, 2020) has led to an improvement in data coverage for this time period but the reliability and ambiguity of data remain troubling. Directional data often result in apparent

polar wander paths (APWP) with rapid oscillations between two widely-separated sets of poles (Abrajevitch & Van der Voo, 2010), making palaeogeographic reconstructions difficult. In addition, palaeointensity studies from Laurentia (Bono et al., 2019; Thallner et al., 2021a) and Baltica (Shcherbakova et al., 2020) suggest a weak sustained field, fundamentally different from younger fields (Kulakov et al., 2019), with minimum palaeointensity values similar to those in short term intensity drops during polarity transitions. Interpretation of the Ediacaran field as non-dipole-dominated and transitional seems reasonable and is supported by high dispersion of virtual geomagnetic poles (VGPs) (Bono et al., 2019; Halls et al., 2015; Thallner et al., 2021a; Veikkolainen & Pesonen, 2014), high reversal frequencies (Bazhenov et al., 2016) as well as the low intensities. However, grouping of VGPs in two distinct clusters could also suggest a field that was at times dominated by the contribution of an equatorial dipole (Abrajevitch & Van der Voo, 2010).

Palaeomagnetic directional data become less controversial at the Ediacaran - Cambrian transition after 550 Ma (e.g., McCausland et al., 2011; Meert, 2014). This could imply a more stable and dipole dominated field, but high reversal frequencies of $\geq$ 20 reversals/Myr have been reported for the Early and Middle Cambrian (Gallet et al., 2019; Levashova et al., 2021). The hyperactive episodes in the Ediacaran and the Cambrian seem similar, so palaeointensity data becomes vital for the understanding of the field in this time. However, a large data gap exists for palaeointensities with no records between the late Ediacaran around 561 Ma (Shcherbakova et al., 2020) and the mid Cambrian at 522 Ma (McClelland & Briden, 1996). The youngest reliable palaeomagnetic result for the Ediacaran comes from the Skinner Cove Formation (McCausland & Hodych, 1998) in western Newfoundland, Canada. The Skinner Cove Formation formed in a shallow marine seamount setting near Laurentia and was obducted onto the Laurentian rifted margin in the Ordovician as a structurally lower slice in a thrust stack including Ordovician ophiolitic rocks (Hodych et al., 2004; McCausland & Hodych, 1998). Directional analysis revealed a shallow 'A' direction of D = 144.4°, I = 31.5°, α_{95} = 10.8°, k = 21.1, for ten sites upon tilt-correction, implying that Laurentia was at low latitudes (19°S ± 9°) at the Ediacaran - Cambrian transition (McCausland & Hodych, 1998). VGP dispersion of Skinner Cove with ∼13.5° (Veikkolainen & Pesonen, 2014) is low compared to other Ediacaran poles (e.g., ∼26°, Sept Îles, Bono et al., 2019; ∼19° Grenville Dykes, Thallner et al., 2021a). This study aims to provide the first palaeointensity estimates for the end of the Ediacaran to decrease the size of the data gap between the late Ediacaran and the mid Cambrian.

3.2 Samples and Methods

The specimens used in this study were drilled vertically from oriented block samples of the Skinner Cove Formation in McCausland and Hodych (1998) and were pre-selected for this study according to their demagnetisation behaviour and the evidence for primary magnetisation given in McCausland and Hodych (1998). In this study, we used specimens from 10 palaeomagnetic sampling sites (Figure 3.1), including the Red Fire Brook Member trachyte flow (SC06), the Main Sea Stack Member ankaramite (SC01), trachybasalt (SC03, SC15) and alkali basalt flows (SC05, SC09), mafic dykes (SC11, SC13) and trachyte dykes (SC14) as well as from an intraformational conglomerate (SCTS) that passed a conglomerate test (McCausland & Hodych, 1998). From the trachybasalt and amygdaloidal alkali basalt clasts in the conglomerate, only trachybasalt clasts were used for palaeointensity experiments since demagnetisation behaviour and scanning electron microscope backscatter images suggest that the amygdaloidal alkali basalt clasts carry a thermo-chemical overprint (McCausland & Hodych, 1998). U-Pb (TIMS) dating of zircons from the site 2 ankaramite flow of McCausland and Hodych (1998) provided an age of 550.5^{+3}_{-2} Ma (Cawood et al., 2001). The same ankaramite flow of the Main Sea Stack Member has also been dated to an age of 550 ± 5 Ma by measuring U-Th-Pb isotopes (Hodych et al., 2004), agreeing well with the age of Cawood et al. (2001). An overlying trachyte flow at site SC06 of the Red Fire Brook Member gave an age of 556 ± 5 Ma, agreeing within error with the ankaramite site 2 flow age (Hodych et al., 2004).

Rock magnetic measurements and palaeointensity experiments were carried out at University of Liverpool's geomagnetism laboratory. A variable field translation balance (VFTB) was used for measurements of induced remanent magnetisation (IRM), hysteresis parameters and thermomagnetic curves up to 700°C in an applied field of 240 µT. Temperature dependence of susceptibility was measured on an AGICO MFK-1A (CS4) Kappabridge in air between 40°C and 700°C. Incremental heating and cooling cycles were performed in 100°C increments between 150 and 650°C. A Hitachi TM300 tabletop microscope was used for taking scanning electron microscope images of one specimen from five sites. An additional magnetic field map was measured for one specimen using a quantum diamond microscope (QDM) at the Harvard Palaeomagnetics Lab (Fu et al., 2020; Glenn et al., 2017) with resolution of ∼4.7 µm after the specimen was given an anhysteretic remanent magnetisation (ARM) in a bias field of 50 µT.

Microwave-Thellier experiments were performed on 107 specimens using the high frequency (14 GHz) Tristan microwave system and SQUID magnetometer (Suttie et al., 2010) following either the IZZI (Tauxe & Staudigel, 2004; Yu et al., 2004) or Coe

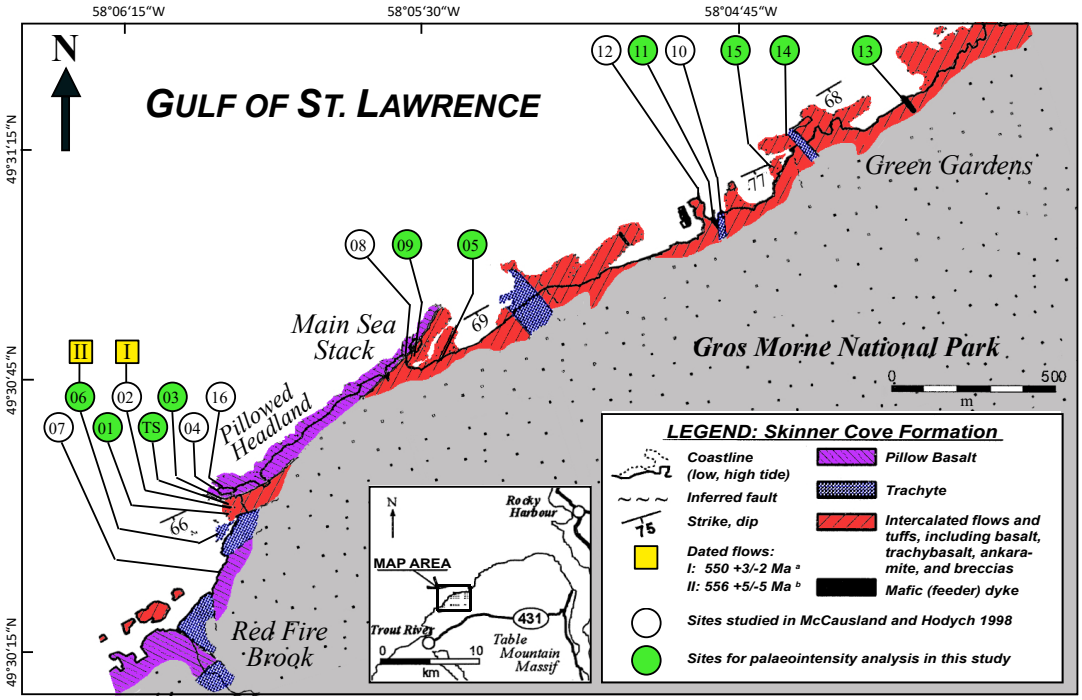

FIGURE 3.1: Map of site locations of the Skinner Cove Formation with south-easterly dipping volcaniclastic rocks and lava flows in western Newfoundland. Shown are sites used for directional analysis (McCausland & Hodych, 1998) and palaeointensity analysis (this study). Modified from Figure 2 in McCausland and Hodych (1998), a) Cawood et al. (2001), b) Hodych et al. (2004).

protocol (Coe, 1967). All experiments included 4 - 5 pTRM checks. Additionally, 3 - 4 pTRM-tail checks (Riisager & Riisager, 2001) were performed during Coe protocol experiments. Laboratory fields between 3 and 30 µT were applied in angles of 45° - 90° to the ChRM of the sample to detect multidomain effects (Yu & Tauxe, 2005) and field dependencies.

Thermal Thellier experiments were performed on 14 specimens in IZZI protocol with pTRM checks using an MMTD80 oven and measured on an AGICO JR6 spinner magnetometer. Possible chemical alterations during the heating steps were monitored by measuring the susceptibility after each heating step with a Bartington MS2 susceptibility meter. Heatings were made in increments of 20 - 50°C between 100 and 550°C with a laboratory field of 10 µT. Before each measurement, specimens were 'cleaned' with a 2 mT AF demagnetisation step using an AGICO LDA5 demagnetiser to remove soft remanences picked up during laboratory handling and improve linearity of Arai plots (Dunlop et al., 2005).

Method	Selection criteria									
MW&TH Thellier	N	f	β	Q	MAD	α	DRAT	CDRAT	$DRAT_{Tail}$	$\lvert k' \rvert$
	4	0.35	0.1	1	10	10	10	10	10[a]	0.48
[b]	4	0.25	0.1	1	10	10	15	15	10[a]	0.48
	N	f	β	r^2	MAD	α	$\lvert k' \rvert$	f_{resid}	$\lvert b_{AA} \rvert$	
pThel	6	0.45	0.1	0.995	15	15	0.2	0.15	0.85 - 1.15	
	N	f	r^2_N	r^2_T	MAD	α	$slope_T$			
Shaw	5	0.35	0.995	0.995	15	15	0.95 - 1.05			
[b]	5	0.25	0.99	0.99	10	10	0.9 - 1.1[b]			

TABLE 3.1: Standard palaeointensity definition (SPD, Paterson et al., 2014) selection criteria used for palaeointensity experiments. Thermal (TH) and microwave (MW) Thellier experiments used the modified SELCRIT2 criteria (Biggin et al., 2007a; Paterson et al., 2015). Pseudo-Thellier experiments (pThel) used the selection criteria of Paterson et al. (2016). Selection criteria for Shaw experiments were modified from Yamamoto et al. (2010); [a] only used for Coe protocol experiments, [b] relaxed values of selection criteria.

Alternating field (AF) demagnetisations and ARM acquisitions for 33 double heating technique (DHT) Shaw (Tsunakawa & Shaw, 1994) and seven pseudo-Thellier experiments (Paterson et al., 2016; Tauxe et al., 1995) were performed on an automatic 2G RAPID superconducting rock magnetometer using AF fields up to 100 mT. For Shaw experiments, ARMs were given at peak AF field of 100 mT using bias fields of 40 µT or 11.4 µT. Full thermoremanent magnetisations (TRMs) were given twice in temperatures of 620°C and bias fields of 10 µT or 20 µT. Equivalence of the TRM given in the first heating and the ARM corrected TRM given in the second heating was used to confirm that the ARM correction was not affected by thermochemical alteration in the heating steps. In addition to the standard pseudo-Thellier protocol of demagnetisation of natural remanent magnetisation (NRM), followed by a progressive ARM acquisition and an AF demagnetisation of that ARM, eleven pseudo-Thellier experiments were also performed during Shaw experiments, where the progressive ARM acquisition steps were performed instead of the single ARM acquisition step at peak AF after demagnetisation of the NRM. ARM acquisitions for the pseudo-Thellier experiments used bias fields of 11.4 µT, 20 µT or 40 µT. Absolute palaeointensity values from pseudo Thellier results were calculated using the generalised calibration B_{anc} [µT] = B_{ARM} [µT] × $|slope_{PA}|$ / c, where the calibration factor c is defined as 3.280 ± 0.828 (Paterson et al., 2016). These absolute values were given supportive meaning because (a) the number of attempted experiments was very low, (b) the error of absolute palaeointensity from pseudo Thellier experiments associated with the calibration factor is as high as 25%, and (c) different calibration formulas that exist for the calculation of absolute palaeointensities are conflicting for weak fields (de Groot et al.,

2013; de Groot et al., 2015; Paterson et al., 2016). The combined pseudo-Thellier-Shaw experiments produced two non-independent intensity estimates, but only the more robust Shaw intensities were used for calculation of the site means.

Results of palaeointensity experiments were analysed using the selection criteria in Table 3.1. Results passing all criteria were accepted as 'class A' results. Results failing a strict criterion could still be accepted as 'class B' result if they passed a relaxed value (Table 3.1) of the failed criterion. Thermal, microwave, and pseudo Thellier experiments were analysed using palaeointensity.org (Béguin et al., 2020).

3.3 Results

Combined analysis of rock magnetic experiments, SEM backscatter images and a magnetic field map revealed a complex and heterogenous magnetic mineralogy in the studied rocks that can roughly be divided into three types (Figure 3.2, Figure B.1).

Samples with type 1 (Figure 3.2a), seen in sites SC01, SC03, SC05, SC09, SC11 and the trachybasalt clasts in the conglomerate of SCTS, show two Curie temperatures around 520°C and 580°C. Cyclic measurements of temperature dependent susceptibility show that in these samples metastable titanomagnetite is oxy-exsolved to magnetite during heating, leading to irreversible behaviour in thermomagnetic curves and susceptibility versus temperature curves. In type 1 rocks, minor alterations start at low temperatures around 200°C but heating and cooling curves are mostly reversible up to high temperatures > 550° where larger alterations start to occur and magnetite is possibly further oxidised to hematite/maghemite. Rocks of type 1a (Figure 3.2b) from sites SC06, SC14 and SC15 are very similar to rocks of type 1, but susceptibilities and magnetisations are one to two orders of magnitude weaker with a high fraction of a high blocking temperature component with Curie temperature around 660°C giving reversible susceptibility/thermomagnetic curves at high temperatures > 500°C. Similar to type 1 rocks, the fraction of titanomagnetite oxy-exsolves to magnetite and possibly oxidises further to stable hematite/maghemite at high temperatures as well.

Type 2 rocks show single Curie temperatures between 560°C and 600°C (Figure 3.2c), but higher grades of alteration can be seen at low temperatures up to 350°C. SEM backscatter images (Figure 3.3a and b, Figure B.2) performed on rocks of all types show large (< ∼120 µm), sometimes pristine, titanomagnetite grains. In sites SC05 and SC09 these grains show cracks that are likely associated with a volume reduction during maghemitisation (Dunlop et al., 1998). These cracks cannot be seen in the large Ti-Fe-oxide grains of site SC01 and SC11 (Figure 3.3b). However, magnetic field mapping of a specimen of site SC11 (Figure 3.3c) shows that the large Ti-Fe-oxide grains

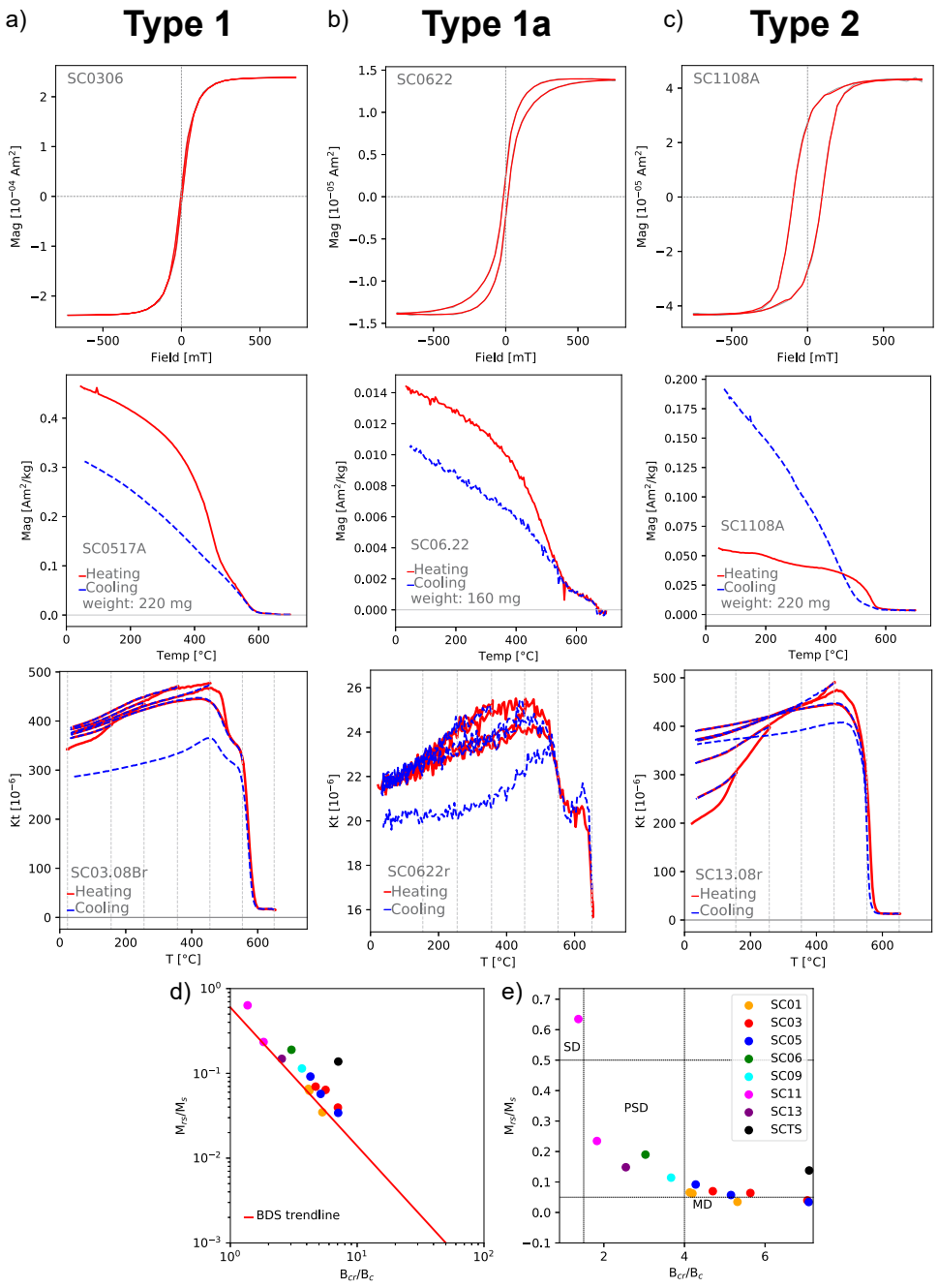

FIGURE 3.2: Rock magnetic results: a-c) show hysteresis loops processed with Hystlab (Paterson et al., 2018), thermomagnetic curves and cyclic curves of temperature dependent susceptibility for different magnetic mineralogy types; d,e) diagrams showing the ratio of saturation remanence and saturation magnetisation versus ratio of coercivity of remanence and coercivity d) with bulk domain stability (BDS) trendline (Paterson et al., 2017) and e) in a Day et al. (1977) plot.

are not the remanence carriers. Instead, remanence seems to be carried by grains that are too small to be observable on the SEM.

Rocks in sites SC11 and SC13 (both mafic dykes) are highly heterogenous and magnetic mineralogy of type 1 and type 2 can be found in sister specimens of the same core. Hysteresis parameters plotted together with the trendline of bulk domain stability (Paterson et al., 2018) and in the Day plot (Figure 3.2d, e) suggest a mixture of magnetic domain types for all sites.

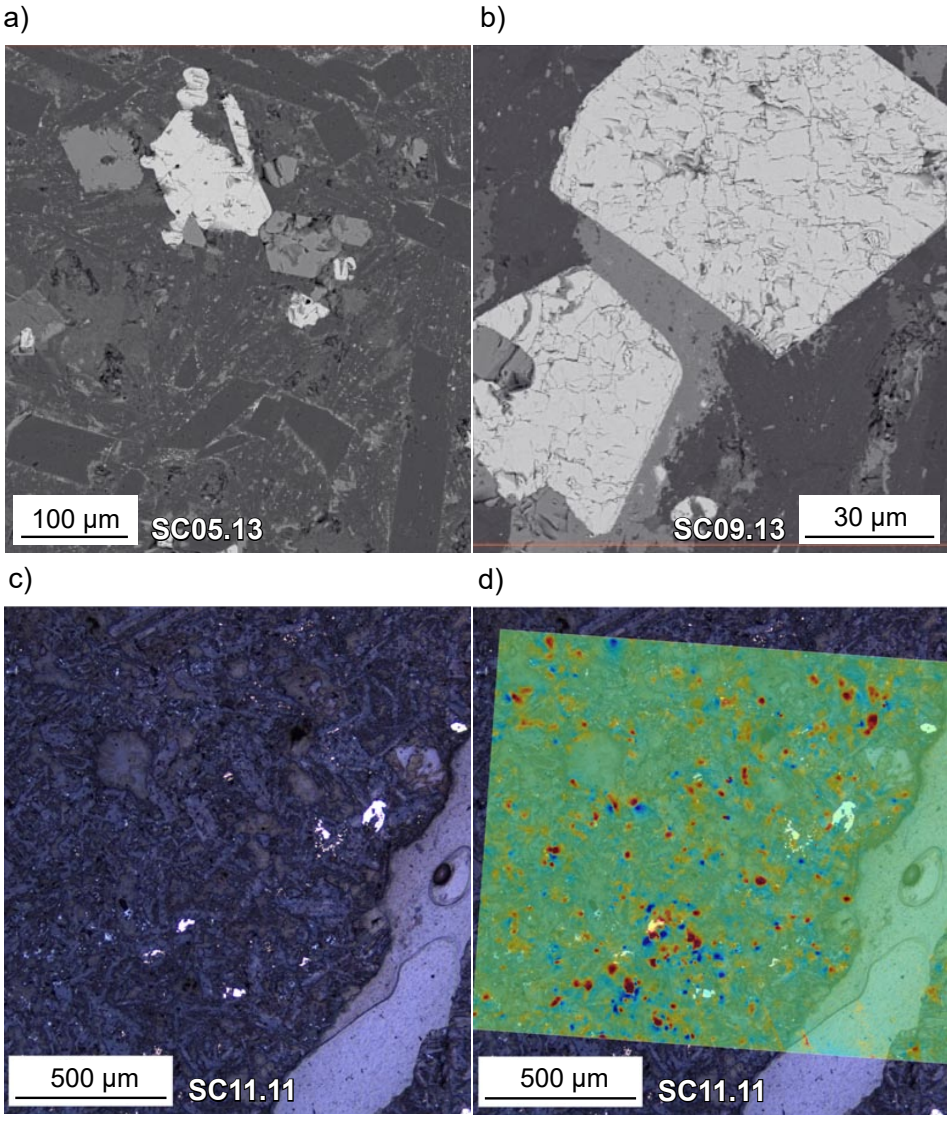

FIGURE 3.3: Scanning electron microscopy images of specimens from sites SC05 (a) and SC09 (b) showing cracked (Ti-)magnetite grains; c) QDM image for a specimen of site SC11 (binned by a factor of 4), showing a magnetic field map on top of an SEM image.

The success rates of palaeointensity experiments were greatly influenced by the associated magnetic mineralogy types of the specimens studied. The overall success rate for sites with specimens of type 1 mineralogy was 33% which is about twice as high as the success rates for sites with type 1a (14%) and sites with types 1+2 (17%). This was visible for thermal and microwave Thellier experiments where the majority of accepted results came from sites with magnetic mineralogy of type 1 as well as for Shaw experiments with 80% passes from sites with type 1 specimens, 25% passes from type 1a and no passes from type 2 specimens. Overall, Shaw experiments gave the highest success rate (61%). For Thellier-type experiments, microwave and thermal experiments performed equally well (21% and 20% success rates for microwave and thermal experiments, respectively). However, due to the small required specimen size for microwave Thellier experiments and the limited amount of available sample material, the less time-consuming microwave experiments were preferred (N_{MW} = 107, N_{TH} = 14, N_S = 33). Site mean averages of passing intensity results are summarised in Table 3.2. For the site mean values, unweighted specimen level results from thermal Thellier, microwave Thellier and Shaw experiments were averaged. Palaeointensities from pseudo-Thellier experiments are given for comparison, but were not used for calculation of the mean results. The obtained palaeointensities range from 2.6 to 10.3 µT (0.65 - 2.25 $\times 10^{22} Am^2$).

Microwave and thermal Thellier results of each specimen with their critical values of SPD (Biggin & Paterson, 2014) are listed in Supplementary Tables B.1 and B.2. Of the 21 and 3 accepted palaeointensity results from microwave and thermal Thellier experiments, all but one were accepted as class A result, passing all strict selection criteria. For the one class B result, DRAT and CDRAT had to be relaxed. As is often the case when measuring weak palaeointensities, specimens showed two slope behaviour in Thellier experiments (e.g., Bono et al., 2019; Hawkins et al., 2019; Shcherbakova et al., 2020; Thallner et al., 2021a), as shown in Figure 3.4. A single oxidation event as cause for the L-shaped Arai plots (Shcherbakov et al., 2020) is unlikely as the change in slope generally coincided with a change in direction (Figure 3.4a and b) after overprints were removed around integrals of ∼100 W·s or temperatures of ∼400°C. This change in direction was not always clearly visible (e.g., Figure 3.4d) and in 15 experiments, the slopes in the temperature range between 20°C and 320°C or the power integral range between 0 and 99 W·s pass selection criteria and result in palaeointensities between 22 µT and 156 µT.

Site	Directions*					Intensities [μT]						VDM [10^{22}Am^2]		pThel [μT]		Q_{PI}
	N/n_{dir}	Dec	Inc	α_{95}	k	N/n_{PI}	N/n_{TH}	N/n_{MW}	N/n_S	PI	σ_{PI}	VDM	σ_{VDM}	N/n_{pT}	PI	
SC01	5	146.5	19.5	12.0	41.9	19/6	2/0	13/3	4/3	7.2	3.6	1.78	0.89	1/0	-	7
SC03	6	142.7	56.0	9.2	54.4	30/5	3/0	21/0	6/5	6.1	1.9	1.10	0.34	3/2	6.2	6
SC05	6	138.3	59.8	13.9	24.1	26/10	2/1	20/6	4/3	6.0	1.7	1.03	0.29	2/1	4.2	7
SC09	6	133.6	38.3	38.3	10.7	10/2	0/0	9/2	1/0	10.3	1.8	2.25	0.39	1/0	-	6
SC11	4	156.7	28.8	17.5	28.6	14/3	3/0	10/2	1/1	2.9	1.0	0.68	0.24	2/1	0.9	7
SC13	5	128.9	16.9	14.5	28.7	4/0	0/0	4/0	0/0	-	-	-	-	0/0	-	-
SC14	9	151.1	17.2	11.1	22.4	7/2	1/0	2/0	4/2	2.6	0.01	0.65	0.00	2/0	-	6
SC15	5	145.8	23.2	8.5	81.9	7/1	0/0	3/0	4/1	7.0	-	1.70	-	2/0	-	6
SC06	6	155.9	19.7	14.0	23.7	7/0	0/0	3/0	4/0	-	-	-	-	2/1	4.4	-
SCTS	-	-	-	-	-	30/15	3/2	22/8	5/5	9.0	4.8	2.03*	1.08*	2/0	-	7

TABLE 3.2: Palaeointensity results: Site identifiers, ChRM Directions*: tilt-corrected site mean characteristic directional data from McCausland and Hodych (1998), palaeointensity data: N/N_{int}: total/accepted number of specimens for each method (MW: microwave Thellier, TH: thermal Thellier, S: Shaw experiments), PI: site mean palaeointensity estimate [μT], σ_{PI}: standard deviation of palaeointensity estimate [μT], VDM: virtual dipole moments [10^{22}Am^2] (*: VADM), σ_{VDM}: standard deviation of VDMs [10^{22}Am^2], pThel: palaeointensity estimates from pseudo-Thellier experiments (not used for calculation of mean intensities), Q_{PI}: Q_{PI} (Biggin & Paterson, 2014) scores for intensity results (see Table 3.3 and discussion for details).

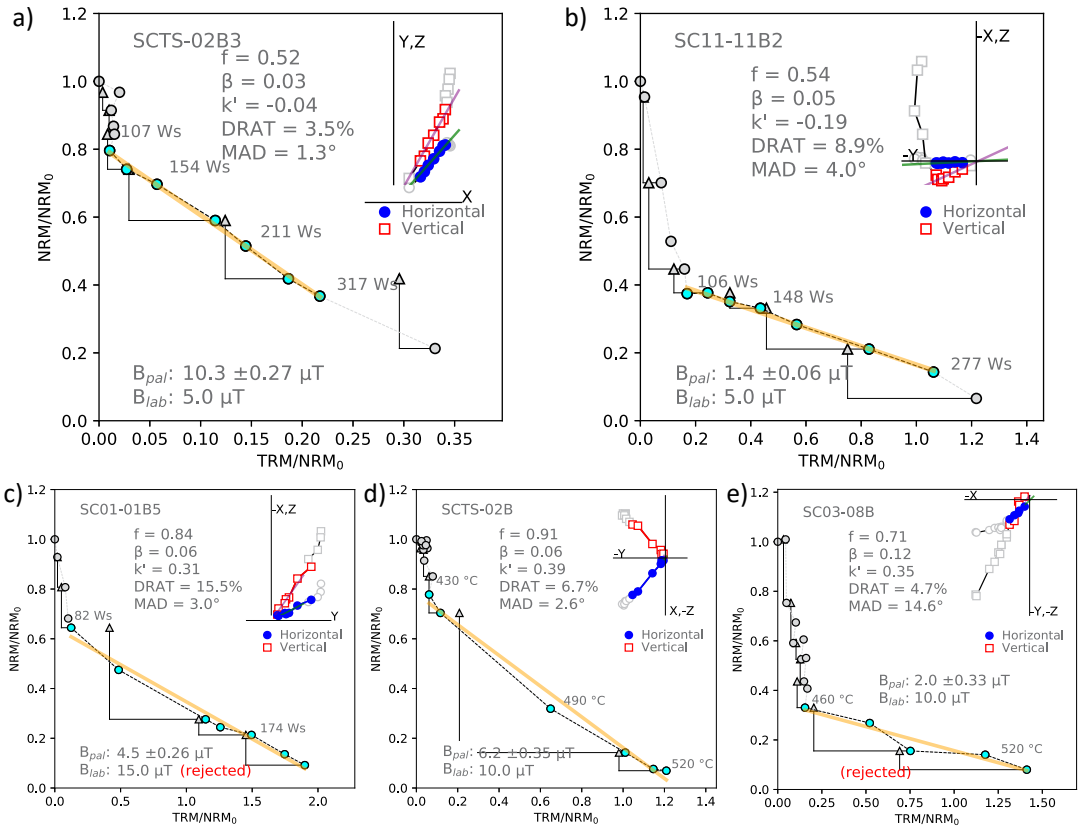

FIGURE 3.4: Representative Arai plots and associated orthogonal plots of microwave and thermal Thellier experiments. Temperatures [°C] and power integrals [W·s] of every other step are shown for the part of the slope that was used for the determination (cyan) of the best-fit line (solid yellow).

These slope fits are in the blocking temperature range of the overprints (McCausland & Hodych, 1998) and do not represent the ancient field at 550 Ma. The main reasons for failure of Thellier experiments were thermochemical alterations during the experiments and MD effects. Of all failing Thellier results, 74% failed due to alteration as seen by high DRAT and/or CDRAT values. Here, the main alteration appeared to happen between 100 - 140W·s or 460 - 520°C (e.g., Figure 3.4c). Larger increases of susceptibility (> 10%) at these temperatures are only seen for specimens of site SC11 with magnetic mineralogy of type 2, that were rejected with high low q and high DRAT values. MD effects (Figure 3.4e), leading to zig-zagging and high β and/or k' values accounted for 49% and 36% of fails, respectively. However, 4 out of 5 experiments using the Coe-protocol showed tail checks with acceptably low values below 10%. For the thermal Thellier experiments, all rejected results showed high β and/or k' values and only 45% failed because of high DRAT/CDRAT values. This was not the case for microwave experiments where only 45% of the rejected results showed high β

and/or k' values but 79% failed with unacceptable pTRM checks (see Supplementary Tables B.1 and B.2).

Shaw experiments (Figure 3.5a) resulted in a high success rate of 61%. Of the 20 accepted results, 10 passed as class A and 10 as class B result. The mean palaeointensity value from all accepted class A results (6.6 ± 3.7 µT) was slightly higher than the mean intensity from the class B results (3.9 ± 2.5 µT), but they agreed reasonably well. For 8 of the 10 class B results, r^2 of the best fit line on the NRM-TRM1* plot had to be relaxed to $r^2 \leq 0.990$, while $slope_T$ and f had to be relaxed for 6 and 3 results, respectively. Most of the rejected results came from type 1a sites SC06, SC14 and SC15, where the high coercivity fraction and the overall weak magnetisation led to low values of r^2 and high values of α. Rejected results from other sites failed due to high values of $slope_T$ of low values of r^2 of the TRM1-TRM2* plot. Eleven of the 18 pseudo-Thellier experiments were performed during the Shaw experiments. Doing so allowed us to recover intensity estimates in case of high thermal alteration or breaking specimens during the TRM steps. While we chose not to use pseudo-Thellier results for the calculation of the mean palaeointensities because of the reasons outlined in the method section, they can be useful for comparison to the results of the heating methods, especially since a large number of results was rejected because of suspected thermal alterations during the experiment.

Pseudo-Arai plots (Figure 3.5b) look similar to thermal and microwave Thellier methods, often showing the same two-slope behaviour, suggesting that the L-shape in the Arai plots of the heating methods is not related to a single oxidation event during laboratory heating (Shcherbakov et al., 2020). Curvatures of the selected best-fit line segment were generally low. Rejected pseudo-Thellier results all failed due to low r^2 of the best fit line in the pseudo-Arai plot. The shape of the demag-demag plots of NRM_{left} versus ARM_{left} (bottom left in Figure 3.5b) generally resembled the shape of the pseudo-Arai plots. When the whole coercivity range is considered in the ARM_{gained} versus ARM_{left} plots (bottom right in Figure 3.5b), some parts can show slight differences of the slopes and higher values of k'. However, the selected coercivity ranges show very low curvatures and the ARM-ARM slopes are well within 15% of -1, indicating reciprocity of ARM in the selected segments (Paterson et al., 2016). The pseudo-Thellier results agreed well with the mean intensity values from the other methods (Table 3.2). Pseudo-Thellier results for sites SC03 and SC05 are from specimens that provided accepted intensities from the Shaw experiment that were then used in the calculation of the site mean. This shows that the accepted results from the heating methods for these sites are not biased by undetected thermal alterations. Specimen results and critical values for Shaw and pseudo-Thellier experiments are

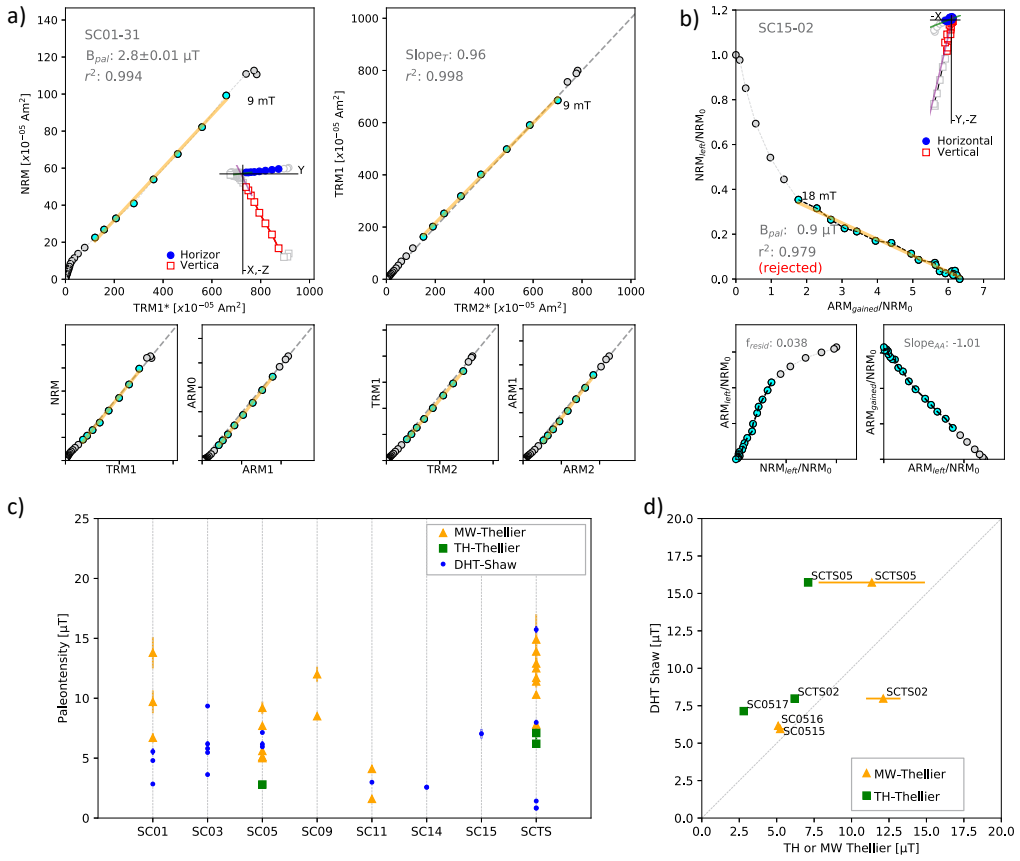

FIGURE 3.5: a) Shaw result showing diagrams of remaining NRM versus remaining ARM corrected TRM of the first heating (TRM1*) that are used for palaeointensity determination (top left) and diagrams of remaining TRM of the first heating versus remaining ARM corrected TRM of the second heating (TRM2*) that are used to assess the validity of ARM correction (top right). Bottom diagrams show remaining magnetisations of NRM, uncorrected TRMs and ARMs of the first heating (left) and the second heating (right); b) pseudo-Thellier diagrams show pseudo-Arai plots of remaining NRM versus gained ARM (top), plots of remaining ARM versus remaining NRM (bottom left) and ARM left versus ARM gained (bottom right); c) Palaeointensity results by method (yellow triangles: microwave Thellier, green squares: thermal Thellier, blue dots: double-heating Shaw) plotted for each site with accepted results, error bars show standard errors of intensity determinations; d) comparison of palaeointensities gained from sister specimens of the same core. Intensities from the DHT-Shaw method are plotted against results from thermal Thellier experiments (green squares) and microwave Thellier experiments (yellow triangles). Error bars show one standard deviation of intensities of sister specimens.

listed in Supplementary Tables B.3 and B.4, respectively. In addition, raw measurement data of all palaeointensity experiments are available on the MagIC database (www2.earthref.org/MagIC).

3.4 Discussion

We report 7 new site mean palaeointensity values in the range of 2.6 - 10.3 µT (0.65 - 2.25 $\times 10^{22}$Am^2) from cooling units N > 1 palaeointensity estimates. The reliability of the palaeointensity estimates was assessed using the Q_{PI} criteria (Biggin & Paterson, 2014), listed in Table 3.3. All sites pass the AGE criterion due to radiometric dating of two flows (Cawood et al., 2001; Hodych et al., 2004) and sensible demagnetisation behaviour. The STAT criterion requires N $\geq$ 5 and SD/mean $\leq$ 25% which is generally hard to achieve for very low intensity estimates and none of our sites pass this requirement even though the standard deviations of four sites with more than the required minimum of 5 intensity estimates are generally small (< 5 µT).

SEM backscatter images showed large Ti-Fe-oxide grains covered in cracks suggesting maghemitisation (Dunlop et al., 1998). However, a QDM magnetic map showed that these grains do not carry any magnetisation, even after being given a 50 µT ARM. A definitive reason as to why these large grains are not magnetic could not be found. Although our compositional analysis did not identify the chemical composition or crystallography of the large Fe-Ti-oxide grains and it cannot be ruled out that these grains are outside of ferromagnetic compositional range, a likely explanation could lie in the large size of the grains, as large grains may form closure domains to minimise demagnetisation energy, minimise stray fields and with that reduce their net magnetisation (Dunlop & Özdemir, 1997). While maghemitisation cannot be fully ruled out, no maghemite was seen in thermomagnetic or temperature dependent susceptibility curves, suggesting that the magnetic minerals that carry the magnetisation have not been affected by secondary processes. No baked contact tests were possible as contacts with basement rocks are not observed for the Skinner Cove formation (McCausland, 1998). The sites in the exposed section showed only minor variations in their bedding orientation, which expectedly led to an inconclusive fold test result, as the clustering of characteristic directions did not change significantly after tilt correction (McCausland & Hodych, 1998). However, strong support for a primary TRM is given by the positive intraformational conglomerate test in McCausland and Hodych (1998) at site SCTS. The conglomerate test was performed on blocky trachybasalt cobbles that in the field appear to have been drawn from the directly underlying blocky trachybasalt flow SC03 as well as on amygdaloidal alkali basalt clasts in McCausland and Hodych (1998). The amygdaloidal alkali basalt clasts showed a soft viscous remanence component and hard component directions that were scattered, but not random. They were characterised to carry thermochemical overprints and were therefore not used in this study. In contrast, the hard component directions measured in AF demagnetisations of 20 trachybasalt clasts were random at the 95% confidence level, and within-clast

Site	AGE	STAT	TRM	ALT	MD	ACN	TECH	LITH	MAG	Q_{PI}
SC01	1	0	1	1	1	1	1	0	1	7
SC03	1	0	1	1	1	1	0	0	1	6
SC05	1	0	1	1	1	1	1	0	1	7
SC09	1	0	1	1	1	1	0	0	1	6
SC11	1	0	1	1	1	1	1	0	1	7
SC14	1	0	1	1	1	1	0	0	1	6
SC15	1	0	1	1	1	1	0	0	1	6
SCTS	1	0	1	1	1	1	1	0	1	7

TABLE 3.3: Q_{PI} criteria (Biggin & Paterson, 2014) for all sites with accepted palaeointensity results. See section 3.4 of the text for details.

consistency was shown with additional thermal demagnetisations of a sister specimen in the same clast. These trachybasalt cobbles in SCTS and the SC03 trachybasalt flow showed similar petrology and demagnetisation behaviour, suggesting the 'A' remanence direction to be a primary thermal remanence (McCausland & Hodych, 1998) which is supported by similar palaeointensity behaviour seen in this study. All samples used for intensity determination in this study were taken from sites that carry this stable 'A' remanence. We therefore award TRM to all sites. All accepted intensity estimates pass alteration checks from the double heating of the Shaw method and pTRM checks of the Thellier-type experiments, showing that the results have not been biased by alteration and we award ALT to all sites. From rock magnetic analysis and the high failure rate during intensity analysis, it seems likely that some specimens may contain MD grains. Following Biggin and Paterson (2014) that defined the MD criterion as relating to the bias due to MD effects, and not the presence of MD grains, the criterion is still passed by all sites that have accepted intensity results from Shaw experiments as well as thermal or microwave Thellier experiments where curvature and low zig-zagging in IZZI protocol or pTRM-tail checks in Coe-protocol suggest that the accepted intensity results were not biased by MD behaviour. Rejected results from thermal Thellier experiments showed a lot of zig-zagging with β values up to $\sim$0.6. Low γ values in Thellier experiments (mean γ = 3.3°) showed that there are no large TRM anisotropy effects at any of the sites. Cooling rate effects are not seen between samples from the same sites measured using microwave and thermal methods associated with different cooling times (several seconds vs tens of minutes). Using laboratory bias fields in the range of 5 - 20 µT did not reveal any non-linear TRM effects. ACN was therefore passed by all sites.

TECH was passed by all sites using palaeointensity estimates from at least two different methods (excluding pseudo-Thellier). On average, microwave Thellier results (9.0 ± 3.7 µT, n = 21) were slightly higher than results from thermal Thellier (5.4 ± 1.9 µT,

n = 3) and Shaw experiments (5.3 ± 3.4 μT, n = 20) but agreed reasonably well within sites (Figure 3.5c). Large and growing numbers of palaeointensity studies using the microwave method (Biggin et al., 2007b; Böhnel et al., 2003; Grappone et al., 2019, 2020; Hill et al., 2002; Lloyd et al., 2021a) have demonstrated that this method produces palaeointensity determinations with a similar degree of reliability to the thermal Thellier method. Differences of intensity results between microwave and thermal Thellier experiments that have been reported previously (Biggin, 2010; Laj et al., 2011) have been tied to the usage of the original Thellier (Thellier & Thellier, 1959) and perpendicular (Kono & Ueno, 1977) protocols that failed to detect non-ideal behaviour of magnetic carriers in those studies (Grappone et al., 2020). Using double heating protocols for both thermal and microwave experiments, equivalent palaeointensities have been reported for Ediacaran aged lava flows with non-ideal magnetic mineralogy (Shcherbakova et al., 2020). Equivalence of intensity results between DHT-Shaw and thermal Thellier as well as microwave experiments have been demonstrated in several studies as well (Lloyd et al., 2021a; Yamamoto et al., 2007b; Yamamoto et al., 2010). In this study, a thorough analysis of differences in results from the different methods is hampered by the low number of accepted results but direct comparisons of intensity results of sister specimens are shown in Figure 3.5d. All sites fail LITH as all site means only consist of samples from the same lithologies. Raw measurement data is published on the MagIC database. Therefore, all sites pass the MAG criterion leading to overall Q_{PI} scores of 6 - 7. These are comparable to Q_{PI} scores of other Ediacaran intensities (e.g., 6 - 8 in Shcherbakova et al. (2020)).

Several recent studies have reported uniquely weak field strengths for the Ediacaran period (Bono et al., 2019; Shcherbakova et al., 2020; Thallner et al., 2021a) with most VDMs and palaeomagnetic dipole moments (PDMs) below 1 $\times 10^{22}$ Am^2 between 561 and 598 Ma. With only two entries in the PINT database (Biggin et al., 2015), the data coverage of the Cambrian requires augmenting. Palaeointensity estimates between 3 $\times 10^{22}$ Am^2 and 5 $\times 10^{22}$ Am^2 have been reported for the Cambrian (Didenko & Pechersky, 1989; McClelland & Briden, 1996; Trindade et al., 2012). This suggests that the field in the Cambrian was about 3 times stronger than the field in the Ediacaran. The only available intensity estimates for the Ordovician and Silurian are conflicting and from studies utilising now obsolete methodology (Schwarz & Symons, 1969; Tunyi, 1986), leaving a large data gap until the Devonian, where reliable palaeointensities have been reported (Hawkins et al., 2019) to be almost as weak as in the Ediacaran.

Our new 550 Ma Skinner Cove dipole moment estimates of 0.65 - 2.25 $\times 10^{22}$ Am^2 fall between the Ediacaran and Cambrian field strengths (Figure 3.6) and may suggest a strong increase of the field strength around the Ediacaran-Cambrian transition. This, in turn, may favour inner core nucleation (Bono et al., 2019) or a cyclic increase and

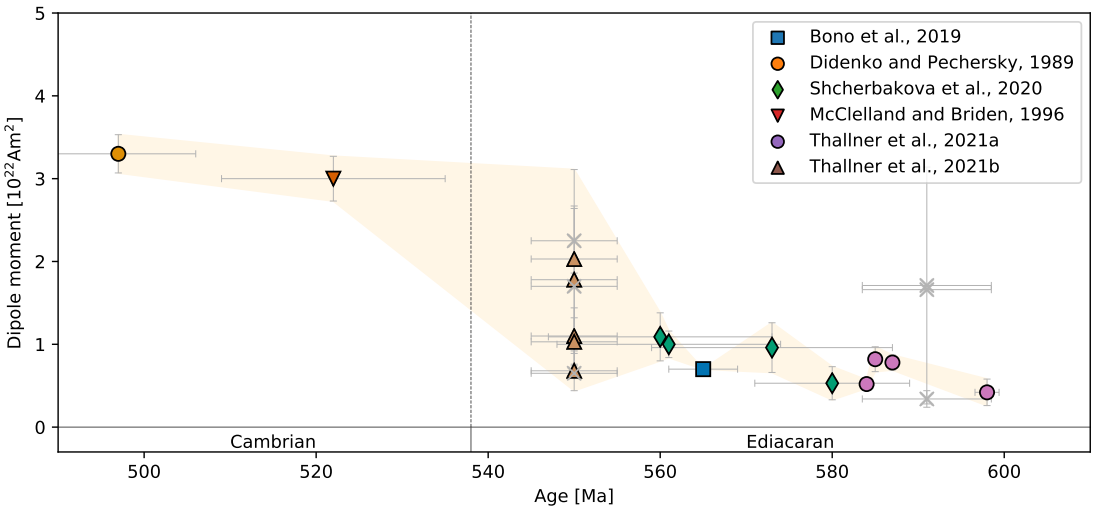

FIGURE 3.6: Ediacaran and Cambrian virtual dipole moments from the PINT database (Biggin et al., 2015) between 480 and 620 Ma together with Ediacaran intensity data from recent studies. The data point from Bono et al. (2019) represents a palaeomagnetic dipole moment instead of a VDM. Grey crosses represent intensities with N $\leq$ 3. Error bars and shaded area show one standard deviation for VDM strength and published uncertainties of age estimates.

decrease of the field strength between the Ediacaran and Devonian, similar to what is observed between the Devonian and Jurassic as well as between Jurassic and present day (Biggin et al., 2012; Kulakov et al., 2019). A likely candidate for producing such ∼200 Myr periodicity would be variations in lowermost mantle conditions linked, ultimately, to nonstationary rates of subduction flux at Earth's surface (Hounslow et al., 2018). This mechanism of geodynamo forcing remains to be explored in detail however. Furthermore, without new and reliable intensity estimates between the Ediacaran and Devonian, the nature of these palaeomagnetic variations will remain uncertain.

The morphology of the Ediacaran field is less clear than its weak nature: Abrajevitch and Van der Voo (2010) and Halls et al. (2015) report and compile published evidence of unusual, possibly non-dipolar directional behaviour but this appears to be at odds with the high dipolarity inferred from the data of Bazhenov et al. (2016) and Levashova et al. (2021).

Angular dispersion of VGPs decreases from values between 19° and 26° (at high and low latitudes respectively) at ∼585 Ma and ∼565 Ma (Bono et al., 2019; Thallner et al., 2021a) to 13.5 ± 1.4° for the Skinner Cove Formation at 550 Ma (Veikkolainen & Pesonen, 2014). However, the VGP dispersion of Skinner Cove has to be taken with some caution. If the Skinner Cove VGP dispersion is analysed with modern criteria

and sites with $n \leq 4$ or $k \leq 30$ are excluded (Cromwell et al., 2018), then insufficient data remain to calculate VGP dispersion.

Unlike other Ediacaran studies that show two directional components (Abrajevitch & Van der Voo, 2010), the Skinner Cove direction appears to be more consistent with a stable GAD field. An 'anomalous' B magnetisation direction is reported from site SC07 of the uppermost Wallace Brook member of the Skinner Cove Formation (McCausland & Hodych, 1998). However, the bedding orientation of site SC07, based on pillow orientations and local tuff, is notably different from the bedding orientations of all other sites. When viewed in geographic coordinates (Supplementary Figure B.3), the SC07 site mean 'anomalous' B direction is approximately antipodal to the site mean directions of the primary A magnetisation. Recalculating the magnetisation direction of site SC07 using the average bedding from all Skinner Cove sites (Supplementary Table B.5) shows that, in tilt-corrected coordinates (Supplementary Figure B.3), the site SC07 magnetisation direction may represent a reversed polarity to that of the Skinner Cove A magnetisation (McCausland, 1998). Given the uncertainty of the appropriate structural correction for site SC07, we cannot resolve its status as an 'anomalous' B magnetisation direction versus a reversal of Skinner Cove A magnetisation, and leave this question to future work.

The observations of decreasing VGP dispersion and increasing field strength both support the field stabilizing at the Ediacaran-Cambrian transition. In contrast, magnetostratigraphic data from the late Ediacaran (Bazhenov et al., 2016) and the Early Cambrian (Levashova et al., 2021) as well as the Middle Cambrian (Gallet et al., 2019) suggest that the hyperactive state of the field in the Ediacaran could extend into the mid-Cambrian in a single or several recurring hyperactivity events. While reversal frequencies in the Early Cambrian are still rather poorly constrained, Gallet et al. (2019) point out a similarity between the late Ediacaran and mid Cambrian hyperactivity episodes that could be connected to a reconfiguration of flow patterns in the outer core at a critical point of the aspect ratio of inner to outer core radii, where geodynamo simulations show a weaker field and higher reversal frequencies at the transition between small and large inner core regimes (Lhuillier et al., 2019). If the Ediacaran weak field state of the geodynamo does end with the rising palaeointensities at the Ediacaran-Cambrian transition, then the hyperactivity episodes (or their triggers) might be fundamentally different. A thorough investigation of this topic will not be possible without a good record of magnetostratigraphy and high quality palaeointensity data for the Cambrian.

3.5 Conclusion

In this multi-method palaeointensity study of the 550 Ma Skinner Cove Formation, we report new palaeointensities (site mean ± 1 σ, N > 1) of 2.6 ± 0.01 μT - 10.3 ± 1.8 μT (0.65 ± 0.01 $\times 10^{22}$ Am^2 - 2.25 ± 0.39 $\times 10^{22}$ Am^2) from 7 sites in flows, dykes and the positive intraformational conglomerate test. These new intensities suggest a rise of field strength at the Ediacaran-Cambrian transition. Reliable high quality palaeointensity data for the whole of the Cambrian, Ordovician and Silurian are urgently required to further investigate palaeomagnetic variations during this time and to explore the possibility of a subsequent strong field period before the Devonian.

Chapter 4

A palaeointensity study of the Volyn Traps, Ukraine

Thesis context

Up to this point, the Ediacaran field strength behaviour was defined exclusively by studies of Laurentian localities. Regional weak-field anomalies, such as the present-day South Atlantic anomaly, can persist over long time scales (Engbers et al., 2020) and it is therefore not impossible, that the weak Ediacaran palaeointensities from Laurentia describe a local feature of the field. To address this possibility, we joined the study of Shcherbakova et al. (2020) as collaborators to measure the first palaeointensities for the continent Baltica. In this study, we conducted thermal Thellier, microwave Thellier and Wilson experiments on volcanic rocks from the Ukrainian Volyn Traps. The resulting palaeointensities agreed well with the field strength determinations from Laurentia and suggested that the weak intensities were indeed a global feature of the Ediacaran field. However, only a small section of the Volyn traps was available for examination in this study.

In this chapter, we add to the results of Shcherbakova et al. (2020) and measure palaeointensities on previously unexplored sections of the Volyn Traps, that we were able to sample in collaboration with the groups of the Geophysical Observatory Borok of the Russian Academy of Sciences and the Institute of Geophysics of the National Academy of Sciences of Ukraine. The sampled succession of numerous basalt flows and tuff layers will enable the determination of palaeointensities as well as a magnetic polarity profile, which could offer additional insight into the relation between directional and intensity behaviour of the Ediacaran field.

This chapter is submitted for publication in Geophysical Journal International as Thallner, D., Shcherbakova,V. V.,Bakhmutov, V. G., Shcherbakov, V. P., Zhidkov, G. V., Poliachenko, I. B., Biggin, A. J.: New palaeodirections and palaeointensity data from

extensive profiles through the Ediacaran section of the Volyn Basalt Province (NW-Ukraine).
In this study, I performed microwave, double-heating Shaw, and thermal IZZI-Thellier experiments. All Wilson experiments and the Coe-Thellier experiments were performed by the co-authors at GO-BOROK. Measurements and analysis of directional data was performed by the co-authors from the National Academy of Sciences of Ukraine. Field work was conducted by myself and the collaborators in Ukraine. The first draft of the publication was written by myself, Andy Biggin, Valia Shcherbakova, Valery Shcherbakov and Vladimir Bakhmutov.

Abstract

Changes of the geomagnetic field over geologic time scales can be used to study the evolution and processes of its sources in Earth's deep interior. As a stark contrast to the geomagnetic field behaviour of the recent past, the field in the late Neoproterozoic is defined by ambiguous polar wander paths, ultra-low field strengths and a period of extreme hyperactivity. Palaeointensity data from this time are still scarce and conclusions made from these data suffer from large uncertainties brought by a low sampling density. In this study, we present new palaeomagnetic and palaeointensity data from quarry outcrops and five deep drill cores, covering the longest and most complete profiles through the Ediacaran units in the Volyn Basalt Province (NW-Ukraine) to date. Palaeodirectional analysis of thermal and alternating field demagnetisation experiments reveal at least six reversals in the profile as well as four palaeopoles that agree with previously published poles. Whole-rock palaeointensity estimates from a multi-method approach, utilising thermal and microwave Thellier experiments in Coe- and IZZI-protocol as well as Wilson and double-heating-Shaw experiments, produce instantaneous palaeointensity estimates of 2.1 - 11.1 μT and virtual dipole moments of 0.31 - 1.67 $\times 10^{22}$ Am^2. Virtual dipole moments for units sampled by drill cores were calculated using absolute inclination data from these samples. Small-scale variations of palaeointensities throughout the profile not only show extremely weak field strengths around polarity changes, but could also suggest that the field strength never fully recovered between reversals. These new results increase the density of intensity data coverage for Baltica in the Late Ediacaran and, in combination with previously published Ediacaran dipole moments, support an extremely weak field that seems to increase in strength towards the Ediacaran-Cambrian transition.

4.1 Introduction

Long-term secular variation of Earth's geomagnetic field, generated in Earth's core and recorded in palaeomagnetic data from ancient rocks, are one of the few ways of observing the history of Earth's deep interior (Sprain et al., 2018). While palaeosecular variation has been a natural part of the geomagnetic field since the earliest claimed appearance of an active geodynamo around 4.2 Ga (Tarduno et al., 2015), much attention has recently been given to time periods where the geomagnetic field differed remarkably from what is expected from a field following the geocentric axial dipole hypothesis. In particular, incompatible and complex palaeomagnetic directions point to non-uniformitarian fields in the mid-Palaeozoic Devonian (van der Boon et al., n.d.) and the Neoproterozoic Ediacaran (Abrajevitch & Van der Voo, 2010; Halls et al., 2015; Kirschvink et al., 1997; McCausland et al., 2007). For both of these periods, extreme reversal frequencies of up to 20 reversals/myr have been suspected as well (Bazhenov et al., 2016; Hansma et al., 2015; Levashova et al., 2021). To fully describe the geomagnetic field, information about the strength of the field is essential. Recent whole-rock palaeointensity estimates from Devonian aged Siberian rocks (∼360 - 375 Ma; Hawkins et al., 2019; Shcherbakova et al., 2017) and the first time averaged palaeointensities from single-crystal measurements from Ediacaran rocks of the Sept-Îles complex in Laurentia (∼565 Ma; Bono et al., 2019) show that the geomagnetic field at these times was about one order of magnitude weaker than the present-day field. For the Ediacaran, the time-averaged palaeointensities from the Sept-Îles complex were complemented by similarly low palaeointensities from the Baltican Volyn Traps (560 - 580 Ma; Shcherbakova et al., 2020), suggesting that the Ediacaran weak field was a global phenomenon and not a local anomaly. Due to the unclear drifting histories of Laurentia and Baltica (Meert, 2014), a regional extent of this anomaly cannot be ruled out. Additional palaeointensities from the Grenville dykes (580 - 600 Ma; Thallner et al., 2021a) and the Skinner Cove formation (550 Ma; Thallner et al., 2021b) hint at a greater temporal extent of the Ediacaran weak field. Apart from the Sept-Îles results, all Ediacaran field strength estimates were gathered from whole-rock palaeointensity experiments on rocks from fast cooled units. These estimates come with the disadvantage of being spot readings of the field strength. Given the currently low spatial and temporal sampling density in a hyperactive field, it is theoretically possible that all these intensities sample transitional fields and periods of much stronger (or slightly weaker) fields are completely missed (Thallner et al., 2021a). This study takes aims to improve the sampling density of directional and whole rock intensity measurements of the Volyn traps and samples new rock units to expand the Ediacaran palaeomagnetic and palaeointensity data of Baltica.

4.2 General geology

Ediacaran episodes of intensive basaltic and alkaline magmatism in NW-Baltica occurred between 626 and 550 Ma and were linked to the opening of the Iapetus Ocean (e.g., Tegner et al., 2019). As a result, the Volyn Large Igneous Province (Volyn Basalt Province – VBP), located along the Trans-European Suture Zone (Tornquist Zone) at the Western margin of the East European Craton, were formed as a typical continental flood basalt province (Figure 4.1a). With a length of 800 km and a width of 300 km in the central part, the area occupies over 200,000 km^2 in SW Belarus, N Moldova, NE Romania, E Poland and NW Ukraine (Stratyhrafiya [...], 2013).

A brief description of the general geological situation of the Volyn traps in Ukraine is given in Shcherbakova et al. (2020), where palaeodirections and palaeointensities of the Volyn traps were studied at several sites from three quarries. The present study continues to investigate rocks of the VBP using new samples from quarries as well as several drill cores, as large parts of the Volyn Series have only been sampled in boreholes. A schematic map of the VBP, its geology, locations of sampling sites and boreholes, as well as a summarized stratigraphic scheme of the lower Vendian of the Brest-Volyn structural-facial zone are shown in Figure 4.1a - d.

In the studied stratigraphic section of the Volyn Series, basalts and tuffs were formed during separate stages of Vendian trap magmatism from magma chambers of different depths (Melnychuk, 2010). Following the classification in Stratyhrafiya [...] (2013), the Volyn Series is represented by the suites Brody (bottom), Gorbashy, Zabo-lottya, Babyne, Luchichiv and Ratne (top). Of these, the Zabolottya, Babyne, Luchichiv and Ratne suites were sampled in this study. The Zabolottya suite with a thickness of up to 230 m is mainly composed of up to seven olivine basalt flows and volcanoclastic sediments (tuff layers). The composition of the up to 200 m thick Babyne suite is dominated by tuffs and comprises one or two tholeiitic basalt flows in its centre. The Luchichiv suite comprises up to five zonal sheets of tholeiitic basalts and volcanoclastic rocks with thicknesses between 15 - 117 m. The Ratne suite includes the Zoryani volcanomictic layers (up to 63 m thick) and the Yakushiv layers (up to 135 m thick), and is represented by up to seven zonal layers of volcanoclastic rocks with high Ti content.

The four youngest suites were formed cyclically where eruptions of basaltic lava were preceded by significant emissions of pyroclastic material. The effusive beds of the Zabolottya, Luchichiv and Ratne suites are well correlated in boreholes and can be traced over tens of kilometres. The basaltic rocks of the Volyn Series can be followed to the North of the city of Rivne where they are represented over 125 km as an elongated strip with a size of 12 - 14 km times 22 km (Figure 4.1b). Here the thick basaltic

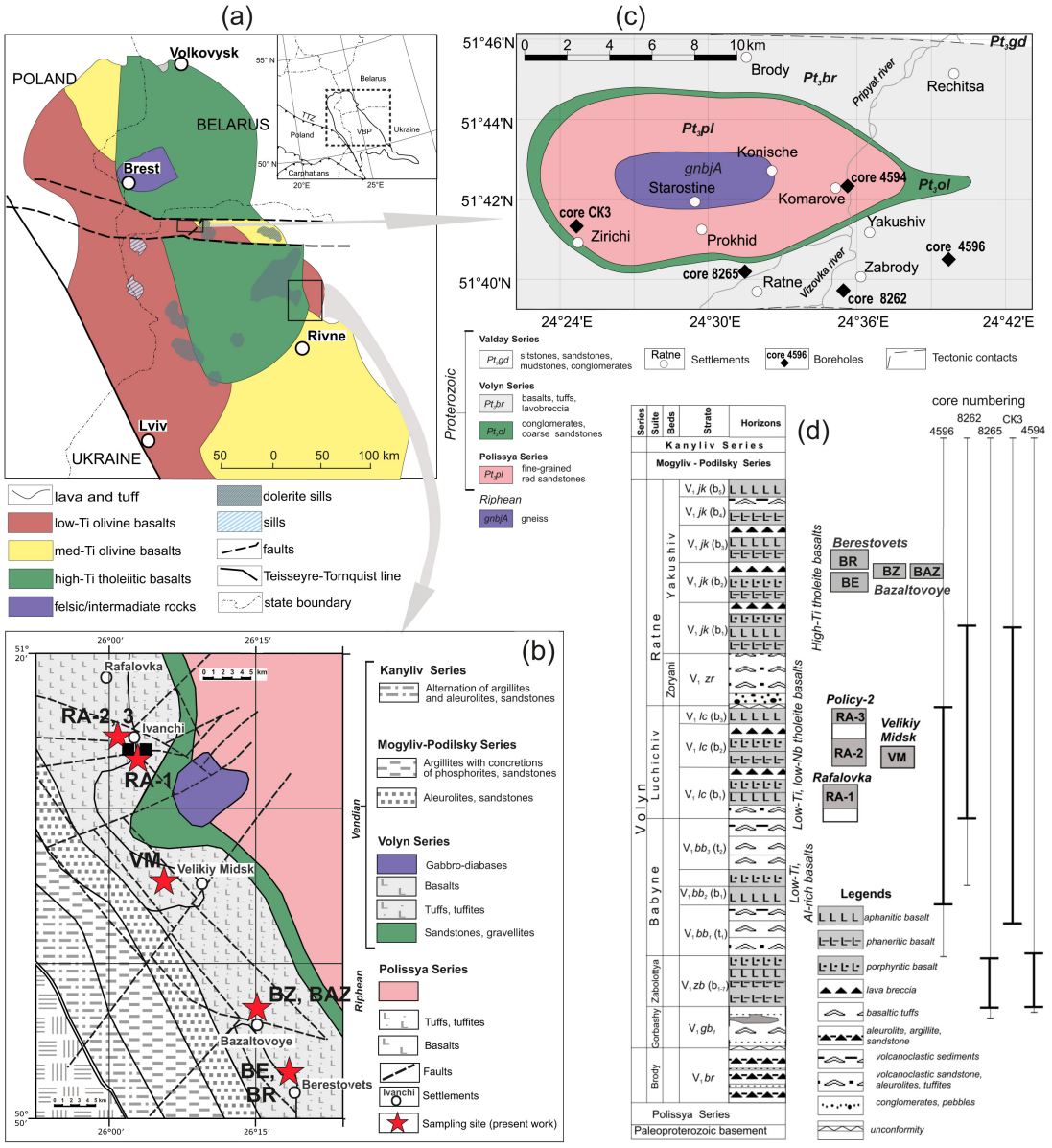

FIGURE 4.1: (a) Schematic map of the Volyn Large Igneous Province (VBP). (1) Lava and Tuff facies; (2,3) olivine basalts of the lower sequence: (2) low-Ti, (3) moderate-Ti content; (4) high-Ti tholeiitic basalts of the upper sequence; (5) felsic and intermediate rocks; (6,7) dolerite sills; (8) faults; (9) Teisseyre-Tornquist line; (10) state boundaries. Adopted from Nosova et al. (2008). (b) Geology and locations of the sampling sites. (c) Geology and locations of boreholes. (d) Summarized stratigraphic scheme of the lower Vendian of the Brest-Volyn structural-facial zone according to Stratyhrafiya [...], (2013); the stratigraphic positions of outcrops and cores are displayed to the right. Thin (thick) lines of boreholes show the whole depth (sampling interval) of each core. The stratigraphic position of the site VM is shown approximated in regards to sites RA-1 and RA-3. The scale on this diagram is arbitrary. Modified from Figure 1 in Shcherbakova et al. (2020).

layers are exposed as outcrops in quarries and have been extensively used for palaeomagnetic studies over the last 20 years (Elming et al., 2007; Glevasskaya et al., 2006; Glevasskaya et al., 2000; Iosifidi et al., 2000; Nawrocki et al., 2004). The results of these studies are summarised in Shcherbakova et al. (2020). Large parts of the Volyn series are known from boreholes (Figure 4.1d), and rocks of the Zabolottya and Babyne suite are only available from core samples. In addition to samples from several quarries close to the villages of Ivanchi, Velikiy Midsk, Berestovets and Bazaltovoe (Figure 4.1b), we used samples from five boreholes located north of the village Ratne (Figure 4.1c) that reveal the most complete stratigraphic succession of the Volyn Series.

4.3 Ages of rocks

Stratigraphically, the Ediacaran age of the Volyn traps is supported by the presence of complexes of acritarchs and filamentous algae in deposits of the Volyn and the Mogyliv-Podilsky series, which is consistent with the generally accepted concept of the Ediacaran composition of the territory of the East European craton. Stratigraphic and radioisotope constraints (Shcherbakova et al., 2020 and references therein) clearly indicate that the Volyn basalts are Ediacaran in age and restrict the timing of their formation to 580 - 545 Ma. For the sites studied in Shcherbakova et al. (2020), the estimated age constraints are even narrower, ranging from 580 to 561 Ma.

Estimating the accumulation duration of the whole stratigraphic succession of the Volyn traps is difficult as there are no age estimates for the middle and lower part of the VBP (Babyn, Zabolottya and Gorbashy suites). However, based on literature concerning the formation of the Volyn traps, as well as from studies of other Large Igneous Provinces (LIP), simplified assumptions about the accumulation duration can be made. A distinguishing feature of LIPs, as exemplified by continental flood basalts, is the high magma emplacement rate (e.g., Storey et al., 2007) where aggregate magma volumes of > 1 Mkm^3 are emplaced in an intraplate setting and characterised by igneous pulse(s) of short duration(s) ($\sim$1 - 5 Myrs), during which a large percentage (> 75 %) of the total igneous volume are emplaced (Bryan & Ernst, 2008). Analyses of geochronological studies of LIPs (e.g., Bryan et al., 2010) and references therein) have revealed two main features relevant to the timing of eruptions of LIP formations: 1) 70 - 90 % of the eruptions are produced during one or two main pulses of eruptive activity; 2) these pulses, or even the whole duration of activity in the LIP, can happen in very short timeframes of < 5 Myrs, and in some cases possibly even < 1 Myr. For LIPs of any age, the errors on the age estimates are too large that individual formations within the pulses of activity, or individual eruptions could be resolved. In many cases, the age errors encompass the age range of almost all eruptive units from top to bottom

of the LIP body (e.g., Barry et al., 2010). The duration of formation of the VBP is still somewhat disputed in literature. Shumlyanskyy et al. (2006) suggested a rapid formation of the Volyn traps (several million years). The interval between the formation of the basalts of the Luchichiv and Zoryani suites is firmly established by the presence of a weathering crust. The corresponding duration of the break of magmatic activity was estimated by Kuzmenkova et al. (2011) to be between 2 and 19 Myrs. U-Pb data for the youngest group of zircons, isolated from high-Ti basalts indicate that different processes were separated by an interval of about 60 Myrs (Shumlyanskyy et al., 2016). However, such a long interval is unlikely to correspond to the duration of the outpouring basalts that form LIPs ($\sim$1 - 5 Myrs; Bryan and Ernst, 2008), even for LIPs as large as the Siberian one. There is therefore no reason to believe that the relatively small VBP was formed over a longer time interval.

Several magnetozones could be distinguished in magnetostratigraphic studies on samples from several boreholes (Glevasskaya et al., 2006) and show four alternating polarity intervals in a composite stratigraphic section near the Rafalovka region with two normal, one reverse and one transitional polarity. Taking into account recent estimates for reversal rates of about 15 reversals per million years for the period between 560 - 545 Ma (Levashova et al., 2021; Llanos et al., 2005; Popov et al., 2002; Popov et al., 2005), the accumulation time of the Ratne suite should not be more than $\sim$0.5 million years. This agrees with the hypothesis that the formation of the VBP did not take longer than several million years.

4.4 Palaeomagnetic sampling and methods

Palaeomagnetic samples were taken from quarry outcrops and borehole samples. For boreholes, all samples were taken first as hand samples which were then cut into specimens, focussing on basalts and baked contacts. In each quarry outcrop, palaeomagnetic samples were drilled directly in profiles of 10 - 40 cores from bottom to top of the exposed units.

For the evaluation of variation of the magnetic susceptibility (MS) and the determination of sampling levels before sampling, the susceptibility was measured along the core CK3 with a handheld KT-6 kappameter. A total of 126 core segments were taken from core CK3 with the 'up-down' orientation. Taking into account remagnetisation problems in palaeomagnetic studies of lava flows (e.g., Valet et al., 1998; Vella et al., 2017) the sampling was performed mainly from the bottom parts of the basaltic flows, where the rocks could not have been reheated by the overlying flow. The samples were cut into 20 mm cubic specimens with a diamond saw.

Experiments for palaeodirectional analysis were conducted at the Institute of Geophysics of the National Academy of Sciences of Ukraine, Kiev. Stepwise demagnetisations were done in a shielded room as thermal demagnetisations (TD) in steps of 10 - 50°C up to temperatures of 600 - 670°C using an MMTD80 oven, and alternating field (AF) demagnetisations in steps of 10 - 20 mT up to a peak field of 100 mT using an LDA-3A demagnetiser. Magnetisations were measured using an AGICO JR-6 spinner magnetometer, and the characteristic remanent magnetisations (ChRM) were analysed with Remasoft 3.0 (Chadima and Hrouda, 2006). Anisotropy of magnetic susceptibility (AMS) was measured on all samples with an MFK-1 Kappabridge, and anisotropy parameters were calculated with the ANISO software (Jelínek & Bucha, 1973).

Rock magnetic and palaeointensity experiments were performed at the University of Liverpool's Geomagnetism laboratory and the palaeomagnetic laboratory of the Geophysical Observatory 'Borok' (GO Borok) of the Institute of the Earth of the Russian Academy of Sciences. To estimate the thermal stability and the Curie temperatures T_c of the magnetic minerals in the rocks, continuous thermomagnetic curves $M_s(T)$ of the saturation magnetisation were measured on a custom-made Curie balance in temperatures up to 700°C in external fields of 450 mT while heating in air. The Curie point Tc was determined as the temperature corresponding to the minimum of the derivative $dM_s(T)/dT$ (e.g., Fabian et al., 2013). Temperature dependent susceptibilities were measured with an MFK1 Kappabridge between 40°C and 700°C. Hysteresis loop parameters were measured at room temperature on variable field translation balances (VFTB) and analysed using the automatic fitting of the MATLAB program HystLab (Paterson et al., 2018). Additional assessments of the domain state were made by measuring tails of partial thermoremanent magnetisation and calculating the thermomagnetic criterion (Shcherbakova et al., 2000).

Scanning electron microscope (SEM) backscatter images were produced at GO Borok RAS on a Tescan Vega II LMU microscope using polished thin sections etched with hydrochloric acid.

To increase the robustness of palaeointensity estimates, a multimethod approach was used to determine palaeointensities, utilising four different methods: thermal Thellier (TH), microwave Thellier (MW), Wilson, and combined experiments of double-heating Shaw (DHT-S) and pseudo-Thellier (pT). A total of 243 thermal Thellier experiments were undertaken using the Coe (1967) and IZZI (Tauxe & Staudigel, 2004; Yu et al., 2004) protocols with 5 - 8 pTRM checks in 15 - 20 temperature steps to maximum temperatures of 585 - 650°C. Experiments using the Coe protocol were either

Method	Selection criteria									
MW&TH	N	FRAC	β	Q	MAD	α	DRAT	CDRAT	$\text{DRAT}_{\text{Tail}}$	$\lvert k' \rvert$
Thellier	4	0.25	0.1	1	15	15	15	15	10^a	0.27
	r^2	D								
Wilson	0.95	0.95								
	N	f	r_N^2	r_T^2	MAD	α	slope_{T}		$\lvert k' \rvert$	
Shaw	5	0.15	0.99	0.99	15	15	0.9 - 1.1		0.2	
	N	f	β	r^2	MAD	α	$\lvert k' \rvert$	f_{resid}	$\lvert b_{AA} \rvert$	
pThel	6	0.45	0.1	0.995	15	15	0.2	0.15	0.85 - 1.15	

TABLE 4.1: Standard palaeointensity definitions (SPDv1.2, Biggin and Paterson, 2014) selection criteria of palaeointensity experiments. Microwave (MW) and thermal (TH) Thellier as well as Wilson selection criteria follow Shcherbakova et al. (2020) and Muxworthy (2010). Selection criteria of DHT Shaw and pseudo Thellier experiments are based on the criteria in Thallner et al. (2021b) and Lloyd et al. (2021b).

performed fully automatised on a three component thermomagneter with a sensitivity of 8 - 10 Am^2 ('ORION', GO Borok) or heated in a small furnace in a magnetic screen and measured on an AGICO-JR6 spinner magnetometer. For IZZI protocol experiments, specimens were heated in an MMTD80 oven and measured on a 2G RAPID superconducting rock magnetometer. Bias fields were applied in the range of 1 - 20 µT.

Microwave Thellier experiments were conducted on 63 specimens using University of Liverpool's Tristan microwave system with SQUID magnetometers (Suttie et al., 2010). Experiments were done in IZZI protocol with 4 - 5 pTRM checks as well as in Coe protocol with 4 - 5 pTRM checks and 4 - 5 pTRM tail checks (Riisager & Riisager, 2001) in 8 - 12 steps using high frequency (14 GHz) microwaves with progressively increased power and exposure times up to peak integrals of 100 - 450 W.s. Bias fields were varied between 5 - 20 µT and applied in angles of 45 - 90° to the specimen's ChRM (Yu & Tauxe, 2005).

Wilson experiments (Muxworthy, 2010; Wilson, 1961) were continuously measured during continuous thermal demagnetisations and full thermal remagnetisations for 131 specimens in bias fields of 10 - 20 µT on a 3D VSM. The thermal demagnetisations and remagnetisations were performed using temperature steps up to 450° - 620°C. The temperature range used for the determination of palaeointensities was chosen to be close to the temperature interval where the ChRM was isolated during thermal demagnetisations of sister specimens. In contrast to the Thellier-type experiments, in the Wilson method, specimens are given a full TRM, making this method domain state independent.

Double heating (DHT) Shaw (Tsunakawa & Shaw, 1994) experiments were performed on 139 specimens using the 2G Rapid system. They were conducted using a protocol, that combines the DHT Shaw method with the pseudo-Thellier method (de Groot et al., 2013; Paterson et al., 2016; Tauxe et al., 1995) where all single ARM acquisitions at peak AF field of the standard DHT Shaw method (e.g., Yamamoto et al., 2010) were replaced by several ARM acquisition steps at progressively increasing AF fields (e.g., Thallner et al., 2021b). Full TRMs were given twice in a bias field of 10 µT at a temperature of 610°C. The double heating Shaw method checks for possible thermochemical alterations during the heatings by comparing the AF demagnetisations of the first TRM and the ARM corrected TRM of the second heating. ARMs were given up to peak AF fields of 100 mT in a bias field of 11.4 µT. Values of absolute palaeointensities from pseudo-Thellier experiments were calculated using the generalised calibration equation of $B_{pal} = |b| * B_{lab}/3.208$ (Paterson et al., 2016).

Selection criteria for all methods are shown in Table 4.1. They were chosen to resemble selection criteria used in previously published palaeointensity studies of Ediacaran rocks (Shcherbakova et al., 2020; Thallner et al., 2021a; Thallner et al., 2021b).

4.5 Results

4.5.1 Palaeomagnetic directions from quarry samples

The basalt samples show a stable high temperature characteristic component (ChRM) of natural remanent magnetisation (NRM) with $T_b > 500$°C. Results of the new specimens that sample equivalents of the flows of Shcherbakova et al. (2020), were used to recalculate these directions and are given in Table 4.1 together with the palaeomagnetic direction of the newly sampled top of flow RA-1 (RA-1b). Our new directions agreed well with the directions in Shcherbakova et al. (2020) and the recalculation of flow directions did not lead to significant changes of directions.

The flows of the Policy-2 and Rafalovka quarries are stratigraphically correlated with each other. Their magnetic parameters are shown in Supplementary Figure C.1. The initial values of NRM and magnetic susceptibility for basalts and tuffs differ by two orders of magnitude. In basalt samples, the Königsberger ratios Q (Koenigsberger, 1938) range from 0.5 to 3. Most basalt samples show Q ratios > 1, while Q ratios for tuff samples are mostly < 1 ($Q_{mean} = 0.5$). The declination and inclination of the initial NRM and ChRM component of the magnetisation, identified as result of principal component analysis, are shown in the right panel of Supplementary Figure C.1. The flows of the Rafalovka section have a positive inclination, while the Policy-2 section

Site	Location/ rocks	NRM [Am^{-1}]	Magnetic Susceptibility	n	Dec	Inc	k	α_{95}
Velikiy Midsk quarry, 51.093°N, 26.086°E								
VM	basalt	0.5-4.1 1.7	0.03-0.05 0.035	(21)	(30.6)	(-77.2)	(120)	(2.9)
Policy-2 quarry, 51.244° N, 26.016° E								
RA-3	basalt	0.4-2.5 1.16	0.03-0.07 0.005	8 (4)	23.8 (17.6)	-57.0 (-53.8)	111 (110)	5.3 (2.8)
RAt2-3	tuff	0.02-1.15 0.22	0.0005-0.037 0.0008	14 (9)	30.0 (29.5)	-59.7 (-65.4)	72 (160)	4.7 (4.1)
RA-2	basalt	0.28-4.1 2.0	0.037-0.076 0.04	35 (16)	48.4 (49.4)	-82.0 (-81.4)	102 (153)	2.4 (3.0)
Rafalovka quarry, 51.235° N, 26.046° E								
RA-1b	basalt	1.48-5.2 2.4	0.046-0.1 0.006	(11)	(278.2)	(62.2)	(23)	(9.8)
Rafalovka quarry, 51.228° N, 26.051° E								
RA-1a	basalt	1.15-2.49 1.58	0.045-0.074 0.056	26 (16)	293.3 (294.7)	82.1 (82.8)	36 (29)	4.8 (7.9)
RAc	baked contact	0.68-1.18 0.82	0.009-0.013 0.01	(10)	(293.9)	(72.9)	(289)	(2.8)
RAt2	green tuff	0.016-0.055 0.026	0.001-0.019 0.0012	(11)	(157.1)	(66.8)	(12)	(14)
RAt1	red tuff	0.01-0.02 0.015	0.0006-0.001 0.0008	(8)	(156.3)	(76.0)	(5)	(29.6)

TABLE 4.2: Site-mean palaeomagnetic directions and statistical parameters (ChRM component of thermal demagnetization). NRM is natural remanent magnetization range and mean values; magnetic susceptibility range and mean values; n is number of samples which yielded the ChRM-component; Dec is declination; Inc is inclination; k is the precision parameter; α_{95} is half-angle of cone of 95 per cent confidence, in degrees. The site-mean directions from Table 2a of Shcherbakova et al. (2020) are given in brackets.

shows negative inclinations, indicating a polarity change of the geomagnetic field between the flows RA-1 and RA-2. With thicknesses of 11 m and 14 m, the flows RA-1 and RA-2 are rather thick and show variations of declination and inclination within them. The palaeomagnetic directions of the underlying tuffs (RAt) differ significantly from the directions of the overlying RA-1 basalts and the baked contact zone. Here declinations between tuffs and basalts differ by about 130° (Table 4.2, Supplementary Figure C.1) while inclinations show only small differences.

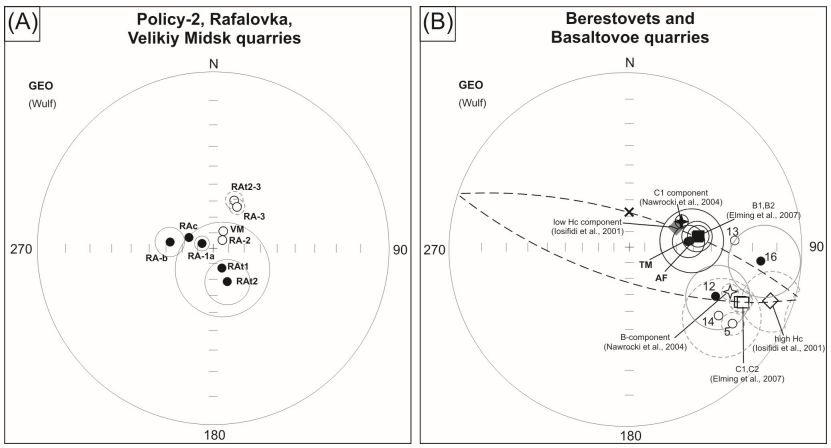

FIGURE 4.2: Paleomagnetic directions identified on high-Ti samples from the Berestovets and Basaltovoe quarries (circles) that did not produce successful palaeointensity estimates; site numbers are given in accordance with Supplementary Table C.1. AF and TH – the mean of 4 sites according to results of temperature demagnetization in the range of 150 - 420°C and for 4 sites according to alternating magnetic field demagnetization in the range of 2 - 25 mT (respectively). The results of component isolation by other authors are given: by squares - (Elming et al., 2007), rhomb - (Iosifidi et al., 2000), and a star - (Nawrocki et al., 2004). Open (filled) symbols are projections onto the lower (upper) hemisphere, the results are presented with confidence level of α_{95}. The cross shows the direction of the present geomagnetic field in research area. The plane of the remagnetisation circle is shown by the dotted line.

The polarity reversal itself was not recorded in the traps. It took place after the effusion of the flow RA-1 and before the effusion of the flows RA-2 and RA-3, where the secular variation seems to be smaller, possibly due to a more stable state of the field after the reversal.

The high-Ti samples of the Berestovets and Bazaltovoe quarries show average Königsberger ratios (Q values) between 1.9 and 3.9 (Supplementary Table C.1). Primary ChRM directions were found at low to intermediate coercivities of < 80 mT and intermediate temperatures between 200 and 420°C. These directions are given in Table 4.3 and shown in Figure 4.2, together with previously published directions.

4.5.2 Palaeomagnetic results from borehole core samples

Boreholes from the Ratne village area exposed the traps of the Volyn series from the lower part of the Zabolottya suite to the Ratne suite. The stratigraphic position of the studied suites (from bottom to top) is Zabolottya, Babine, Luchichiv and Ratne, which includes the Zoryani and Yakushiv layers (Figure 4.1d). The Zabolottya suite is represented by the cores C8265 and C4596. The most preserved core sections are from the borehole CK3. In this borehole, both the Babyne and Ratne suites are well exposed, but the Luchichiv suite is reduced. The lower part of the Luchichiv suite is

Site *Lab*	n **N**	Dec	Inc	α_{95}	k	Plat	Plon	A_{95}	Ref
Berestovets, 50.873° N, 26.303° E									
BE(1) AF	16	81.9	53.4	6.0	39	30.5	98.6	6.9	[1]
BE(3) TH	22	76.0	53.6	4.1	58	34.2	102.4	4.8	[1]
BR(4) AF	7	63.1	49.9	14.7	18	39.9	114.8	16.0	[1]
BR(6) TH	10	83.0	54.7	9.5	27	30.7	96.8	11.3	[1]
Lulea,Low Hc	13	83.2	53.7	6.8	38	29.9	97.5	7.9	[2]
Lulea,Low Tb	5	85.5	42.4	7.5	103	21.5	103.5	7.2	[2]
Kiev,Low Hc	7	77.0	51.0	10.1	37	31.9	101.8	11.2	[2]
Mean	**7**	**78.6**	**51.5**	**4.8**	**159**	**31.3**	**102.3**	**5.6**	
Basaltovoe, 50.915° N, 26.236° E									
BAZ(7) AF	7	113.0	40.8	17.5	13	5.2	84.3	16.5	[1]
BAZ(10) TH	7	103.0	54.0	19.3	11	19.4	84.5	22.6	[1]
BZ(12) AF	14	71.9	55.8	7.0	34	38.4	103.8	8.5	[1]
BZ(15) TH	12	77.0	47.4	7.3	36	29.9	107	7.6	[1]
Lulea,Low Hc	9	85.5	46.2	9	34	23.7	101.1	9.2	[2]
Lulea,Low Tb	11	95.3	44.8	11.8	16	17	95	11.8	[2]
Kiev,Low Hc	10	64.6	48.8	10.3	23	38.3	114.4	11	[2]
St.Petersburg,Low Hc	15	67.8	55.7	4.3	79	40.6	105.8	5.2	[3]
basalt(C1)	21	67	55	3.9	67	40	102	4.9	[4]
Mean	**9**	**83.7**	**51.0**	**8.1**	**42**	**28.5**	**99.5**	**10.1**	

TABLE 4.3: Paleomagnetic directions and poles, calculated from the low-coercive / medium-temperature component of "high-Ti" basalts of the Ratne suite. Numbers in brackets for each site name correspond to components given in Supplementary Table C.1. n is the number of samples which yielded the ChRM-component; N is number of sites included in the calculated mean; Dec, Inc, mean declination and inclination, respectively; α_{95} cone of confidence at a 95 per cent probability level, in degrees; Plat, Plon, latitude and longitude of the palaeomagnetic pole; A_{95}, confidence circle of the pole at a 95 per cent probability level, in degrees; the site mean directions represents data from the basalt flows in [1]: this study, [2]: Elming et al. (2007), [3]: Iosifidi et al. (2000), [4]: Nawrocki et al. (2004); site means used for calculation of palaeomagnetic mean poles are shown in bold.

exposed in the core C4596 together with an upper part of the Babine suite. The core sections of borehole C8262 comprise units from the Luchichiv and Ratne suites.

Similar to what was observed for samples from the quarry sections, the MS and NRM intensities between tuffs and basalts strongly differ by up to two orders of magnitude (Figure 4.3c, d). Along the cores, magnetic susceptibility also varied within basalt flows and can change several times within a unit flow. The largest scatter of susceptibility was recorded in core segments containing mixtures of lava breccia, conglomerates and basalt layers.

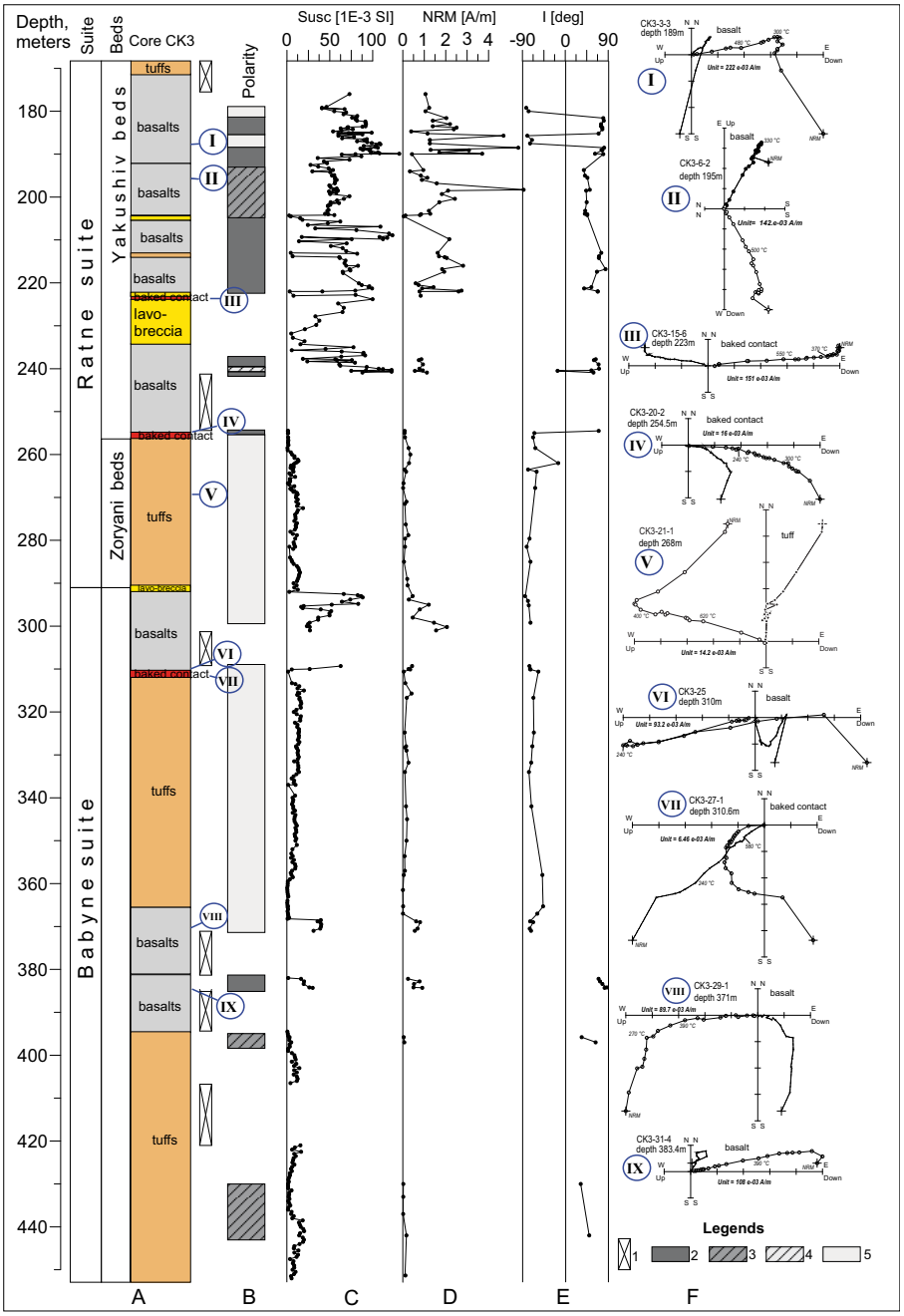

FIGURE 4.3: Rock magnetic and magnetic polarity data from core CK3: A: stratigraphy; B: polarity; C: volume normalised magnetic susceptibility; D: initial NRM intensity; E: inclination of the ChRM component; F: demagnetisation diagrams obtained after stepwise thermal treatment on horizontal (filled markers) and vertical (open markers) planes. Declinations are arbitrary due to the limitations of the core sample orientations Roman numerals show the position of the demagnetised samples in the core. Legends: 1 – no core section, 2 – steep positive inclination, 3 – shallow positive ($0 < I < 45°$) inclination, 4 – shallow negative ($0 > I > -45°$) inclination, 5 – steep negative inclination.

The high temperature ChRM component in the basalt specimens was found at unblocking temperatures above 500 - 580°C and up to 640°C. Samples of baked tuffs and tuffs were only fully demagnetised at temperatures of 665 - 670°C, indicating the presence of hematite. Examples of stepwise thermal demagnetisations are presented in Figure 4.3f. The inclinations of the ChRM component of core sections from the borehole CK3 are shown in Figure 4.3e. In some cases, the directional data showed puzzling results, where dual polarity directions were found in neighbouring samples at the same sampling levels. Such antipodal directions recorded in single samples were rejected as we could not be certain that these core segments were not misoriented during sampling and packing of the segments at the time of drilling. The identified polarity intervals with positive, negative and intermediate (± 45°) inclinations are shown in Figure 4.3b.

The inclinations of the ChRM component of samples from the other cores are presented in Figure 4.4. Some suites can be stratigraphically correlated between different boreholes (see Figure 4.1d) allowing the determination of changes of inclination throughout large parts the Volyn series.

In the lowermost exposed parts of the series, basalts of the Zabolottya suite with a thickness of about 60 m, exposed in the cores C8265 and C4594 are characterised by a positive inclination. Four samples of the core C4594 showed negative inclinations. These were not accepted as polarity changes and instead interpreted as misoriented because a) no evidence points to time gaps during basalt accumulation as neither tuffs nor lavabreccia layers are observed between the basalt flows, b) the samples occupy a relatively short interval (∼4 meters, compared to the total basalt thickness of 60 m), and c) no negative inclinations were measured in samples of the core C8265.

The basal and top tuff layer of the Babyne suite in core CK3 (Figure 4.3a) showed shallow positive and negative inclinations, respectively. The results for the two basalt flows between these tuff segments demonstrate a change from positive to negative inclinations. A similar trend can be observed in the data from the lowermost basalt flow in the core C4596.

The stratigraphically higher Luchichiv suite is completely absent in the core CK3, but well exposed in the cores C4596 and C8262, and a minimum of two polarity reversals were observed. Unfortunately, the lack of marking horizons prevented the correlation of the Luchichiv basalts between the two cores. However, their stratigraphic position in the section of the Volyn series, an approximately equal thickness, and a similar pattern of polarity horizons suggest that the Luchichiv suite is fairly well represented in the C4596 and C8262 cores.

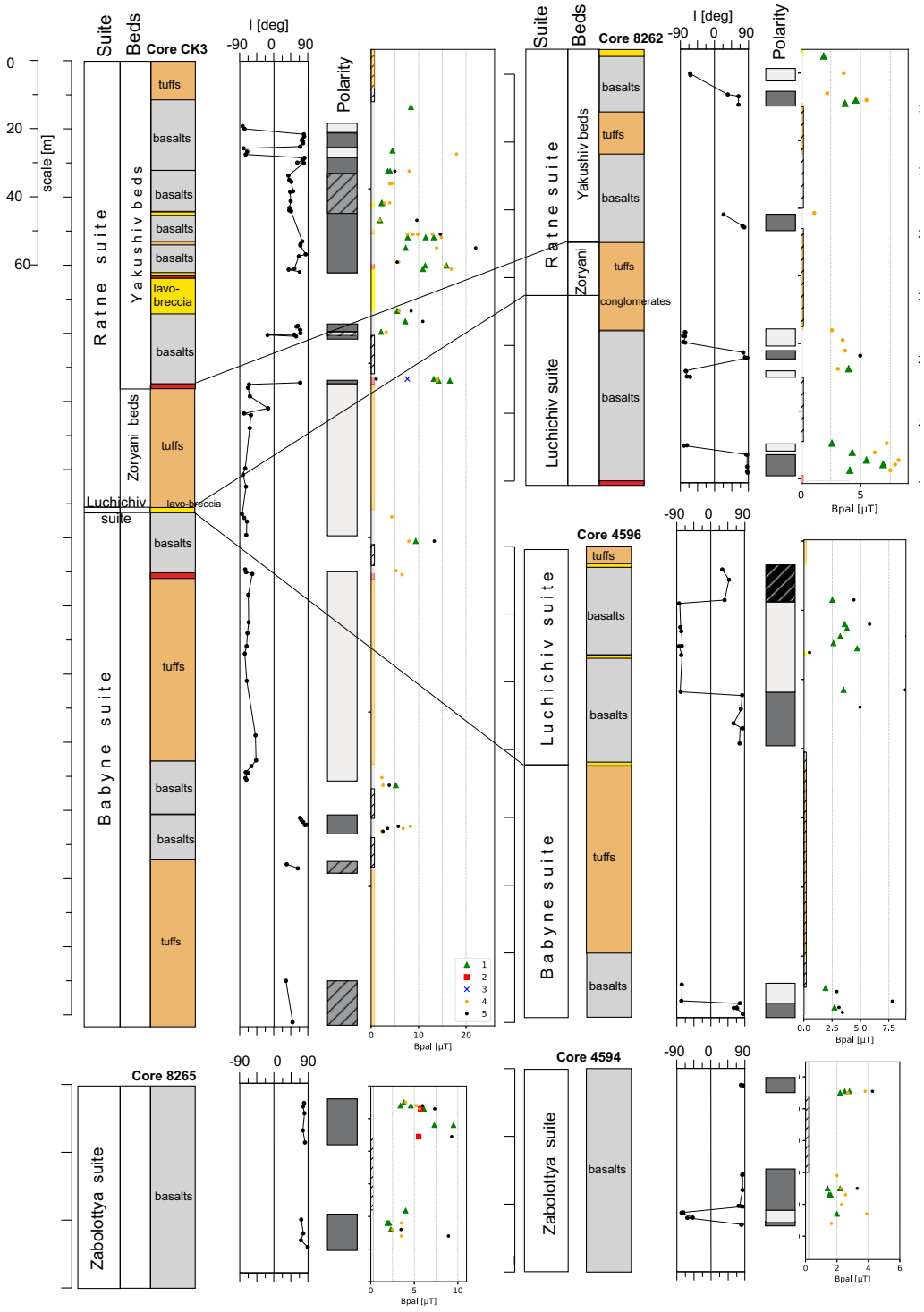

FIGURE 4.4: Stratigraphy and magnetic inclination of ChRM from core samples. The legend is the same as in Figure 4.3. Legend for palaeointensities: 1: thermal Thellier, 2: microwave Thellier, 3: DHT-Shaw, 4: Wilson, 5: pseudo-Thellier

The data for the Zoryani beds in core CK3 show negative inclinations for tuff samples, whereas the baked tuffs and overlying basalt flows of the Yakushiv beds are characterised by predominantly steep positive inclinations with one section of shallow positive inclination in the upper part. In addition, some samples in the topmost basalt flow of the Yakushiv beds reveal a negative inclination. A similar polarity pattern was found in the upper basalt flow of the core C8262. However, the possibility of orientation errors due to incorrect up-down orientation of the core segments cannot be excluded and it is unclear if these directions record actual polarity reversals.

Thus, throughout the Volyn series, we were able to distinguish at least 6 polarity reversals. These results are in good agreement with data from other boreholes of the region that show three field polarity changes recorded in the Volyn series above the top of the Babyne suite (Glevasskaya et al., 2006).

4.5.3 Magnetic properties

The magnetic properties of the rocks varied along the studied profile (Supplementary Figure C.1). Similar to what was reported in Shcherbakova et al. (2020), most rocks of the Luchichiv suite showed Curie temperatures of 550 - 590°C indicating the presence of (low-Ti-)titanomagnetite. These samples showed a good thermal stability of the carriers with mostly reversible curves of temperature dependent magnetisation and susceptibility (Figure 4.5f and 4.5g, Figure 4.7a4 - c4) with only small decreases of M_s(T) and κ(T) with each progressive temperature step. Thermomagnetic and temperature dependent susceptibility curves for basalt and baked tuff core samples from the Ratne, Babyne and Zabolottya suites showed another Curie temperature of 650°C (Fig 4.5g). A completely different behaviour is seen in the high-Ti basalts from the Ratne suite, sampled in the Berestovets/Bazaltovoe quarries. Here, Curie temperatures between 320°C and 400°C (Figure 4.5h) are seen in the thermomagnetic and susceptibility curves. These phases were not fully reversible, suggesting higher grades of weathering leading to their exclusion from palaeointensity experiments.

Measurements of AMS for basalts of the Policy-2 and Rafalovka quarries show that the basalts are magnetically foliated and characterised by a low degree of anisotropy, with values of P $\leq$ 1.05 (mean P = 1.03). The mean direction of the AMS ellipsoid axis Kmax is Dec = 330°, Inc = 5°, whereas the mean direction of K_{min} is subvertical (inc = 80°), similar to reports for rocks of the Rafalovka quarry in Elming et al. (2007). The underlying tuffs of the Rafalovka quarry (RAt-1 and RAt-2) show oblate shapes for AMS ellipsoids and insignificant degrees of anisotropy (mean P = 1.007) with the directions for K_{max} and K_{int} in the horizontal plane, and the direction of K_{min} perpendicular to the horizontal plane.

AMS measurements of the Berestovets/Basaltovoe basalts show that the rocks are characterised by foliation and lineation with low degrees of anisotropy ($1.01 \leq P \leq 1.05$). The mean direction of K_{max} is Dec = 234°, Inc = 74° in Berestovets samples, whereas the columnar basalts of Basaltovoe show a subvertical K_{max} (Dec = 248°, Inc = 74°).

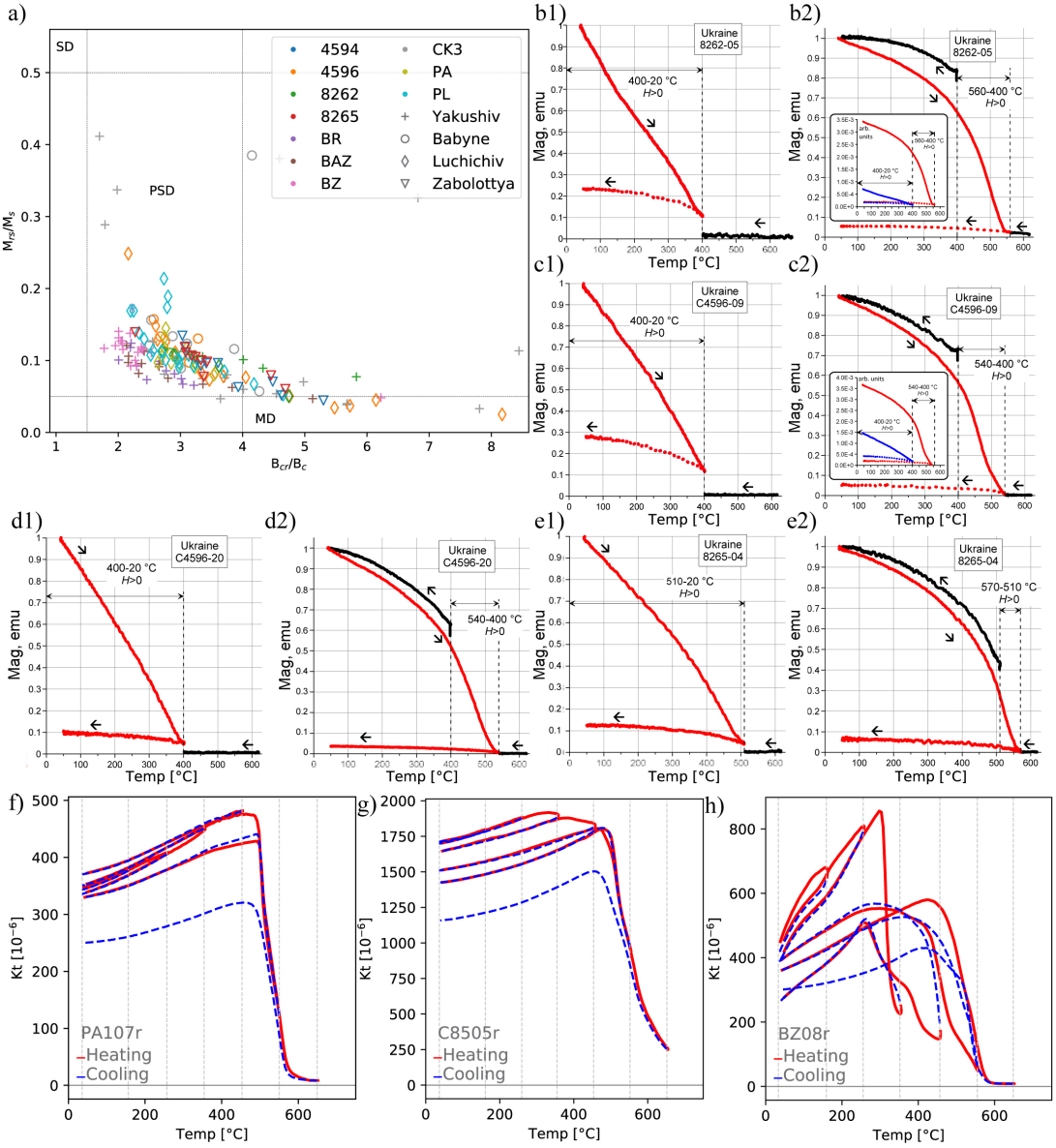

FIGURE 4.5: Representative rock magnetic data: (a) hysteresis data in a (Day et al., 1977) plot; (b - e) thermomagnetic criterion for specimens from the Yakushiv (b1, b2), Luchichiv (c1, c2), Babyne (d1, d2) and Zabolottya (e1, e2) suites, showing curves of pTRMs(T1,T2) (Shcherbakov et al., 2001) f - h) susceptibility versus temperature curves in 100°C increments between 50°C and 650°C.

Samples of basalts and tuffs in core CK3 showed predominantly magnetically foliated samples with low degrees of anisotropy ($1.003 \leq P \leq 1.05$, mean P = 1.011), and a subvertical mean direction of K_{min} (inc = 84°)

Ratios of magnetic remanence to saturation remanence (M_{rs}/M_s) and coercivity of remanence to coercivity ($B_{cr}/_{Bc}$) from hysteresis loop parameters of quarry samples from the Luchichiv suite and core samples along the whole profile cluster in the 'PSD' area of the Day plot (Figure 4.5a) and suggest a mixture of magnetic domain types, presumably a mixture of fine SD and coarse MD grains (Dunlop, 2002). Results for specimens from the Berestovets and Basaltovoe quarries predominantly show smaller ratios of B_{cr}/B_c. A smaller cluster of hysteresis parameter ratios of predominantly baked tuff samples is shifted to the right of the day plot due to a larger fraction of higher coercive minerals. Domain states of magnetic grains for the studied suites were quantitatively characterised by the thermomagnetic criterion (Shcherbakov et al., 2001), where two pTRMs were induced in a low-temperature interval (400 - 20°C, Figure 4.5b1 - d1) and a high-temperature interval (540 - 400°C, Figure 4.5b2 - d2). These show very small tails of pTRM for all samples in the high-temperature interval (Figure 4.5b, c), demonstrating SD, or small PSD behaviour of the magnetic grains carrying the ChRM which is encouraging in terms of their potential for reliable palaeointensity determinations. In the low-temperature intervals, considerably larger pTRM tails can be seen, indicating PSD to MD behaviour.

In addition to the coarse grains of the Luchichiv suite, seen in SEM backscattering images (Shcherbakova et al., 2020), SEM observations in this collection reveal that the magnetic fraction of samples is represented by titanomagnetite grains with an average size of 20 - 30 µm. In these samples, oxy-exsolution structures in the titanomagnetite grains co-exist with single-phase oxidation structures under natural conditions, as shown in Figure 4.6 for a sample from the Zabolottya suite. This is consistent with the co-existence of SD and MD grains, seen in the pTRM tail experiments, where the SD behaviour, linked to the oxy-exsolution structures, is characteristic for the high-temperature range that carries the ChRM. For accepted palaeointensity determinations, reversible thermomagnetic curves, positive pTRM checks in Thellier experiments, and similarity of NRM and TRM curves in Wilson experiments (e.g., Figure 4.7c for a specimen of the Babyne suite) strongly suggest that the low blocking-temperature grains, associated with MD behaviour and single-phase oxidation do not contribute to the utilised NRM component. While the lower temperature phase will acquire pTRM in the palaeointensity experiments, we performed careful checks (outlined in the next section) to verify that it did not bias the accepted palaeointensity results.

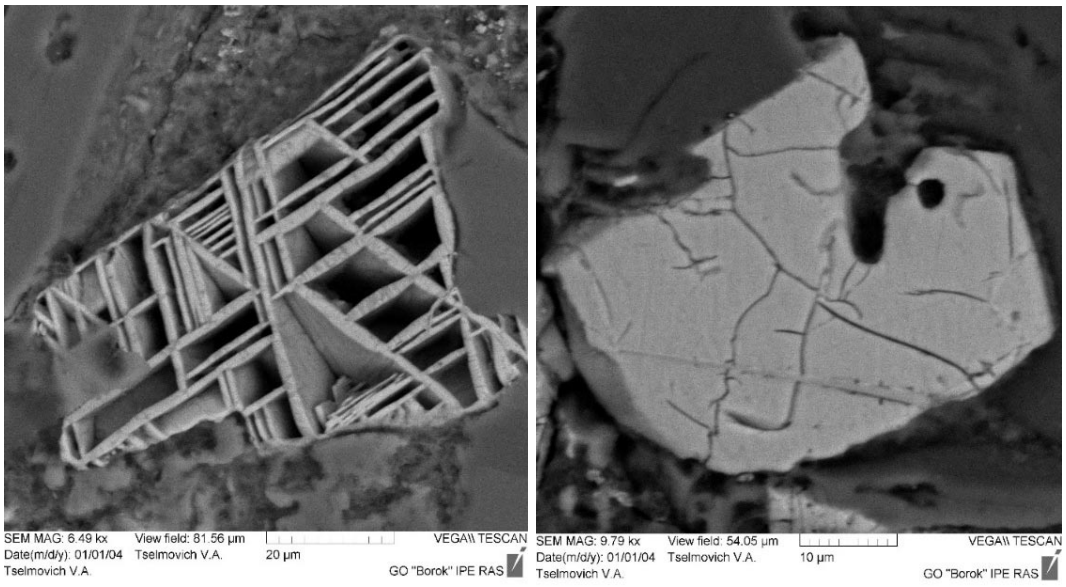

FIGURE 4.6: Microphotographs in backscattered electrons imaging mode of titanomagnetite grains from Sample 4594-01(Zabolottya suite). The left column demonstrates a good example of the exsolution into ilmenite lamellae and magnetite cells. This photograph was taken after the polished sections were etched with hydrochloric acid. The right column presents an example of single-phase oxidation

4.5.4 Palaeointensity results

Palaeointensity experiments were conducted on 117 specimens of the Rafalovka/ Policy-2 quarries (sites RA, PL), 286 specimens of the borehole core-samples (CK3, C8262, C4596, C8264, C4594) and 175 specimens of the Berestovets/Bazaltovoe quarries (BAZ, BR, BZ). Results from the different methods are shown along the borehole profiles in Figure 4.4.

Thermal Thellier experiments showed a high success rate for specimens from the drill cores and the Rafalovka quarries. For these localities, 62 of 129 experiments performed on the drill core specimens and 24 of 36 experiments performed on the specimens of the Rafalovka quarries passed the selection criteria given in Table 4.1, corresponding to success rates of 48.1% and 66.7%, respectively. In contrast, no results from the 78 experiments performed on specimens of the Berestovets/Bazaltovoe quarries were accepted. In agreement with the directional analysis, all Thellier experiments showed two magnetisation components, with secondary magnetisations that were generally removed at temperatures of 450 - 500°C and high temperature ChRMs. Temperatures of the directional changes between the two components in the Zijderveld diagrams correspond to changes of slopes in Arai diagrams, leading to two-sloped Arai plots

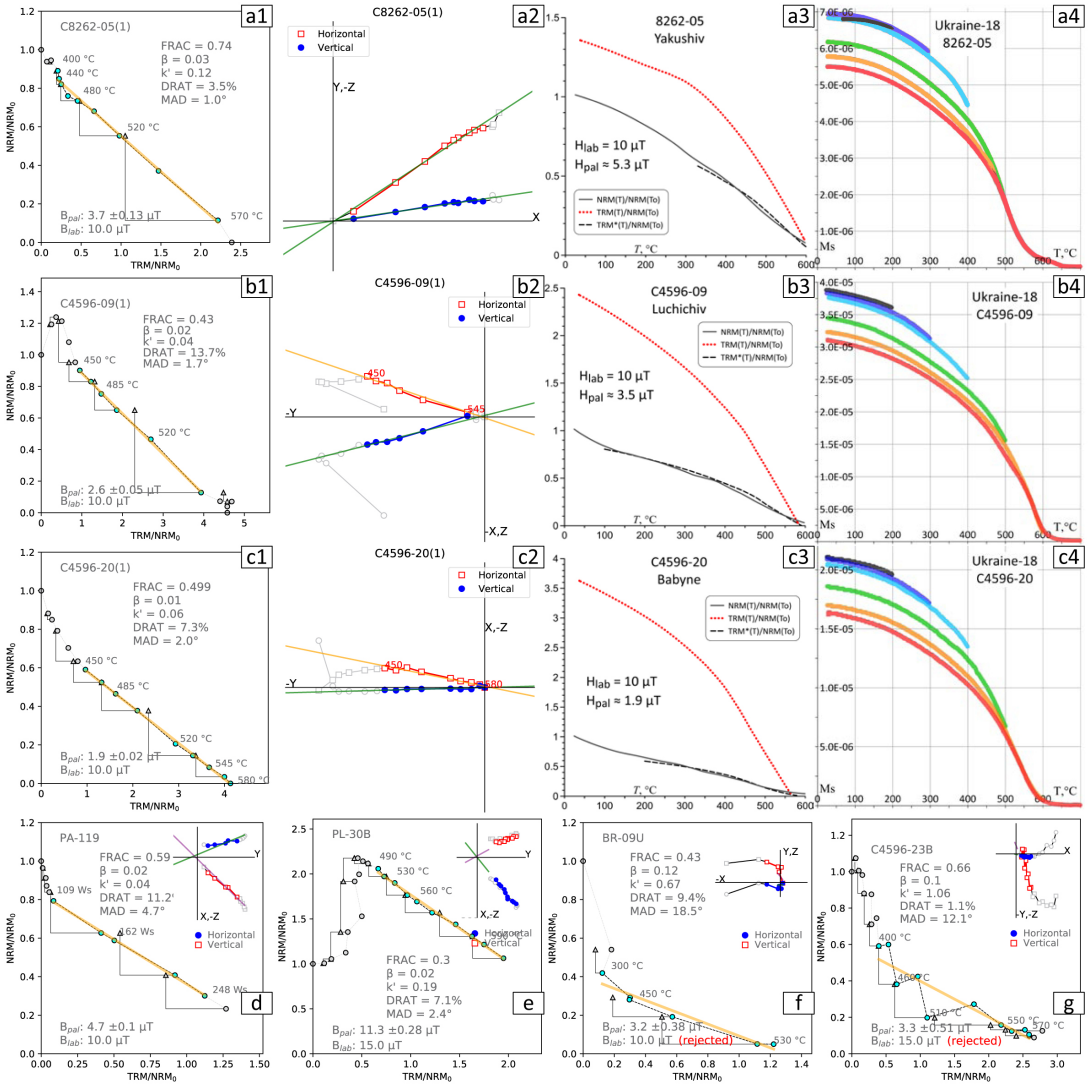

FIGURE 4.7: Representative plots of magnetic properties and results of thermal Thellier, microwave Thelllier and Wilson experiments for all investigated suites of the Volyn trap series. All magnetisations are normalised to the NRM value of the sample. Panels show results for samples from the Yakushiv suite (a1 - a4), the Luchichiv suite (b1 - b4), and the Babyne suite (c1 - c4) - (a1 - c1) Arai-Nagata diagrams with pTRM checks (triangles) and critical values for the selected best-fit line (yellow), (a2 - c2) orthogonal plots of directional data associated with the Thellier experiments shown in (a1 - c1). Coloured points correspond to the selected best-fit line, (a3 - c3) results of Wilson experiments on sister specimens, (a4 - c4) strong field thermomagnetic curves heated to incrementally higher temperatures up to 700°C; d) shows an accepted microwave Thellier result from the Luchichiv suite; e) shows the two-slope behaviour for samples, where the overprint direction is antipodal to the ChRM; f) and g) show examples of results from the Ratne suite and Babyne suite, that were rejected with high curvatures and 'zig-zagging'

(Figure 4.7a - g) resembling the results seen in (Shcherbakova et al., 2020). The shape of

the two-sloped Arai plots deviated from the expected shape of a steep slope in the low-temperature range and a shallow slope in the high temperature range for specimens with a ChRM direction in the opposite direction of the overprint (Figure 4.7e), supporting that the two slopes are representing two components with different field strengths and not concave-up shapes associated with non-ideal MD behaviour, even if a directional change at this temperature is not clearly visible (e.g., Figure 4.7a1 and 4.7a2). For all accepted results, the high-temperature slopes (> 450°C), chosen for palaeointensity determination, showed low scatter, good linearity and passing pTRM checks. Thellier results of specimens from the Berestovets/Bazaltovoe quarries also showed two components and corresponding changes of gradients in Arai plots but high curvature and DRAT/CDRAT values as well as large zig-zagging in the high-temperature parts of the slopes of all specimens suggested that these slopes have been severely biased by laboratory alteration and MD effects and were therefore rejected. Compared to the quarry samples, samples from the drill cores were more likely to break during heating. Wilson experiments had success rates similar to Thellier experiments with 77 of 131 results passing selection criteria. Accepted Wilson results showed a high similarity between the demagnetisation of the NRM and the demagnetisation of a laboratory TRM in the high temperature range, giving additional confidence in a thermal origin of the ChRM.

Success rates of microwave-Thellier experiments were significantly lower than success rates of other methods with 4 of 12 quarry specimens (33.3%) and 2 of 39 drill core specimens (5.1%) accepted. Rather than failing selection criteria, the low success rates were mainly caused by specimens fracturing during the quick heating process of the microwave method, most likely due to vaporisation of water content. Arai plots of accepted results from specimens that did not fracture, resembled the Arai plots of the thermal experiments and showed two slopes (Figure 4.7d).

A similar effect of samples fracturing during heating was observed during Shaw experiments. In contrast to microwave experiments however, this was only the case for Shaw experiments of specimens from drill cores, where 35 specimens fractured in the first heating at temperatures around 500°C and only 1 of 48 experiments (2.1%) led to an accepted result. Reducing the heating rate from 50°C/min to 10°C/min did not decrease the number of fractured specimens/heating. Thanks to the combination of the Shaw experiments with the pseudo-Thellier protocol, samples that did fracture during heating could still be analysed as pseudo-Thellier experiments. For the calculation of success rates however, they were treated as failed Shaw experiment. Rafalovka quarry samples, that were less likely to fracture, showed a much higher success rate with 15 of 50 results (30%) passing selection criteria. Results were mostly rejected due to failure of the slope$_T$ criterion, suggesting that the ARM correction of these experiments was

not valid and the resulting palaeointensities would have been biased by laboratory alteration (Tanaka & Komuro, 2009). Absolute values from pseudo-Thellier experiments, calibrated with the generalised calibration equation in (Paterson et al., 2016) mostly agreed with the results from the other methods along the borehole profiles (Figure 4.4). However, absolute pseudo-Thellier intensity estimates from the Policy-2 quarry showed extreme variations of ∼30 µT within the same unit flow and disagreed with results from Thellier, microwave, Wilson and Shaw results (Supplementary Tables C.2 - C.4). In addition, several high-palaeointensity outliers in the borehole profiles in the Babyne and Luchichiv suite (Figure 4.4) lead to an increased dispersion of palaeointensities. Therefore, absolute palaeointensity values from pseudo-Thellier experiments were not used for calculation of the mean flow intensities.

Combining the results of the four methods, 185 specimens from 20 units of 4 suites of the Volyn series. Of those, 16 units produced average palaeointensity results between 2.2 and 11.1 µT (0.31 - 1.67 $\times 10^{22} Am^2$) from three or more independent intensity estimates, as shown in Table 4.4. A list of all results with their critical parameters is given in Supplementary Tables C.2 - C.6. The reliability of intensity determinations was assessed with the Q_{PI} criteria (Biggin & Paterson, 2014) and shows Q_{PI} values between 6 and 8 for the different flows (Table 4.4). The criteria that were not awarded to certain units were STAT, TECH and LITH. None of the units passed the STAT criterion. Even though 12 of the 20 units provided more than the minimum of 5 individual intensity determinations, all of the standard deviations between 0.8 - 7.5 µT exceeded the limit of stdev/mean $\leq$ 25%. Despite the low success rates in the core samples, only 5 units failed to produce intensity results from more than one method, awarding the TECH criterion to the remaining 15 units. The LITH criterion was only awarded to 2 units, where the intensity results were measured on both basalt and baked tuff samples.

Suite	Strat	ID	Unit	Samples	$\lvert inc \rvert$	N/n_{th}	N/n_{mw}	N/n_{wl}	N/n_s	N/n_{PI}	PI	σ	VDM	σ	Q_{PI}
Yakushiv	V1jk	BAZ		BAZ (01-12)	51	19/0	8/0	11/0	10/0	48/0					
		BR		BR (01-13)	51.5	26/0	3/0	12/0	12/0	53/0					
		BZ		BZ (01-20)	51	33/0	3/0	19/0	19/0	74/0					
		C8262	flow 1	C8262 (01-05)	55	6/4	0/0	5/3	1/0	12/7	3.5	1.5	0.64	0.28	7
				C8262 (01)	*-64R*	*1/1*	*0/0*	*1/0*	*1/0*	*3/1*	*2.2*		*0.36*	*0.00*	
				C8262 (02-05)	*55N*	*5/3*	*0/0*	*4/3*	*0/0*	*9/6*	*3.7*	*1.5*	*0.68*	*0.28*	
		C8262	flow 2	C8262 (07-09)	76	1/0	1/0	2/1	1/0	5/1	1.1	0.15	0.00	6	
		CK3	flow 1	CK3 (01-04)	80	3/2	0/0	2/1	0/0	5/3	10.6	7.5	1.43	1.01	7
		CK3	flow 2	CK3 (05-08)	45	5/3	3/0	6/4	2/0	16/7	4.5	2.0	0.92	0.41	7
		CK3	flow 3a	CK3 (09-10)	70	3/2	2/0	2/2	1/0	8/4	2.1	0.4	0.31	0.06	7
		CK3	flow 3b	CK3 (11-16)	70	12/7	3/0	10/10	3/0	28/17	11.1	3.5	1.67	0.53	7
		CK3	flow 4	CK3 (17-21)	70	11/6	5/0	4/4	4/1	24/11	9.6	5.4	1.44	0.81	8
Luchichiv	V1lc	Policy-2	RA-3	PL (37-48)	-57	1/1	1/0	0/0	7/1	9/2	8.1	1.3	1.44	0.22	7
		Policy-2	RAt2-3	PL (29-36)	-59.7	1/1	0/0	0/0	2/0	3/1	11.3	1.94	0.00	6	
		Policy-2	RA-2	PL (01-28)	-82	16/13	4/2	8/8	16/2	44/25	9.5	2.5	1.26	0.33	8
		Rafalovka	RA-1b	PA (115-132)	62.2	16/8	1/1	11/11	15/6	43/26	4.3	1.2	0.71	0.19	7
		Rafalovka	RA-1a	PA (101-114)	82.1	2/1	6/1	0/0	10/6	18/8	7.3	2.3	0.97	0.31	7
		C8262	flow 3	C8262 (10-21)	83	17/7	4/0	10/9	4/0	35/16	5.2	1.9	0.69	0.25	7
				C8262 (10-12)	*-87R*	*2/0*	*1/0*	*2/2*	*1/0*	*6/2*	*3.1*	*0.8*	*0.40*	*0.11*	
				C8262 (13-14)	*80N*	*2/0*	*1/0*	*2/1*	*1/0*	*6/1*	*4.0*		*0.54*	*0.00*	
				C8262 (15-17)	*-75.5R*	*4/2*	*0/0*	*2/2*	*1/0*	*7/4*	*4.2*	*1.9*	*0.60*	*0.27*	
				C8262 (18-21)	*86N*	*9/5*	*2/0*	*4/4*	*1/0*	*16/9*	*6.3*	*1.5*	*0.83*	*0.19*	

Table 4.4 (continues on next page)

Suite	Strat	ID	Unit	Samples	$\lvert inc \rvert$	N/n_{th}	N/n_{mw}	N/n_{wl}	N/n_{s}	N/n_{PI}	PI	σ	VDM	σ	Q_{PI}
		C4596	flow 1	C4596 (05-19)	81	14/9	4/0	0/0	11/0	29/9	3.2	0.8	0.43	0.11	7
				C4596 (01-04)	*38N*	*2/0*	*2/0*	*3/0*	*2/0*	*9/0*					
				C4596 (05-12)	*-85R*	*9/7*	*4/0*	*0/0*	*6/0*	*19/7*	*3.4*	*0.8*	*0.45*	*0.10*	
				C4596 (13-19)	*77N*	*5/2*	*0/0*	*0/0*	*5/0*	*10/2*	*2.6*	*0.8*	*0.36*	*0.12*	
Babyne	V1bb	CK3	flow 5	CK3 (22-27)	-81.5	7/1	2/0	4/4	1/0	14/5	5.8	2.6	0.77	0.35	7
		CK3	flow 6	CK3 (28-29)	-76	5/1	3/0	2/2	2/0	12/3	3.1	1.8	0.44	0.25	7
		CK3	flow 7	CK3 (30-32)	86	2/0	2/0	3/3	3/0	10/3	6.7	3.5	0.87	0.46	6
		C4596	flow 2	C4596 (20-25)	77.5	7/2	0/0	0/0	6/0	13/2	2.3	0.6	0.31	0.09	6
				C4596 (20-22)	*-78R*	*4/1*	*0/0*	*0/0*	*3/0*	*7/1*	*1.8*	*0.25*	*0.00*		
				C4596 (23-25)	*77N*	*3/1*	*0/0*	*0/0*	*3/0*	*6/1*	*2.7*	*0.37*	*0.00*		
Zabolottya	V1zb	C4594		C4594 (01-08)	77.5	16/8	2/0	9/8	2/0	29/16	2.4	0.8	0.33	0.11	7
				C4594 (01-06)	*86N*	*13/7*	*2/0*	*5/5*	*2/0*	*22/12*	*2.3*	*0.8*	*0.30*	*0.10*	
				C4594 (07-08)	*-69R*	*3/1*	*0/0*	*2/2*	*0/0*	*5/3*	*2.8*	*1.1*	*0.43*	*0.17*	
				C4594 (09-10)	*80N*	*0/0*	*0/0*	*2/1*	*0/0*	*2/1*	*2.1*		*0.28*	*0.00*	
		C8265		C8265 (01-10)	86.9	18/10	4/2	8/7	5/0	35/19	5.2	2.9	0.67	0.38	7

TABLE 4.4: Palaeointenstiy results: suite, strat, ID: core/quarry, flow number, samples, Inc: absolute inclinations of unit flows following classification in Figure 4.1; N/n: number of attempted/successful palaeointensity experiments (TH: thermal Thellier, MW: microwave Thellier, Wl: Wilson, S: DHT-Shaw, PI: all methods); PI, Stdev: unweighted average and standard deviation of palaeointensity results in µT, VDM: virtual dipole moment [$\times 10^{22} Am^2$], Q_{PI} score (Biggin & Paterson, 2014). Italic values show inclinations, experiment numbers and field strengths in case of dual polarity directions within the same unit.

4.6 Discussion

In this study, we present new palaeomagnetic directions and palaeointensities from the Ratne, Luchichiv, Babyne, and Zabolottya suites of the Volyn series. Directional analysis of oriented samples from the Policy-2 and Rafalovka quarries for the Luchichiv suite as well as from the Berestovets and Bazaltovoe quarries for the Ratne suite produced new palaeomagnetic directions. Combining the new data (Table 4.2) of the basalt flows (RA-2 and RA-3) as well as the baked tuff (Rat2-3) from the Policy-2 quarry, we get a mean palaeomagnetic direction of Dec = 29.3°, Inc = -66.4°, α_{95} = 21.9°, which is very close to the mean palaeomagnetic direction of Dec = 25.9°, Inc = -67.2°, α_{95} = 22.8°, reported in Shcherbakova et al. (2020). New directions of the Rafalovka quarry from flows RA-1a (Dec = 293.2°, Inc = 82.1°, α_{95} = 4.8°) and RA-1b (Dec = 278.2°, Inc = -67.2°, α_{95} = 9.8°) correspond well to the direction presented in Shcherbakova et al. (2020). Thus, these new directions do not significantly change the palaeomagnetic poles presented in Shcherbakova et al. (2020) which are now calculated as 24.25°N, 9.62°E, A_{95} = 33.65° (Policy-2/Velikiy Midsk, 561 ± 13 Ma) and 44.8°N, 342°E, A_{95} = 9.2° (Rafalovka, 580 ± 9 Ma).

The studied sections in the quarries of Berestovets and Bazaltovoe, correspond to sites 3 and 4 and the components B1 and B2 in Elming et al. (2007), respectively. Palaeomagnetic poles including our presented directions are 31.3 °N, 102.3°E, A_{95}: 5.6° for Berestovets and 28.5°N, 99.5°E, A95: 10.1° for Bazaltovoe (Table 4.3). Exact ages for these two palaeomagnetic poles are unknown. Elming et al. (2007) constrained the age to 545 - 580 Ma, using their 40Ar/39Ar plateau age of 585 ± 7 Ma and a K/Ar age of 545.5 Ma (Savchenko et al., 1984). U-Pb zircon ages for rhyolitic dacites and basalts of the Ratne suite are 567 ± 11 Ma and 569 ± 12 Ma, respectively (Poprawa et al., 2020). The stratigraphy of the Volyn series further constrains this age to be younger than the highest studied sections of the Luchichiv suite at Policy-2 (561 ± 13Ma).

The good agreement of our directions with previously published data is an argument for a thermal origin of the magnetisation, which is critical for the reliability of palaeointensity experiments. This is supported by baked contact tests in the core CK-3 (Figure 4.3f) and the Rafalovka quarry (Shcherbakova et al., 2020) as well as by the presence of high temperature exsolution structures seen in electron microscopy images (Figure 4.6a and Figure 6 a,b in Shcherbakova et al., 2020). However, shrinkage cracks that were also seen in SEM images (Figure 4.6b and Figure 6c in Shcherbakova et al., 2020) point to low temperature oxidation events. Strong-field thermomagnetic curves of the drill core samples and the quarry samples from the associated Luchichiv and Zabolottya suites show only minor low temperature oxidations. This is further

supported by the similarity of NRM and TRM curves measured during Wilson experiments and we believe that palaeointensities from these rocks are reliable. In contrast, reliability of the high titanium basalts from quarries of the Ratne suite, with irreversible thermomagnetic curves and temperature dependent susceptibilities is questionable but palaeointensities from these rocks were already rejected during analysis of the experiments.

The virtual dipole moments of 0.31 - 1.67 $\times 10^{22}$ Am^2 measured in the profiles agree well with published time averaged field strengths of units with a similar age from Laurentia (0.7 $\times 10^{22}$ Am^2; Bono et al., 2019), supporting a global distribution of a weak field as reported in Shcherbakova et al. (2020). Spot readings of palaeointensities both earlier and later in the Ediacaran are similar as well (Figure 4.8) with dipole moments of 0.3 - 0.8 $\times 10^{22}$ Am^2 at 600 - 585 Ma (Thallner et al., 2021a) and 0.6 - 2.2 $\times 10^{22}$ Am^2 at 550 Ma (Thallner et al., 2021b). The possibility of these spot readings sampling reversals and/or transitional fields and therefore missing stronger fields between reversals has been an issue that casted doubt on the extent of the weak field in the Ediacaran (Thallner et al., 2021a). The profiles of absolute palaeointensities presented in this study give a better sampling density and allow to assess field strengths along a polarity profile (Figure 4.4).

As expected, measured palaeointensities in profile sections, where shallow inclinations or polarity changes point to transitional fields or reversals, are always low, as seen e.g., in the top two basalt flows of the Yakushiv beds in core CK3 (Figure 4.4) or the bottom of core C4594, with intensity values rarely exceeding 5 µT ($\sim$0.6 - 0.7 $\times 10^{22}$ Am^2). Profile sections with steep inclinations and no indications of transitional fields can show stronger intensities of $\sim$10 µT ($\sim$1.5 $\times 10^{22}$ Am^2) as in the lower Yakushiv beds and the top of the Babyne suite in core CK3. This is not seen in all sections of the profile. In core C8265, the basalts showing only steep positive inclinations result in palaeointensities as low as those in the transitional sections. In the units from the Rafalovka/Policy-2 quarries, the palaeointensities of flows with reverse polarity (RA-2 and RA-3) are approximately twice as high as in the flow with normal polarity (RA-1) – a feature that is not seen in any of the core sections. A probable explanation would be that RA1 recorded a point of weak field leading up to a reversal, whereas the intensity, recorded in the other flows represent a field, where the strength had already recovered. It should however be noted that these 'high' palaeointensities are still almost an order of magnitude weaker than the present-day field.

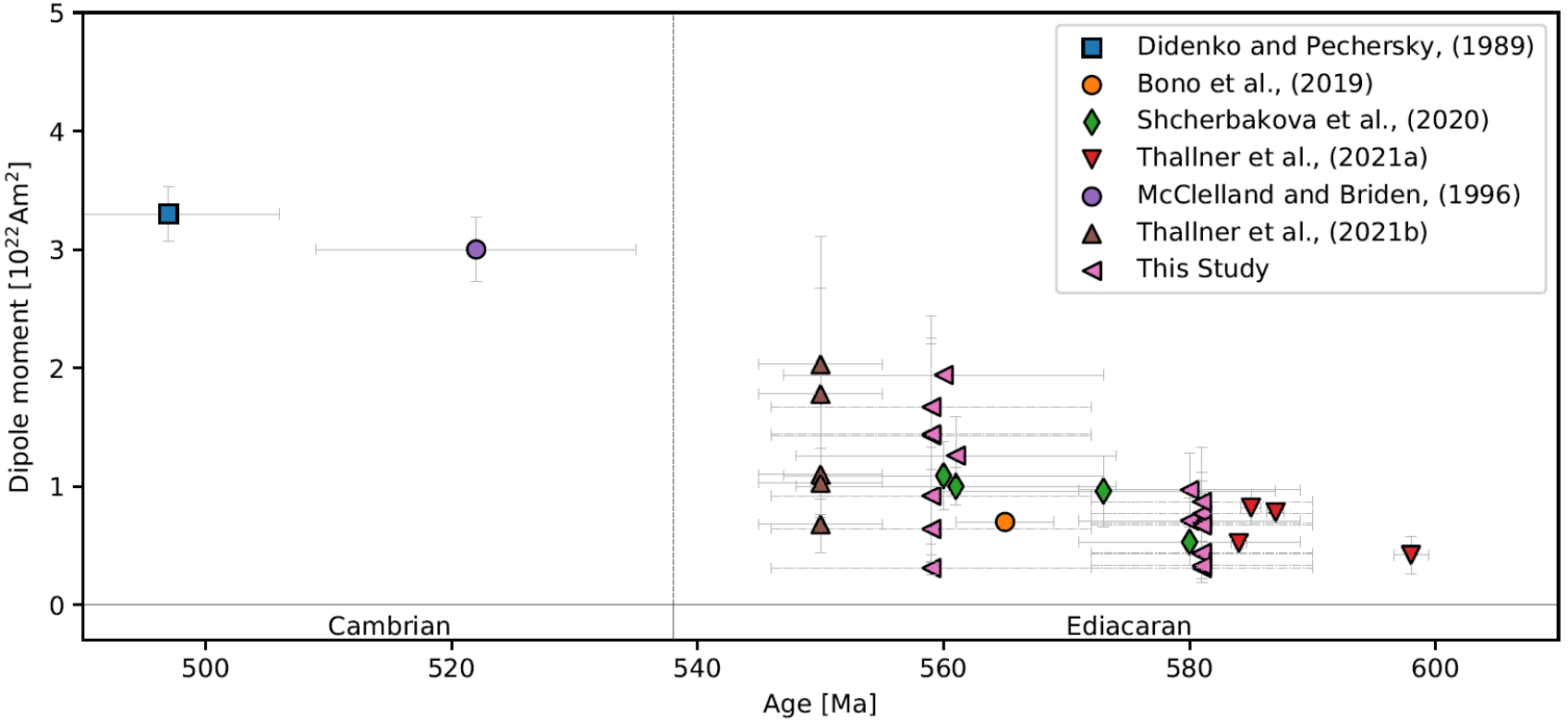

FIGURE 4.8: Virtual and palaeomagnetic dipole moments of the Ediacaran and Cambrian. Error bars show one standard deviation for dipole moments and standard errors for ages. Dashed error bars represent age errors estimated from the average age uncertainties of the dated flows. Plotted are all sites with n $\geq$ 3 intensity determinations. Estimates of this study are plotted according to their stratigraphic relations to the results from Shcherbakova et al. (2020).

This may be a hint that the field strength never fully recovered between reversals and a stable dipole field configuration was never reached before the field reversed again – a scenario that is not implausible in a time where reversal frequencies of up to and maybe even exceeding 20 reversals/Myr are reported (Bazhenov et al., 2016; Levashova et al., 2021). To get a better understanding of this, one would not necessarily need absolute palaeointensities. A comprehensive study of relative palaeointensities would however require a more complete profile section that was available from the cores in this study. The relative palaeointensity estimates that are available from the pseudo-Thellier analysis of the combined pseudo-Thellier-DHT-Shaw experiments in this study are difficult to be trusted, as relative intensity differences of almost 400% within the same unit flow (Supplementary Table C.6) suggest that these experiments did not work for these rocks.

Looking at virtual dipole moments on a longer timescale (Figure 4.8), the intensity differences between transitional and (seemingly) non-transitional fields are less striking than the change in field strength with time. While the ages of most of the core sections are not entirely clear, plotting their intensities according to their stratigraphic constraints in relation to the results published in Shcherbakova et al. (2020) shows that the field strength recorded in the Volyn traps remarkably follows the trend set by the palaeointensities from the Laurentian Grenville dykes and the Skinner Cove formation, and seem to confirm a rising field strength towards the end of the Ediacaran. This is consistent with an increase of field strength at the onset of inner core nucleation, as predicted from geodynamo models (Driscoll, 2016). It also fits within the framework of a possible ~200 Myr cyclicity of strong and weak fields (Biggin et al., 2012; Hawkins et al., 2021; Meert et al., 2016) with field strengths in the Devonian similar to the ones in the Ediacaran (Hawkins et al., 2019; Shcherbakova et al., 2017) and another weak field in the Jurassic compared to the stronger present-day field (Kulakov et al., 2019). The exact causes of such a cycle and an answer to the question if it was started by the onset of inner core nucleation at the end of the Ediacaran as suggested by Bono et al. (2019) will not be found without a better data coverage of the Precambrian.

4.7 Conclusion

We present palaeodirectional and palaeointensity data for the longest and most complete profile section of the Volyn Basaltic province to date. New palaeomagnetic directions from oriented samples were measured and show good agreement with previously published data, supporting the established complex apparent polar wander path of Baltica. Polarity changes from inclinations throughout the sections from core samples reveal at least 6 reversals recorded in the Volyn traps. Palaeointensities from

multimethod palaeointensity determinations result in weak virtual dipole moments between 0.31 ± 0.11 $\times 10^{22}$ Am^2 and 1.67 ± 0.78 $\times 10^{22}$ Am^2 (site mean ± 1 σ, N > 1).

Throughout the profile, the field strength shows minimum values where the directions suggest that the recorded field was transitional and/or close to a reversal. Between these points however, the field strength never fully recovers, suggesting that the field was in a continuous transition-like state. In comparison to previously published intensity estimates from Baltica and Laurentia, the new palaeointensities agree with the time averaged field strength from the Sept-Îles (Bono et al., 2019), but also seem to support a rising field strength towards the end of the Ediacaran as suggested by the higher intensities of the Skinner Cove formation (Thallner et al., 2021b). On the other side, following the seemingly continuous decrease of field strength, seen in all Ediacaran intensity data, the time period between 600 Ma and 650 Ma offers itself as a prime target for future palaeointensity studies.

Chapter 5

Characterisation of the Ediacaran geomagnetic field

5.1 Introduction

The geomagnetic field, generated in Earth's core and shielding the planet from solar winds in space, links internal and external processes throughout Earth's history. The contributions of the geomagnetic field observed on the surface of the Earth are mainly determined by its internal sources and spatial and temporal variations of this internally generated field can provide valuable insight into the magnetohydrodynamic processes of the outer core and the interactions between inner core, outer core, and mantle at their respective boundaries (Aubert et al., 2013; Johnson & McFadden, 2015; Olson et al., 2013; Sprain et al., 2019).

The timescale and a possible cyclicity of some of these variations, such as variations in VGP dispersion, reversal frequency and field strength, show similarities to the cycles of convective overturn in the mantle (Biggin et al., 2012; McFadden et al., 1991). This has led to the hypothesis that long-term secular variation could be driven by such deep Earth processes and therefore store information about deep Earth evolution through geologic time. Following this, numerical geodynamo simulations are a useful tool to study Earth evolution by tying variations of the geomagnetic field to predictions of deep Earth processes. Although numerical geodynamo simulations are continuously improving in capturing features of the geomagnetic fields (see Sprain et al., 2019 and references therein), they are still limited by computational power (or lack thereof), making it difficult to determine how 'Earth-like' given simulations are, especially if their non-dimensional Ekman and Prandtl numbers differ by several orders of magnitude from the geophysical values for Earth (Aubert et al., 2010). The quality of a numerical geodynamo simulation is generally determined by its ability to produce an 'Earth-like' geomagnetic field (e.g., Christensen et al., 2010), which may be assessed

by the Quality of Paleomagnetic Modeling (Q_{PM}) criteria (Sprain et al., 2019) that calculate a non-parametric misfit score between simulated data and measured data and assign a total Q_{PM} score to the model (see section 1.5.3). In Sprain et al. (2019), the 'Earth-like' geomagnetic field was defined by the time-averaged field of the last 10 million years that captures a representative variability of field behaviour in time scales of > 10^5 - 10^7 years and is well constrained by measurement data (Bono et al., 2021; Cromwell et al., 2018; Ogg, 2012). Statistically, the time-averaged geomagnetic field is defined by the angular dispersion of VGPs as a function of latitude (approximated by the phenomenological model G parameters a and b, (McFadden et al., 1988), the deviation of directions from a GAD field (given by the inclination anomaly; Johnson et al., 2008; Tauxe and Kent, 2004), the variance of virtual dipole moments, and the reversal frequency. Constraining the long-term geomagnetic field behaviour through geologic time becomes increasingly difficult towards older time periods as both quantity and quality of palaeomagnetic data decrease. To date, reasonable characterisations for geomagnetic field behaviour are given in recent studies for the last 10 Ma (Bono et al., 2021; Cromwell et al., 2018), for the Cretaceous Normal Superchron (CNS, 84 - 126 Ma) and Early-Cretaceous-Jurassic interval (pre-CNS, 126 - 198 Ma; Biggin et al., 2008; Doubrovine et al., 2019; Kulakov et al., 2019), the Permian-Carboniferous Reversed Superchron (de Oliveira et al., 2018), and the Precambrian between 0.5 and 3 Ga (Smirnov et al., 2011; Veikkolainen & Pesonen, 2014). No attempts have been made to characterise the field of the Ediacaran period, as both coverage and quality of palaeomagnetic data in the Ediacaran were thought to provide little hope of success.

The extremely weak Ediacaran palaeointensities in Bono et al. (2019) and chapters 2 - 4 were interpreted as possible signal of the onset of inner core nucleation at the end of the Ediacaran. Such a young inner core age would, however, require a high thermal conductivity of the core. This would impede thermal convection in the core prior to inner core nucleation, and a working geodynamo, capable of generating a geomagnetic field for billions of years (Biggin et al., 2011; Tarduno et al., 2015) without the additional forces of compositional convection could be difficult to maintain (O'Rourke et al., 2017; Pozzo et al., 2012). A possible source of additional power could come from the precipitation of light elements in the core (Badro et al., 2016; O'Rourke et al., 2017). Models of core evolution suggest that MgO, which can dissolve into the iron melt of the core at temperature levels that are reached during giant impacts (e.g., Moon-forming impact; Badro et al., 2016; O'Rourke et al., 2017), could have provided compositional convection sufficient to power the early geodynamo. The decreasing strength of the geomagnetic field in the time leading up to the ICN could then be explained by a decrease in convection due to the reduced temperature and the associated reduced dissolution of MgO (Badro et al., 2016). However, the system might be more

complex due to additional precipitation of SiO and FeO in the core that would also be capable of driving the early geodynamo (Mittal et al., 2020). The resulting large uncertainties for parameters in thermal evolution models still lead to a wide range of possible timings of inner core formation between 400 Ma and 1.0 Ga (Davies et al., 2021). This shows the importance of finding the palaeomagnetic signature of ICN. How this signature would look like, is not entirely clear, however. Many numerical geodynamo models predict a decrease in field strength leading up to ICN and a jump in intensity after the core formation due to the added power supply from compositional convection (Aubert et al., 2009; Driscoll, 2016). Other numerical geodynamo simulations, linked to the thermo-chemical evolution of the core suggest that the ICN would show little impact on the surface field strength due to a strong dipolar early (Landeau et al., 2017). A bistability in these models would, however, also allows for a multipolar and weak field state before the formation of the inner core (Landeau et al., 2017). A long term trend of decreasing field strength in the Precambrian from palaeointensity data was suggested by Bono et al. (2019), using only palaeointensities from slow-cooled units. Some intensity estimates from fast cooled units agree with this trend (Lloyd et al., 2021a), whereas other studies present palaeointensities similar to the present day field (Sprain et al., 2018). Better constraints on the long-term behaviour of the geomagnetic field in the Precambrian will depend on an improved distribution of palaeomagnetic and palaeointensity data.

The previous chapters were a large step towards eliminating data gaps in the palaeomagnetic record and have dealt with the determination of the strength of the geomagnetic field in the Ediacaran. The results from these chapters were used to make assumptions about the state of the field at that time. However, there are several factors that complicate a characterisation of the field from its strength alone:

Factor 1, data coverage:

Palaeointensities severely under-sample the Ediacaran both in time and space. As mentioned in the previous chapters, other than the Sept-Îles data point (Bono et al., 2019), all VDMs are spot readings of the field that have little significance for the state of the geodynamo on their own and only provide significant information about the field through their quantity and their good agreement. However, with the exception of one of the Grenville Dykes at 598 Ma (Chapter 2), all published and measured palaeointensities are from cooling units with ages between 550 and 590 Ma (see Figure 4.8). For the 100 million years of the Ediacaran, ten million years are only represented by a single data point, while for 50 million years – half of the Ediacaran – no field strength estimates exist at all. A field characterisation from palaeointensities would therefore only apply for the second half of the Ediacaran. Palaeogeographic reconstructions for

the time between ∼580 and 540 Ma (Li et al., 2013; McCausland et al., 2011; Meert & Lieberman, 2004; Robert et al., 2021) come with slight differences due to the ambiguous apparent polar wander paths, but generally place all continents on the same hemisphere of the planet. All available palaeointensities only cover Laurentia and Baltica, but due to the range of ages, they (apparently) sample the field at a range of latitudes. Nevertheless, even with good sampling coverage over all continents, the data will always be constrained to one hemisphere and any asymmetries of the field morphology could be difficult to see.

Factor 2, reliability of intensity estimates:

The reliability of the measured weak intensities can (and will) be questioned. Historically, underestimates of the field have been attributed to MD behaviour of the rocks (Smirnov et al., 2017). This topic has been discussed in each of the previous chapters and while it is impossible to achieve absolute certainty that MD behaviour does not influence the results, all steps have been taken to ensure that no biased intensity estimates were accepted (see discussions in Chapters 2 - 4). Another issue might be the more recently introduced theory of fragile magnetisation (Tauxe et al., 2020), where experimental results from 'aging' experiments on lava samples have demonstrated that rocks can lose the stored information of the magnetic field over timescales of several years. These 'aging effects' lead to changes in the blocking and unblocking spectra, resulting in curved plots that, if undetected, lead to severely underestimated field strengths. Tauxe et al. (2020) suggest, that the use of additivity checks (Krása et al., 2003) and a curvature criterion (Paterson, 2011) might help to detect these aging processes in Arai plots. The curvature criterion has been used in intensity analysis in this thesis, but rather than the quantification of curvature of the whole temperature range (k), we used the curvature of the best-fit line (k'), because the distinct two slopes from two NRM components with different intensities made the use of k impossible. In addition, the definition of a 'straight' line in Tauxe et al. (2020) of $k \leq 0.164$ differs from the definition ($k' \leq 0.48$ in Chapters 2 and 3, and $k' \leq 0.27$ in Chapter 4) in this thesis and all other studies of Ediacaran palaeointensities, since criteria used for palaeointensities of laboratory-induced TRMs are not very practical to use for palaeointensities from ancient TRMs. The theory of fragile magnetisations is still very new, and experimental data have so far only been obtained for magnetite grains as carriers. The majority of palaeointensities presented here are carried by titanomagnetite grains of different shapes and sizes, and neither a theoretical framework nor experimental data exist to show the extent of influence caused by aging for these carriers. Until simulated rock and palaeomagnetic experiments using micromagnetic models provide a better understanding of fragile magnetisation, we can only acknowledge

that this may be an issue and treat our intensity data as reliable estimates for the time being.

The robustness of palaeointensities is supported by the fact that fundamentally different methods of palaeointensity determination lead to agreeing field strength estimates in chapters 2 - 4. However, differences can be seen between methods regarding the numbers of accepted results. In chapters 2 and 3, microwave Thellier experiments produced a much larger number of accepted results than thermal Thellier experiments. This difference cannot easily be explained by different responses of the magnetic carriers to the two demagnetisation methods, if microwave and thermal demagnetisations are equivalent (see section 1.4.2). A likely is a sampling bias due to the low number of available sample material. Microwave Thellier experiments required only a fraction of the sample material that a thermal experiment needed. Because of that, only one or two samples per site were available for thermal Thellier experiments whereas microwave Thellier experiments could be performed on > 10 specimens per site. This allowed for more microwave experiments to be done on sites that showed promising rock magnetic and intensity results, which improved the success rates of microwave experiments.

The high Q_{PI} scores that were achieved for all field strength estimates in this thesis point to a high reliability of results. Q_{PI} scores were assigned in a non-prioritised fashion (see 1.4.7). This assures that the best practice guidelines for palaeointensity experiments were followed, which have repeatedly demonstrated in historical data to provide intensity estimates that represent the recorded field (e.g., Schnepp et al., 2020a; Suttie et al., 2011).

Factor 3, intensity and directional behaviour are not independent

As with every vector field, information about the intensity on its own cannot characterise the field without directional information. This is especially the case for a dataset consisting of spot readings of the field. In theory, all the weak intensity values could sample transitional fields/reversals in an otherwise strong field. From the amount of available data, it would be highly unlikely, that all units cooled during a reversal, but the published high reversal frequencies ($\geq$ 20 Myr^{-1}) for the mid- and late Ediacaran (Bazhenov et al., 2016; Levashova et al., 2021) imply that it is not impossible. With such high reversal frequencies, it would also be possible, that the field strength never fully recovered after a reversal and the field stayed in a transitional state between reversals. In the previous chapters, this was assumed from the inverse relationship between field strength and reversal frequencies, as predicted from geodynamo simulations, and seen in long-term variation of palaeomagnetic data (Aubert et al., 2010;

Biggin et al., 2012; Sprain et al., 2019; Tarduno & Cottrell, 2005).

The variability of the geomagnetic field is usually described by the dispersion of virtual geomagnetic poles (VGPs) or palaeomagnetic directions (see section 1.5.1). In this chapter, we analyse directional palaeosecular variation in the Ediacaran to obtain a statistical description of the Ediacaran field behaviour. Solutions of numerical dynamo simulations can then be compared to statistical characteristics of the Ediacaran field, to find a simulation that produces a similar field behaviour. Such a simulation could then give valuable information about the deep Earth properties and the state of the geodynamo that led to the anomalous Ediacaran field.

5.2 Sources of data

The Paleomagia database (Veikkolainen et al., 2014b) was used as basis for the collection of data. Excluding all entries from sediments and metamorphic rocks that average out PSV, the search for igneous rocks with ages between 540 Ma and 650 Ma led to a collection of 129 database entries. A similar search on the MagIC database did not reveal any studies with relevant data that were not already included in the Paleomagia database. Broadly following the approaches taken in Veikkolainen and Pesonen (2014), Cromwell et al. (2018) and Doubrovine et al. (2019), database entries that did not meet a set of minimum criteria were excluded as not relevant for this study.

The primary criteria to exclude irrelevant data were:

1. Publication of data: The data must be published in a peer-reviewed journal with an assigned DOI and report site-level directional data with statistical estimates of k and/or α_{95} for either specimen-mean or sample-mean data. There was no requirement for raw measurement data to be supplied as supplementary data but information about the applied demagnetisation methods had to be given.

2. Data quality: The 129 database entries list data from 63 studies that were published between 1959 and 2018. An expected inverse correlation of data quality and age of publication is subtle and rather subjective. An objective estimate of data quality is provided in the Paleomagia database by listing the modified Van der Voo criteria (MV; Van der Voo, 1990; Veikkolainen et al., 2014a). In order to exclude low-quality data, we required each data entry to have an MV ≥ 3.

3. Primary magnetisation and cooling time: Only data from fast-cooled rocks were used in this study. All directions from slow-cooled units, where authors claim that PSV had been averaged out, were not used. In addition, all studies where a

remagnetisation was suspected, were excluded. Evidence for primary magnetisation from field tests was preferred, but not required.

4. Number of sites: In modern PSV studies, a minimum number of sites (N) ≥ 9 is required for the calculation of robust VGP dispersion estimates (Biggin et al., 2008). In this first round of data filtering, we have removed all database entries of data from less than five sites.

After application of these primary filters, and removal of data that were listed in multiple entries, a total of 41 database entries were remaining, that can be divided into three quality groups based on their number of sites:

Group C: this group accounts for 18 datasets that should not be used for analysis of palaeosecular variation, as they are either from a low ($5 \leq N \leq 9$) number of sites, include directions calculated from great circles, or represent groups of VGPs that have been determined through nonstandard approaches to data analysis. This includes all data from studies, where palaeomagnetic poles were found by dividing scattered data on stereoplots into seemingly arbitrary subgroups (Piper, 1981), or the discrimination between site-data and locality-data is difficult when data from multiple studies were averaged (e.g., Elming et al., 2007; Shcherbakova et al., 2020). The averaging of directional data from multiple studies is the current standard of analysing palaeopoles for Eastern European and Russian localities (see data in Chapter 4). In some cases, this can make a pole position more robust. However, the dispersion of VGPs can often not be calculated for these geomagnetic poles because the raw measurement data before averaging is mostly not accessible.

Group B: the intermediate quality class comprises 16 datasets with $N \geq 9$ sites that were published without giving estimates of VGP dispersion, like the Sierra de las Animas complex (578 Ma; Rapalini et al., 2015), and/or have not been included in the PSV study of Veikkolainen and Pesonen (2014) because of a low number of samples, tilt-corrected site directions, age uncertainties or unknown reasons. Datasets in this category can contain a wide range of data quality with some low-quality site-level data. Additional criteria to filter out these sites will be discussed below.

Group A: the highest quality group comprises 7 datasets that have the same minimum number of sites as Group B datasets ($N \geq 9$). In contrast to Group B datasets, the datasets of Group A all have published VGP dispersion values. For their analysis of Precambrian secular variation, Veikkolainen and Pesonen (2014) already analysed the entries in the Palaeomagia database from studies published before the year 2014. In their study, dispersion values were calculated for the two Ediacaran datasets that passed their selection criteria. These two low-latitude localities were the Dokhan volcanic formation (596 Ma; Nairn et al., 1987) and the Skinner Cove formation (551

Ma; McCausland and Hodych, 1998), reporting between-site dispersion values of S_b = 12.5° and Sb = 13.5°, respectively. No other dispersion values from Ediacaran data had been published in any publication before 2014. Since then, new directional data and associated dispersion values have been added to the database from the Grenville Dykes (580 - 598 Ma; Halls et al., 2015), and the Moroccan Quarzazate and Taroudannt groups (536 - 562 Ma; Robert et al., 2017). For the Grenville Dykes, two between-site dispersion values of S_b = 18.5° and S_b = 19.0° have been reported for the steep and shallow directional groups in Thallner et al. (2021a). Robert et al. (2017) calculated three dispersion values for the Quarzazate and Taroudannt group (Fajjoud-Tadoughast formation: S = 31.1°; Djebel Boho formation: S = 30.9°; Adrar-n-Takoucht formation: S = 23.9°), but did not correct for within-site scatter. It should be noted that the data of the Djebel Boho formation is not included in the Palaeomagia database because the mean age of 536 Ma is just outside of the Ediacaran. It will however be included in this study. In contrast, the published VGP dispersion of S = 26° from single crystal experiments from one site of the Sept-Îles complex (Bono et al., 2019) will not be included, because no within-site scatter correction can be applied to the single crystal directions.

Despite a low number of high-quality data, the collection shows a decent distribution over latitudes between 0° and 60°. For a statistical assessment of PSV dispersions and their latitude dependence in directional and polar space, we use fits of model A (Irving & Ward, 1964) and model G (McFadden et al., 1988), respectively, so that the secular variation can be quantitatively compared to other time periods. Following Sprain et al. (2019), we use the terms VGPa and VGPb for the model G parameters a and b. Throughout this chapter, we will compare the Ediacaran data to PSV10 (Cromwell et al., 2018), the pre-CNS dataset (Doubrovine et al., 2019) and the PSV of the whole Precambrian (Veikkolainen & Pesonen, 2014).

5.3 VGP dispersion and latitude dependence of published dispersion estimates

In a first step, we calculated the model fits for all published between-site dispersion estimates (Group A). For this, we corrected the reported scatter estimates for within site scatter if it had not been done in the original study (e.g., Robert et al., 2017). The results are shown in Figure 5.1 as mean values and 95% confidence limits. It should be noted that in polar space, the presentation of confidence limits (dashed lines) can be misleading. The typical way, in which the minimum (maximum) uncertainties are depicted in literature, is by plotting the model G function using $VGPa_{min}$ ($VGPa_{max}$) and $VGPb_{min}$ ($VGPb_{max}$) from the bootstrap method (e.g., Tauxe, 2010). The parameters

VGPa and VGPb are not independent, however, and the plots of confidence limit estimates, using the minimum and maximum values from both VGPa and VGPb, overestimate the 95% confidence region (Doubrovine et al., 2019). This is shown by their deviation from the shaded grey area in Figure 5.1, which represents the confidence limits, estimated numerically for each latitude from the bootstrap draws (Doubrovine et al., 2019).

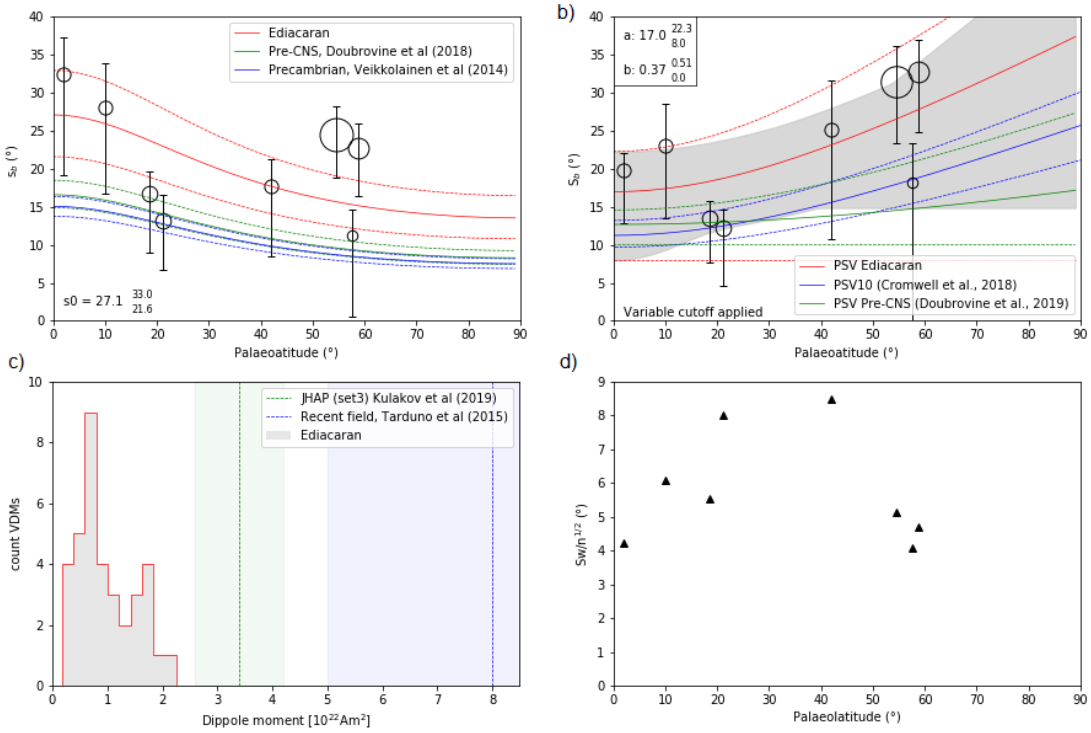

FIGURE 5.1: Model A and model G parameters as well as VDM distribution from published (Group A) data, compared to published values for the Jurassic (green; Doubrovine et al., 2019; Kulakov et al., 2019) and the 'modern' field (blue; Cromwell et al., 2018; Tarduno et al., 2015). (a) latitude dependence of angular dispersion of directions and model A fits; (b) latitude dependence of VGP dispersion and model G fits. Solid lines in (a)-(b) show the model fits to the data, dashed lines give the 95% confidence ranges from bootstrapped minimum (maximum values) of S_0, or VGPa and VGPb. Marker sizes correspond to the number of sites (VGPs) N per geomagnetic pole; error bars show 95% confidence limits of the dispersion estimates. (c) histogram of all published dipole moments of the Ediacaran in comparison to the confidence ranges of the Jurassic (green) and the last 800 kyrs (blue). (d) mean within site scatter, normalised by number of samples, calculated in directional space.

At first glance, the results plotted in Figure 5.1 show an expectedly large uncertainty in both directional and polar space due to the low number of results. Estimates of VGPa and VGPb of 17.0° and 0.51, respectively, are both higher than seen in other time periods, but the complete confidence intervals for the pre-CNS and PSV10 data fall within the Ediacaran confidence range. In directional space, the model A fits for

other time periods are at lower dispersions but outside of the confidence range of the Ediacaran. However, the latitude dependence of Ediacaran angular dispersion data does not follow the model A prediction at all. Looking at Figure 5.1a - b, an argument could be made that the data comprises two groups – one group of low dispersion estimates (Skinner Cove formation, Dokhan volcanics, Grenville Dykes steep), that fall within the confidence range of the model G fit for PSV10, and a second group with the rest of the collection with higher dispersion estimates. However, based on such a low number of data points, this interpretation would be rather speculative. In addition, this collection of Group A data suffers from another major drawback: since there are no standards for minimum numbers of sites, samples per site, and precision parameters, each study that supplied the dispersion estimates used different criteria to filter their data. On top of that, a cutoff for the exclusion of transitional directions was only applied for the data of the Grenville dykes.

5.4 Towards a coherently filtered dataset

To ensure a consistent level of data quality for category A data, and to decide which of the category B data could be included, selection criteria have to be developed and applied. In previous studies, these criteria were defined for each palaeomagnetic pole by minimum values of the precision parameter (k), a minimum number of samples per site (nn), and a minimum number of site-means per dataset (N). The actual numbers differed for each study, with k value criteria ranging from 'any as long as reported' (Veikkolainen & Pesonen, 2014) to strict values such as $k \geq 50$ (Cromwell et al., 2018) and values of nn between $nn \geq 4$ per site (Cromwell et al., 2018) to $nn \geq 30$ per study (Veikkolainen & Pesonen, 2014). For the minimum number of sites per dataset, all recent PSV studies agree on a minimum of N = 9.

With the low number (and quality) of available data, the use of strict criteria would quickly lead to the rejection of all available datasets. Finding a balance between excluding low quality data and retaining a reasonable number of datasets posed an additional challenge. To study the effects of different criteria and their combinations, we filtered Group A and B datasets with increasingly strict criteria for N, nn and k, and calculated their model G fits. For this, we changed the minimum required value of k in 9 steps between 10 and 100 in combination with values of N between 5 and 9 and nn between 1 and 9 (in steps of 3). The resulting model G fits gave values of VGPa in the range of 14 - 22° and VGPb in the range of 0.3 - 0.5. The results of term VGPa roughly showed a linear correlation with the chosen value of k, while the resulting values for VGPb had a high dispersion for all k values. Depending on the choice of N, changes in the criterion nn mostly affected the size of the remaining number of datasets, but

had a lesser effect on the model G parameters than the actual number of remaining datasets. To explore this further, the same range of criteria was applied to all datasets, including the low-quality Group C data.

The effects of different criteria on model G fits to the remaining data is shown in Figure 5.2. Based on these results, a minimum number of sites of N $\geq$ 9 and a maximum within-site scatter of $S_w/\sqrt{nn} > 10°$ was used as criteria to remove unreliable VGPs for the final analysis. This choice was based mainly on the behaviour of VGPa (Figure 5.2a, c), as VGPb did not show systematic changes depending on specific choices of k, nn, and N (Figure 5.2b, d).

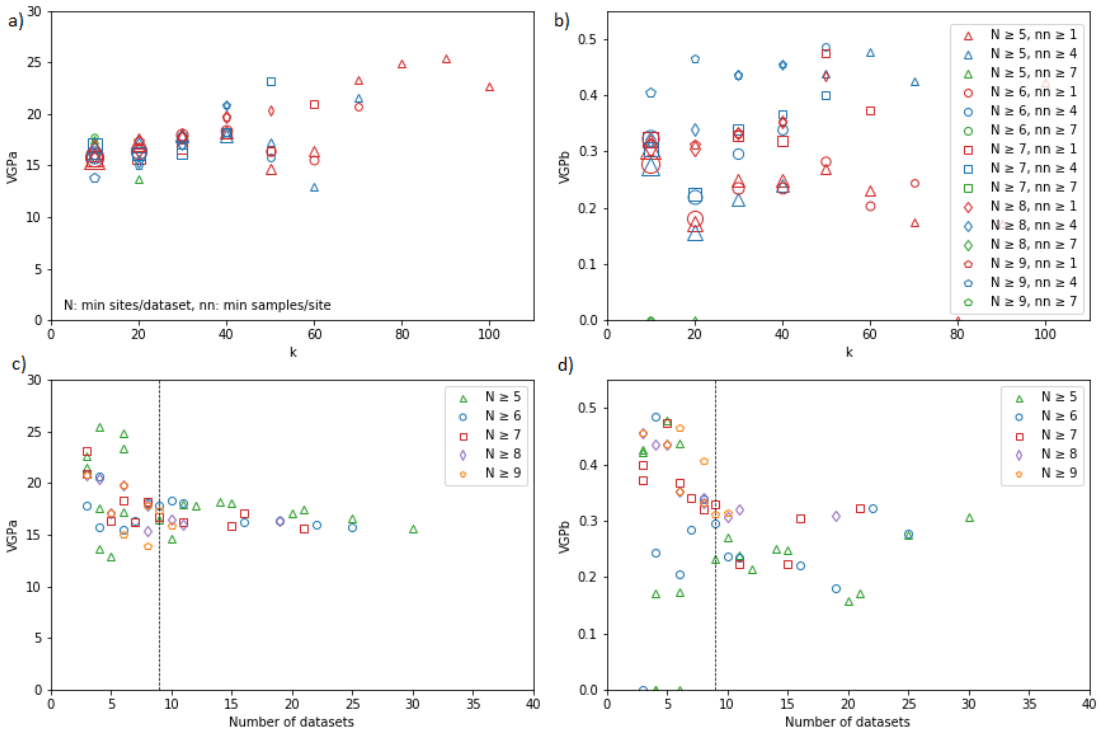

FIGURE 5.2: Influence of data filters on model G fits. (a-b) changes of VGPa and VGPb due to filtering with different precision parameter (k), number of VGPs per geomagnetic pole (N), and number of samples per site (nn); (c-d) changes of VGPa and VGPb showing the data of (a-b) plotted as function of the number of datasets that were used for the model G fits. Different symbols represent the minimum number VGPs per geomagnetic pole.

Estimates of VGPa increased with increasingly strict values of k (Figure 5.2a), which is seen for all choices of N and nn. However, the notion that stricter k criteria progressively filter out lower-quality directions is not entirely true for the full range of k values. At the lower end, the relaxed k criteria allow for sites to be used that, with their enormous within-site scatters, lead to the exclusion of datasets because the between-site dispersion values become negative after correction for S_w, and these datasets are

automatically excluded as unreliable. Although somewhat counterintuitive, decreasing the minimum required k actually leads to the exclusion of some of the lowest-quality data. Therefore, resulting estimates of VGPa remain fairly constant for datasets filtered by $k \leq 60$ at VGPa = 17.1 ± 1.9°. Using datasets filtered by larger values of k results in higher VGPa estimates (23.1 ± 1.9°), but these results are based on fits to less than nine remaining datasets. For such low numbers of included datasets, the range of resulting model G parameters increases substantially for both VGPa (Figure 5.2c) and VGPb (Figure 5.2d). No major systematic dependence on the choice of k and nn can be seen for datasets with $k \leq 60$, but a specific choice of criteria can still influence the results (e.g., VGPa at k = 50 in Figure 5.2a). However, constraining the site-level quality with the definition of minimum values for k and nn seems less important if the impact of low-quality directions can be removed by the within site correction.

Doubrovine et al. (2019) explored the influence of the mean within-site dispersion on corrections of between-site scatter for datasets of directions drawn from Fisher distributions with values of $k = (180/\pi)^2 * 2nn/s_w^2$ for the range of $0° \leq s_w/\sqrt{nn} \leq 10$. They found a small positive bias, introduced by s_w, that increases with increasing within-site noise. Their results showed that this bias was smaller than 0.5° for $s_w/\sqrt{nn} \leq 10°$ and less than 0.2° for $s_w/\sqrt{nn} \leq 5°$. Following these results, instead of defining specific criteria for k and nn, we use a limit for the within-site dispersion and exclude all sites from datasets with $s_w/\sqrt{nn} > 10°$. For a site with nn = 4 samples, that would be equivalent to $k \geq \sim 16.5$, which seems rather low, but represents a compromise between not biasing the estimates of Sb, and retaining datasets with $N \geq 9$ sites from some of the published data (with median k = 27) for analysis. To avoid the introduction of artefacts from the conversion to polar space (Cox, 1970; Doubrovine et al., 2019), this criterion was calculated and applied in directional space.

Significant changes of the reliability of results can be introduced through changes in the minimum number of included sites per dataset. Biggin et al. (2008) showed that the dispersion uncertainty limits from datasets with N < 18 are unreliable. For the Ediacaran, only 3 usable datasets with N > 18 are available in the Paleomagia database and therefore datasets with N < 18 sites have to be included. As minimum requirement, we will use the current standard of $N \geq 9$ (Cromwell et al., 2018; Doubrovine et al., 2019). Datasets with N < 9 (Group C) will be shown, but not included in the calculation of latitude dependence of dispersion.

5.5 Treatment of outliers

Values of S_b are heavily influenced by outliers from transitional directions. The established way of determining palaeosecular variation is to exclude this data and focus on

the VGP dispersion of 'normal' secular variation of a stable field, using only the data between field reversals or excursions. There is of course no universally accepted way of removing such outliers. Assuming that the majority of VGPs cluster in a Fisherian (Fisher, 1953) distribution (or reasonably close to one) around a mean pole, whereas outlier VGPs are much further away from the mean, the technical approach of removing outliers is realised by the introduction of a maximum threshold of angular deviation – a cutoff angle – to select datapoints that should be removed from the dataset (see section 1.5.1). Such a cutoff angle is either defined by an arbitrary fixed value, or found by an iterative process (Vandamme, 1994). Both approaches come with drawbacks and PSV studies often use both (e.g., Biggin et al., 2008; Doubrovine et al., 2019), or neither if the authors are certain that their primary selection criteria have already removed outliers, and the application of any cutoff value would systematically bias the results to lower dispersions (e.g., Veikkolainen and Pesonen, 2014). For the analysis of PSV from geodynamo simulation outputs, the application of a variable cutoff was shown to be highly effective, and led to a clear power law relationship between VGPa and the degree of axial dipole dominance over the remaining non-axial dipole (Biggin et al., 2020).

One of the main drawbacks of using a fixed cutoff angle is that there is no universally accepted angle that can be used to define transitional data, making it a subjective selection process. In presumably non-uniformitarian fields, using a fixed cutoff value can lead to extreme cases, where randomly distributed VGPs (that can pass a conglomerate test) are forced to resemble a bimodal distribution of a 'normal' dipolar field (van der Boon et al., n.d.). A variable cutoff is less prone to selecting outlier VGPs subjectively, but it was formulated on the assumption that the distribution of VGPs is Fisherian, and transitional datapoints are outside of this distribution. If this is the case, the iterative process is very effective in selecting outliers. However, if the outliers are numerous and/or in extreme angles from the mean pole, then the search for an optimum cutoff angle can fail, if the initial guess of dispersion/cutoff is larger than the maximum Δ_i of the outliers and the iterative process never starts. Additional issues can be introduced if a dataset comprises VGPs with extreme values of ${S_w}^2/n > \Delta_i^2$. If such a VGP (and its negative contribution to S_b) is removed as outlier, then the cutoff angle increases and the iterative process is stopped.

From the weak intensity results in chapters 2 - 4 and the notoriously anomalous directional data in the Ediacaran, it seems likely that the fraction of transitional data points will be high, and the use of a fixed cutoff may influence the outcome of this study. In this chapter, we apply all three cutoff approaches, but only use datasets, where outliers were removed by a variable cutoff for our final PSV estimates. Results from datasets treated with a 45° fixed cutoff angle as well as results from datasets without any cutoff

will be shown for comparison. To mitigate the issues with a variable cutoff that can be caused by a large number of outliers, we developed and tested a modified variable cutoff, that was found to produce negligible impact in its current form. Therefore, the original Vandamme cutoff will be used in this chapter. For the development of a modified cutoff approach, an attempt was made to improve the determination of the initial dispersion/cutoff guess of the Vandamme (1994) process. Instead of calculating the initial dispersion value as S_b of the full dataset, a distribution of S_b was determined from 2500 draws of random subsets of VGPs (Figure 5.3). To test the effectiveness of this modified Vandamme cutoff, it was applied to synthetic data in the following steps:

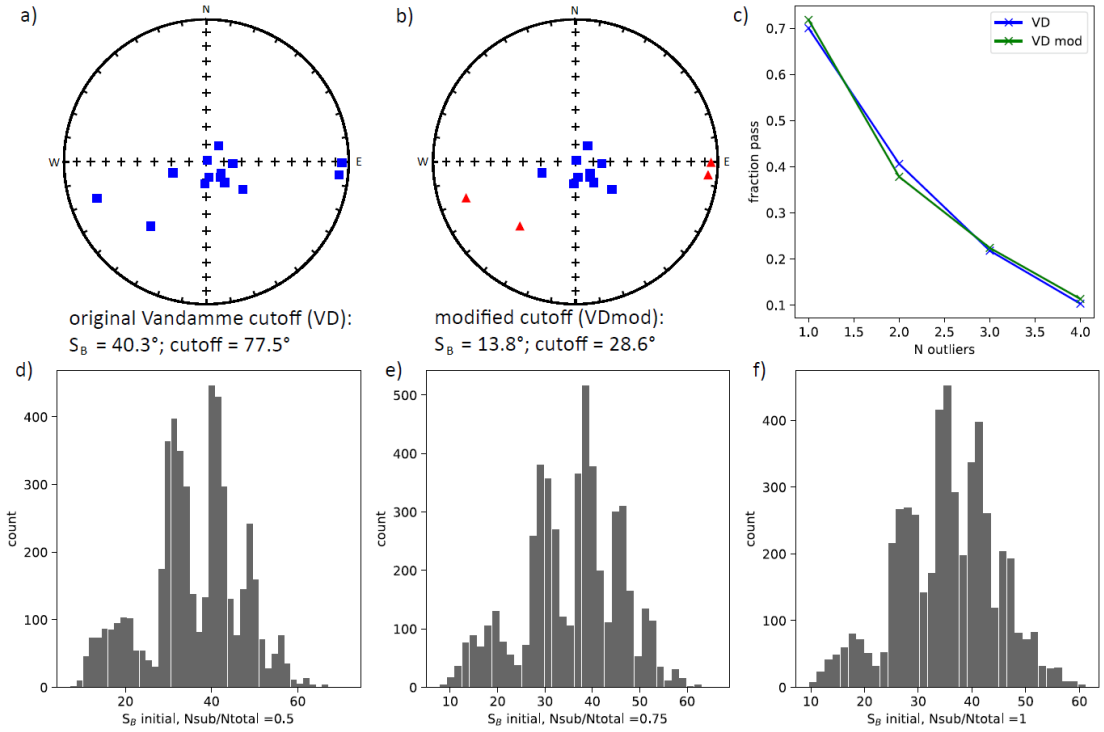

FIGURE 5.3: Tests of a modified variable (Vandamme, 1994) cutoff estimation. a-b): stereoplots with synthetic Fisherian VGPs on the upper hemisphere with four added outliers, blue squares: accepted datapoints, red triangles: excluded outlier VGPs; c) comparison of original Vandamme cutoff (VD, blue) to its modified version (VD mod, green); d-f: histograms of initial guesses of Sb for different data subsets of (d) n_{sub} = 0.5 * n_{total}, (e) n_{sub} = 0.75 * n_{total}, and (f) n_{sub} = n_{total}

1. 10 directions were drawn from a Fisherian (Fisher, 1953) distribution around a mean pole at Dec: 0°, Inc: 60° (k = 50, S_w set to ∼0) using the pmagpy toolbox (Tauxe et al., 2016). These directions were converted to pole space (assuming a site latitude of 45°), and a reference value of $S_{b\ ref}$ was calculated for these VGPs (without cutoff) as reference.

2. 1 - 4 datapoints with random inclinations between 0° and 10° were added to 500 datasets each. Random declinations were restricted to values between 270° and 90° to avoid reversed polarity outlier VGPs.
3. The VGP dispersion $S_{b\,VD}$ was calculated using the original Vandamme cutoff (Vandamme, 1994).
4. VGP dispersions $S_{b\,VDmod}$ were calculated with the modified Vandamme cutoff, where the initial guess of S_b was set as the median S_b from 2500 draws. At each draw, S_b was calculated for a subset of random VGPs (N_{sub} = 0.5 * N_{total}, replacement allowed).
5. The VGP dispersions from the different cutoffs were compared to the reference dispersion to determine the effectiveness of each cutoff. The application of the original and modified Vandamme cutoffs was counted as successful if $S_{b\,VD}$ = $S_{b\,ref}$ or $S_{b\,VDmod}$ = $S_{b\,ref}$.

Depending on the number of outliers, bootstrapping S_b led to a multimodal distribution of S_b values that changed according to the fraction of N_{subset}/N_{total} (Figure 5.3d - f). Using the median S_b from the distribution with N_{sub}/N_{total} = 0.5 as initial guess improved the performance for some datasets, and the modified cutoff was able to remove outliers, where the original Vandamme cutoff failed to recognise these data points as outliers (Figure 5.3a - b). However, for the majority of datasets, both original and modified cutoff led to the same results, and in some cases, the modified version performed worse than the original. The direct comparison of performance (Figure 5.3c) shows, that both cutoff variants struggled to reproduce the reference value of S_b for datasets, where multiple outliers were added. Using different sizes of subsets did not improve the performance of the modified cutoff, suggesting that the approach of using the median of the distribution as initial guess is too simple and not effective. The idea of bootstrapping the initial guess seems promising, but will require additional research outside of the scope of this chapter.

5.6 Results and discussion

5.6.1 An observation-based model for Ediacaran PSV

The angular dispersions of the final collection of datasets are given in Table 5.1 and shown in Figure 5.4. The values of angular dispersions (S_b and s_b) were calculated from all datasets with N $\geq$ 9 sites and $s_w/\sqrt{nn} < 10$ after excluding outlier VGPs according to the (Vandamme, 1994) cutoff. A total of 9 datasets satisfied these primary selection criteria (Supplementary Table D.1). The use of a fixed 45° cutoff as

well as not using any cutoff at all (Figure 5.4a) only leads to a change for one of the datasets (Fajjoud-Tadoughast Formation; Robert et al., 2017). For lower-quality Group C datasets with $5 \geq N \geq 9$ sites, that are shown for comparison with grey triangles in Figure 5.4a,d, using different cutoffs influences the results for about half of the datasets. Figure 5.4 also shows the angular dispersions of these datasets as a function of latitude and compares the fits of model G (Figure 5.4b) and model A (Figure 5.4e) to published model fits for PSV10 (Cromwell et al., 2018), the Jurassic (Doubrovine et al., 2019) and the Precambrian (Veikkolainen & Pesonen, 2014).

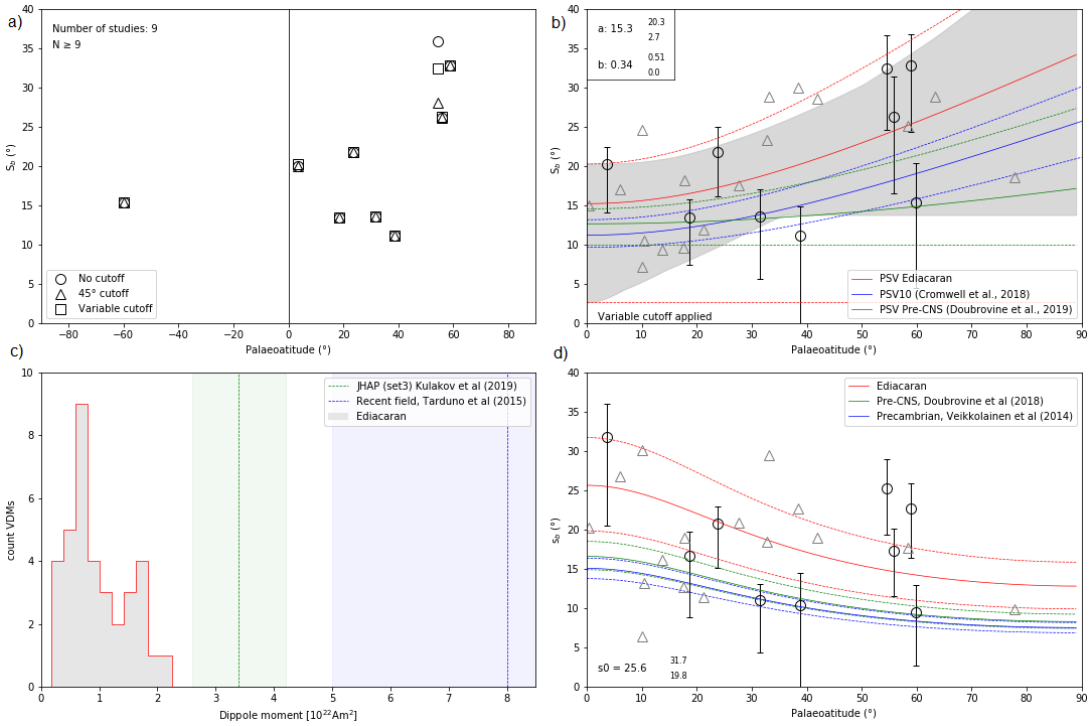

FIGURE 5.4: Model A and model G parameters as well as VDM distribution from Ediacaran data, compared to published values for the Jurassic (green; Doubrovine et al., 2019; Kulakov et al., 2019) and the 'modern' field (blue; Cromwell et al., 2018; Tarduno et al., 2015). Data points in black satisfy the primary selection criteria (see text) and were used for the model fits. Data points in grey from lower-quality datasets are shown for comparison. (a) angular dispersion of VGPs versus latitude for different types of cutoffs; (b) latitude dependence of VGP dispersion and model G fits. Solid lines in (a)-(b) show the model fits to the data, dashed lines give the 95% confidence ranges from bootstrapped minimum (maximum values) of s_0, or VGPa and VGPb; error bars show 95% confidence limits of the dispersion estimates. (c) histogram of all published dipole moments of the Ediacaran. (d) latitude dependence of angular dispersion of directions and model A fits

Treatment of all data following the same criteria leads to slight differences in the results, compared to the published dispersions of the Group A data shown in Figure 5.1. These differences are connected to different sites being excluded or retained when

max($s_w/\sqrt{nn}$) is used as filter instead of min(nn) or min(k). Less than 9 sites of the Dokhan volcanics dataset, one of the two Ediacaran dispersion values included in (Veikkolainen & Pesonen, 2014), satisfy the $s_w/\sqrt{nn}$ criterion. This dataset is therefore not included in our final result. In contrast, the $s_w/\sqrt{nn}$ criterion allows for two more VGPs of the Grenville Dyke (steep) pole to be included in the analysis, and the resulting S_b value for this dataset changes from 18.5° in chapter 2 to 15.4° in this analysis. The model G fit to the angular dispersions of the selected VGPs (Figure 5.4b) of VGPa = 15.3°, VGPb = 0.34 suggests enhanced secular variation compared to other time periods. However, neither the symmetric, nor the antisymmetric model G terms are well constrained due to the low number and high scatter of results as well as the lack of data at latitudes above 60°. Similarly, the equatorial dispersion of model A for the results in directional space (Figure 5.4d) is higher than for the other time periods, but this result is of little significance since the datapoints do not follow the model A prediction at all.

Following the interpretation of the data in Figure 5.1, an argument could be made that the dispersions presented in Figure 5.4 comprise two groups of data, with approximately half of the datapoints, representing a 'normal' dipole dominated field, roughly plotting in the range of the Jurassic model G/model A fits and the other half showing significantly higher dispersions. Most of the poles in the 'high-dispersion' group have magnetisation ages between 562 Ma and 588 Ma (with the exception of one dataset at ∼536 Ma) whereas the ages of the poles in the 'low-dispersion' group are either younger (551 Ma) or older (615 - 588 Ma).

Rock unit	Age [Ma]	λ	N	S_b	S_b upper	S_b lower	s_b	s_b upper	s_b lower	$\frac{s_w}{\sqrt{nn}}$	ID	Reference
Djebel Boho Formation	536	58.9	13	32.8	24.4	36.8	22.7	16.4	25.9	4.9	N/A	[1]
Skinner Cove Formation	551	18.6	10	13.5	7.6	15.7	16.7	8.8	19.7	5.5	8321	[2]
Fajjoud-Tadoughast Formation	562	54.5	18	32.5	24.6	36.7	25.2	19.4	29.0	5.1	13380	[1]
Bull Arm Boavista/Argentia	570	23.7	15	21.9	16.2	25.1	20.7	15.1	23.0	5.5	10270	[3]
Alnö carbonatite complex	584	55.8	10	26.4	16.6	31.5	17.3	11.6	20.2	5.9	10067	[4]
Grenville Dykes (shallow)	588	3.6	14	20.2	14.1	22.5	31.8	20.6	36.0	5.6	10836	[5]
Grenville Dykes (steep)	588	-59.9	10	15.4	4.6	20.4	9.5	2.7	12.9	4.5	10836	[5]
Lynn-Mattapan volcanics	597	38.7	9	11.2	-3.7	14.9	10.4	-2.9	14.5	4.5	100012	[6]
Long Range dykes	615	31.6	9	13.6	5.7	17.1	11.0	4.4	13.1	5.9	6934	[7]

TABLE 5.1: Summary of Ediacaran PSV data of this study, recalculated from filtered data according to consistent criteria (see text): Age: average age of magnetisations; λ: magnetic latitude calculated from the palaeomagnetic pole; N: number of sites; S_b, S_b upper, S_b lower: VGP dispersion with upper and lower 95% confidence bounds; s_b, s_b upper, s_b lower: dispersion of directions with upper and lower 95% confidence bounds; ID: data ID in the Palaeomagia database (Veikkolainen et al., 2014b), References: [1] Robert et al. (2017), [2] McCausland and Hodych (1998), [3] Pisarevsky et al. (2012), [4] Meert et al. (2007), [5] Halls et al. (2015), [6] Thompson et al. (2007), [7] Murthy et al. (1992)

An analysis of the field strengths associated with the two groups is also difficult, because palaeointensity measurements exist only for the datasets of the Grenville Dykes and the Skinner Cove formation. The expectation that the datasets of the low-dispersion group show substantially higher intensities than the datasets of the high-dispersion group is correct at low latitudes where the palaeointensities of the low-dispersion Skinner Cove dataset are about twice as strong as the intensities of the high-dispersion dataset of the Grenville Dykes (shallow). At higher latitudes, the intensities of the Grenville Dykes (steep) dataset that would be associated with the low-dispersion group are extremely low again. Based on this small amount of data, the palaeointensities of the two groups are not significantly different. Following Sprain et al. (2019), the variability of VDMs was calculated using V% = VDM_{iqr}/VDM_{med}. The resulting value of V% = 1.04 is higher that the values for younger fields of V% (1-10 Ma) = 0.863 and V% (0-1 Ma) = 0.534 (Sprain et al., 2019).

5.6.2 Comparison to numerical geodynamo model results

The statistical field model estimates for the Ediacaran directional PSV and VDM variability, determined in the previous section can be used as the basis for seeking geodynamo models that predict a similar field behaviour. This comparison will of course be impeded by the enormous confidence ranges for both VGPa and VGPb. With the available PSV data, it is difficult to ascertain if these results actually represent an anomalous field that is not well described by model G, or if proper model fits are prevented by the low amount (and quality) of the observational data. To confirm that the latter is not the case and to explore whether the statistical estimates can be used for comparison to the outputs of geodynamo models, synthetic datasets of similarly low quality were 'down-sampled' from geodynamo simulations. This also allowed comparison with results from studies that more fully sampled model solutions (Biggin et al., 2020; Meduri et al., 2021; Sprain et al., 2019).

To simulate 'real' palaeomagnetic datasets, VGPs for PSV analysis were down-sampled from solutions of geodynamo models in the following steps:

1. Random latitudes and longitudes were drawn for 15 localities (= datasets).
2. For each of these datasets, 15 timesteps from the full time series of Gauss coefficients were randomly chosen as 'sites' (compared to 500 timesteps used in Biggin et al. (2020)).
3. For each site, a field vector was determined from the set of Gauss coefficients (up to degree and order 10) for the site's latitude, longitude and time step.

4. To introduce within-site scatter, a set of 10 'sample' directions was drawn from a Fisher distribution with k = 20 around the sampled field vector. These directions were averaged to gain an 'apparent' site-mean field vector, defined by declination, inclination, k and intensity. This mean direction was then used to calculate the associated VGP, an apparent palaeolatitude and the VDM for this site.

5. VGPs calculated from site mean directions were flipped to the same polarity in case of dual polarity data.

6. Following the same approach as in the previous section, all VGPs with $s_w / \sqrt{nn}$ > 10 were removed from each dataset, and outlier VGPs were selected and removed according to the Vandamme (1994) cutoff. Datasets were retained if N $\geq$ 9 VGPs remained in the dataset.

7. Angular dispersions of VGPs and directions were calculated for all remaining datasets to fit a model G and a model A curve.

8. Steps 1) - 7) were repeated 250 times to bootstrap confidence intervals of the model fits for each dynamo model. A larger number of random draws was prevented by the (lack of) available computing power.

Estimates for VGPa, VGPb and V% were determined for 11 geodynamo models using the MagIC code, (Meduri et al., 2021; Supplementary Table D.2) using the steps above. The comparison of results with actual statistical estimates for these models using the sampling approach in Sprain et al. (2019) and Biggin et al. (2020) is shown in Figure 5.5.

These comparisons show surprisingly equivalent results from both sampling approaches. Estimates of VGPa (Figure 5.5a) from models with intermediate Rayleigh numbers plot in the range between 10 - 20° and show the expected increase in confidence ranges, but only a small positive bias for the estimates from the approach with low sample numbers and added S_w. This bias increases for models with higher VGPa dispersion, indicating that it is related to the variable cutoff and the reduced efficiency for datasets where the decreased number of VGPs increases the relative frequency of transitional VGPs, that are then less likely to be removed. This suggests that datasets with low numbers of palaeomagnetic observations overestimate VGPa for highly variable fields. No systematic bias can be seen for median estimates of VGPb (Figure 5.5b) as most median values plot close to the unit slope. The 95% confidence range for VGPb of all dynamo models increased to large intervals resembling the observed Ediacaran data and suggest that VGPb will not be useful for the comparison between observational data and geodynamo model solutions.

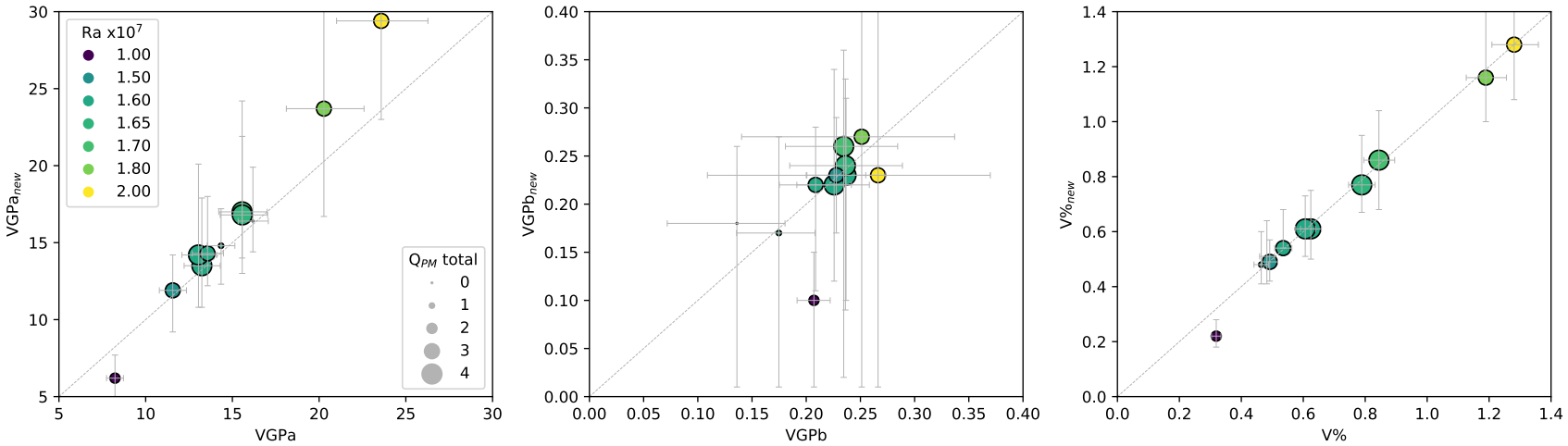

FIGURE 5.5: Statistical estimates for directional PSV and variability of dipole moments of 12 geodynamo simulations. Shown are comparisons of actual estimates for parameters VDMa (a), VDMb (b) and V% (c) from Biggin et al. (2020) and Sprain et al. (2019), and Meduri et al. (2021) on the x-axis versus the estimates from a sampling procedure designed to simulate imperfect palaeomagnetic datasets on the y-axis (see details in the main text). Shown are median values with 95% confidence ranges. Colours of data points represent the range of modified Rayleigh numbers of the specific models. Sizes of datapoints were chosen according to the total Q_{PM} score of each model.

The best fit between results of both sampling approaches was seen in estimates of VDM variability (Figure 5.5c). No systematic differences were found related to the Q_{PM} scores of the models. A negative bias of VGPa, VGPb and V% can be seen for the non-reversing model MAGB004. Possible explanations could be the removal of non-transitional VGPs by the cutoff, or the decrease of S_b by the correction for S_w. Overall, the similarity of results from both approaches gives some confidence that a tentative comparison of the statistical model parameters from the low number of Ediacaran observational data to well-sampled geodynamo model solutions could give valuable information about deep Earth properties in the Ediacaran, or at least help rule out some scenarios predicted by geodynamo models.

Selected results of the PSV analysis for palaeomagnetically sampled models are shown in Figure 5.6 for the models MAGB001 (Figure 5.6a), MAGM003 (Figure 5.6b) and MAGS002 (Figure 5.6c), as examples for different types of field behaviour in terms of reversal frequency, PSV dispersion and VDM variability. MAGB001 shows a stable field with a single reversal and a low number of excursions (Figure 5.6a1). Increasing the Rayleigh number led to the results of MAGM003 that shows multiple reversals/excursions, an area of hyperactivity and high PSV dispersions (Figure 5.6b1). Running the model with a lower Rayleigh number gives the results of MAGS002, that shows only a single excursion, no reversals, and little dispersion due to PSV (Figure 5.6c1). None of the models showed VGP dispersions that could be interpreted as one group of 'high dispersion' and one group of 'low dispersion' (Figure 5.6a2, b2, c2), even if the model switched between times of hyperactivity and stable fields (e.g., Figure 5.6b1). In contrast, all histograms of VDM distributions (Figure 5.6a3, b3, c3) show a bimodal distribution for models that produce at least one excursion and/or reversal, where a low dipole moment peak can be attributed to transitional fields. This is supported by the difference in VDM distributions between the full dataset and datasets where transitional timesteps have been isolated by the cutoff for the determination of model G fits. The difference in V% between models and Ediacaran observations increases with decreasing numbers of reversals and/or excursions. If V% is calculated using only VDMs of the sites that were defined as 'transitional' by the variable cutoff (Figure 5.6a4, b4, c4), then this difference decreases, or stays the same in case of models with mainly transitional fields like MAGM003, where V% of the full VDM distribution is already similar to the observed Ediacaran value, which could be seen as support for the existence of a transitional field in the Ediacaran (or an accidental sampling bias towards units that have recorded a transitional field).

A quantitative comparison between the observed Ediacaran data and all geodynamo models that are currently available (Biggin et al., 2020; Meduri et al., 2021; Sprain et al., 2019) was done using the statistical field model estimates of VGPa and V% from

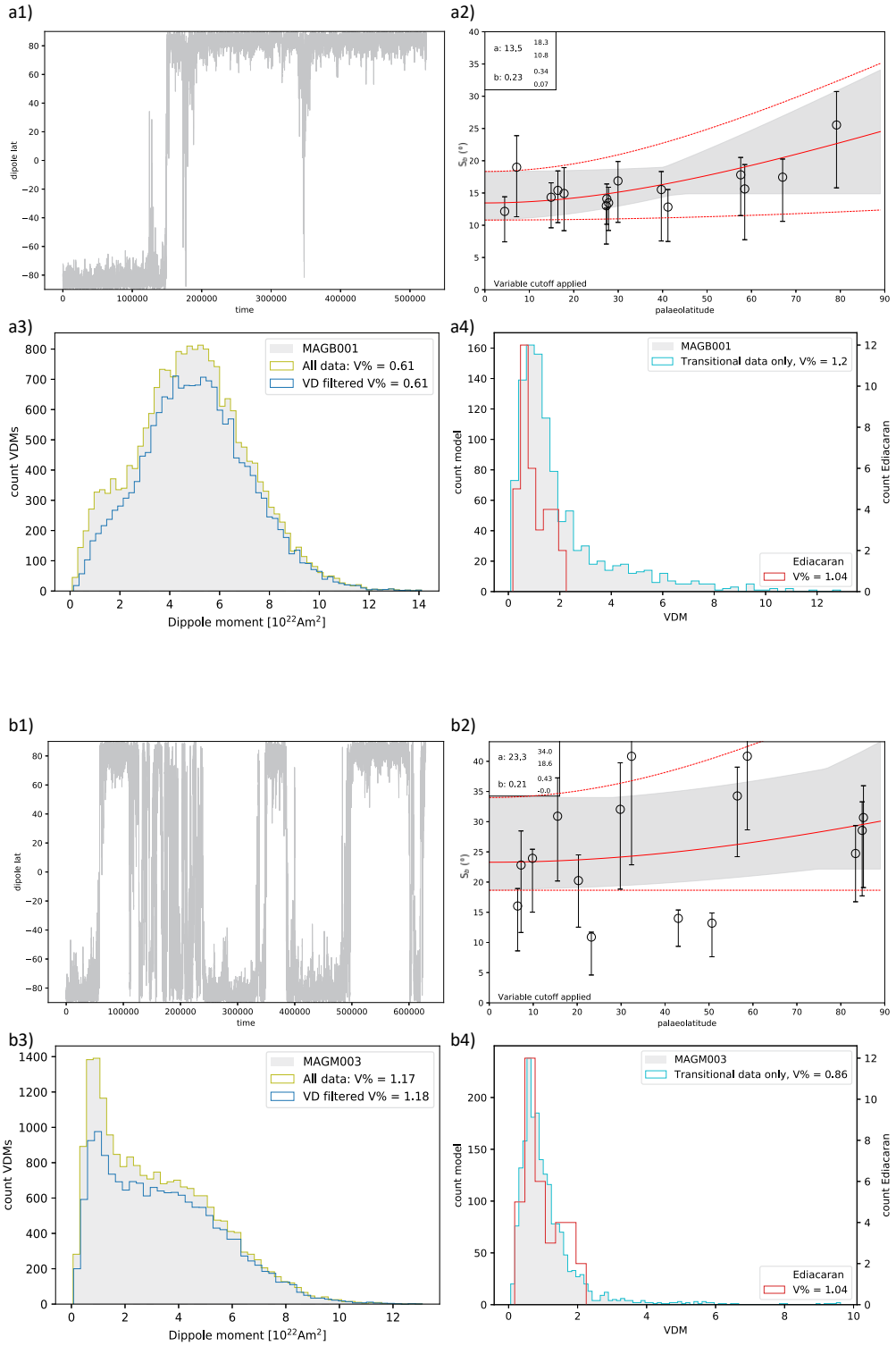

(A) Figure 5.6 (continues on next page)

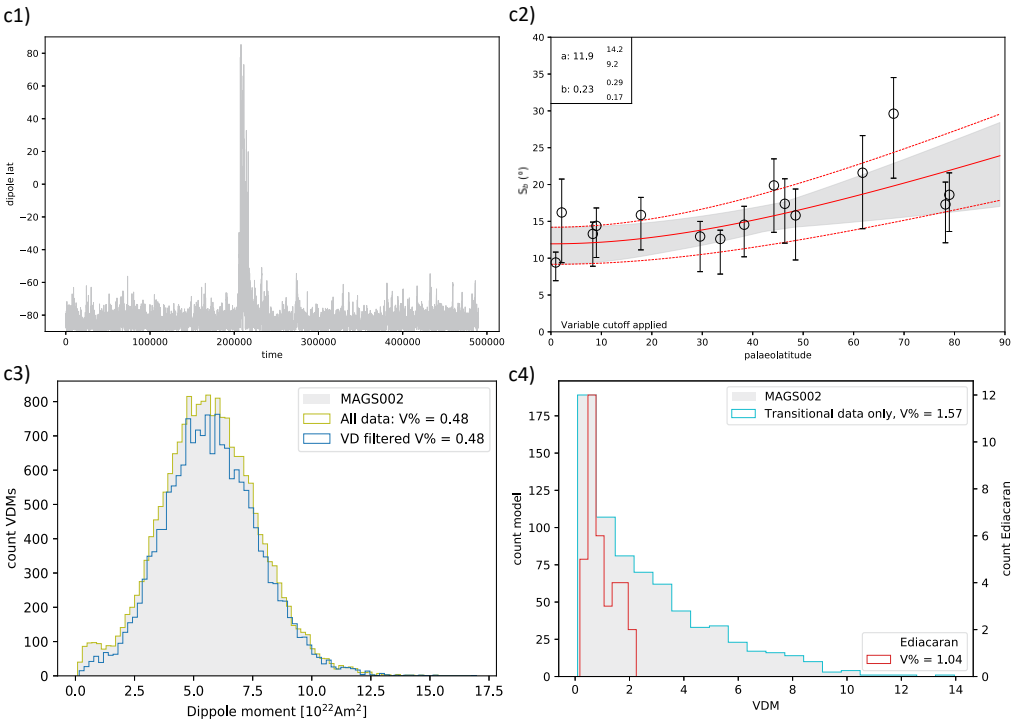

FIGURE 5.6: Statistical field models for solutions of geodynamo simulations (Supplementary Table D.2). Datasets were created using the approach described in section 5.6.2 to simulate real palaeomagnetic data. a) model MAGB001: a1) Dipole latitude (g_0^1) for the complete time range of the model. a2) Model G fits for 250 draws of 15 datasets. Values of S_b and their 95% confidence range error bars show one random example of the 250 draws. a3) Distribution of sampled VDMs. The distribution of all VDMs is shown in red/grey. Blue displays the distribution of VDMs for all VGPs that have not been excluded as 'transitional' outliers by the cutoff; a4) VDM distributions of VGPs that are considered 'transitional' by the cutoff (= difference between 'All data' and 'Filtered data only' histograms in a3), compared to the VDM distribution of Ediacaran observational data (red); (b1 - b4) same as in (a) for model MAGM003; (c1 - c4) same as in (a) for model MAGS002.

Sprain et al. (2019) and Biggin et al. (2020). From the available 88 models (Supplementary Table D.2; Biggin et al., 2020; Meduri et al., 2021; Sprain et al., 2019), 7 show VDM distributions where the Ediacaran value of V% = 1.04 falls within their 95% confidence range. The majority of these models also show high values of VGP dispersion (VGPa $\geq 29°$, Figure 5.8), that are significantly different from the observed Ediacaran PSV as their confidence ranges do not coincide with the (large) Ediacaran confidence range. Only one model (LEDA010, Figure 5.7; Biggin et al., 2020; Meduri et al., 2021; Sprain et al., 2019) is able to reproduce both V% and VGPa of the Ediacaran field. However,

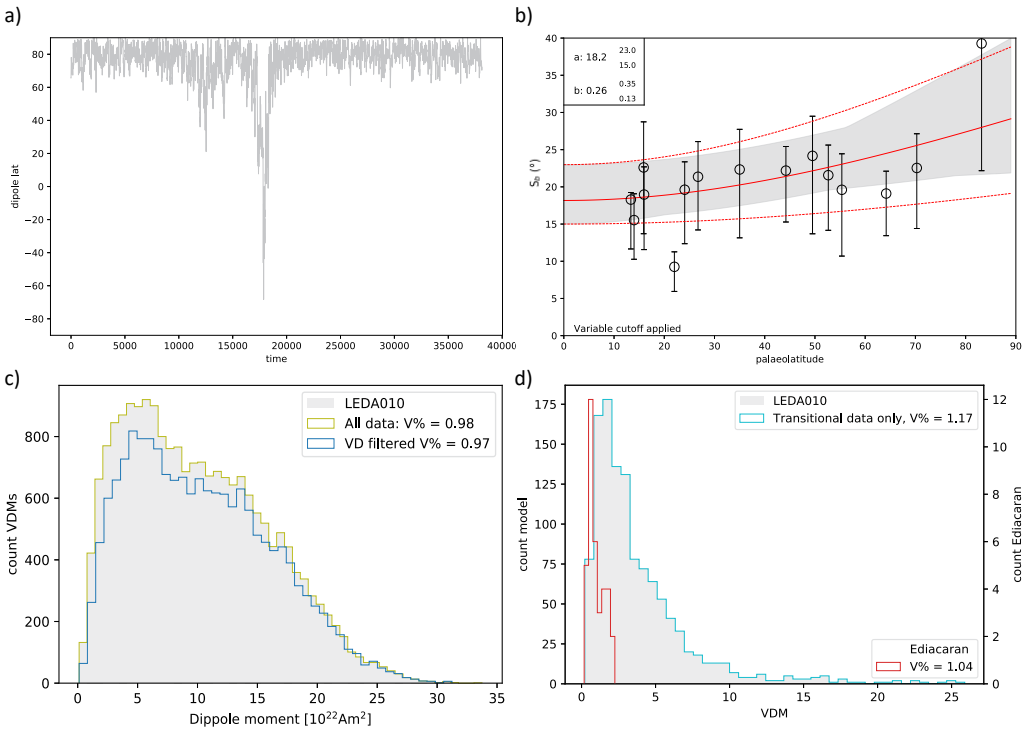

FIGURE 5.7: Statistical field model for solutions of geodynamo simulation LEDA010 (Supplementary Table D.2) See caption of Figure 5.6. a) Dipole latitude (g_0^1) for the complete time range of the model. b) Model G fits for 250 draws of 15 datasets. Values of S_b and their 95% confidence range error bars show one random example of the 250 draws. c) Distribution of sampled VDMs. The distribution of all VDMs is shown in red/grey. Blue displays the distribution of VDMs for all VGPs that have not been excluded as 'transitional' outliers by the cutoff; d) VDM distributions of VGPs that are considered 'transitional' by the cutoff (= difference between 'All data' and 'Filtered data only' histograms in c).

this model does not produce a reversal for the duration of the simulation (∼9 magnetic diffusion times = ∼1.8 Ma), whereas reversing frequencies of ≥ 20 Myr^{-1} have been reported for the Ediacaran (Bazhenov et al., 2016; Levashova et al., 2021). Instead, this model is characterised by one large excursion surrounded by more stable periods with large variations in dipole latitude. The high V% of LEDA010 makes this model solution an outlier compared to all other models with a non-reversing stable dipolar regime (Figure 5.8). From the model parameters and boundary conditions for LEDA010 (Supplementary Table D.2), it is unclear why this model produced an outlier V% that agreed with the Ediacaran data. The model was run with intermediate values of Ek = 5 $\times 10^{-4}$, Ra = 200, and Pm = 10, a present-day aspect ratio (ar = 0.35), homogeneous heat flux, an insulating inner core, and fixed temperature (fixed flux) as thermal

boundary conditions for the inner (outer) boundary. In contrast to the Ediacaran field, this high V% is not related to an exceptionally weak field. The true dipole moment of LEDA010 (TDM = 25.8 $\times 10^{22}$Am^2) is even stronger than the TDM of a comparable model (LEDA021, TDM = 19.9 $\times 10^{22}$Am^2), that was run using the same parameters as LEDA010 with a larger Rayleigh number of Ra = 400 and resulted in a stable dipolar field (τ_T = 0.002, VGPa = 23.6°, V% = 0.58).

Since none of the 88 models succeeded to reproduce all characteristics of the Ediacaran field, the question arises as to what the models are missing and why they can reproduce field behaviours from younger time periods, but not from the Ediacaran. A definitive answer to this question has not been found in this chapter, as there are multiple possibilities that could affect the results. There is a lot of parameter space that could be covered by future model runs. However, doing that may not lead to a better match to the Ediacaran observational data because of the following reasons:

1 – Different time intervals

The palaeomagnetic data from the Ediacaran covers about 100 Myrs (∼50 Myrs for intensity data). In contrast, the geodynamo simulations were run over much shorter timescales (median duration t_{sim} = 6.9 magnetic diffusion times = ∼1.4 Myrs). While this duration should be sufficient to capture PSV, the comparison to the Ediacaran data relies on the assumption that the Ediacaran TAF does not change over the much longer time period. As discussed further below, this assumption may be problematic.

2 – Inner core size/absence

One of the of the major factors drawing attention to the Ediacaran is the possible timing of the onset of inner core nucleation at the end of this period. Only 3 of the 88 tested models used an aspect ratio that differed from the present-day aspect ratio of 0.35 (see Supplementary Table D.2). Smaller inner core sizes with aspect ratios of 0.1 and 0.2 were only used in the models LEDA051, LEDA052 and LEDA053 (Biggin et al., 2020). These three models showed median VGPa values between 16.1° and 18.3° - close to the Ediacaran observations – but a lower VDM variance of V% $\leq$ 0.7. Irrespective of the correct thermal conductivity of the core, the present-day aspect ratio that was used in the vast majority of models, is not realistic for the Ediacaran. An additional challenge is introduced, if the inner core started to form in the late Ediacaran, as inferred from palaeomagnetic data (Bono et al., 2019), and the energy source of the geodynamo changed within the observation period.

3 – CMB heat flux pattern

The fixed heat flux patterns that were used for all models were either homogeneous outer boundaries, varied according to a present-day tomographic model, or a recumbent pattern of spherical harmonic degree l = 2 and order m = 0 (Biggin et al., 2020; Meduri et al., 2021). With the extreme tectonic activities before and throughout the Ediacaran – the breakup of Rodinia, the formation of Gondwanaland, and maybe even true polar wander events (Li et al., 2013; Robert et al., 2021) – the CMB heat flow patterns would not be expected to remain a static boundary condition for the whole Ediacaran.

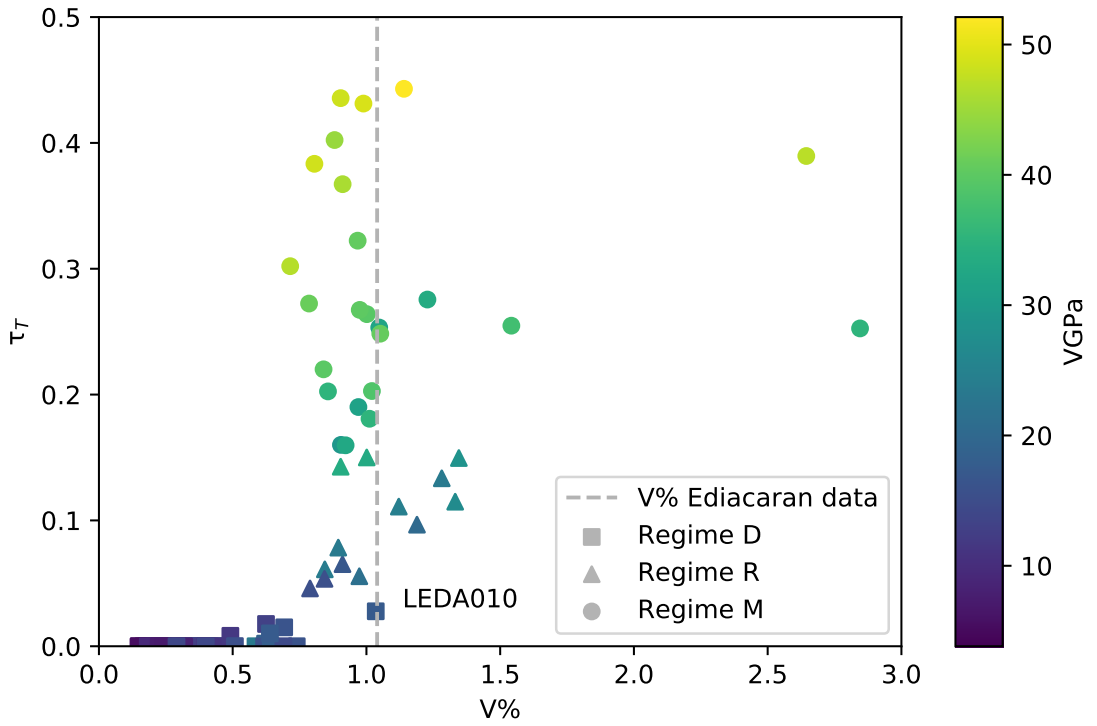

FIGURE 5.8: Dipole variance of Ediacaran observational data (grey dashed line) in comparison to numerical geodynamo simulation outputs, plotted against the relative transition time (τ_T, Sprain et al., 2019). Different symbols represent different reversal regimes of the models, as defined in Meduri et al. (2021): Stable dipolar (D, $\tau_T < 0.0375$), reversing (R, $0.0375 \leq \tau_T \leq 0.15$), and multipolar (M, $\tau_T < 0.15$). The colourbar represents VGP dispersion in terms of VGPa. LEDA010 is highlighted as the only model that shows similar estimates for V% and VGPa to the Ediacaran.

4 – Regime changes

The data in this chapter and the previous chapters - an extended weak field period with puzzling directions (Chapter 2) followed by an increase in field strength (Chapters 3, 4), possibly combined with two groups showing low and high VGP dispersions

(Chapter 5) – support the idea of a changing field regime. It is unlikely that a single geodynamo simulation with its fixed parameter space can capture this behaviour. Dividing the Ediacaran data into two (or more) smaller groups might improve the fit to multiple solutions of geodynamo simulations. This will, however, not be possible until the spatial and temporal distribution of (high quality) palaeomagnetic data for the Ediacaran (and the adjacent periods) is improved substantially.

5.7 Conclusions

We have calculated statistical field models from a filtered selection of the currently available collection of Ediacaran palaeomagnetic data. After filtering using what was determined to be the optimal criteria, estimates for VGP dispersion have been calculated as VGPa = 15.3° ($95\%_{min}$ = 2.7°, $95\%_{max}$ = 20.3°) and VGPb = 0.34 ($95\%_{min}$ = 0, $95\%_{max}$ = 0.51). The variability of Ediacaran virtual dipole moments was calculated as V% = 1.04. The usefulness of these statistical estimates, based on a low number of data, was assessed by simulating similar low-quality datasets from solutions of numerical geodynamo simulations and the comparison of statistical parameters determined from these datasets to the properly sampled statistical parameters used for the determination of each model's reliability in terms of Q_{PM} (Sprain et al., 2019).

The quantitative comparison of the new statistical field model for the observed Ediacaran data to the outputs of 88 numerical geodynamo simulations showed that the model of the observed Ediacaran data – despite the enormous confidence ranges of the statistical parameters – describes a geomagnetic field that is so unique that none of the geodynamo simulations has been able to reproduce it. The statistical field model of the Ediacaran is however based on a low number of measurements and a better data coverage of full-vector palaeomagnetic data coverage is needed to improve constraints on Ediacaran field models.

Chapter 6

Conclusions

The primary aim of this thesis was the determination of geomagnetic field strength in the Ediacaran in order to characterise the field at that time and to find an explanation for its anomalous behaviour. The studies presented in the previous chapters provide new constraints for the palaeointensity behaviour in the second half of the Ediacaran and form a solid foundation for future studies attempting to characterise the Ediacaran field.

This final chapter summarises the key findings and implications of this thesis and gives suggestions for future research that can improve our understanding of the Ediacaran geomagnetic field.

6.1 Summary of results

The studies presented in Chapters 2 - 4 add 27 new, reliable (Q_{PI} = 6 - 9) palaeointensity estimates of 2.6 - 10.3 µT (0.3 - 2.25 $\times 10^{22}$ Am^2) to the record. These exceptionally weak estimates were obtained from rocks of two continents (Laurentia and Baltica) and cover the time period between ∼550 - 600 Ma (Figure 4.8). The field strength in this time period was previously defined by one single data point from single crystal palaeointensity experiments at 565 Ma (Bono et al., 2019).

The presence of an extended weak field period in the Ediacaran, as previously inferred from directional data (e.g., Meert et al., 2016), was confirmed by the results of the palaeointensity study of the Canadian Grenville dykes (580 - 598 Ma) presented in Chapter 2. The palaeointensity results from 15 sites across 6 dykes are in the range between 1.4 - 7.6 µT (0.33 - 1.76 $\times 10^{22}$ Am^2). Four of these dykes provided mean palaeointensity estimates (0.42 - 0.82 $\times 10^{22}$ Am^2) based on more than three individual results from successful microwave Thellier and Shaw experiments. All results from thermal Thellier experiments had to be rejected in order to ensure that no intensities were accepted that could possibly be biased by MD behaviour. Agreeing palaeointensities

from calibrated pseudo-Thellier results suggested that the presented results were not biased by laboratory alteration. Although based on a low number of results, it was possible to compare intensity behaviour of the two incompatible 'steep' and 'shallow' components for the first time. The resulting palaeointensity and VGP dispersion estimates were almost identical for both directional components which hints at a transitional field as suggested by Halls et al. (2015).

The first constraints for geomagnetic field strength at the end of the Ediacaran, presented in Chapter 3, were obtained from rocks of the Skinner Cove Formation (551 Ma, Newfoundland). Results from thermal Thellier, microwave Thellier and Shaw experiments provided palaeointensity estimates of 2.6 - 10.3 µT (0.65 - 2.25 $\times 10^{22} Am^2$) for seven sites in flows, dykes and an intraformational conglomerate. A possible maghemitisation of the titanomagnetite carriers was suggested by the presence of large, cracked grains that were seen in scanning electron microscope images. However, rock magnetic measurements did not show any signals related to maghemite and a magnetic field map from quantum diamond microscope measurements suggested that the large grains in question did not carry any remanence. In addition, the primary nature of the magnetisation was confirmed by a positive conglomerate test in McCausland and Hodych (1998).

A global extent of the Ediacaran weak field was suggested by the first palaeointensity estimates for Baltica from rocks of the Ukrainian Volyn Traps (Shcherbakova et al., 2020). Additional palaeointensity experiments on an extended profile of the Volyn Traps, presented in Chapter 4, revealed palaeointensities of 2.1 - 11.1 µT (0.31 - 1.67 $\times 10^{22} Am^2$) from 16 cooling units. These intensities were determined from results of thermal Thellier, microwave Thellier, Shaw and Wilson experiments and agree well with the field strength estimates of Shcherbakova et al. (2020) and follow the trend set by the studies of the Laurentian localities. The correlation of these intensity to the measured magnetic polarity profile of the section suggests that the weakest intensities occurred close to reversals and that the field strength did not fully recover between these reversals.

As discussed in Chapter 5, there are limitations to the presented intensity results. Even though the studies presented in this thesis add a large number of results to the palaeointensity record, the spatial and temporal distribution of data is still insufficient to cover the whole Ediacaran. In addition to the risk that undetected MD behaviour could lead to severe underestimates of measured palaeointensities (Smirnov et al., 2017), fragile magnetisation and 'aging' effects of the magnetic carriers (Tauxe et al., 2020) could introduce further uncertainties. Within the framework of our current understanding of remanence acquisition and preservation, all presented intensity results

satisfy all criteria to be considered reliable.

New estimates of VGP dispersion for the Ediacaran were calculated in Chapter 5 using filtered data from the Paleomagia database (Veikkolainen et al., 2014b). Only nine published datasets satisfied the used quality criteria which led to large 95% confidence ranges of the determined model G (McFadden et al., 1988) parameters of both VGPa (2.7 - 20.3°) and VGPb (0.0 - 0.51). In addition, the variance of virtual dipole moments was calculated as V% = 1.04. These estimates, although based on a low number of data, suggest enhanced palaeosecular variation in the Ediacaran compared to other time periods (Cromwell et al., 2018; Doubrovine et al., 2019; Veikkolainen & Pesonen, 2014). Despite the large confidence ranges, none of the 88 tested geodynamo model solutions (Biggin et al., 2020; Meduri et al., 2021; Sprain et al., 2019) was able to capture the full range of Ediacaran field behaviour.

6.2 Implications and future work

The new intensity data from Laurentia and Baltica, summarised above, agree exceptionally well and point towards a clear trend in the global long-term field behaviour. This trend describes an extended period of extremely weak field between ∼565 - 600 Ma, followed by an increase in field strength around ∼550 - 560 Ma, which agrees with the expected palaeomagnetic signature due to the onset of inner core growth at that time (Aubert et al., 2009; Bono et al., 2019; Driscoll, 2016). This increase of field strength is hovever a qualitative observation based on only two data points in the Cambrian and the less chaotic APWPs after the Ediacaran, which suggest a stronger field. A statistical analysis of the weak Ediacaran intensities before 565 Ma and the seemingly stronger intensities after that time (Figure 6.1), using a two-sample Kolmogorov-Smirnov test, showed that the null hypothesis of both groups belonging to the same distribution cannot be rejected at the 5% significance level (D = 0.277; p-value = 0.647). This is also the case when the two Cambrian intensities are included in the group of 'increased' intensities (D = 0.343; p-value = 0.354). Completely different causes for the observed field strength behaviour, possibly related to reconfigurations of the convection patterns in the outer core due to unusual core-mantle heat flow patterns, cannot be ruled out however, especially since the change from weak to strong field would also fit within the observed ∼200 Myr periodicity of field strength variation (Figure 6.1) in younger time periods (Biggin et al., 2012). It is thus entirely possible that the Ediacaran intensity estimates represent another cycle in such a periodic decrease and increase of field strengths, which may even continue deeper into the Precambrian. However, the field strengths in the Ordovician, Silurian and the early-mid Neoproterozoic are are largely unknown. Additional palaeointensity data would

be required to study the long term field strength behaviour for these periods. Without further context from such measurements, the data presented in this thesis could support a late Ediacaran onset of inner core nucleation (Bono et al., 2019).

The comparison of the palaeointensity results in chapters 2 and 3 to the ones in Chapter 4 highlights the importance of large sample collections. This is true for all palaeointensity studies, but especially vital to studies of Precambrian rocks due to the low success rates. Future palaeointensity studies should aim for a sufficient number of samples, as shown in Chapter 4. Even though it is not strictly necessary - and not always possible - these samples should be collected as oriented samples to be able to compare the directional information to other available palaeomagnetic data. A large number of samples would also allow for a higher number of rock magnetic experiments. For highly heterogeneous rock collections, as in Chapter 3, a high amount of rock magnetic data is essential for the analysis of results. The success rates of palaointensity studies can be improved by following a strategic approach, where results from rock magnetic measurements are used to identify promising sites first, after which initial palaeointensity measurements are performed for all of these sites. Then, additional palaeointensity measurements can be conducted on sites where rocks showed good success rates in the initial intensity measurements. Performing multiple different methods of rock magnetic and palaeointensity experiments on sister-specimens of the same sample has been especially useful for analysis in this thesis and is highly recommended for future palaeointensity studies.

The presented studies of the Grenville dykes and the Volyn Traps provided opportunities to study some of the directional components that define the anomalous Ediacaran APWPs. Palaeodirections (and weak intensities) from both localities hint at a highly transitional field (Halls et al., 2015; Shcherbakova et al., 2020). The steep and shallow directional components of the Grenville dykes also showed similar VGP dispersion and intensities. This could be seen as support for periods of an equatorial dipole dominated field (Abrajevitch & Van der Voo, 2010). In contrast, these results argue against IITPW events (e.g., Kirschvink et al., 1997; Robert et al., 2021), or against a GAD-like TAF, where a latitudinal dependence would be expected for VGP dispersions and intensities. These implications are however based on a very low amount of data. New, high quality full-vector palaeomagnetic data and improved age estimates of other localities that show both steep and shallow components could add better constraints. Localities like the 572 Ma Catoctin Basalts (Meert et al., 1994) or the 543 - 581 Ma Sobral dykes (Guerreiro & Sial, 1982) could be promising targets for such studies. In addition, palaeointensity estimates for the early Ediacaran would be invaluable to assure that the geodynamo did not fully collapse just before the formation of the inner core.

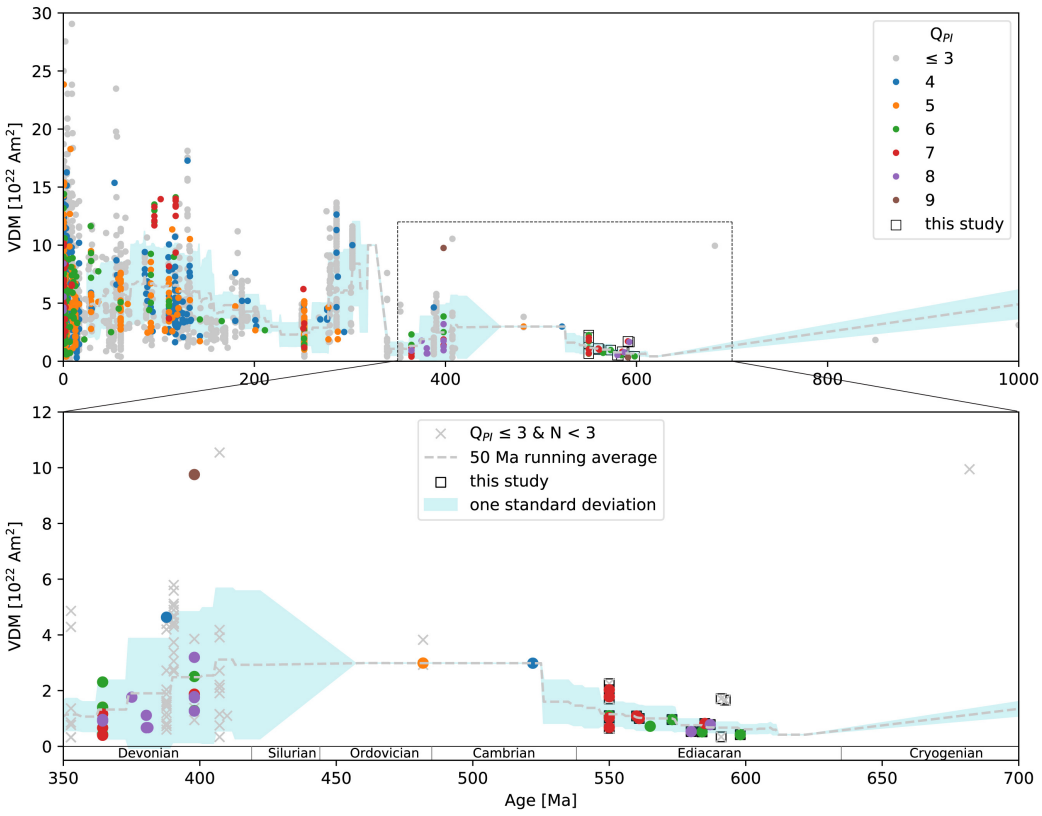

FIGURE 6.1: Virtual dipole moments between 700 Ma and present-day from the latest update of the PINT database (v8.0) with their associated Q_{PI} values (Bono et al., 2021). Dashed lines and shaded areas show a 20 Myr running average and one standard deviation, respectively. Dipole moments in grey with $Q_{PI} \leq 3$ were excluded for the determination of the running average.

Additional (high quality) data for the whole range of the Ediacaran would also be needed for future studies of Ediacaran PSV. In light of the unsolved controversy about the anomalous directions (and the possibility of a non-GAD-like field), the determination of VGP dispersion and its latitudinal dependence will have to take a more complex approach than the one taken in Chapter 5. Instead of using the magnetic palaeolatitude, such a study would have to be based on palaeolatitudes from palaeogeographic reconstructions that are based more on geological than palaeomagnetic constraints. A better defined field behaviour would also increase the chance that numerical geodynamo models can be found that are able to reproduce the Ediacaran field.

With the seemingly infinite amount of research that can still be undertaken in and around the Ediacaran period, the anomalous field at that time will continue to puzzle scientists for the foreseeable future.

References

Abrajevitch, A., & Van der Voo, R. (2010). Incompatible Ediacaran paleomagnetic directions suggest an equatorial geomagnetic dipole hypothesis. *Earth and Planetary Science Letters*, *293*(1-2), 164–170. https://doi.org/10.1016/j.epsl.2010.02.038

Aitken, M. J. (1988). Comparison of results for some samples technique , and the agreement is magnetism , determination of ancient direction deviation of a sample from the predicted value mere 1 % of its radius . One of the few signals Earth ' s field , initially by means of m. *Reviews of Geophysics*, *26*(1), 3–12.

Amit, H., Deschamps, F., & Choblet, G. (2015). Numerical dynamos with outer boundary heat flux inferred from probabilistic tomography - Consequences for latitudinal distribution of magnetic flux. *Geophysical Journal International*, *203*(2), 840–855. https://doi.org/10.1093/gji/ggv332

Aubert, J., Finlay, C. C., & Fournier, A. (2013). Bottom-up control of geomagnetic secular variation by the Earth's inner core. *Nature*, *502*(7470), 219–223. https://doi.org/10.1038/nature12574

Aubert, J., Gastine, T., & Fournier, A. (2017). Spherical convective dynamos in the rapidly rotating asymptotic regime. *Journal of Fluid Mechanics*, *813*, 558–593. https://doi.org/10.1017/jfm.2016.789

Aubert, J., Labrosse, S., & Poitou, C. (2009). Modelling the palaeo-evolution of the geodynamo. *Geophysical Journal International*, *179*(3), 1414–1428. https://doi.org/10.1111/j.1365-246X.2009.04361.x

Aubert, J., Tarduno, J. A., & Johnson, C. L. (2010). Observations and models of the long-term evolution of earth's magnetic field. *Space Science Reviews*, *155*(1-4), 337–370. https://doi.org/10.1007/s11214-010-9684-5

Aubert, J., & Wicht, J. (2004). Axial vs. equatorial dipolar dynamo models with implications for planetary magnetic fields. *Earth and Planetary Science Letters*, *221*(1-4), 409–419. https://doi.org/10.1016/S0012-821X(04)00102-5

Badro, J., Siebert, J., & Nimmo, F. (2016). An early geodynamo driven by exsolution of mantle components from Earth's core. *Nature*, *536*(7616), 326–328. https://doi.org/10.1038/nature18594

Barry, T. L., Self, S., Kelley, S. P., Reidel, S., Hooper, P., & Widdowson, M. (2010). New 40Ar/39Ar dating of the Grande Ronde lavas, Columbia River Basalts, USA: Implications for duration of flood basalt eruption episodes. *Lithos*, *118*(3-4), 213–222. https://doi.org/10.1016/j.lithos.2010.03.014

Bazhenov, M. L., Levashova, N. M., Meert, J. G., Golovanova, I. V., Danukalov, K. N., & Fedorova, N. M. (2016). Late Ediacaran magnetostratigraphy of Baltica: Evidence for Magnetic Field Hyperactivity? *Earth and Planetary Science Letters*, *435*, 124–135. https://doi.org/10.1016/j.epsl.2015.12.015

Béguin, A., Filippidi, A., de Lange, G. J., & de Groot, L. V. (2019). The evolution of the Levantine Iron Age geomagnetic Anomaly captured in Mediterranean sediments. *Earth and Planetary Science Letters*, *511*, 55–66. https://doi.org/10.1016/j.epsl.2019.01.021

Béguin, A., Paterson, G. A., Biggin, A. J., & de Groot, L. V. (2020). Paleointensity.org: An Online, Open Source, Application for the Interpretation of Paleointensity Data. *Geochemistry, Geophysics, Geosystems*, *21*(5), 1–15. https://doi.org/10.1029/2019GC008791

Biggin, A. J., Holme, R., Hounslow, M. H., & Davies, C. J. (2017). Going deep: Determining earth evolution from palaeomagnetism.

Biggin, A. J., Piispa, E. J., Pesonen, L. J., Holme, R., Paterson, G. A., Veikkolainen, T., & Tauxe, L. (2015). Palaeomagnetic field intensity variations suggest Mesoproterozoic inner-core nucleation. *Nature*, *526*(7572), 245–248. https://doi.org/10.1038/nature15523

Biggin, A. J., Steinberger, B., Aubert, J., Suttie, N., Holme, R., Torsvik, T. H., Van Der Meer, D. G., & Van Hinsbergen, D. J. (2012). Possible links between long-term geomagnetic variations and whole-mantle convection processes. *Nature Geoscience*, *5*(8), 526–533. https://doi.org/10.1038/ngeo1521

Biggin, A. J., Bono, R. K., Meduri, D. G., Sprain, C. J., Davies, C. J., Holme, R., & Doubrovine, P. V. (2020). Quantitative estimates of average geomagnetic axial dipole dominance in deep geological time. *Nature Communications*, *11*(1), 1–9. https://doi.org/10.1038/s41467-020-19794-7

Biggin, A. J., de Wit, M. J., Langereis, C. G., Zegers, T. E., Voûte, S., Dekkers, M. J., & Drost, K. (2011). Palaeomagnetism of Archaean rocks of the Onverwacht Group, Barberton Greenstone Belt (southern Africa): Evidence for a stable and potentially reversing geomagnetic field at ca. 3.5Ga. *Earth and Planetary Science Letters*, *302*(3-4), 314–328. https://doi.org/10.1016/j.epsl.2010.12.024

Biggin, A. J., & Paterson, G. A. (2014). A new set of qualitative reliability criteria to aid inferences on palaeomagnetic dipole moment variations through geological time. *Frontiers in Earth Science*, *2*, 1–9. https://doi.org/10.3389/feart.2014.00024

Biggin, A. J., Perrin, M., & Dekkers, M. J. (2007a). A reliable absolute palaeointensity determination obtained from a non-ideal recorder. *Earth and Planetary Science Letters*, *257*(3-4), 545–563. https://doi.org/10.1016/j.epsl.2007.03.017

Biggin, A. J., Perrin, M., & Shaw, J. (2007b). A comparison of a quasi-perpendicular method of absolute palaeointensity determination with other thermal and microwave techniques. *Earth and Planetary Science Letters*, *257*(3-4), 564–581. https://doi.org/10.1016/j.epsl.2007.03.016

Biggin, A. J., van Hinsbergen, D. J., Langereis, C. G., Straathof, G. B., & Deenen, M. H. (2008). Geomagnetic secular variation in the Cretaceous Normal Superchron and in the Jurassic. *Physics of the Earth and Planetary Interiors*, *169*(1-4), 3–19. https://doi.org/10.1016/j.pepi.2008.07.004

Biggin, A. J. (2010). Are systematic differences between thermal and microwave Thellier-type palaeointensity estimates a consequence of multidomain bias in the thermal results? *Physics of the Earth and Planetary Interiors*, *180*(1-2), 16–40. http://dx.doi.org/10.1016/j.pepi.2010.03.005

Böhnel, H., Biggin, A. J., Walton, D., Shaw, J., & Share, J. A. (2003). Microwave palaeointensities from a recent Mexican lava flow, baked sediments and reheated pottery. *Earth and Planetary Science Letters*, *214*(1-2), 221–236. https://doi.org/10.1016/S0012-821X(03)00370-4

Bono, R. K., Biggin, A. J., Holme, R., Davies, C. J., Meduri, D. G., & Bestard, J. (2020). Covariant Giant Gaussian Process Models With Improved Reproduction of Palaeosecular Variation. *Geochemistry, Geophysics, Geosystems*, *21*(8). https://doi.org/10.1029/2020GC008960

Bono, R. K., Paterson, G. A., Boon, A. V. D., Engbers, A., Grappone, J. M., Handford, B., Louise, M. A., Lloyd, S., Sprain, C. J., Thallner, D., & Biggin, A. J. (2021). The PINT database : A definitive compilation of absolute palaeomagnetic intensity determinations since 4 billion years ago. *Geophysical Journal International*.

Bono, R. K., & Tarduno, J. A. (2015). A stable ediacaran earth recorded by single silicate crystals of the ca. 565 Ma sept-Iles intrusion. *Geology*, *43*(2), 131–134. https://doi.org/10.1130/G36247.1

Bono, R. K., Tarduno, J. A., Nimmo, F., & Cottrell, R. D. (2019). Young inner core inferred from Ediacaran ultra-low geomagnetic field intensity. *Nature Geoscience*, *12*(2), 143–147. https://doi.org/10.1038/s41561-018-0288-0

Braginsky, S. I., & Roberts, P. H. (1995). Equations governing convection in earth's core and the geodynamo. *Geophysical & Astrophysical Fluid Dynamics*, *79*(1-4), 1–97. https://doi.org/10.1080/03091929508228992

Brown, M. C., Gratton, M. N., Shaw, J., Holme, R., & Soler, V. (2009). Microwave palaeointensity results from the Matuyama-Brunhes geomagnetic field reversal. *Physics of the Earth and Planetary Interiors*, *173*(1-2), 75–102. https://doi.org/10.1016/j.pepi.2008.11.001

Bryan, S. E., & Ernst, R. E. (2008). Revised definition of Large Igneous Provinces (LIPs). *Earth-Science Reviews*, *86*(1-4), 175–202. https://doi.org/10.1016/j.earscirev.2007.08.008

Bryan, S. E., Peate, I. U., Peate, D. W., Self, S., Jerram, D. A., Mawby, M. R., Marsh, J. S., & Miller, J. A. (2010). The largest volcanic eruptions on Earth. *Earth-Science Reviews*, *102*(3-4), 207–229. https://doi.org/10.1016/j.earscirev.2010.07.001

Burns, S. J., & Matter, A. (1993). Carbon isotope record of the latest Proterozoic from Oman. *Eclogae Geologicae Helvetiae*, *86*, 595–607.

Butler, R. F. (1992). *Paleomagnetism: magnetic domains to geologic terranes*. https://doi.org/10.5860/choice.29-5708

Canfield, D. E., Knoll, A. H., Poulton, S. W., Narbonne, G. M., & Dunning, G. R. (2020). Carbon isotopes in clastic rocks and the neoproterozoic carbon cycle. *American Journal of Science*, *320*(2), 97–124. https://doi.org/10.2475/02.2020.01

Carter-Stiglitz, B., Moskowitz, B., Solheid, P., Berquó, T. S., Jackson, M., & Kosterov, A. (2006). Low-temperature magnetic behavior of multidomian titanomagnetites: TM0, TM16, and TM35. *Journal of Geophysical Research: Solid Earth*, *111*(12), 1–12. https://doi.org/10.1029/2006JB004561

Cawood, P. A., McCausland, P. J., & Dunning, G. R. (2001). Opening Iapetus: Constraints from the Laurentian margin in Newfoundland. *Bulletin of the Geological Society of America*, *113*(4), 443–453. https://doi.org/10.1130/0016-7606(2001)113<0443:OICFTL>2.0.CO;2

Chadima and Hrouda. (2006). Remasoft 3.0: A user-friendly paleomagnetic data browser and analyzer. *Travaux Géophysiques*, *27*, 20–21.

Chen, M., & Liu, K. (1986). The geological significance of newly discovered microfossils from the Upper Sinian (Doushantuo Age) phosphorites (China). *Scientia Geologica Sinica*, *1*(1), 46–53.

Christensen, U. R., & Wicht, J. (2015). Numerical Dynamo Simulations. In *Treatise on geophysics: Second edition* (pp. 245–277). https://doi.org/10.1016/B978-0-444-53802-4.00145-7

Christensen, U. R., Aubert, J., & Hulot, G. (2010). Conditions for Earth-like geodynamo models. *Earth and Planetary Science Letters*, *296*(3-4), 487–496. https://doi.org/10.1016/j.epsl.2010.06.009

Coe, R. S. (1967). Paleo-intensities of the Earth's magnetic field determined from Tertiary and Quaternary rocks. *Journal of Geophysical Research*, *72*(12), 3247–3262. https://doi.org/10.1029/jz072i012p03247

Conbhuí, P., Williams, W., Fabian, K., Ridley, P., Nagy, L., & Muxworthy, A. R. (2018). Merrill: Micromagnetic earth related robust interpreted language laboratory. *Geochemistry, Geophysics, Geosystems*, *19*(4), 1080–1106. https://doi.org/10.1002/2017GC007279

Condon, D., Zhu, M., Bowring, S., Wang, W., Yang, A., & Jin, Y. (2005). U-Pb ages from the Neoproterozoic Doushanto Formation, China. *Science*, *308*, 95–98.

Constable, C. G., & Johnson, C. L. (1999). Anisotropic paleosecular variation models: Implications for geomagnetic field observables. *Physics of the Earth and Planetary Interiors*, *115*(1), 35–51. https://doi.org/10.1016/S0031-9201(99)00065-5

Constable, C. G., & Parker, R. L. (1988). Statistics of the geomagnetic secular variation for the past 5 m.y. *Journal of Geophysical Research*, *93*(B10), 11569–11581. https://doi.org/10.1029/jb093ib10p11569

Cox, A. (1962). Analysis of Present Geomagnetic Field for Comparison with Paleomagnetic Results. *Journal of geomagnetism and geoelectricity*, *13*(101), 101–112. https://doi.org/10.5636/jgg.13.101

Cox, A. (1970). Latitude Dependence of the Angular Dispersion of the Geomagnetic Field. *Geophysical Journal of the Royal Astronomical Society*, *20*(3), 253–269. https://doi.org/10.1111/j.1365-246X.1970.tb06069.x

Creer, K. M. (1962). The dispersion of the geomagnetic field due to secular variation and its determination for remote times from paleomagnetic data. *Journal of Geophysical Research*, *67*(9), 3461–3476. https://doi.org/10.1029/jz067i009p03461

Creer, K. M., Irving, E., & Runcorn, S. (1954). The Direction of the Geomagnetic in Great Field in Remote Epochs in Great Britain. *Journal of geomagnetism and geoelectricity*, *6*, 163–168.

Cromwell, G., Johnson, C. L., Tauxe, L., Constable, C. G., & Jarboe, N. A. (2018). PSV10: A Global Data Set for 0–10 Ma Time-Averaged Field and Paleosecular Variation Studies. *Geochemistry, Geophysics, Geosystems*, *19*(5), 1533–1558. https://doi.org/10.1002/2017GC007318

Cromwell, G., Tauxe, L., & Halldõrsson, S. A. (2015). New paleointensity results from rapidly cooled Icelandic lavas: Implications for Arctic geomagnetic field strength. *Journal of Geophysical Research: Solid Earth*, *120*(5), 2913–2934. https://doi.org/10.1002/2014JB011828

Cych, B., Morzfeld, M., & Tauxe, L. (2021). Bias Corrected Estimation of Paleointensity (BiCEP): An Improved Methodology for Obtaining Paleointensity Estimates. *Geochemistry, Geophysics, Geosystems*, *22*(8), 1–30. https://doi.org/10.1029/2021gc009755

Darwin, C. (1859). *On the Origin of Species by Means of Natural Selection* (1st ed.). John Murray.

Davies, C. J., Bono, R. K., Meduri, D. G., Aubert, J., Greenwood, S., & Biggin, A. J. (2021). Dynamo constraints on the long-term evolution of Earth's magnetic field strength. *Geophysical Journal International*, *228(1)*, 316–336. https://doi.org/10.1093/gji/ggab342

Davies, C. J., & Constable, C. G. (2014). Insights from geodynamo simulations into long-term geomagnetic field behaviour. *Earth and Planetary Science Letters*, *404*, 238–249. https://doi.org/10.1016/j.epsl.2014.07.042

Davies, C. J., Gubbins, D., Willis, A. P., & Jimack, P. K. (2008). Time-averaged paleomagnetic field and secular variation: Predictions from dynamo solutions based on lower mantle seismic tomography. *Physics of the Earth and Planetary Interiors*, *169*(1-4), 194–203. https://doi.org/10.1016/j.pepi.2008.07.021

Day, R., Fuller, M., & Schmidt, V. A. (1977). Hysteresis properties of titanomagnetites: Grain-size and compositional dependence. *Physics of the Earth and Planetary Interiors*, *13*(4), 260–267. https://doi.org/10.1016/0031-9201(77)90108-X

de Groot, L. V., Biggin, A. J., Dekkers, M. J., Langereis, C. G., & Herrero-Bervera, E. (2013). Rapid regional perturbations to the recent global geomagnetic decay revealed by a new Hawaiian record. *Nature Communications*, *4*, 1–7. https://doi.org/10.1038/ncomms3727

de Groot, L. V., Béguin, A., Kosters, M. E., van Rijsingen, E. M., Struijk, E. L., Biggin, A. J., Hurst, E. A., Langereis, C. G., & Dekkers, M. J. (2015). High paleointensities for the Canary Islands constrain the Levant geomagnetic high. *Earth and Planetary Science Letters*, *419*, 154–167. https://doi.org/10.1016/j.epsl.2015.03.020

Dekkers, M. J., & Böhnel, H. N. (2006). Reliable absolute palaeointensities independent of magnetic domain state. *Earth and Planetary Science Letters*, *248*(1-2), 508–517. https://doi.org/10.1016/j.epsl.2006.05.040

de Oliveira, W. P., Franco, D. R., Brandt, D., Ernesto, M., da Ponte Neto, C. F., Zhao, X., de Freitas, F. B. V., & Martins, R. S. (2018). Behavior of the paleosecular variation during the permian-carboniferous reversed superchron and comparisons to the low reversal frequency intervals since precambrian times. *Geochemistry, Geophysics, Geosystems*, *19*(4), 1035–1048. https://doi.org/10.1002/2017GC007262

Di Chiara, A., Tauxe, L., Levy, T. E., Najjar, M., Florindo, F., & Ben-Yosef, E. (2021). The strength of the Earth's magnetic field from pre-pottery to Pottery Neolithic, Jordan. *Proceedings of the National Academy of Sciences of the United States of America*, *118*(34). https://doi.org/10.1073/pnas.2100995118

Didenko, A. N., & Pechersky, D. M. (1989). Direction and intensity of the geomagnetic field in the Middle Devonian and Lower Ordovician: southern Mugodjary ophiolites (Urals). *Physics of the Earth and Planetary Interiors*, *58*(4), 289–306. https://doi.org/10.1016/0031-9201(89)90101-5

Doubrovine, P. V., Veikkolainen, T., Pesonen, L. J., Piispa, E., Ots, S., Smirnov, A. V., Kulakov, E. V., & Biggin, A. J. (2019). Latitude Dependence of Geomagnetic Paleosecular Variation and its Relation to the Frequency of Magnetic Reversals: Observations From the Cretaceous and Jurassic. *Geochemistry, Geophysics, Geosystems*, *20*(3), 1240–1279. https://doi.org/10.1029/2018GC007863

Driscoll, P. E. (2016). Simulating 2 Ga of geodynamo history. *Geophysical Research Letters*, *43*(11), 5680–5687. https://doi.org/10.1002/2016GL068858

Droser, M. L., Tarhan, L. G., & Gehling, J. G. (2017). The rise of animals in a changing environment: global ecological innovation in the late Ediacaran. *Annual Review of Earth and Planetary Sciences*, *45*, 593–617.

Dunlop, D. J., & Özdemir. (2007). Magnetizations in Rocks and Minerals. In *Treatise on geophysics: Second edition* (pp. 255–308). https://doi.org/10.1016/B978-0-444-53802-4.00102-0

Dunlop, D. J. (2002). Theory and application of the Day plot (M rs / M s versus H cr / H c) 2. Application to data for rocks, sediments, and soils. *Journal of Geophysical Research*, *107*(B3), 1–22. https://doi.org/10.1029/2001jb000487

Dunlop, D. J., & Argyle, K. S. (1997). Thermoremanence, anhysteretic remanence and susceptibility of submicron magnetites: Nonlinear field dependence and variation with grain size. *Journal of Geophysical Research*, *102*, 20199–20210.

Dunlop, D. J., & Özdemir, Ö. (1997). *Rock magnetism: Fundamentals and frontiers*. Cambridge University Press. https://doi.org/10.1017/CBO9780511612794

Dunlop, D. J., Özdemir, Ö., & Fuller, M. D. (1998). Rock Magnetism: Fundamentals and Frontiers. *Physics Today*, *51*(9), 64–66. https://doi.org/10.1063/1.882466

Dunlop, D. J., Zhang, B., & Özdemir, Ö. (2005). Linear and nonlinear Thellier paleointensity behavior of natural minerals. *Journal of Geophysical Research: Solid Earth*, *110*(1), 1–15. https://doi.org/10.1029/2004JB003095

Elming, S. Å., Kravchenko, S. N., Layer, P., Rusakov, O. M., Glevasskaya, A. M., Mikhailova, N. P., & Bachtadse, V. (2007). Palaeomagnetism and 40Ar/39Ar age determinations of the Ediacaran traps from the southwestern margin of the East European Craton, Ukraine: Relevance to the Rodinia break-up. *Journal of the Geological Society*, *164*(5), 969–982. https://doi.org/10.1144/0016-76492005-163

Engbers, Y. A., Biggin, A. J., & Bono, R. K. (2020). Elevated paleomagnetic dispersion at Saint Helena suggests long-lived anomalous behavior in the South Atlantic.

Proceedings of the National Academy of Sciences of the United States of America, *117*(31), 18258–18263. https://doi.org/10.1073/pnas.2001217117

Evans, D. A., & Raub, T. D. (2011). Chapter 7: Neoproterozoic glacial palaeolatitudes: A global update. In *Geological society memoir* (pp. 93–112). https://doi.org/10.1144/M36.7

Evans, D. A. (2003). True polar wander and supercontinents. *Tectonophysics*, *362*(1-4), 303–320. https://doi.org/10.1016/S0040-1951(02)000642-X

Evans, D. A. (2013). Reconstructing pre-Pangean supercontinents. *Bulletin of the Geological Society of America*, *125*(11-12), 1735–1751. https://doi.org/10.1130/B30950.1

Eyles, N., & Eyles, C. H. (1989). Glacially-influenced deep-marine sedimentation of the late Precambrian Gaskiers Formation, Newfoundland, Canada. *Sedimentology*, *36*, 601–620.

Fabian, K., Shcherbakov, V. P., & McEnroe, S. A. (2013). Measuring the Curie temperature. *Geochemistry, Geophysics, Geosystems*, *14*(4), 947–961. https://doi.org/10.1029/2012GC004440

Fabian, K. (2003). Some additional parameters to estimate domain state from isothermal magnetization measurements. *Earth and Planetary Science Letters*, *213*(3-4), 337–345. https://doi.org/10.1016/S0012-821X(03)00329-7

Fabian, K., & Leonhardt, R. (2010). Multiple-specimen absolute paleointensity determination: An optimal protocol including pTRM normalization, domain-state correction, and alteration test. *Earth and Planetary Science Letters*, *297*(1-2), 84–94. https://doi.org/10.1016/j.epsl.2010.06.006

Fisher, R. (1953). Dispersion on a Sphere. *Proceedings of the Royal Society A: Mathematical, Physical and Engineering Sciences*, *217*(1130), 295–305. https://doi.org/10.1098/rspa.1953.0064

Ford, T. D. (1958). Precambrian fossils from Charnwood Forest. *Proceedings of the Yorkshire Geological Society*, *31*, 211–217.

Fu, R. R., Lima, E. A., Volk, M. W., & Trubko, R. (2020). High-Sensitivity Moment Magnetometry With the Quantum Diamond Microscope. *Geochemistry, Geophysics, Geosystems*, *21*(8), 1–17. https://doi.org/10.1029/2020GC009147

Gallet, Y., Pavlov, V., & Korovnikov, I. (2019). Extreme geomagnetic reversal frequency during the Middle Cambrian as revealed by the magnetostratigraphy of the Khorbusuonka section (northeastern Siberia). *Earth and Planetary Science Letters*, *528*. https://doi.org/10.1016/j.epsl.2019.115823

Garland, G. D. (1979). The contributions of Carl Friedrich Gauss to geomagnetism. *Historia Mathematica*, *6*(1), 5–29. https://doi.org/10.1016/0315-0860(79)90100-9

Gehling, J. G., & Droser, M. L. (2018). Ediacaran scavenging as a prelude to predation. *Emerging Topics in Life Science*, *2*, 213–222.

Gerya, T. (2019). Geodynamics of the early Earth: Quest for the missing paradigm. *Geology*, *47*(10), 1006–1007. https://doi.org/10.1130/focus102019.1

Geyer, G., & Landing, E. (2017). The Precambrian-Phanerozoic and Ediacaran-Cambrian boundaries: A historical approach to a dilemma. *Geological Society Special Publication*, *448*(1), 311–349. https://doi.org/10.1144/SP448.10

Gissinger, C., Petitdemange, L., Schrinner, M., & Dormy, E. (2012). Bistability between equatorial and axial dipoles during magnetic field reversals. *Physical Review Letters*, *108*(23). https://doi.org/10.1103/PhysRevLett.108.234501

Glaessner, M. F. (1959). Precambrian Coelenterata from Australia, Africa and England. *Nature*, *183*, 1472–1473.

Glatzmaier, G. A., & Roberts, P. H. (1995). A three-dimensional self-consistent computer simulation of a geomagnetic field reversal. *Nature*, *337*(21), 203–209. https://doi.org/10.1038/377203a0

Glenn, D. R., Fu, R. R., Kehayias, P., Le Sage, D., Lima, E. A., Weiss, B. P., & Walsworth, R. L. (2017). Micrometer-scale magnetic imaging of geological samples using a quantum diamond microscope. *Geochemistry, Geophysics, Geosystems*, *18*(8), 3254–3267. https://doi.org/10.1002/2017GC006946

Glevasskaya, A. M., Kravchenko, S. N., & Kosovskiy, Y. A. (2006). Magnitostratigrafiya trappovoy formatsii yugo-zapadnoy okrainy Vostochno-Yevropeyskoy platformy [Magnetostratigraphy of the trap formation of the southwestern margin of the East European Platform]. *Geofizicheskiy zhurnal [Geophysical Journal]*, *28*(5), 121–130.

Glevasskaya, A. M., Mikhailova, N. P., & Kravchenko, S. N. (2000). Magnitostratigrafiya trappovoy formytsii Yugo-Vostochnoy okrainy Vostochno-Yevropeyskoy platformy [Magnetostratigraphy of trappean formation of the East- European platform]. *Geofizicheskiy zhurnal [Geophysical Journal]*, *22*(2), 3–18.

Grabau, A. W. (1922). The Sinian System. *Bulletin of the Geological Society of China*, *1*, 1–4.

Grappone, J. M., Biggin, A. J., Barrett, T. J., Hill, M. J., & Sprain, C. J. (2020). Comparison of Thermal and Microwave Paleointensity Estimates in Specimens Displaying Non-Ideal Behavior in Thellier-Style Paleointensity Experiments. *Journal of Geophysical Research: Solid Earth*, *125*(8). https://doi.org/10.1029/2020JB019802

Grappone, J. M., Biggin, A. J., & Hill, M. J. (2019). Solving the mystery of the 1960 Hawaiian lava flow: Implications for estimating Earth's magnetic field. *Geophysical Journal International*, *218*(3), 1796–1806. https://doi.org/10.1093/gji/ggz252

Gratton, M. N., Shaw, J., & Brown, L. L. (2007). Absolute palaeointensity variation during a precursor to the Matuyama-Brunhes transition recorded in Chilean lavas. *Physics of the Earth and Planetary Interiors*, *162*(1-2), 61–72. https://doi.org/10.1016/j.pepi.2007.03.003

Gratton, M. N., Shaw, J., & Herrero-Bervera, E. (2005). An absolute palaeointensity record from SOH1 lava core, Hawaii using the microwave technique. *Physics of the Earth and Planetary Interiors*, *148*(2-4), 193–214. https://doi.org/10.1016/j.pepi.2004.09.009

Greve, A., Hill, M. J., Turner, G. M., & Nilsson, A. (2017). The geomagnetic field intensity in New Zealand: Palaeointensities from Holocene lava flows of the Tongariro Volcanic Centre. *Geophysical Journal International*, *211*(2), 814–830. https://doi.org/10.1093/GJI/GGX327

Greve, A., Kars, M., & Dekkers, M. J. (2021). Fluid Accumulation, Migration and Anaerobic Oxidation of Methane Along a Major Splay Fault at the Hikurangi Subduction Margin (New Zealand): A Magnetic Approach. *Journal of Geophysical Research: Solid Earth*, *126*(2). https://doi.org/10.1029/2020JB020671

Gromme, C., Wright, T., & Peck, D. (1969). Magnetic Properties and Oxidation of Iron-Titanium Oxide Minerals in Alae and Makaopuhi Lava Lakes, Hawaii. *J Geophys Res*, *74*(22), 5277–5293. https://doi.org/10.1029/jb074i022p05277

Gubbins, D., & Herrero-Bervera, E. (2007). *Encyclopedia of GEOMAGNETISM AND PALEOMAGNETISM*.

Gubbins, D., Willis, A. P., & Sreenivasan, B. (2007). Correlation of Earth's magnetic field with lower mantle thermal and seismic structure. *Physics of the Earth and Planetary Interiors*, *162*(3-4), 256–260. https://doi.org/10.1016/j.pepi.2007.04.014

Guerreiro, S. D. C., & Sial, A. N. (1982). Paleomagnetismo de un enxame de diques do Cambriano, na regiao de Sobral, Ceara. *Annais do XXXII Congresso Brasileiro de Geologia Salvador*, 1609–1614.

Halgedahl, S. L., Day, R., & Fuller, M. (1980). The effect of cooling rate on the intensity of weak-field TRM in single- domain magnetite. *Journal of Geophysical Research*, *85*(B7), 3690–3698. https://doi.org/10.1029/JB085iB07p03690

Halls, H. C., Lovette, A., Hamilton, M., & Soderlund, U. (2015). A paleomagnetic and U-Pb geochronology study of the western end of the Grenville dyke swarm: Rapid changes in paleomagnetic field direction at ca. 585Ma related to polarity reversals? *Precambrian Research*, *257*(October), 137–166. https://doi.org/10.1016/j.precamres.2014.11.029

Halls, H. C., McArdle, N. J., Gratton, M. N., Hill, M. J., & Shaw, J. (2004). Microwave paleointensities from dyke chilled margins: A way to obtain long-term variations in geodynamo intensity for the last three billion years. *Physics of the Earth*

and Planetary Interiors, *147*(2-3 SPEC.ISS.), 183–195. https://doi.org/10.1016/j.pepi.2004.03.013

Halverson, G. P., & Hurtgen, M. T. (2007). Ediacaran growth of the marine sulfate reservoir. *Earth and Planetary Science Letters*, *263*, 32–44.

Hansma, J., Tohver, E., Yan, M., Trinajstic, K., Roelofs, B., Peek, S., Slotznick, S. P., Kirschvink, J., Playton, T., Haines, P., & Hocking, R. (2015). Late Devonian carbonate magnetostratigraphy from the Oscar and Horse Spring Ranges, Lennard Shelf, Canning Basin, Western Australia. *Earth and Planetary Science Letters*, *409*, 232–242. https://doi.org/10.1016/j.epsl.2014.10.054

Harrison, R. J., & Feinberg, J. M. (2008). FORCinel: An improved algorithm for calculating first-order reversal curve distributions using locally weighted regression smoothing. *Geochemistry, Geophysics, Geosystems*, *9*(5). https://doi.org/10.1029/2008GC001987

Hawkins, L. M., Anwar, T., Shcherbakova, V. V., Biggin, A. J., Kravchinsky, V. A., Shatsillo, A. V., & Pavlov, V. E. (2019). An exceptionally weak Devonian geomagnetic field recorded by the Viluy Traps, Siberia. *Earth and Planetary Science Letters*, *506*, 134–145. https://doi.org/10.1016/j.epsl.2018.10.035

Hawkins, L. M., Grappone, J. M., Sprain, C. J., Saengduean, P., Sage, E. J., Thomas-Cunningham, S., Kugabalan, B., & Biggin, A. J. (2021). Intensity of the Earth's magnetic field: Evidence for a Mid-Paleozoic dipole low. *Proceedings of the National Academy of Sciences of the United States of America*, *118*(34). https://doi.org/10.1073/pnas.2017342118

Hejda, P., & Zelinka, T. (1990). Modelling of hysteresis processes in magnetic rock samples using the Preisach diagram. *Physics of the Earth and Planetary Interiors*, *63*(1-2), 32–40. https://doi.org/10.1016/0031-9201(90)90057-5

Hill, M. J., Gratton, M. N., & Shaw, J. (2002). A comparison of thermal and microwave palaeomagnetic techniques using lava containing laboratory induced remanence. *Geophysical Journal International*, *151*(1), 157–163. https://doi.org/10.1046/j.1365-246X.2002.01745.x

Hill, M. J., Pan, Y., & Davies, C. J. (2008). An assessment of the reliability of palaeointensity results obtained from the Cretaceous aged Suhongtu section, Inner Mongolia, China. *Physics of the Earth and Planetary Interiors*, *169*(1-4), 76–88. https://doi.org/10.1016/j.pepi.2008.07.023

Hill, M. J., & Shaw, J. (1999). Palaeointensity results for historic lavas from Mt Etna using microwave demagnetization/remagnetization in a modified Thellier-type experiment. *Geophysical Journal International*, *139*(2), 583–590. https://doi.org/10.1046/j.1365-246X.1999.00980.x

Hill, M. J., & Shaw, J. (2000). Magnetic field intensity study of the 1960 Kilauea lava flow, Hawaii, using the microwave palaeointensity technique. *Geophysical Journal International*, *142*(2), 487–504. https://doi.org/10.1046/j.1365-246X.2000.00164.x

Hill, M. J., & Shaw, J. (2007). The use of the 'Kono perpendicular applied field method' in microwave palaeointensity experiments. *Earth, Planets and Space*, *59*(7), 711–716. https://doi.org/10.1186/BF03352734

Hodych, J. P., Cox, R. A., & Košler, J. (2004). An equatorial Laurentia at 550 Ma confirmed by Grenvillian inherited zircons dated by LAM ICP-MS in the Skinner Cove volcanics of western Newfoundland: Implications for inertial interchange true polar wander. *Precambrian Research*, *129*(1-2), 93–113. https://doi.org/10.1016/j.precamres.2003.10.012

Hoffman, K. A., & Biggin, A. J. (2005). A rapid multiple-sample approach to the determination of absolute paleointensity. *Journal of Geophysical Research: Solid Earth*, *110*(12), 1–9. https://doi.org/10.1029/2005JB003646

Hoffman, K. A., Constantine, V., & Morse, D. L. (1989). Determination of absolute multi-specimen procedure. *Letters to Nature*, *339*(May), 295–297.

Hoffman, P. F., Kaufman, A. J., Halverson, G. P., & Schrag, D. P. (1998). A neoproterozoic snowball earth. *Science*, *281*(5381), 1342–1346. https://doi.org/10.1126/science.281.5381.1342

Hoffman, P. F., & Li, Z. X. (2009). A palaeogeographic context for Neoproterozoic glaciation. *Palaeogeography, Palaeoclimatology, Palaeoecology*, *277*, 158–172.

Hofmann, H. J., Narbonne, G., & Aitken, M. J. (1990). Ediacaran remains from intertillite beds in northwestern Canada. *Geology*, *18*, 1305–1325.

Hospers, J. (1954). Rock Magnetism and Polar Wandering. *Nature*, *173*(441), 29–34.

Hounslow, M. W., Domeier, M., & Biggin, A. J. (2018). Subduction flux modulates the geomagnetic polarity reversal rate. *Tectonophysics*, *742-743*(May), 34–49. https://doi.org/10.1016/j.tecto.2018.05.018

Hsieh, W. P., Goncharov, A. F., Labrosse, S., Holtgrewe, N., Lobanov, S. S., Chuvashova, I., Deschamps, F., & Lin, J. F. (2020). Low thermal conductivity of iron-silicon alloys at Earth's core conditions with implications for the geodynamo. *Nature Communications*, *11*(1), 1–7. https://doi.org/10.1038/s41467-020-17106-7

Hyodo, H., & Dunlop, D. J. (1993). Effect of anisotropy on the paleomagnetic contact test for a Grenville Dike. *Journal of Geophysical Research*, *98*(B5), 7997–8017. https://doi.org/10.1029/92JB02915

Iosifidi, A. G., Bachtadse, V., Khramov, A. N., & Kusnetzova, A. V. (2000). Palaeomagnetic data for Vendian basalts from Ukraine. *International Conference on Problems of Geocosmos*, 74–75.

Irving, E., & Ward, M. A. (1964). A statistical model of the geomagnetic field. *Pure and Applied Geophysics PAGEOPH*, *57*(1), 47–52. https://doi.org/10.1007/BF00879707

Jackson, A., & Finlay, C. (2015). *Geomagnetic Secular Variation and Its Applications to the Core* (Vol. 5). Elsevier B.V. https://doi.org/10.1016/B978-0-444-53802-4.00099-3

Jackson, M., & Solheid, P. (2010). On the quantitative analysis and evaluation of magnetic hysteresis data. *Geochemistry, Geophysics, Geosystems*, *11*(4). https://doi.org/10.1029/2009GC002932

Jelínek, V., & Bucha, V. (1973). Precision A.C. bridge set for measuring magnetic susceptibility of rocks and its anisotropy. *Studia Geophysica et Geodaetica*, *17*(1), 36–48. https://doi.org/10.1007/BF01614027

Jenkins, R. J. F. (1981). The concept of an 'Ediacaran Period' and its stratigraphic significance in Australia. *Transactions of the Royal Society of South Australia*, *105*, 179–194.

Jensen, S., Gehling, J. G., & Droser, M. L. (1998). Ediacara-type fossils in Cambrian sediments. *Nature*, *393*, 567–569.

Johnson, C. L., Constable, C. G., Tauxe, L., Barendregt, R., Brown, L. L., Coe, R. S., Layer, P., Mejia, V., Opdyke, N. D., Singer, B. S., Staudigel, H., & Stone, D. B. (2008). Recent investigations of the 0-5 Ma geomagnetic field recorded by lava flows. *Geochemistry, Geophysics, Geosystems*, *9*(4), 1–31. https://doi.org/10.1029/2007GC001696

Johnson, C. L., & McFadden, P. (2015). The Time-Averaged Field and Paleosecular Variation. In *Treatise on geophysics: Second edition* (pp. 385–417). https://doi.org/10.1016/B978-0-444-53802-4.00105-6

Johnson, C. L., & Constable, C. G. (1996). Palaeosecular variation recorded by lava flows over the past five million years. *Philosophical Transactions of the Royal Society A: Mathematical, Physical and Engineering Sciences*, *354*(1704), 89–141. https://doi.org/10.1098/rsta.1996.0004

Johnson, C. L., Mittelholz, A., Langlais, B., Russell, C. T., Ansan, V., Banfield, D., Chi, P. J., Fillingim, M. O., Forget, F., Haviland, H. F., Golombek, M., Joy, S., Lognonné, P., Liu, X., Michaut, C., Pan, L., Quantin-Nataf, C., Spiga, A., Stanley, S., … Banerdt, W. B. (2020). Crustal and time-varying magnetic fields at the InSight landing site on Mars. *Nature Geoscience*, *13*(3), 199–204. https://doi.org/10.1038/s41561-020-0537-x

Kageyama, A., & Sato, T. (1995). Computer simulation of a magnetohydrodynamic dynamo. *Physics of Plasmas*, *2*(5).

Kirschvink, J. L. (1980). The least-squares line and plane and the analysis of palaeomagnetic data. *Geophysical Journal of the Royal Astronomical Society*, *62*(3), 699–718. https://doi.org/10.1111/j.1365-246X.1980.tb02601.x

Kirschvink, J. L., Ripperdan, R. L., & Evans, D. A. (1997). Evidence for a large-scale reorganization of Early Cambrian continental masses by inertial interchange true polar wander. *Science*, *277*(5325), 541–545.

Kissel, C., & Laj, C. (2004). Improvements in procedure and paleointensity selection criteria (PICRIT-03) for Thellier and Thellier determinations: Application to Hawaiian basaltic long cores. *Physics of the Earth and Planetary Interiors*, *147*(2-3 SPEC.ISS.), 155–169. https://doi.org/10.1016/j.pepi.2004.06.010

Kitahara, Y., Yamamoto, Y., Ohno, M., Kuwahara, Y., Kameda, S., & Hatakeyama, T. (2018). Archeointensity estimates of a tenth-century kiln: first application of the Tsunakawa–Shaw paleointensity method to archeological relics. *Earth, Planets and Space*, *70*(1), 1–16. https://doi.org/10.1186/s40623-018-0841-5

Knoll, A. H., Walter, M. R., Narbonne, G. M., & Christie-Blick, N. (2006). The Ediacaran period: A new addition to the geologic time scale. *Lethaia*, *39*(1), 13–30. https://doi.org/10.1080/00241160500409223

Koenigsberger, J. G. (1938). Natural residual magnetism of eruptive rocks. *Terr. Magn. Atmos. Elec.*, *43*, 119–320.

Königsberger, J. (1936). Die Abhängigkeit der natürlichen remanenten Magnetisierung bei Eruptivgesteinen von deren Alter und Zusammensetzung. *Beitr. Angew. Geophys.*, *5*, 193–246.

Kono, M. (1985). Changes in TRM and ARM in a basalt due to laboratory heating. *Physics of the Earth and Planetary Interiors1*, *46*(1-3), 1–8.

Kono, M., & Ueno, N. (1977). Paleointensity determination by a modified thellier method. *Physics of the Earth and Planetary Interiors*, *13*(4), 305–314. https://doi.org/10.1016/0031-9201(77)90114-5

Korte, M., & Constable, C. G. (2005). The geomagnetic dipole moment over the last 7000 years - New results from a global model. *Earth and Planetary Science Letters*, *236*(1-2), 348–358. https://doi.org/10.1016/j.epsl.2004.12.031

Korte, M., & Constable, C. (2011). Improving geomagnetic field reconstructions for 0-3ka. *Physics of the Earth and Planetary Interiors*, *188*(3-4), 247–259. https://doi.org/10.1016/j.pepi.2011.06.017

Korte, M., & Mandea, M. (2019). Geomagnetism: From Alexander von Humboldt to Current Challenges. *Geochemistry, Geophysics, Geosystems*, *20*(8), 3801–3820 . https://doi.org/10.1029/2019GC008324

Krása, D., Heunemann, C., Leonhardt, R., & Petersen, N. (2003). Experimental procedure to detect multidomain remanence during Thellier-Thellier experiments.

Physics and Chemistry of the Earth, *28*(16-19), 681–687. https://doi.org/10.1016/S1474-7065(03)00122-0

Kulakov, E. V., Sprain, C. J., Doubrovine, P. V., Smirnov, A. V., Paterson, G. A., Hawkins, L., Fairchild, L., Piispa, E. J., & Biggin, A. J. (2019). Analysis of an Updated Paleointensity Database (QPI-PINT) for 65–200 Ma: Implications for the Long-Term History of Dipole Moment Through the Mesozoic. *Journal of Geophysical Research: Solid Earth*, *124*(10), 9999–10022. https://doi.org/10.1029/2018JB017287

Kuzmenkova, O. F., Shumlyanskyy, L. V., Nosova, A. A., Voskoboynikova, T. V., & Grakovich, I. Y. (2011). Petrology and correlation of trap formations of the Vendian in the adjacent areas of Belarus and Ukraine. *Litasfiera [Lithosphere]*, *35*(January), 3–11.

Labrosse, S., & Macouin, M. (2003). The inner core and the geodynamo. *Comptes Rendus - Geoscience*, *335*(1), 37–50. https://doi.org/10.1016/S1631-0713(03)00013-0

Laj, C., Kissel, C., Davies, C., & Gubbins, D. (2011). Geomagnetic field intensity and inclination records from Hawaii and the Réunion Island: Geomagnetic implications. *Physics of the Earth and Planetary Interiors*, *187*(3-4), 170–187. https://doi.org/10.1016/j.pepi.2011.05.007

Landeau, M., Aubert, J., & Olson, P. (2017). The signature of inner-core nucleation on the geodynamo. *Earth and Planetary Science Letters*, *465*, 193–204. https://doi.org/10.1016/j.epsl.2017.02.004

Landing, E. (1994). Precambrian-Cambrian boundary global stratotype ratified and a new perspective of Cambrian time. *Geology*, *22*(179-182).

Lattard, D., Engelmann, R., Kontny, A., & Sauerzapf, U. (2006). Curie temperatures of synthetic titanomagnetites in the Fe-Ti-O system: Effects of composition, crystal chemistry, and thermomagnetic methods. *Journal of Geophysical Research: Solid Earth*, *111*(12). https://doi.org/10.1029/2006JB004591

Lawley, E. A. (1970). The intensity of the geomagnetic field in Iceland during neogene polarity transitions and systematic deviations. *Earth and Planetary Science Letters*, *10*(1), 145–149. https://doi.org/10.1016/0012-821X(70)90076-2

Le Goff, M., & Gallet, Y. (2004). A new three-axis vibrating sample magnetometer for continuous high-temperature magnetization measurements: Applications to paleo- and archeo-intensity determinations. *Earth and Planetary Science Letters*, *229*(1-2), 31–43. https://doi.org/10.1016/j.epsl.2004.10.025

Lee, J. S. (1924). Geology of the Gorge District of the Yangtze (from Ichang to Tzekuei) with special reference to the development of the Gorges. *Bulletin of the Geological Society of China*, *3*, 351–392.

Leonhardt, R. (2006). Analyzing rock magnetic measurements: The RockMagAnalyzer 1.0 software. *Computers and Geosciences*, *32*(9), 1420–1431. https://doi.org/10.1016/j.cageo.2006.01.006

Leonhardt, R., Heunemann, C., & Krasa, D. (2004a). Analyzing absolute paleointensity determinations: Acceptance criteria and the software ThellierTool4.0. *Geochemistry, Geophysics, Geosystems*, *5*(12), 1–11. https://doi.org/10.1029/2004GC000807

Leonhardt, R., Krása, D., & Coe, R. S. (2004b). Multidomain behavior during Thellier paleointensity experiments: A phenomenological model. *Physics of the Earth and Planetary Interiors*, *147*(2-3 SPEC.ISS.), 127–140. https://doi.org/10.1016/j.pepi.2004.01.009

Leonhardt, R., & Soffel, H. C. (2002). A reversal of the Earth's magnetic field recorded in mid-Miocene lava flows of Gran Canaria: Paleointensities. *Journal of Geophysical Research: Solid Earth*, *107*(B11), EPM 5–1–EPM 5–11. https://doi.org/10.1029/2001jb000949

Levashova, N. M., Golovanova, I. V., Rudko, D. V., Danukalov, K. N., Rudko, S. V., Yu, S. R., & Meert, J. G. (2021). Late Ediacaran magnetic field hyperactivity: Quantifying the reversal frequency in the Zigan Formation, Southern Urals, Russia. *Gondwana Research*, *94*, 133–142. https://doi.org/10.1016/j.gr.2021.02.018

Levi, S., & Merrill, R. T. (1976). A comparison of ARM and TRM in magnetite. *Earth and Planetary Science Letters*, *32*, 171–184.

Lhuillier, F., Hulot, G., Gallet, Y., & Schwaiger, T. (2019). Impact of inner-core size on the dipole field behaviour of numerical dynamo simulations. *Geophysical Journal International*, *218*(1), 179–189. https://doi.org/10.1093/gji/ggz146

Li, Y. X., & Kodama, K. P. (2016). Detecting and correcting for paleomagnetic inclination shallowing of sedimentary rocks: A review. *Frontiers in Earth Science*, *4*(February), 1–6. https://doi.org/10.3389/feart.2016.00007

Li, Z. X., Bogdanova, S. V., Collins, A. S., Davidson, A., De Waele, B., Ernst, R. E., Fitzsimons, I. C., Fuck, R. A., Gladkochub, D. P., Jacobs, J., Karlstrom, K. E., Lu, S., Natapov, L. M., Pease, V., Pisarevsky, S. A., Thrane, K., & Vernikovsky, V. (2008). Assembly, configuration, and break-up history of Rodinia: A synthesis. *Precambrian Research*, *160*(1-2), 179–210. https://doi.org/10.1016/j.precamres.2007.04.021

Li, Z. X., Mitchell, R. N., Spencer, C. J., Ernst, R., Pisarevsky, S., Kirscher, U., & Murphy, J. B. (2019). Decoding Earth's rhythms: Modulation of supercontinent cycles by longer superocean episodes. *Precambrian Research*, *323*(January), 1–5. https://doi.org/10.1016/j.precamres.2019.01.009

Li, Z. X., Evans, D. A., & Halverson, G. P. (2013). Neoproterozoic glaciations in a revised global palaeogeography from the breakup of Rodinia to the assembly of Gondwanaland. *Sedimentary Geology*, *294*, 219–232. https://doi.org/10.1016/j.sedgeo.2013.05.016

Linnemann, U., Ovtcharova, M., Schaltegger, M., Gaertner, A., Hautmann, M., Geyer, G., & Al., E. (2019). New high-resolution age data from the Ediacaran-Cambrian boundary indicate rapid, ecologically driven onset of the Cambrian explosion. *Terra Nova*, *31*, 49–58.

Llanos, M. P. I., Tait, J. A., Popov, V., & Abalmassova, A. (2005). Palaeomagnetic data from Ediacaran (Vendian) sediments of the Arkhangelsk region, NW Russia: An alternative apparent polar wander path of Baltica for the Late Proterozoic-Early Palaeozoic. *Earth and Planetary Science Letters*, *240*(3-4), 732–747. https://doi.org/10.1016/j.epsl.2005.09.063

Lloyd, S. J., Biggin, A. J., Halls, H., & Hill, M. J. (2021a). First Palaeointensity Data from the Cryogenian and their potential implications for Inner Core Nucleation Age. *Geophysical Journal International*. https://doi.org/10.1093/gji/ggab090

Lloyd, S. J., Paterson, G. A., Thallner, D., & Biggin, A. J. (2021b). Improvements to the Shaw-Type Absolute Palaeointensity Method. *Frontiers in Earth Science*, *9*(July), 1–11. https://doi.org/10.3389/feart.2021.701863

Lowrie, W., & Fichtner, A. (2020). *Fundamentals of Geophysics* (Vol. 79). https://doi.org/10.1017/9781108685917

Masters, T. G., Johnson, S., Laske, G., & Bolton, H. (1996). A gaussian model for simulated geomagnetic field reversals. *Philosophical Transactions of the Royal Society of London. Series A: Mathematical, Physical and Engineering*, *354*. https://doi.org/10.1098/rsta.1996.0054

Mawson, D., & Sprigg, R. C. (1959). Subdivision of the Adelaide System. *The Australian Journal of Science*, *13*, 69–72.

McCausland, P. J. A., & Hodych, J. P. (1998). Paleomagnetism of the 550 Ma Skinner Cove volcanics of western Newfoundland and the opening of the Iapetus Ocean. *Earth and Planetary Science Letters*, *163*(1-4), 15–29. https://doi.org/10.1016/S0012-821X(98)00171-X

McCausland, P. J. A. (1998). *Palaeomagnetism of the Skinner Cove Formation of Western Newfoundland and the birth of the Iapetus Ocean* (Thesis (Masters) March). Memorial University of Newfoundland. research.library.mun.ca/6554/

McCausland, P. J. A., Hankard, F., Van der Voo, R., & Hall, C. M. (2011). Ediacaran paleogeography of Laurentia: Paleomagnetism and 40Ar-39Ar geochronology of the 583Ma Baie des Moutons syenite, Quebec. *Precambrian Research*, *187*(1-2), 58–78. https://doi.org/10.1016/j.precamres.2011.02.004

McCausland, P. J. A., Van der Voo, R., & Hall, C. M. (2007). Circum-Iapetus paleogeography of the Precambrian-Cambrian transition with a new paleomagnetic constraint from Laurentia. *Precambrian Research*, *156*(3-4), 125–152. https://doi.org/10.1016/j.precamres.2007.03.004

McClelland, E., & Briden, J. C. (1996). An improved methodology for Thellier-type paleointensity determination in igneous rocks and its usefulness for verifying primary thermoremanence. *Journal of Geophysical Research: Solid Earth*, *101*(B10), 21995–22013. https://doi.org/10.1029/96jb02113

McElhinny, M. W., & McFadden, P. L. (1997). Palaeosecular variation over the past 5 Myr based on a new generalized database. *Geophysical Journal International*, *131*(2), 240–252. https://doi.org/10.1111/j.1365-246X.1997.tb01219.x

McFadden, P. L., & McElhinny, M. W. (1984). A physical model for palaeosecular variation. *Geophysical Journal of the Royal Astronomical Society*, *78*(3), 809–830. https://doi.org/10.1111/j.1365-246X.1984.tb05072.x

McFadden, P. L., & Merrill, R. T. (1984). Lower mantle convection and geomagnetism. *Journal of Geophysical Research*, *89*(B5), 3354–3362. https://doi.org/10.1029/JB089iB05p03354

McFadden, P. L., Merrill, R. T., & McElhinny, M. W. (1988). Dipole/quadrupole family modeling of paleosecular variation. *Journal of Geophysical Research*, *93*(B10). https://doi.org/10.1029/jb093ib10p11583

McFadden, P. L., Merrill, R. T., McElhinny, M. W., & Sunhee Lee. (1991). Reversals of the Earth's magnetic field and temporal variations of the dynamo families. *Journal of Geophysical Research*, *96*(B3), 3923–3933. https://doi.org/10.1029/90JB02275

McKenzie, N. R., Hughes, N. C., Myrow, P., Choi, D. K., & Park, T. (2011). Trilobites and zircons link north China with the eastern Himalaya during the Cambrian. *Geology*, *39*, 591–594.

Meduri, D. G., Biggin, A. J., Davies, C. J., Bono, R. K., Sprain, C. J., & Wicht, J. (2021). Numerical Dynamo Simulations Reproduce Paleomagnetic Field Behavior. *Geophysical Research Letters*, *48*(5), 1–10. https://doi.org/10.1029/2020GL090544

Meert, J. G., & Lieberman, B. S. (2004). A palaeomagnetic and palaeobiogeographical perspective on latest Neoproterozoic and early Cambrian tectonic events. *Journal of the Geological Society*, *161*(3), 477–487. https://doi.org/10.1144/0016-764903-107

Meert, J. G., van der Voo, R., & Payne, T. W. (1994). Paleomagnetism of the Catoctin volcanic province: a new Vendian- Cambrian apparent polar wander path for North America. *Journal of Geophysical Research*, *99*(B3), 4625–4641. https://doi.org/10.1029/93JB01723

Meert, J. G. (2014). Ediacaran-Early Ordovician paleomagnetism of Baltica: A review. *Gondwana Research*, *25*(1), 159–169. https://doi.org/10.1016/j.gr.2013.02.003

Meert, J. G., Levashova, N. M., Bazhenov, M. L., & Landing, E. (2016). Rapid changes of magnetic Field polarity in the late Ediacaran: Linking the Cambrian evolutionary radiation and increased UV-B radiation. *Gondwana Research*, *34*, 149–157. https://doi.org/10.1016/j.gr.2016.01.001

Meert, J. G., Walderhaug, H. J., Torsvik, T. H., & Hendriks, B. W. (2007). Age and paleomagnetic signature of the Alnø carbonatite complex (NE Sweden): Additional controversy for the Neoproterozoic paleoposition of Baltica. *Precambrian Research*, *154*(3-4), 159–174. https://doi.org/10.1016/j.precamres.2006.12.008

Melnychuk, V. (2010). Evolutionary model of Early Vendian trap magmatism in the southwestern part of the Eastern European platform (in Ukrainian). *Geologichnyy zhurnal*, *1*, 77–85.

Merrill, R. T., McElhinny, M. W., & McFadden, P. L. (1998). Chapter 3 Foundations of paleomagnetism. In *International geophysics* (pp. 69–114). https://doi.org/10.1016/S0074-6142(96)80004-0

Merrill, R. T., & McFadden, P. L. (2003). The geomagnetic axial dipole field assumption. *Physics of the Earth and Planetary Interiors*, *139*(3-4), 171–185. https://doi.org/10.1016/j.pepi.2003.07.016

Mittal, T., Knezek, N., Arveson, S. M., McGuire, C. P., Williams, C. D., Jones, T. D., & Li, J. (2020). Precipitation of multiple light elements to power Earth's early dynamo. *Earth and Planetary Science Letters*, *532*, 116030. https://doi.org/10.1016/j.epsl.2019.116030

Monster, M. W., de Groot, L. V., Biggin, A. J., & Dekkers, M. J. (2015). The performance of various palaeointensity techniques as a function of rock magnetic behaviour - A case study for La Palma. *Physics of the Earth and Planetary Interiors*, *242*, 36–49. https://doi.org/10.1016/j.pepi.2015.03.004

Murthy, G. S. (1971). The Paleomagnetism of Diabase Dikes from the Grenville Province. *Canadian Journal of Earth Sciences*, *8*(7), 802–812. https://doi.org/10.1139/e71-075

Murthy, G. S., Gower, C., Tubrett, M., & Patzold, R. (1992). Paleomagnetism of Eocambrian Long Range dykes and Double Mer Formation from Labrador, Canada. *Canadian Journal of Earth Sciences*, *29*(6), 1224–1234.

Muxworthy, A. R. (2010). Revisiting a domain-state independent method of palaeointensity determination. *Physics of the Earth and Planetary Interiors*, *179*(1-2), 21–31. https://doi.org/10.1016/j.pepi.2010.01.003

Nagata, T. (1943). The natural remanent magnetism of volcanic rocks and its relation to geomagnetic phenomena. *Bull. Earthquake Res. Inst. Univ. Tokyo*, *21*, 1–196.

Nagata, T. (1953). *Rock Magnetism* (1st ed.). Maruzen, Tokyo.

Nagata, T., Arai, Y., & Momose, K. (1963). Secular Variation of the Geomagnetic Total Force during the Last 5000 Years. *Journal of Geophysical Research*, *68*(18), 5277–5281. https://doi.org/10.1029/j.2156-2202.1963.tb00005.x

Nagy, L., Williams, W., Muxworthy, A. R., Fabian, K., Almeida, T. P., Conbhuí, P., & Shcherbakov, V. P. (2017). Stability of equidimensional pseudo–single-domain magnetite over billion-year timescales. *Proceedings of the National Academy of Sciences of the United States of America*, *114*(39), 10356–10360. https://doi.org/10.1073/pnas.1708344114

Nairn, A. E., Perry, T. A., Ressetar, R., & Rogers, S. (1987). A paleomagnetic study of the Dokhan volcanic formation and younger granites, eastern desert of Egypt. *Journal of African Earth Sciences*, *6*(3), 353–365. https://doi.org/10.1016/0899-5362(87)90078-9

Narbonne, G. M., Laflamme, M., Trusler, P. W., Dalrymple, R. W., & Greentree, C. (2014). Deep-water Ediacaran fossils from northwestern Canada: taphonomy, ecology, and evolution. *Journal of Paleontology*, *88*, 207–223.

Narbonne, G. M., Myrow, P., Landing, E., & Anderson, M. M. (1987). A candidate stratotype for the Precambrian-Cambrian boundary, Fortune Head, Burin Peninsula, southeastern Newfoundland. *Canadian Journal of Earth Sciences*, *24*, 277–293.

Nawrocki, J., Boguckij, A., & Katinas, V. (2004). New Late Vendian palaeogeography of Baltica and the TESZ. *Geological Quarterly*, *48*(4), 309–316.

Néel, L. (1949). Théorie du traînage magnétique des ferromagnétiques en grains fins avec application aux terres cuites. *Annales de Géophysique*, *5*, 99–136.

Néel, L. (1955). Some theoretical aspects of rock magnetism. *Phil. Mag. Suppl.*, *4*, 225–239.

Nosova, A. A., Larionova, Y. O., Veretennikov, N. V., & Yutkina, E. V. (2008). Correlation of neoproterozoic volcanism in the southeastern White Sea region and western Urals: New age data on the Solozero basalts (Onega Graben). *Doklady Earth Sciences*, *419*(1), 303–307. https://doi.org/10.1134/S1028334X08020268

Ogg, J. G. (2012). Geomagnetic polarity time scale. *The Geologic Time Scale 2012*, 85–113. https://doi.org/10.1016/B978-0-444-59425-9.00005-6

Olson, P., & Christensen, U. R. (2006). Dipole moment scaling for convection-driven planetary dynamos. *Earth and Planetary Science Letters*, *250*(3-4), 561–571. https://doi.org/10.1016/j.epsl.2006.08.008

Olson, P., Deguen, R., Hinnov, L. A., & Zhong, S. (2013). Controls on geomagnetic reversals and core evolution by mantle convection in the Phanerozoic. *Physics of the Earth and Planetary Interiors*, *214*, 87–103. https://doi.org/10.1016/j.pepi.2012.10.003

O'Rourke, J. G., Korenaga, J., & Stevenson, D. J. (2017). Thermal evolution of Earth with magnesium precipitation in the core. *Earth and Planetary Science Letters*, *458*, 2618–2644. https://doi.org/10.1016/j.epsl.2016.10.057

Özdemir, Ö., & Moskowitz, B. M. (1992). Magnetostriction in Aluminium-substituted titanomagnetites. *Geophysical Research Letters*, *19*, 2361–2364.

Paterson, G. A. (2011). A simple test for the presence of multidomain behavior during paleointensity experiments. *Journal of Geophysical Research: Solid Earth*, *116*(10). https://doi.org/10.1029/2011JB008369

Paterson, G. A., Biggin, A. J., Hodgson, E., & Hill, M. J. (2015). Thellier-type paleointensity data from multidomain specimens. *Physics of the Earth and Planetary Interiors*, *245*, 117–133. https://doi.org/10.1016/j.pepi.2015.06.003

Paterson, G. A., Heslop, D., & Muxworthy, A. R. (2010). Deriving confidence in paleointensity estimates. *Geochemistry, Geophysics, Geosystems*, *11*(7). https://doi.org/10.1029/2010GC003071

Paterson, G. A., Heslop, D., & Pan, Y. (2016). The pseudo-Thellier palaeointensity method: New calibration and uncertainty estimates. *Geophysical Journal International*, *207*(3), 1596–1608. https://doi.org/10.1093/gji/ggw349

Paterson, G. A., Muxworthy, A. R., Yamamoto, Y., & Pan, Y. (2017). Bulk magnetic domain stability controls paleointensity fidelity. *Proceedings of the National Academy of Sciences of the United States of America*, *114*(50), 13120–13125. https://doi.org/10.1073/pnas.1714047114

Paterson, G. A., Tauxe, L., Biggin, A. J., Shaar, R., & Jonestrask, L. C. (2014). On improving the selection of Thellier-type paleointensity data. *Geochemistry, Geophysics, Geosystems*, *15*(4), 1180–1192. https://doi.org/10.1002/2013GC005135

Paterson, G. A., Zhao, X., Jackson, M., & Heslop, D. (2018). Measuring, Processing, and Analyzing Hysteresis Data. *Geochemistry, Geophysics, Geosystems*, *19*(7), 1925–1945. https://doi.org/10.1029/2018GC007620

Peng, S., Babcock, L., & Ahlberg, P. (2020). *The Cambrian Period*. BV. https://doi.org/10.1016/b978-0-12-824360-2.00019-x

Petrovský, E. D., & Kapička, A. (2006). On determination of the Curie point from thermomagnetic curves. *Journal of Geophysical Research: Solid Earth*, *111*(12), 1–10. https://doi.org/10.1029/2006JB004507

Pike, C. R., Roberts, A., & Verosub, K. L. (1999). Characterizing interactions in fine magnetic particle systems using first order reversal curves. *Journal of Applied Physics*, *85*.

Piper, J. D. (1981). Palaeomagnetic study of the (Late Precambrian) West Greenland kimberlite-lamprophyre suite: definition of the Hadrynian Track. *Physics of the Earth and Planetary Interiors*, *27*(3), 164–186. https://doi.org/10.1016/0031-9201(81)90014-5

Pisarevsky, S. A., McCausland, P. J., Hodych, J. P., O'Brien, S. J., Tait, J. A., & Murphy, J. B. (2012). Paleomagnetic study of the late Neoproterozoic Bull Arm and Crown Hill formations (Musgravetown Group) of eastern Newfoundland: Implications for Avalonia and West Gondwana paleogeography. *Canadian Journal of Earth Sciences*, *49*(1), 308–327. https://doi.org/10.1139/e11-045

Pisarevsky, S. A., Murphy, J. B., Cawood, P. A., & Collins, A. S. (2008). Late Neoproterozoic and early Cambrian palaeogeography: Models and problems. *Geological Society Special Publication*, *294*, 9–31. https://doi.org/10.1144/SP294.2

Popov, V. V., Iosifidi, A., Khramov, A., Tait, J., & Bachtadse, V. (2002). Paleomagnetism of Upper Vendian sediments from the Winter Coast, White Sea region, Russia: Implications for the paleogeography of Baltica during Neoproterozoic times. *Journal of Geophysical Research: Solid Earth*, *107*(B11), EPM 10–1–EPM 10–8. https://doi.org/10.1029/2001jb001607

Popov, V. V., Khramov, A. N., & Bachtadse, V. (2005). Palaeomagnetism, magnetic stratigraphy, and petromagnetism of the Upper Vendian sedimentary rocks in the sections of the Zolotitsa River and in the Verkhotina Hole, Winter Coast of the White Sea, Russia. *Russian Journal of Earth Sciences*, *7*(2), 1–29. https://doi.org/10.2205/2005ES000167

Poprawa, P., Krzemińska, E., Pacześna, J., & Amstrong, R. (2020). Geochronology of the Volyn volcanic complex at the western slope of the East European Craton – Relevance to the Neoproterozoic rifting and the break-up of Rodinia/Pannotia. *Precambrian Research*, *346*(November 2019), 105817. https://doi.org/10.1016/j.precamres.2020.105817

Pozzo, M., Davies, C., Gubbins, D., & Alfè, D. (2012). Thermal and electrical conductivity of iron at Earth's core conditions. *Nature*, *485*(7398), 355–358. https://doi.org/10.1038/nature11031

Prevot, M., Mankinen, E. A., Coe, R. S., & Gromme, C. S. (1985). The Steens Mountain (Oregon) geomagnetic polarity transition 2. Field intensity variations and discussion of reversal models (USA) . *Journal of Geophysical Research*, *90*(B12). https://doi.org/10.1029/jb090ib12p10417

Prévot, M. (1981). Some aspects of magnetic viscosity in subaerial and submarine volcanic rocks. *Geophysical Journal of the Royal Astronomical Society*, *66*(1), 169–192. https://doi.org/10.1111/j.1365-246X.1981.tb05952.x

Pu, J. P., Bowring, S. A., Ramezani, J., Myrow, P., & Raub, T. D. (2016). Dodging snowballs: geochronology of the Gaskiers glaciation and the first appearance of the Ediacaran biota. *Geology*, *44*, 955–958.

Quidelleur, X., & Courtillot, V. (1996). On low-degree spherical harmonic models of paleosecular variation. *Physics of the Earth and Planetary Interiors*, *95*(1-2), 55–77. https://doi.org/10.1016/0031-9201(95)03115-4

Quidelleur, X., Valet, J.-P. .-., Courtillot, V., & Hulot, G. (1994). Long-term geometry of the geomagnetic field for the last five million years: An updated secular variation database. *Geophysical Research Letters*, *21*(15), 1639–1642. https://doi.org/10.1029/94GL01105

Rapalini, A. E., Tohver, E., Bettucci, L. S., Lossada, A. C., Barcelona, H., & Pérez, C. (2015). The late Neoproterozoic Sierra de las Ánimas Magmatic Complex and Playa Hermosa Formation, southern Uruguay, revisited: Paleogeographic implications of new paleomagnetic and precise geochronologic data. *Precambrian Research*, *259*, 143–155. https://doi.org/10.1016/j.precamres.2014.11.021

Riisager, P., & Riisager, J. (2001). Detecting multidomain magnetic grains in Thellier palaeointensity experiments. *Physics of the Earth and Planetary Interiors*, *125*(1-4), 111–117. https://doi.org/10.1016/S0031-9201(01)00236-9

Robert, B., Besse, J., Blein, O., Greff-Lefftz, M., Baudin, T., Lopes, F., Meslouh, S., & Belbadaoui, M. (2017). Constraints on the Ediacaran inertial interchange true polar wander hypothesis: A new paleomagnetic study in Morocco (West African Craton). *Precambrian Research*, *295*, 90–116. https://doi.org/10.1016/j.precamres.2017.04.010

Robert, B., Domeier, M., & Jakob, J. (2021). On the origins of the Iapetus ocean. *Earth-Science Reviews*, 103791. https://doi.org/10.1016/j.earscirev.2021.103791

Roerts, A. P., Tauxe, L., Heslop, D., Zhao, X., & Jiang, Z. (2018). A critical appraisal of the "Day" diagram. *Journal of Geophysical Research: Solid Earth*, *123*, 2618–2644. https://doi.org/10.1002/2017JB015247

Rolph, T. C., & Shaw, J. (1985). A new method of palaeofield magnitude correction for thermally altered samples and its application to Lower Carboniferous lavas. *Geophysical Journal of the Royal Astronomical Society*, *80*(3), 773–781. https://doi.org/10.1111/j.1365-246X.1985.tb05124.x

Sagnotti, L. (2013). Demagnetization Analysis in Excel (DAIE). An open source workbook in Excel for viewing and analyzing demagnetization data from paleomagnetic discrete samples and u-channels. *Annals of Geophysics*, *56*(1). https://doi.org/10.4401/ag-6282

Sahoo, S. K., Planavsky, N. J., Jiang, G., Kendall, B., Owens, J. D., Wang, X., & Al., E. (2016). Oceanic oxygenation events in the anoxic Ediacaran ocean. *Geobiology*, *14*, 457–468.

Savchenko, N. A., Bernadskaya, L. G., Dolgova, V. I., Butirlinov, N. V., Bugaenko, V. N., Semka, V. A., Bondarenko, V. G., & Plakhotny, L. G. (1984). *Palaeovolcanism of the Ukraine.* Naukova Dumka, Kiev, pp. 252. (in Russian).

Schmidt, P. W., & Williams, G. E. (2010). Ediacaran palaeomagnetism and apparent polar wander path for Australia: No large true polar wander. *Geophysical Journal International*, *182*(2), 711–726. https://doi.org/10.1111/j.1365-246X.2010.04652.x

Schnepp, E., Thallner, D., Arneitz, P., & Leonhardt, R. (2020a). New archeomagnetic secular variation data from Central Europe, II: Intensities. *Physics of the Earth and Planetary Interiors*, *309*(November), 106605. https://doi.org/10.1016/j.pepi.2020.106605

Schnepp, E., Thallner, D., Arneitz, P., Mauritsch, H., Scholger, R., Rolf, C., & Leonhardt, R. (2020b). New archaeomagnetic secular variation data from Central Europe. I: Directions. *Geophysical Journal International*, *220*(2), 1023–1044. https://doi.org/10.1093/gji/ggz492

Schwarz, E. J., & Symons, D. T. (1969). Geomagnetic intensity between 100 million and 2500 million years ago. *Physics of the Earth and Planetary Interiors*, *2*(1), 11–18. https://doi.org/10.1016/0031-9201(69)90014-4

Selkin, P. A., Gee, J. S., & Tauxe, L. (2007). Nonlinear thermoremanence acquisition and implications for paleointensity data. *Earth and Planetary Science Letters*, *256*(1-2), 81–89. https://doi.org/10.1016/j.epsl.2007.01.017

Shaar, R., & Tauxe, L. (2015). Instability of thermoremanence and the problem of estimating the ancient geomagnetic field strength from non-single-domain recorders. *Proceedings of the National Academy of Sciences of the United States of America*, *112*(36), 11187–11192. https://doi.org/10.1073/pnas.1507986112

Shaw, J. (1975). Strong Geomagnetic Fields during a single Icelandic Polarity Transition. *Geophysical Journal of the Royal Astronomical Society*, *40*(3), 345–350. https://doi.org/10.1111/j.1365-246X.1975.tb04136.x

Shaw, J., Walton, D., Yang, S., Rolph, T. C., & Share, J. A. (1996). Microwave archaeointensities from Peruvian ceramics. *Geophysical Journal International*, *124*(1), 241–244. https://doi.org/10.1111/j.1365-246X.1996.tb06367.x

Shcherbakov, V. P., Gribov, S. K., Aphinogenova, N. A., & Tselmovich, V. A. (2020). Single Phase Oxidation of Ferrimagnetic Grains as a Cause of L-Shaped Arai – Nagata Diagrams. *Izvestiya, Physics of the Solid Earth*, *56*(5), 665–674. https://doi.org/10.1134/S1069351320050109

Shcherbakov, V. P., Gribov, S. K., Lhuillier, F., Aphinogenova, N. A., & Tsel'movich, V. A. (2019). On the Reliability of Absolute Palaeointensity Determinations on Basaltic Rocks Bearing a Thermochemical Remanence. *Journal of Geophysical Research: Solid Earth*, *124*(8), 7616–7632. https://doi.org/10.1029/2019JB017873

Shcherbakov, V. P., Shcherbakova, V. V., Vinogradov, Y. K., & Heider, F. (2001). Thermal stability of pTRMs created from different magnetic states. *Physics of the*

Earth and Planetary Interiors, *126*(1-2), 59–73. https://doi.org/10.1016/S0031-9201(01)00244-8

Shcherbakova, V. V., Bakhmutov, V. G., Thallner, D., Shcherbakov, V. P., Zhidkov, G. V., & Biggin, A. J. (2020). Ultra-low palaeointensities from East European Craton, Ukraine support a globally anomalous palaeomagnetic field in the Ediacaran. *Geophysical Journal International*, *220*(3), 1920–1946. https://doi.org/10.1093/gji/ggz566

Shcherbakova, V. V., Biggin, A. J., Veselovskiy, R. V., Shatsillo, A. V., Hawkins, L. M., Shcherbakov, V. P., & Zhidkov, G. V. (2017). Was the Devonian geomagnetic field dipolar or multipolar? Palaeointensity studies of Devonian igneous rocks from the Minusa Basin (Siberia) and the Kola Peninsula dykes, Russia. *Geophysical Journal International*, *209*(2), 1265–1286. https://doi.org/10.1093/gji/ggx085

Shcherbakova, V. V., Shcherbakov, V. P., & Heider, F. (2000). Properties of partial thermoremanent magnetization in pseudosingle domain and multidomain magnetite grains. *Journal of Geophysical Research: Solid Earth*, *105*(B1), 767–781. https://doi.org/10.1029/1999jb900235

Shumlyanskyy, L. V., Andreasson, P., Melnychuk, V., & Derevska, K. (2006). Vik formuvannya bazal'tiv volyns'koyi trapovoyi formatsiyi za poperednimy rezul' tatamy doslidzhennya tsyrkoniv ion-ionnym mikrozondovym metodom [Age of formation of the basalts of the Volynian flood basalt province: preliminary results of investigation. *Geokhimiya ta rudoutvorennya*, *24*, 21–29.

Shumlyanskyy, L. V., Nosova, A., Billström, K., Söderlund, U., Andréasson, P. G., & Kuzmenkova, O. (2016). The U–Pb zircon and baddeleyite ages of the Neoproterozoic Volyn Large Igneous Province: implication for the age of the magmatism and the nature of a crustal contaminant. *Gff*, *138*(1), 17–30. https://doi.org/10.1080/11035897.2015.1123289

Smirnov, A. V., Kulakov, E. V., Foucher, M. S., & Bristol, K. E. (2017). Intrinsic paleointensity bias and the long-term history of the geodynamo. *Science Advances*, *3*(2). https://doi.org/10.1126/sciadv.1602306

Smirnov, A. V., Tarduno, J. A., & Evans, D. A. (2011). Evolving core conditions ca. 2 billion years ago detected by paleosecular variation. *Physics of the Earth and Planetary Interiors*, *187*(3-4), 225–231. https://doi.org/10.1016/j.pepi.2011.05.003

Smirnov, A. V., & Tarduno, J. A. (2005). Thermochemical remanent magnetization in Precambrian rocks: Are we sure the geomagnetic field was weak? *Journal of Geophysical Research: Solid Earth*, *110*(6), 1–12. https://doi.org/10.1029/2004JB003445

Smith, P. J. (1967). Estimates of the Devonian geomagnetic field intensity in Scotland. *U. S. Geological Survey Professional Paper*, D164–D168. https://doi.org/10.1111/j.1365-246X.1979.tb00171.x

Sokolov, B. S. (1952). On the age of the old sedimentary cover of the Russian platform. *Izvestiya Akademii Nauk SSSR, Seriya geologicheskaya*, *5*, 21–31.

Sprain, C. J., Biggin, A. J., Davies, C. J., Bono, R. K., & Meduri, D. G. (2019). An assessment of long duration geodynamo simulations using new paleomagnetic modeling criteria (QPM). *Earth and Planetary Science Letters*, *526*. https://doi.org/10.1016/j.epsl.2019.115758

Sprain, C. J., Swanson-Hysell, N. L., Fairchild, L. M., & Gaastra, K. (2018). A field like today's? The strength of the geomagnetic field 1.1 billion years ago. *Geophysical Journal International*, *213*(3), 1969–1983. https://doi.org/10.1093/gji/ggy074

Starchenko, S. V. (2017). Energy geodynamo parameters compatible with analytical, numerical, paleomagnetic models and observations. *Izvestiya, Physics of the Solid Earth*, *53*(6), 908–921. https://doi.org/10.1134/S1069351317050135

Storey, M., Duncan, R. A., & Tegner, C. (2007). Timing and duration of volcanism in the North Atlantic Igneous Province: Implications for geodynamics and links to the Iceland hotspot. *Chemical Geology*, *241*(3-4), 264–281. https://doi.org/10.1016/j.chemgeo.2007.01.016

Stratyhrafiya verkhnoho proterozoyu Ukrayiny u dvokh tomakh. T.1: Stratyhrafiya verkhnoho proterozoyu, p. t. m. U. [o. t. U. P., & in two volumes. Vol.1: Stratigraphy of the Upper Proterozoic. in Ukrainian], P. U. (2013). National Academy of Sciences of Ukraine, Institute of Geological Sciences. *ed. Gozhyk, P.F., Kiev, Logos*.

Suttie, N., Holme, R., Hill, M., & Shaw, J. (2011). Consistent treatment of errors in archaeointensity implies rapid decay of the dipole prior to 1840. *Earth and Planetary Science Letters*, *304*, 13–21. https://doi.org/10.1016/j.epsl.2011.02.010

Suttie, N., Shaw, J., & Hill, M. J. (2010). Direct demonstration of microwave demagnetization of a whole rock sample with minimal heating. *Earth and Planetary Science Letters*, *292*(3-4), 357–362. https://doi.org/10.1016/j.epsl.2010.02.002

Symons, D. T. A., & Chiasson, A. D. (1991). Cambrian apparent polar wander path for North America. *Canadian Journal of Earth Sciences*, *28*(3), 355–363.

Tanaka, H., & Komuro, N. (2009). The Shaw paleointensity method: Can the ARM simulate the TRM alteration? *Physics of the Earth and Planetary Interiors*, *173*(3-4), 269–278. https://doi.org/10.1016/j.pepi.2009.01.003

Tanczyk, E. I., Lapointe, P., Morris, W. A., & Schmidt, P. W. (1987). A paleomagnetic study of the layered mafic intrusion at Sept- Iles, Quebec (Canada). *Canadian Journal of Earth Sciences*, *24*(7), 1431–1438. https://doi.org/10.1139/e87-135

Tarduno, J. A., Blackman, E. G., & Mamajek, E. E. (2014). Detecting the oldest geodynamo and attendant shielding from the solar wind: Implications for habitability. *Physics of the Earth and Planetary Interiors*, *233*, 68–87. https://doi.org/10.1016/j.pepi.2014.05.007

Tarduno, J. A., & Cottrell, R. D. (2005). Dipole strength and variation of the time-averaged reversing and nonreversing geodynamo based on Thellier analyses of single plagioclase crystals. *Journal of Geophysical Research: Solid Earth*, *110*(11), 1–10. https://doi.org/10.1029/2005JB003970

Tarduno, J. A., Cottrell, R. D., Davis, W. J., Nimmo, F., & Bono, R. K. (2015). A Hadean to Paleoarchean geodynamo recorded by single zircon crystals. *Science*, *349*, 521–524. https://doi.org/10.1126/science.aaa9114

Tarduno, J. A., Cottrell, R. D., Watkeys, M. K., Hofmann, A., Doubrovine, P. V., Mamajek, E. E., Liu, D., Sibeck, D. G., Neukirch, L. P., & Usui, Y. (2010). Geodynamo, solar wind, and magnetopause 3.4 to 3.45 billion years ago. *Science*, *327*(5970), 1238–1240. https://doi.org/10.1126/science.1183445

Tauxe, L., Gee, J. S., Steiner, M. B., & Staudigel, H. (2013). Paleointensity results from the Jurassic: New constraints from submarine basaltic glasses of ODP Site 801C. *Geochemistry, Geophysics, Geosystems*, *14*(10), 4718–4733. https://doi.org/10.1002/ggge.20282

Tauxe, L., Pick, T., & Kok, Y. S. (1995). Relative paleointensity in sediments: A Pseudo-Thellier Approach. *Geophysical Research Letters*, *22*(21), 2885–2888. https://doi.org/10.1029/95GL03166

Tauxe, L., Santos, C., Cych, B., Zhao, X., Roberts, A., Nagy, L., & Williams, W. (2020). Understanding non-ideal paleointensity recording in igneous rocks: Insights from aging experiments on lava samples and the causes and consequences of 'fragile' curvature in Arai plots. *Geochemistry, Geophysics, Geosystems*, 1–24. https://doi.org/10.1029/2020gc009423

Tauxe, L., Shaar, R., Jonestrask, L., Swanson-Hysell, N. L., Minnett, R., Koppers, A. A., Constable, C. G., Jarboe, N., Gaastra, K., & Fairchild, L. (2016). PmagPy: Software package for paleomagnetic data analysis and a bridge to the Magnetics Information Consortium (MagIC) Database. *Geochemistry, Geophysics, Geosystems*, *17*(6), 2450–2463. https://doi.org/10.1002/2016GC006307

Tauxe, L., & Yamazaki, T. (2015). Paleointensities. In *Treatise on geophysics: Second edition* (pp. 461–509). https://doi.org/10.1016/B978-0-444-53802-4.00107-X

Tauxe, L. (2010). *Essentials of Paleomagnetism*. University of California Press. https://doi.org/10.1525/9780520946378

Tauxe, L., Bertram, H. N., & Seberino, C. (2002). Physical interpretation of hysteresis loops: Micromagnetic modeling of fine particle magnetite. *Geochemistry, Geophysics, Geosystems*, *3*(10). https://doi.org/10.1029/2001GC000241

Tauxe, L., & Kent, D. V. (2004). A simplified statistical model for the geomagnetic field and the detection of shallow bias in paleomagnetic inclinations: Was the ancient magnetic field dipolar? In *Geophysical monograph series* (pp. 101–115). https://doi.org/10.1029/145GM08

Tauxe, L., & Staudigel, H. (2004). Strength of the geomagnetic field in the cretaceous normal superchron: New data from submarine basaltic glass of the troodos ophiolite. *Geochemistry, Geophysics, Geosystems*, *5*(2). https://doi.org/10.1029/2003GC000635

Teanby, N., Laj, C., Gubbins, D., & Pringle, M. (2002). A detailed palaeointensity and inclination record from drill core SOH1 on Hawaii. *Physics of the Earth and Planetary Interiors*, *131*(2), 101–140. https://doi.org/10.1016/S0031-9201(02)00032-8

Tegner, C., Andersen, T. B., Kjøll, H. J., Brown, E. L., Hagen-Peter, G., Corfu, F., Planke, S., & Torsvik, T. H. (2019). A Mantle Plume Origin for the Scandinavian Dyke Complex: A "Piercing Point" for 615 Ma Plate Reconstruction of Baltica? *Geochemistry, Geophysics, Geosystems*, *20*(2), 1075–1094. https://doi.org/10.1029/2018GC007941

Termier, H., & Termier, G. (1960). L'Ediacarien, premier etage paleontologique. *Revue generale des sciences pures et appliques et bulletin de l'Association Francaise pour l'Avancement des Sciences*, *67*, 79–87.

Thallner, D., Biggin, A. J., & Halls, H. (2021a). An extended period of extremely weak geomagnetic field suggested by palaeointensities from the Ediacaran Grenville dykes (SE Canada). *Earth and Planetary Science Letters*, (568). https://doi.org/ https://doi.org/10.1016/j.epsl.2021.117025

Thallner, D., Biggin, A. J., McCausland, P. J. A., & Fu, R. R. (2021b). New paleointensities from the Skinner Cove Formation, Newfoundland, suggest a changing state of the geomagnetic field at the Ediacaran-Cambrian transition. *Journal of Geophysical Research: Solid Earth*, (126). https://doi.org/10.1029/2021jb022292

Thellier, E. (1938). *Sur l'aimantation des terres cuites et ses applications geophysiques* (Doctoral dissertation). Universite de Paris.

Thellier, E. (1941). Sur la vérification d'une méthode permettant de déterminer l'intensité du champ terrestre dans le passé. *Comptes rendus de l'Académie des sciences (Paris)*, *212*, 281–283.

Thellier, E., & Thellier, O. (1959). Sur l'intensité du champ magnétique terrestre dans le passé historique et géologique. *Annales de Geophysique*.

Thompson, M. D., Grunow, A. M., & Ramezani, J. (2007). Late Neoproterozoic paleogeography of the Southeastern New England Avalon Zone: Insights from U-Pb geochronology and paleomagnetism. *Bulletin of the Geological Society of America*, *119*(5-6), 681–696. https://doi.org/10.1130/B26014.1

Tikoo, S. M., Weiss, B. P., Cassata, W. S., Shuster, D. L., Gattacceca, J. Ô., Lima, E. A., Suavet, C., Nimmo, F., & Fuller, M. D. (2014). Decline of the lunar core dynamo. *Earth and Planetary Science Letters*, *404*, 89–97. https://doi.org/10.1016/j.epsl.2014.07.010

Torsvik, T. H. (1998). Polar Wander and the Cambrian. *Science*, *279*(5347), 9a–9. https://doi.org/10.1126/science.279.5347.9a

Torsvik, T. H., Van der Voo, R., Preeden, U., Mac Niocaill, C., Steinberger, B., Doubrovine, P. V., van Hinsbergen, D. J., Domeier, M., Gaina, C., Tohver, E., Meert, J. G., McCausland, P. J., & Cocks, L. R. M. (2012). Phanerozoic Polar Wander, Palaeogeography and Dynamics. *Earth-Science Reviews*, *114*(3-4), 325–368. https://doi.org/10.1016/j.earscirev.2012.06.007

Trindade, R. I. F., Macouin, M., Poitou, C., Chauvin, A., & Hill, M. (2012). Earth ' s magnetic field strength in the Early Cambrian : Thellier paleointensity estimates of Itabaiana mafic dykes , Northeast Brazil. *EGU General Assembly 2012, held 22-27 in Vienna, Austria*, *14*, 12542. https://doi.org/2012EGUGA..1412542T

Tsai, V. C., & Stevenson, D. J. (2007). Theoretical constraints on true polar wander. *Journal of Geophysical Research: Solid Earth*, *112*(5). https://doi.org/10.1029/2005JB003923

Tsunakawa, H., & Shaw, J. (1994). The Shaw method of palaeointensity determinations and its application to recent volcanic rocks. *Geophysical Journal International*, *118*(3), 781–787. https://doi.org/10.1111/j.1365-246X.1994.tb03999.x

Tunyi, I. (1986). Palaeointensity of the Geomagnetic Field Determined from Igneous Rocks of the West Carpathians. *Journal of geomagnetism and geoelectricity*, *38*(12), 1279–1295. https://doi.org/10.5636/jgg.38.1279

Ueno, N., Irving, E., & McNutt, R. H. (1975). Paleomagnetism of the Whitestone Anorthosite and Diorite, the Grenville Polar Track, and Relative Motions of the Laurentian and Baltic Shields. *Canadian Journal of Earth Sciences*, *12*(2), 209–226. https://doi.org/10.1139/e75-019

Ueno, N. (1995). Geomagnetic Paleointensity Experiment on Igneous and Metamorphic Rocks From Enderby Land in Napier Complex, Antarctica. *Proceedings of the NIPR Symposium on Antarctic Geosciences*, *8*, 193–200.

Valet, J. P., Kidane, T., Soler, V., Brassart, J., Courtillot, V., & Meynadier, L. (1998). Remagnetization in lava flows recording pretransitional directions. *Journal of Geophysical Research: Solid Earth*, *103*(5), 9755–9775. https://doi.org/10.1029/97jb03544

Van Alstine, D. R., & Gillett, S. L. (1979). Paleomagnetism of Upper Precambrian sedimentary rocks from the Desert Range, Nevada. *Journal of Geophysical Research*, *84*(B9), 4490–4500. https://doi.org/10.1029/JB084iB09p04490

Van der Voo, R. (1990). The reliability of paleomagnetic data. *Tectonophysics*, *184*(1), 1–9. https://doi.org/10.1016/0040-1951(90)90116-P

van der Boon, A., Biggin, A. J., Hounslow, M., Thallner, D., Nawrocki, J., Wojcik, K., Paszkovsky, M., Koenigshof, P., Kabanov, P., Gouwy, S., & Vandenberg, R. (n.d.). A persistent non-uniformitarian paleomagnetic field in the Devonian? *Earth-Science Reviews*.

Vandamme, D. (1994). A new method to determine paleosecular variation. *Physics of the Earth and Planetary Interiors*, *85*(1-2), 131–142. https://doi.org/10.1016/0031-9201(94)90012-4

van Zijl, J. S., Graham, K. W., & Hales, A. L. (1962). The Palaeomagnetism of the Stormberg Lavas, II. The Behaviour of the Magnetic Field During a Reversal. *Geophysical Journal of the Royal Astronomical Society*, *7*(2), 169–182. https://doi.org/10.1111/j.1365-246X.1962.tb00366.x

Veikkolainen, T., Pesonen, L., & Korhonen, K. (2014a). An analysis of geomagnetic field reversals supports the validity of the Geocentric Axial Dipole (GAD) hypothesis in the Precambrian. *Precambrian Research*, *244*(1), 33–41. https://doi.org/10.1016/j.precamres.2013.10.009

Veikkolainen, T., & Pesonen, L. J. (2014). Palaeosecular variation, field reversals and the stability of the geodynamo in the Precambrian. *Geophysical Journal International*, *199*(3), 1515–1526. https://doi.org/10.1093/gji/ggu348

Veikkolainen, T., Pesonen, L. J., & Evans, D. A. (2014b). PALEOMAGIA: A PHP/MYSQL database of the Precambrian paleomagnetic data. *Studia Geophysica et Geodaetica*, *58*(3), 425–441. https://doi.org/10.1007/s11200-013-0382-0

Vella, J., Carlut, J., Valet, J. P., Goff, M. L., Soler, V., & Lopes, F. (2017). Remagnetization of lava flows spanning the last geomagnetic reversal. *Geophysical Journal International*, *210*(2), 1281–1293. https://doi.org/10.1093/gji/ggx212

Waggoner, B. (2003). The Ediacaran biotas in space and time. *Integrative and Comparative Biology*, *43*, 104–113.

Walcott, C. D. (1914). *Abrupt appearance of the Cambrian fauna of the North American Continent* (Vol. 57). Smithsomian Institution. https://repository.si.edu/handle/10088/23425

Walton, D., Share, J. A., Rolph, T. C., & Shaw, J. (1993). Microwave demagnetisation. *Geophysical Research Letters*, *20*, 109–111.

Walton, D., Shaw, J., Share, J. A., & Hakes, J. (1992). Microwave demagnetisation. *J. apppl. Phys*, *71*, 1549–1551.

Wang, Z., & Van der Voo, R. (2004). The hysteresis properties of multidomain magnetite and titanomagnetite/titanomaghemite in mid-ocean ridge basalts. *Earth and Planetary Science Letters*, *220*(1-2), 175–184. https://doi.org/10.1016/S0012-821X(04)00052-4

Wang, Z., Wang, J., Suess, E., Wang, G., Chen, C., & Xiao, S. (2017). Silicified glendonites in the Ediacaran Doushantuo Formation (South China) and their potential paleoclimatic implications. *Geology*, *45*(2), 115–118. https://doi.org/10.1130/G38613.1

Wehland, F., Alt-Epping, U., Braun, S., & Appel, E. (2005). Quality of pTRM acquisition in pyrrhotite bearing contact-metamorphic limestones: Possibility of a continuous record of Earth magnetic field variations. *Physics of the Earth and Planetary Interiors*, *148*(2-4), 157–173. https://doi.org/10.1016/j.pepi.2004.08.008

Wicht, J. (2005). Palaeomagnetic interpretation of dynamo simulations. *Geophysical Journal International*, *162*(2), 371–380. https://doi.org/10.1111/j.1365-246X.2005.02665.x

Wicht, J., & Meduri, D. G. (2016). A gaussian model for simulated geomagnetic field reversals. *Physics of the Earth and Planetary Interiors*, *259*, 45–60. https://doi.org/10.1016/j.pepi.2016.07.007

Wicht, J., & Sanchez, S. (2019). Advances in geodynamo modelling. *Geophysical and Astrophysical Fluid Dynamics*, *113*(1-2), 2–50. https://doi.org/10.1080/03091929.2019.1597074

Wicht, J., Stellmach, S., & Harder, H. (2015). Numerical dynamo simulations: From basic concepts to realistic models. In *Handbook of geomathematics: Second edition* (pp. 779–834). https://doi.org/10.1007/978-3-642-54551-1_16

Wilkinson, M. D., Dumontier, M., Aalbersberg, I. J., Appleton, G., Axton, M., Baak, A., Blomberg, N., Boiten, J. W., da Silva Santos, L. B., Bourne, P. E., Bouwman, J., Brookes, A. J., Clark, T., Crosas, M., Dillo, I., Dumon, O., Edmunds, S., Evelo, C. T., Finkers, R., … Mons, B. (2016). Comment: The FAIR Guiding Principles for scientific data management and stewardship. *Scientific Data*, *3*, 1–9. https://doi.org/10.1038/sdata.2016.18

Williams, W., & Dunlop, D. J. (1989). Three-dimensional micromagnetic modelling of ferromagnetic domain structure. *Nature*, *337*(6208), 634–637. https://doi.org/10.1038/337634a0

Williams, W., Evans, M. E., & Krása, D. (2010). Micromagnetics of paleomagnetically significant mineral grains with complex morphology. *Geochemistry, Geophysics, Geosystems*, *11*(2), 1–8. https://doi.org/10.1029/2009GC002828

Williams, W., & Wright, T. M. (1998). High-resolution micromagnetic models of fine grains of magnetite. *Journal of Geophysical Research: Solid Earth*, *103*(B12), 30537–30550. https://doi.org/10.1029/98jb01120

Wilson, L. R. (1961). The Thermal Demagnetization of Natural Magnetic Moments in Rocks. *Geophysical Journal of the Royal Astronomical Society*, *5*(1), 45–58. https://doi.org/10.1111/j.1365-246X.1961.tb02928.x

Xiao, S., Muscente, A. D., Chen, L., Zhou, C., Schiffbauer, J. D., Wood, A. D., & Al., E. (2014). The Weng'an biota and the Ediacaran radiation of multicellular eukaryotes. *National Science Review*, *1*, 498–520.

Xiao, S., & Narbonne, G. (2020). The Ediacaran Period. In *Geologic time scale 2020* (pp. 521–561). BV. https://doi.org/10.1016/b978-0-12-824360-2.00018-8

Yamamoto, Y., Ishizuka, O., Sudo, M., & Uto, K. (2007a). 40Ar/39 ages and palaeomagnetism of transitionally magnetized volcanic rocks in the Society Islands, French Polynesia: Raiatea excursion in the upper-Gauss Chron. *Geophysical Journal International*, *169*(1), 41–59. https://doi.org/10.1111/j.1365-246X.2006.03277.x

Yamamoto, Y., Tsunakawa, H., Shaw, J., & Kono, M. (2007b). Paleomagnetism of the Datong monogenetic volcanoes in China: Paleodirection and paleointensity during the middle to early Brunhes Chron. *Earth, Planets and Space*, *59*(7), 727–746. https://doi.org/10.1186/BF03352736

Yamamoto, Y., Tsunakawa, H., & Shibuya, H. (2003). Palaeointensity study of the Hawaiian 1960 lava: Implications for possible causes of erroneously high intensities. *Geophysical Journal International*, *153*(1), 263–276. https://doi.org/10.1046/j.1365-246X.2003.01909.x

Yamamoto, Y., & Shaw, J. (2008). Development of the microwave LTD-DHT Shaw method for absolute paleointensity determination. *Physics of the Earth and Planetary Interiors*, *170*(1-2), 15–23. https://doi.org/10.1016/j.pepi.2008.06.021

Yamamoto, Y., Shibuya, H., Tanaka, H., & Hoshizumi, H. (2010). Geomagnetic paleointensity deduced for the last 300kyr from Unzen Volcano, Japan, and the dipolar nature of the Iceland Basin excursion. *Earth and Planetary Science Letters*, *293*(3-4), 236–249. https://doi.org/10.1016/j.epsl.2010.02.024

Yang, T., Chou, Y. M., Ferré, E. C., Dekkers, M. J., Chen, J., Yeh, E. C., & Tanikawa, W. (2020). Faulting Processes Unveiled by Magnetic Properties of Fault Rocks. *Reviews of Geophysics*, *58*(4), 1–60. https://doi.org/10.1029/2019RG000690

Yoshihara, A., & Hamano, Y. (2004). Paleomagnetic constraints on the Archean geomagnetic field intensity obtained from komatiites of the Barberton and Belingwe greenstone belts, South Africa and Zimbabwe. *Precambrian Research*, *131*, 111–142. https://doi.org/10.1016/j.precamres.2004.01.003

Yu, Y. (2010). Paleointensity determination using anhysteretic remanence and saturation isothermal remanence. *Geochemistry, Geophysics, Geosystems*, *11*(2), 1–12. https://doi.org/10.1029/2009GC002804

Yu, Y., Dunlop, D. J., & Özdemir, Ö. (2003). Are ARM and TRM analogs? Thellier analysis of ARM and pseudo-Thellier analysis of TRM. *Earth and Planetary Science Letters*, *205*(3-4), 325–336. https://doi.org/10.1016/S0012-821X(02)01060-9

Yu, Y., & Tauxe, L. (2005). Testing the IZZI protocol of geomagnetic field intensity determination. *Geochemistry, Geophysics, Geosystems*, *6*(5). https://doi.org/10.1029/2004GC000840

Yu, Y., Tauxe, L., & Genevey, A. (2004). Toward an optimal geomagnetic field intensity determination technique. *Geochemistry, Geophysics, Geosystems*, *5*(2). https://doi.org/10.1029/2003GC000630

Zhang, F., Xiao, S., Romaniello, S. J., Hardisty, D., Li, C., Melezhik, V., & Al., E. (2019). Global marine redox changes drove the rise and fall of early animals. *Geobiology*, *17*, 594–610.

Zhang, Y., Yin, L., Xiao, S., & Knoll, A. H. (1998). Permineralized fossils from the terminal Proterozoic Doushanto Formation, South China. *Journal of Paleontology*, *72*, 1–52.

Zhang, Y., Hou, M., Liu, G., Zhang, C., Prakapenka, V. B., Greenberg, E., Fei, Y., Cohen, R. E., & Lin, J. F. (2020). Reconciliation of Experiments and Theory on Transport Properties of Iron and the Geodynamo. *Physical Review Letters*, *125*(7), 78501. https://doi.org/10.1103/PhysRevLett.125.078501

Zhou, C., Huyskens, M. H., Lang, X., Xiao, S., & Yin, Q. (2019). Calibrating the terminations of Cryogenian global glaciatios. *Geology*, *47*, 251–254.

Zhu, M. Y., Babcock, L. E., & Peng, S. (2006). Advances in Cambrian stratigraphy and paleontology: integrating correlation techniques, paleobiology, taphonomy and paleoenvironmental reconstruction. *Palaeoworld*, *15*, 217–222.

Zijderveld, J. (1967). A. C. Demagnetization of Rocks: Analysis of Results. In *Methods in palaeomagnetism* (pp. 254–286). Elsevier. https://doi.org/10.1016/b978-1-4832-2894-5.50049-5

Appendix A

Grenville Dykes supplementary data

The data shown in Appendix A complements the results presented in the main text of Chapter 2. This section is published as supplementary information in Thallner et al. (2021a).

Tables A.1 to A.3 present the results for palaeointensity experiments for each measured specimen together with their critical values, analysed with paleointensity.org (Béguin et al., 2020). These tables are divided by type of palaeointensity experiment. Table A.4 presents the similarity of palaeointensity results on the site-level for different sets of selection criteria and Table A.5 gives the full list of Q_{PI} criteria for all studied units.

Figures A.1 and A.2 present examples of rock magnetic data for each studied site and BSE maps from SEM analysis, respectively. Figure A.3 presents the distributions and dispersions of VGPs with data from Halls et al. (2015).

Raw measurement data can be accessed on the MagIC database, where it is published as Daniele Thallner, Andy Biggin, Henry Halls (2020) "An extended period of extremely weak geomagnetic field suggested by palaeointensities from the Ediacaran Grenville dykes (SE Canada).", Magnetics Information Consortium (MagIC), 10.7288/V4/MAGIC/16863

A.1 Supplementary Tables

TABLE A.1: Thermal and microwave Thellier results and critical SPD values, analysed with paleointensity.org. No critical values are available for MW IZZI experiments of GD3091B2 and GD3091B3 (too weakly magnetised). Colour coded critical values are available in the online version

Specimen	B_{anc}	H_{lab}	I/T_{min}	I/T_{max}	n	FRAC	β	q	k′	MAD_a	α	DRAT	CDRAT	$DRAT_{Tail}$	Method
GD0232B2	3	10	107.35	237.28	5	0.367	0.140	3.6	0.459	2.9	4.1	1.9	2.6		MW IZZI
GD0232B3	2.2	10	128.88	227	4	0.234	0.097	3.4	0.391	4.6	7.4	1.2	3.6		MW IZZI
GD0232B4	3.3	10	104.38	195.81	4	0.267	0.173	1.5	1.046	1.7	1.5	31.7	29.3		MW IZZI
GD0232B5	1.9	3	167.09	427.37	6	0.241	0.056	8.3	0.291	4.7	11.7	20	7.8		MW IZZI
GD02HA2B2	2.5	10	44.39	151.19	6	0.397	0.094	4.4	-0.067	6.2	19.5	14.6	18.5		MW IZZI
GD02HA2B3	2.1	10	67.03	277.14	8	0.431	0.068	9.4	0.438	7	7.8	6	2.1		MW IZZI
GD02HA2B4	9.6	15	43.86	106.88	4	0.206	0.155	2.8	0.571	4.1	5	0.7	0.4		MW IZZI
GD02HA2B5	6.2	15	44.32	102.99	4	0.249	0.141	2.2	0.579	2.8	5.4	4.3	4.8		MW IZZI
GD02HA2B6	4	5	44.91	150	6	0.291	0.084	4.9	0.505	5.8	12.4	13.3	18.9		MW IZZI
GD3301B1	7.6	10	84.88	136.05	4	0.212	0.342	0.6	-1.819	8.3	20.2	17.7	15.1		MW IZZI
GD3301B2	3.8	10	132.12	287.55	4	0.287	0.242	2.0	0.88	5.1	3.4	53.5	73.4		MW IZZI
GD3301B3	2.8	5	136.13	255.78	5	0.185	0.097	5.2	0.237	11.1	2.7	33.2	13		MW IZZI
GD3301B4	7.7	5	62.38	118.12	4	0.307	0.134	2.0	0.622	2.5	5.2	5.1	3.2		MW IZZI
GD3301B5	5.7	15	43.75	97.25	4	0.233	0.154	2.3	0.638	6.1	9.9	9.8	10.8		MW IZZI
GD3301B6	10.5	15	43.78	122.69	6	0.412	0.097	5.7	0.489	7.4	10.2	12	2.4		MW IZZI
GD3382B2	2.7	5	138	651.9	7	0.317	0.091	4.8	-0.424	7.6	21.9	9.7	13.5		MW IZZI
GD3382B3	3.1	5	111.98	293.03	6	0.412	0.082	7.4	0.234	4.2	1.6	9.4	2.3		MW IZZI
GD3382B4	2.9	5	89.15	186.16	5	0.286	0.122	3.6	0.413	6.8	10.5	12.7	18.3		MW IZZI
GD3384B1	1.6	5	123.01	372.33	7	0.299	0.095	4.7	0.317	3.6	9.9	7	2.9		MW IZZI
GD3384B2	2	5	100.09	404.37	10	0.380	0.067	8.2	0.25	3.8	11.2	6.3	13.6		MW IZZI
GD3384B3	3.2	10	114.69	280.13	8	0.398	0.078	8.0	0.203	5.7	6	9.1	12.7		MW IZZI
GD3384B4	3	5	112.66	387.87	9	0.418	0.047	13.5	-0.031	3.4	3	6.9	9.1	5.1	MW IZZI
GD3384B5	1.9	5	112.36	269.95	8	0.255	0.136	2.5	0.255	3.7	15.9	24.1	14.7		MW IZZI
GD0232A	11.6	10	0	150	3	0.006	0.428	0.1	0.152	1.1	24.6	33.1	33.1		TH IZZI
GD3301	2.5	10	460	550	4	0.051	0.030	7.9	-0.006	20.5	28.5	95	129.2		TH IZZI
GD0152B1	2	5	113.39	210.83	4	0.404	0.362	0.8	-1.391	23.8	17.6	66.7	72.7		MW IZZI
GD0152B2	1.8	5	83.66	213.31	5	0.392	0.300	1.6	-1.015	14.8	27.1	52.8	57.5		MW IZZI
GD0161B1	41.3	10	0	119.31	7	0.418	0.144	1.4	-0.721	12.6	41.8	6.1	2.7		MW IZZI
GD1451B1	7.6	5	64.22	200.86	7	0.414	0.090	4.7	0.27	4	9.6	12.8	9.2		MW IZZI
GD1451B2	6	5	84.12	134.89	3	0.236	0.066	2.0	0.242	8.1	22.6	6.7	7.2		MW IZZI
GD0161A	25.1	10	0	150	3	0.004	0.349	0.0	1.519	1.9	29.6	0.7	0.7		TH IZZI
GD1462B	1.9	10	320	490	6	0.368	0.258	0.4	0.749	25.3	73.1	16.9	35.1		TH IZZI
GD2314B2	1.5	10	84.93	139.72	4	0.244	0.038	9.3	-0.033	6.4	11.1	0.7	0.9		MW IZZI
GD2314B3	0.9	5	60.1	127.06	4	0.255	0.224	0.7	0.88	14.3	58.8	3.4	1.4		MW IZZI
GD2315B2	3.6	30	82.7	154.31	4	0.430	0.075	5.8	0.159	7.8	13.4	6	5.7		MW IZZI
GD2315B3	1.1	5	84.89	269.1	10	0.496	0.099	4.9	0.338	4	13.3	7.4	13.7		MW IZZI
GD2315B4	2.1	5	102.65	199.11	6	0.364	0.068	6.2	0.131	3.6	11.9	9.2	11.3		MW IZZI
GD2315B5	1	5	119.12	177.42	5	0.241	0.165	1.5	0.036	1.8	6	9.2	2.3	14.7	MW IZZI
GD2316B2	2.5	10	84.22	214.18	6	0.359	0.051	7.7	0.252	3.1	8.6	7.6	12.5		MW IZZI
GD2316B3	1.8	5	105.59	183.84	6	0.284	0.057	6.3	0.211	1.5	4.9	8.1	12.8		MW IZZI
GD2316B4	2.3	5	85.3	176.19	8	0.367	0.085	4.9	0.446	2.9	9	12	10.9		MW IZZI
GD2316B5	1.5	10	100.19	253.89	8	0.427	0.067	7.6	0.273	5.5	6.3	10	14		MW IZZI
GD2316B6	1.3	5	86.41	199.65	9	0.369	0.091	4.2	0.365	1.6	3.4	6.8	9.3		MW IZZI
GD2318B1	0.7	10	0	165.87	9	0.596	0.491	0.1	1.652	13.6	76.7	9	8.5		MW IZZI
GD2318B2	1.7	10	62.16	152.05	5	0.371	0.062	5.9	0.302	4.2	7.8	0.3	0.2		MW IZZI
GD2318B3	1.5	10	85.11	198.07	7	0.669	0.088	5.4	-0.325	10.3	14.3	13.4	15.3		MW IZZI
GD2318B4	2	5	85.3	266.31	10	0.472	0.069	8.5	0.444	2.9	6.2	8	13.8		MW IZZI
GD2318B5	1.6	5	79.31	174.05	6	0.503	0.068	6.7	0.235	5.4	13	13.3	13.2		MW IZZI
GD2318B6	0.6	5	88.48	204.32	7	0.407	0.108	2.9	0.465	5.2	21.8	15.4	10.4		MW IZZI
GD2322B2	1.9	5	101.66	248.07	6	0.492	0.066	8.6	0.3	3.4	6.4	6.1	5.8		MW IZZI
GD2322B3	2.2	10	99.6	247.57	6	0.483	0.135	4.2	0.613	5.7	10.3	15.4	25.1		MW IZZI
GD2322B4	1.4	20	62.95	216.83	7	0.569	0.092	5.0	-0.036	5.4	6.1	8.2	10.1		MW IZZI
GD2315A	3.9	10	0	510	13	0.584	0.288	1.2	1.01	6.7	19.1	3.8	6.3		TH IZZI
GD2322A	2.7	10	240	490	8	0.300	0.346	0.0	-0.66	3	1.8	6.5	12		TH IZZI
GD1021B2	0.8	10	106.98	203.59	5	0.522	0.178	2.9	0.106	29.1	48.3	12.2	16.9		MW IZZI
GD1021B3	2.3	10	109.14	155.05	3	0.201	0.105	2.1	0.854	4.8	11.9	0.6	1		MW IZZI
GD1021B4	60.9	10	0	59.97	5	0.401	0.129	1.5	0.002	2.1	12.8	0.8	0.8		MW IZZI
GD1021B5	0.8	5	110.38	156.06	3	0.124	0.148	1.2	0.252	3.5	2.9	0.8	0.4		MW IZZI
GD1021B6	3	15	108.47	144.76	3	0.080	0.254	0.4	1.978	4.8	30.3	0.6	0		MW IZZI
GD1021B7	1.1	10	110.15	132.62	3	0.111	0.158	0.0	-0.539	4	20	50.3	56.3		MW IZZI
GD1072B2	1.9	10	120.62	343.9	6	0.471	0.122	3.7	0.798	14.9	20.5	31.9	24.8		MW IZZI
GD1072B3	1.9	5	107.6	178.5	4	0.205	0.067	3.1	-0.201	4.9	24.7	8.7	4		MW IZZI

Table A.1 continued

Specimen	B_{anc}	H_{lab}	I/T_{min}	I/T_{max}	n	FRAC	β	q	k′	MAD_a	α	DRAT	CDRAT	$DRAT_{Tail}$	Method
GD1072B4	4.4	5	88.38	259.05	7	0.428	0.099	5.6	0.361	9.5	16.5	14.9	29.2		MW IZZI
GD1511B1	9.6	10	44.31	122.97	6	0.492	0.037	16.0	0.051	6.3	6.9	16.6	24.3		MW IZZI
GD1511B2	3.9	10	81.59	136.38	4	0.240	0.014	21.5	-0.073	6.8	6.5	67.5	73.9		MW IZZI
GD1511B3	1.4	5	84.59	168.75	5	0.080	0.242	0.8	1.806	17.2	55.4	64.6	77.6		MW IZZI
GD1511B4	4.2	5	144.75	287.41	4	0.380	0.044	2.6	0.277	14.7	40.4	61.6	117		MW IZZI
GD1511B5	7.4	15	44.64	109.34	4	0.409	0.154	2.8	0.481	7.3	14.5	29.7	30.2		MW IZZI
GD1533B1	3.7	10	44.86	145.44	6	0.565	0.049	9.9	0.253	11.5	22.2	11.3	20.7		MW IZZI
GD1533B2	14	10	0	113.94	8	0.728	0.070	8.3	-0.2	4.8	5.4	18.7	12		MW IZZI
GD1533B3	2.7	10	44.33	94.33	4	0.303	0.006	50.8	0.003	6.5	12.3	22.5	10		MW IZZI
GD1533B4	2.6	5	22.08	54.7	3	0.220	0.158	1.0	1.419	9.1	19.3	62.8	62.8		MW IZZI
GD1533B5	5.6	15	0	59.91	4	0.381	0.085	2.8	0.384	5.7	13.8	1.1	1.1		MW IZZI
GD1644B1	1.9	10	68.51	128.34	4	0.237	0.175	1.2	0.455	5.1	22.8	38.2	38.7		MW IZZI
GD1644B2	1.8	10	22.79	174	8	0.655	0.060	7.5	-0.138	8.8	15.1	22.3	16.5		MW IZZI
GD1644B3	2.5	10	88.64	199.75	5	0.509	0.071	6.9	0.259	5.9	4.3	13.3	16.8		MW IZZI
GD1644B4	4.3	5	86.28	278.4	7	0.569	0.078	5.5	-0.263	4.5	5.6	13.9	6.8		MW IZZI
GD1644B5	2.5	5	43.96	97	7	0.494	0.449	0.4	-0.295	12.5	73.2	10.5	15.1		MW IZZI
GD1662B3	1.7	10	67.42	131.25	4	0.262	0.138	2.0	0.635	17.4	48.9	13.8	17.3		MW IZZI
GD1662B4	4.5	10	88.06	138.42	3	0.290	0.251	1.1	-0.179	4	6.1	15	14.4		MW IZZI
GD1942B2	7.9	30	129.03	293.38	5	0.361	0.106	5.4	0.436	0.4	0.4	65.4	97.5		MW IZZI
GD1942B3	20	10	133.1	176.13	3	0.183	0.006	27.4	1.474	0.5	2.8	15.3	23.1		MW IZZI
GD1943B1	26.7	10	81.7	153.65	4	0.461	0.073	3.5	0.394	1.1	2.2	2.9	7		MW IZZI
GD1943B2	13.7	10	86.34	146.22	4	0.373	0.104	2.3	0.913	5.1	11.4	3.8	0.3		MW IZZI
GD1943B3	3.6	10	134.07	168.52	3	0.088	0.308	0.3	-0.073	2.2	10.4	13.8	2.4		MW IZZI
GD1943B4	6.1	5	132.08	251.24	4	0.260	0.146	3.3	0.575	3.4	3.2	22.5	9		MW IZZI
GD1943B5	131.1	15	0	85.83	5	0.391	0.138	1.8	-0.291	0.5	1.4	4	3.5		MW IZZI
GD1943B6	9.7	10	118.01	203.36	6	0.375	0.159	3.1	0.622	1.2	1.9	23.5	7.7		MW IZZI
GD37H53B2	3.8	10	86.55	198.31	5	0.225	0.145	2.1	0.664	7.6	22.7	18	21.1		MW IZZI
GD37H53B3	3.5	10	66.55	108.12	3	0.087	0.280	0.3	1.751	1.7	11	2.5	0		MW IZZI
GD1021A	10.5	10	280	490	7	0.339	0.167	2.4	0.865	5.9	10.3	4.9	16.2		TH IZZI
GD1533B	2.4	10	200	460	8	0.456	0.165	3.1	0.606	15	24.1	33.1	22.7		TH IZZI
GD1651	2.6	10	0	550	15	0.907	0.321	5.8	2.071	21.3	7	20.3	8.9		TH IZZI
GD1911	2.8	10	240	430	6	0.200	0.235	0.2	-0.906	13.2	83.4	14.2	3		TH IZZI
GD3753A	18.5	10	100	360	7	0.331	0.094	5.7	0.241	5.1	7.8	8.3	21		TH IZZI
GD2542B1	2.4	10	22.01	65.72	3	0.272	0.051	1.9	0.513	8.3	34.2	0.4	0.4		MW IZZI
GD2542B2	1.4	5	21.38	62.51	3	0.301	0.004	28.5	-0.422	9.1	32.6	1.7	1.7		MW IZZI
GD2562B2	9.9	10	22.05	83.27	4	0.296	0.016	14.2	0.02	3.8	17.5	9	17.4		MW IZZI
GD2562B3	6.6	10	43.15	171.52	8	0.498	0.145	3.0	0.196	5.1	4	37.5	91.5		MW IZZI
GD2562B4	2.8	15	43.1	200.95	8	0.464	0.135	2.3	-0.065	10.3	41.1	16.9	32.8		MW IZZI
GD2562B5	5	10	0	112.49	6	0.536	0.244	2.1	1.222	3.3	5.7	0.7	1		MW IZZI
GD2562B6	5.4	10	21.59	120.18	6	0.370	0.138	2.4	0.236	2.6	3.9	18.7	41.1		MW IZZI
GD2593B2	12.6	10	63.13	312.04	8	0.738	0.038	19.3	0.041	2.6	2.2	10.4	5.8		MW IZZI
GD2593B3	11.5	15	63.1	130.39	4	0.101	0.138	1.8	0.516	6.8	6.4	60.9	88.2		MW IZZI
GD2593B4	4.6	15	67.35	250.57	6	0.631	0.065	9.1	0.349	6.2	5.7	37.5	38.7		MW IZZI
GD2622B2	9.2	5	71.97	112.57	3	0.234	0.321	0.4	-1.984	14.7	35.9	6.4	11.3		MW IZZI
GD2622B3	2.5	5	40.31	114.68	5	0.511	0.287	0.7	-1.371	36.9	22	24.3	22.3		MW IZZI
GD2632B1	8.4	10	43.03	99.3	5	0.427	0.413	1.0	1.483	15.5	27.8	20.6	25.8		MW IZZI
GD2632B2	1.7	10	41.04	109.38	4	0.431	0.054	7.2	0.088	6.4	11.9	36.8	37.9		MW IZZI
GD2542A	0.9	10	280	550	10	0.810	0.305	0.6	2.264	28.2	26.3	3.9	0.6		TH IZZI
GD2632A	2.2	10	100	400	8	0.473	0.497	0.0	1.625	14.8	62.1	5.6	4.4		TH IZZI
GD3091A	2.5	10	280	490	7	0.158	0.500	0.6	-2.178	11.6	17.6	26.1	43.2		TH IZZI
GD2911B2	3.8	10	61.49	143.5	5	0.235	0.050	2.9	0.213	2.1	10.9	5	6.5		MW IZZI
GD2911B3	3.2	5	112.72	191.33	4	0.411	0.047	5.2	0.147	4.6	17.4	26.6	23.9		MW IZZI
GD2911B4	3	5	81.4	155.79	4	0.641	0.031	12.2	0.028	9.9	4.4	1.1	1.9		MW IZZI
GD2913B1	3.3	5	67.04	113.23	5	0.218	0.142	1.5	-0.162	11.1	36.7	34.9	61.7		MW IZZI
GD2913B2	2.3	5	65.25	112.72	5	0.201	0.094	3.9	-0.198	12	29.8	18.6	14		MW IZZI
GD2913B3	2	5	83.22	108.55	6	0.092	0.236	0.1	1.206	2.8	52	88	145.9		MW IZZI
GD2913B4	6.6	5	83.94	146.32	7	0.266	0.143	1.4	0.059	9.7	24.7	15.2	47.1		MW IZZI
GD2913B5	4.7	5	66.05	122.38	5	0.351	0.079	5.1	-0.13	13	10.6	1.9	1.3		MW IZZI
GD2932B2	4.1	10	64.16	134.28	4	0.280	0.115	1.0	0.755	2.5	13.4	3.8	3.5		MW IZZI
GD2932B3	14	10	0	84.64	5	0.266	0.090	1.4	-0.103	4.8	52	13.7	13.3		MW IZZI
GD2932B4	1.8	5	114.75	158.55	5	0.292	0.098	2.6	0.476	2.9	3.1	16.7	29.5		MW IZZI
GD2932B5	2	5	113.71	219.83	7	0.564	0.038	15.9	0.133	4.7	9.6	15.2	37.5		MW IZZI
GD2932B6	2.2	5	115.8	154.7	5	0.324	0.084	2.9	0.301	5.3	19.9	24.8	41.5		MW IZZI
GD2962B2	1.9	5	140.79	223.1	5	0.236	0.064	4.1	0.22	3.3	16.1	22.9	37.4		MW IZZI
GD2981B1	4.6	10	69.23	146.5	4	0.360	0.049	3.1	0.107	0.9	2.7	15.4	13		MW IZZI
GD2981B2	3.3	5	95.19	198.53	7	0.449	0.054	9.2	0.307	2.4	6.3	14.7	17		MW IZZI
GD2981B3	2.1	5	116.22	163.18	5	0.350	0.080	3.9	0.146	4.3	16.2	34.9	44		MW IZZI
GD2981B4	2.6	5	114.37	157.01	5	0.367	0.054	6.9	0.05	4.9	14.4	16.6	24.6		MW IZZI
GD2981B5	2.9	5	116.3	161.47	5	0.400	0.075	4.2	0.15	3.6	12.2	19.2	22.4		MW IZZI
GD2981B6	2.2	5	115.45	237.25	7	0.562	0.087	6.4	0.437	3	6.6	18.9	42.6		MW IZZI
GD2982B2	3.1	5	96.94	190.38	6	0.391	0.079	5.0	0.329	3.7	12.2	8.8	14.9		MW IZZI

Table A.1 continued

Specimen	B_{anc}	H_{lab}	I/T_{min}	I/T_{max}	n	FRAC	β	q	k′	MAD_a	α	DRAT	CDRAT	$DRAT_{Tail}$	Method
GD2992B2	4.3	10	87.24	141.13	3	0.294	0.112	0.6	0.328	3.2	8.9	2.7	0.9		MW IZZI
GD2992B3	3.6	5	85.13	228.51	6	0.440	0.078	5.8	0.412	2.8	5	14.4	20.6		MW IZZI
GD2992B4	3.3	5	111.17	229.6	5	0.366	0.122	3.2	0.422	2.8	7.7	13.6	13.9		MW IZZI
GD29H72B1	10.4	10	101.29	253.37	8	0.384	0.207	1.5	0.405	10.8	42.5	27.6	16.7		MW IZZI
GD29H81B1	4.2	10	0	149.89	11	0.785	0.190	1.6	1.206	22.5	77.2	89.7	53.6		MW IZZI
GD2932A	2.9	10	460	550	4	0.227	0.006	36.9	-0.015	4.5	18.3	3.8	10.1		TH IZZI
GD294B1	0.6	10	430	550	5	0.171	0.623	0.1	0.969	5.2	66.9	4.8	0.4		TH IZZI
GD2962A	7	10	400	550	6	0.293	0.135	2.3	0.445	3.6	16.7	3.2	7.7		TH IZZI
GD2992A	5.6	10	460	550	4	0.172	0.056	2.7	0.079	2.8	18.6	6.9	10.1		TH IZZI
GD29H31A	5.5	10	400	550	7	0.074	0.579	0.0	0.143	1.3	80.1	65.2	99.2		TH IZZI
GD29H41A	23.4	10	100	550	14	0.296	0.362	0.0	0.315	1.4	27.1	11	3.2		TH IZZI

Specimen	B_{anc}	Stderr	H_{lab}	AF_{min}	AF_{max}	N	FRAC	r_n^2	r_t^2	$Slope_T$	α	MAD_a	MAD_f	k′
GD0211A	30.2	3.0	5	35	100	14	0.07	0.895	0.987	1.04	2.8	4.5	3.1	0.755
GD02HA4	2.2	0.0	10	20	70	8	0.24	0.999	0.998	1.01	6.4	4.9	8.6	0.049
GD3381A	15.1	0.5	10	30	70	6	0.28	0.995	0.984	1.12	14.8	7.2	5.3	0.063
GD3384B	1.2	0.1	5	40	70	7	0.12	0.982	0.996	0.97	16.3	9.4	8.2	0.372
GD14103	0.8	0.1	5	20	70	11	0.14	0.760	0.988	0.93	24.8	20.0	16.9	1.688
GD1452A	1.0	0.2	5	20	50	7	0.09	0.784	0.971	0.93	36.2	24.3	30.2	1.885
GD2321A	0.9	0.0	5	40	65	6	0.26	0.997	0.999	0.99	10.2	10.0	11.3	0.108
GD2341A	1.1	0.0	10	35	75	5	0.31	1.000	1.000	0.93	28.1	7.3	6.1	0.023
GD10163	0.7	0.1	10	25	50	5	0.07	0.926	0.999	1.11	1.9	1.0	6.3	0.946
GD10202A	0.4	0.0	5	25	60	8	0.61	0.937	0.999	1.03	9.3	29.1	19.8	0.524
GD1073A	5.8	1.1	10	2	20	5	0.88	0.900	1.000	1.01	2.0	2.1	1.7	0.796
GD1083A	0.3	0.1	5	20	60	9	0.49	0.835	0.989	1.09	35.0	13.4	15.9	1.01
GD1541A	0.5	0.1	5	25	50	6	0.47	0.913	0.992	1.03	7.1	13.6	23.2	0.668
GD1661A	1.5	0.1	5	30	70	9	0.57	0.975	0.981	1.07	6.5	6.4	6.9	0.102
GD1662A	1.5	0.1	5	25	55	7	0.62	0.977	0.991	1.01	12.0	11.8	11.5	0.336
GD1942A	23.8	3.8	10	25	50	5	0.02	0.928	0.997	1.05	7.5	6.7	3.1	0.72
GD1943A	2.7	0.3	5	25	50	6	0.03	0.944	0.994	0.98	13.3	11.7	4.9	0.696
GD3785A	4.2	0.1	5	18	90	17	1.04	0.994	0.999	0.95	0.7	3.3	4.6	0.086
GD37H44	7.6	0.3	5	50	90	9	0.38	0.990	0.997	1.05	4.6	1.0	4.5	0.153
GD37H53	4.3	0.2	5	27	60	8	0.49	0.993	0.998	1.02	5.8	1.4	4.2	0.068
GD0782A	1.05	0.03	10	20	60	7	0.07	0.997	0.999	1.02	3.83	4.15	7.49	0.062
GD2572A	0.8	0.0	10	15	35	5	0.49	0.998	1.000	1.03	4.8	3.3	10.0	0.108
GD2582A	0.4	0.1	5	25	55	7	0.23	0.882	0.997	1.03	30.1	13.5	16.0	0.567
GD2592A	0.3	0.0	5	25	35	3	0.32	0.999	0.991	0.97	24.8	4.9	13.2	0.174
GD2652A	1.0	0.0	5	21	45	7	0.72	0.991	0.999	1.01	5.5	4.9	6.1	0.187
GD2662A	1.8	0.1	5	24	65	10	0.68	0.994	0.999	1.01	4.7	4.3	4.5	0.075
GD2911A	17.9	0.3	10	30	70	6	0.43	0.999	0.976	0.87	2.6	1.4	1.1	0.073
GD2911B	3.5	0.1	5	15	60	12	0.77	0.998	0.999	0.98	0.1	2.1	3.8	0.028
GD29141	0.4	0.0	5	18	90	17	0.03	0.892	0.999	0.91	35.1	21.6	32.1	0.646
GD291B9	4.6	0.1	10	15	40	6	0.31	0.996	0.999	1.04	2.9	1.5	1.2	0.174
GD2944A	38.3	1.0	10	15	50	7	0.69	0.997	0.989	0.99	4.2	3.3	1.8	0.114
GD2961	3.1	0.1	10	10	50	8	0.92	0.997	0.999	0.95	2.1	1.9	2.2	0.149
GD2991	4.2	0.0	10	15	40	6	0.69	1.000	1.000	0.95	2.5	1.6	1.1	0.033
GD29H43	-2.5	2.2	10	40	100	7	1.51	0.204	0.201	0.25	15.36	13.2	9.82	1.717

TABLE A.2: Shaw results and critical values. No critical values are available for GD0181A, GD0751A, GD1511A, GD15012, GD29H42A, GD29H41B, GD293B2, GD30101 (too weakly magnetised) and GD2593A, GD1641A, GD14121, GD0792A, GD0252T, GD2642, GD1923, GD37H32 (measurement errors). Colour coded critical values are available in the online version

Specimen	B_{anc}	H_{lab}	b	σb	AF_{min}	AF_{max}	n	$B_{1/2ARM}$	f	β	k′	R^2	MAD_{Free}	α	DANG	k'_{AA}	k'_{DD}	R^2_{AA}
GD0211A	26.9	81.2	-1.089	0.108	35	100	14	18.9	0.186	0.099	0.393	0.885	3.1	0.9	2.8	0.077	0.553	0.928
GD3303	4.0	11.4	-1.13	0.177	15	50	7	7.2	0.243	0.157	0.118	0.881	4.2	4.7	7.5	0.001	0.360	0.924
GD3384B	1.9	81.2	-0.077	0.002	27	50	6	30.9	0.38	0.030	0.144	0.997	4.6	7.9	9.1	-0.004	0.145	0.999
GD0101	0.9	11.4	-0.251	0.021	15	100	12	7.8	0.284	0.083	0.209	0.933	15.3	6.1	12.6	0.004	0.322	0.983
GD14103	0.5	81.2	-0.019	0.004	25	60	8	15	0.246	0.193	-0.032	0.79	21	52.6	65.5	0.043	0.574	0.999
GD1452A	0.7	81.2	-0.029	0.006	20	50	7	10.8	0.238	0.192	-0.315	0.825	30.2	26.8	34.8	0.052	0.466	0.999
GD2321A	1.0	81.2	-0.042	0.002	40	65	6	32.2	0.286	0.046	0.071	0.992	11.3	4.0	5.8	-0.624	1.631	0.606
GD2324	0.5	11.4	-0.145	0.025	40	80	5	30.1	0.246	0.176	-0.781	0.91	18.6	33.3	45.1	-0.034	0.779	1.000
GD1018	1.3	11.4	-0.376	0.017	40	100	7	26.9	0.223	0.044	0.085	0.99	4.6	2.3	4.8	0.153	0.126	0.987
GD10202A	0.8	81.2	-0.031	0.002	30	55	6	29.6	0.311	0.056	0.156	0.987	25.2	28.6	31.5	0.205	0.097	0.995
GD1072A	0.2	81.2	-0.007	0.001	25	40	4	26.7	0.317	0.166	0.974	0.946	19.2	12.4	78.4	-0.022	0.854	1.000
GD1083A	0.5	81.2	-0.02	0.003	30	100	15	27.1	0.406	0.158	-0.44	0.702	25.1	12.0	56.1	0.389	0.741	0.946
GD1542	2.4	11.4	-0.696	0.030	50	100	6	24.9	0.087	0.043	-0.036	0.992	15.2	14.1	21.6	0.047	0.357	0.989
GD1541A	0.5	81.2	-0.019	0.003	25	50	6	27.1	0.294	0.151	-1.044	0.911	23.2	61.9	64.0	-0.158	0.582	1.000
GD1661A	1.3	81.2	-0.054	0.003	30	70	9	26	0.339	0.056	0.087	0.978	6.9	5.6	7.9	0.127	0.058	0.996
GD1662A	1.2	81.2	-0.049	0.003	25	55	7	24.7	0.394	0.070	-0.22	0.975	11.5	7.1	8.5	0.149	0.295	0.996
GD1943A	3.2	81.2	-0.129	0.015	25	50	6	24.3	0.376	0.118	0.632	0.945	4.9	10.0	15.4	-1.147	0.982	0.446
GD3785A	3.1	81.2	-0.125	0.002	21	95	17	19.6	0.446	0.020	-0.165	0.994	4.2	2.0	4.3	0.051	0.236	0.998
GD37H44	11.2	81.2	-0.454	0.026	50	90	9	26.2	0.197	0.057	-0.136	0.978	4.5	2.9	3.6	-2.195	1.935	0.355
GD37H53	6.1	81.2	-0.245	0.009	27	60	8	22.7	0.271	0.038	-0.119	0.991	4.2	20.0	22.3	0.002	0.103	0.997
GD2582A	0.3	81.2	-0.011	0.002	27	55	7	24.2	0.326	0.150	0.547	0.891	16	39.7	47.2	0.093	0.449	0.998
GD2592A	0.2	81.2	-0.009	0.002	24	40	5	26	0.185	0.201	-0.592	0.883	20.9	55.8	56.6	0.114	0.479	0.999
GD2652A	0.9	81.2	-0.035	0.002	21	45	7	24.9	0.483	0.049	-0.259	0.988	6.1	3.0	3.6	0.064	0.290	0.999
GD2662A	1.5	81.2	-0.061	0.002	24	65	10	22.7	0.418	0.031	-0.201	0.992	4.5	4.5	6.7	0.030	0.227	1.000
GD2911B	2.7	81.2	-0.11	0.008	35	75	9	23.9	0.234	0.068	-0.081	0.968	4.8	4.7	6.2	0.073	0.122	0.995
GD2913	4.1	81.2	-1.17	0.033	10	40	7	29	0.669	0.028	-0.042	0.996	1.6	1.3	1.6	-0.116	0.084	0.995
GD29141	0.3	81.2	-0.013	0.001	18	95	18	20.8	0.548	0.090	0.381	0.876	31.3	5.5	6.3	0.146	0.346	0.993
GD294B1A	6.5	81.2	-0.264	0.031	0	15	6	18.6	0.767	0.116	0.686	0.947	8.4	15.0	18.4	0.104	0.770	0.997

TABLE A.3: Pseudo-Thellier results and critical values, analysed with paleointensity.org (Béguin et al., 2020). Colour coded critical values are available in the online version

Site	N	A N	Selcrit2 mod PI	Std	A N	MC-crit.C1 PI	Std	A N	Picrit03 PI	Std	A N	TTA PI	Std	A+B N	Selcrit2 mod PI	Std
GD02	13	0			0			2	2.2	0.05	1	1.8		1	2.1	
GD33	17	2	3.05	0.6	1	3.5		4	2.5	0.58	5	2.5	0.59	5	2.6	0.62
GD01	5	0			0			0			0			0		
GD14	6	0			0			0			0			1	7.6	
GD23	24	1	3.6	0.84	9	1.9	0.37	6	1.7	0.37	5	1.7	0.33	12	1.9	0.67
GD10	14	0			0			0			0			0		
GD15	14	0			0			0			0			1	5.6	
GD16	11	0			0			0			0			1	4.3	
GD19	12	0			0			0			0			0		
GD37	7	0			0			0			0			0		
GD29	43	2	3.9	0.85	3	6.8	6.27	6	5.2	4.05	0			3	3.6	0.78
GD07	3	0			0			0			0			0		
GD25	15	1	12.6		0			1	13.3		1	12.3		1	12.6	
GD26	8	0			0			0			0			0		
GD30	5	0			0			0			0			0		
All	197	6	5.8	4.0	13	4.0	2.0	19	5.0	4.3	12	4.6	4.5	25	5.0	3.4

TABLE A.4: Comparison of different sets of selection criteria: Site/Dyke name, total number of experiments, result class and used set of criteria, number of accepted results, intensity (μT), standard deviation. blue fields show average values for the locality. Results are analysed and compared with strict selection criteria from modified SELCRIT2 (Biggin et al., 2007a), MC-crit.C1 (Paterson et al., 2015), PICRIT03 (Kissel & Laj, 2004) and TTA (Leonhardt et al., 2004a). The similarity of results shows a high consistency between the different methods and that there is no significant bias connected to the choice of selection criteria.

Unit	AGE	STAT	TRM	ALT	MD	ACN	TECH	LITH	MAG	Q_{PI}
Augusta Lake	1	1	1	1	1	1	1	0	1	8
Coniston	1	0	1	1	1	1	0	0	1	6
French River	1	0	1	1	1	1	1	0	1	7
Key River	1	1	1	1	1	1	1	1	1	9
Sand Bay	1	1	1	1	1	1	1	0	1	8
Other (GD25)	1	0	1	1	1	1	1	0	1	7
Other (GD26)	1	0	1	1	1	1	0	0	1	6

TABLE A.5: List of Q_{PI} criteria (Paterson et al., 2014) for all sites yielding palaeointensity results.

A.2 Supplementary Figures

FIGURE A.1: Representative rock magnetic measurement plots for each site: left: susceptibility vs temperature plots; centre: thermomagnetic curves; right: hysteresis plots (red: raw data, black: fitted loop)

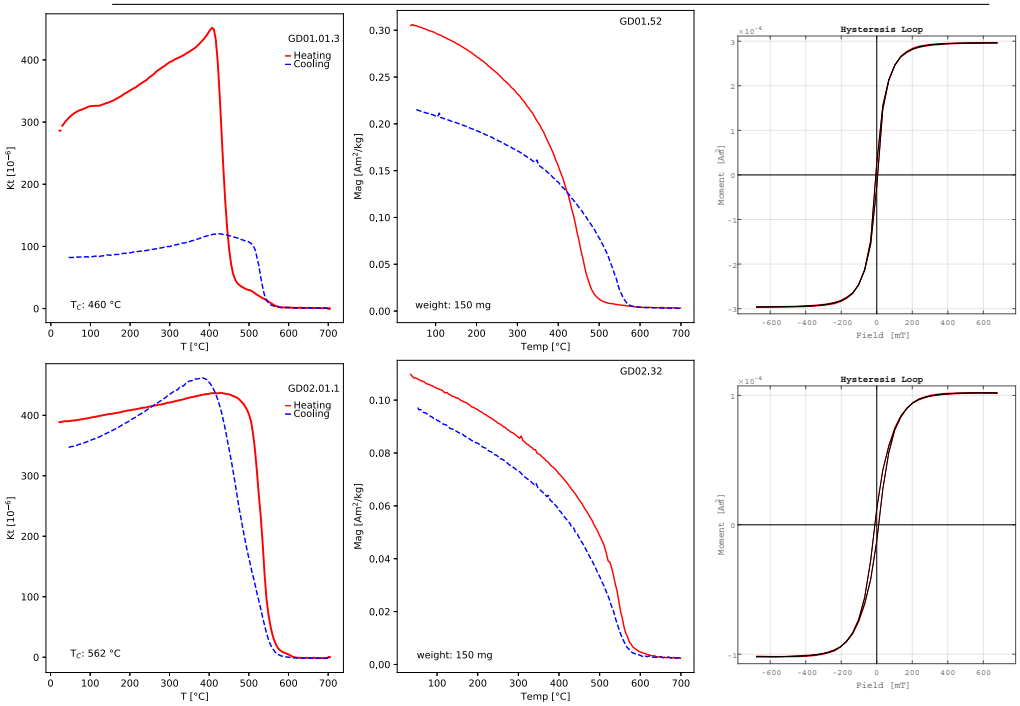

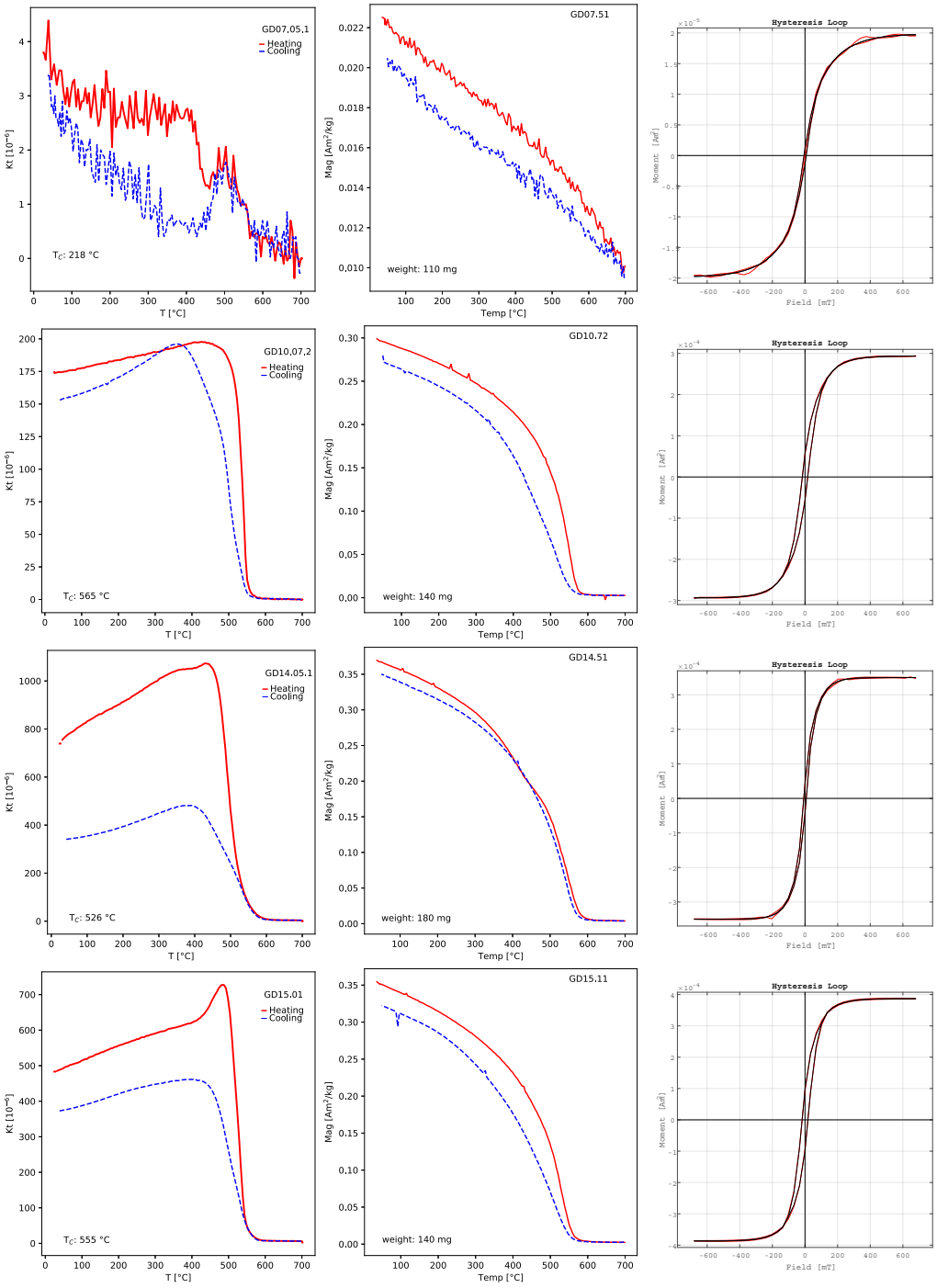

(A) Figure A.1 continued

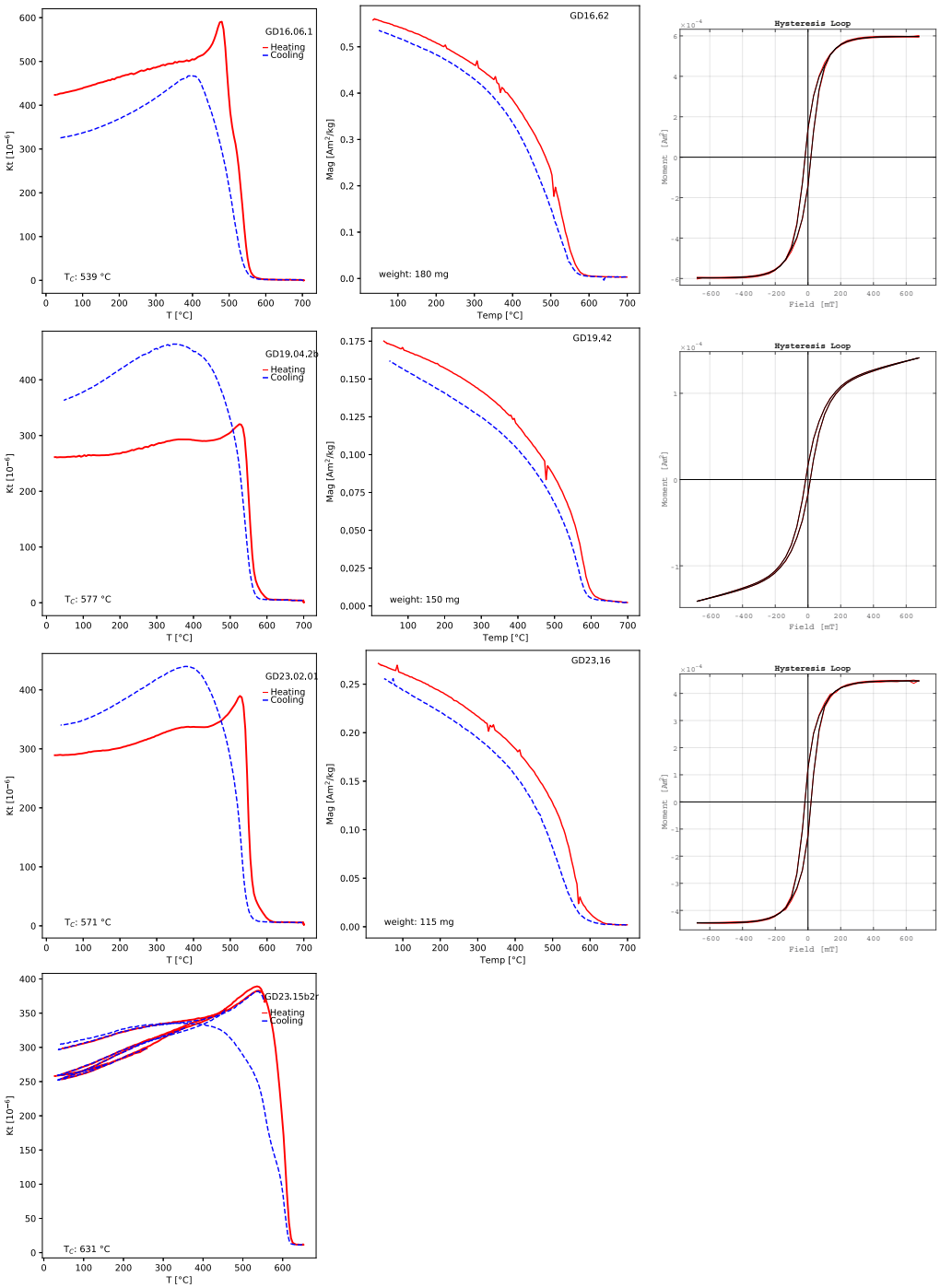

(B) Figure A.1 continued

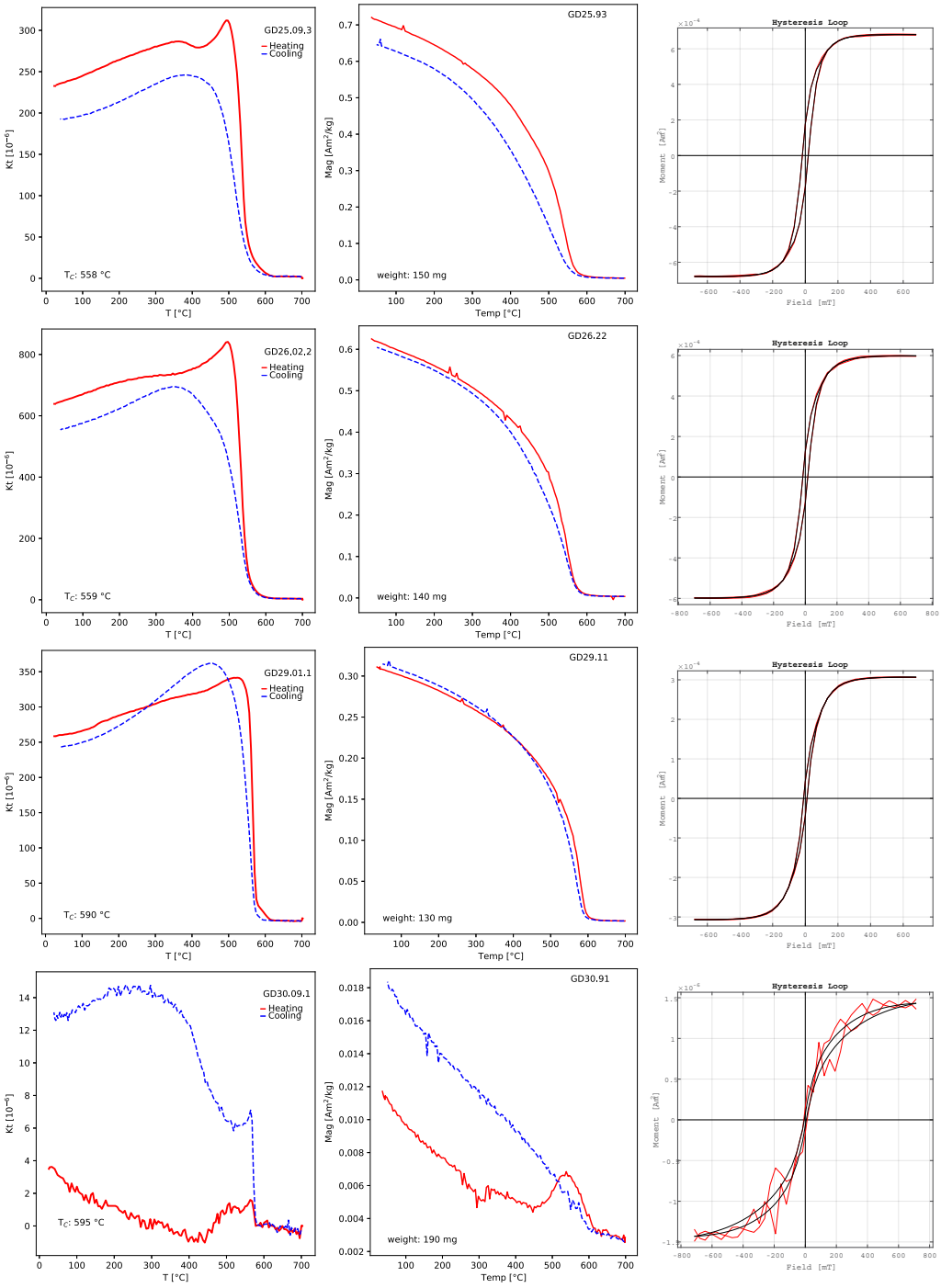

(C) Figure A.1 continued

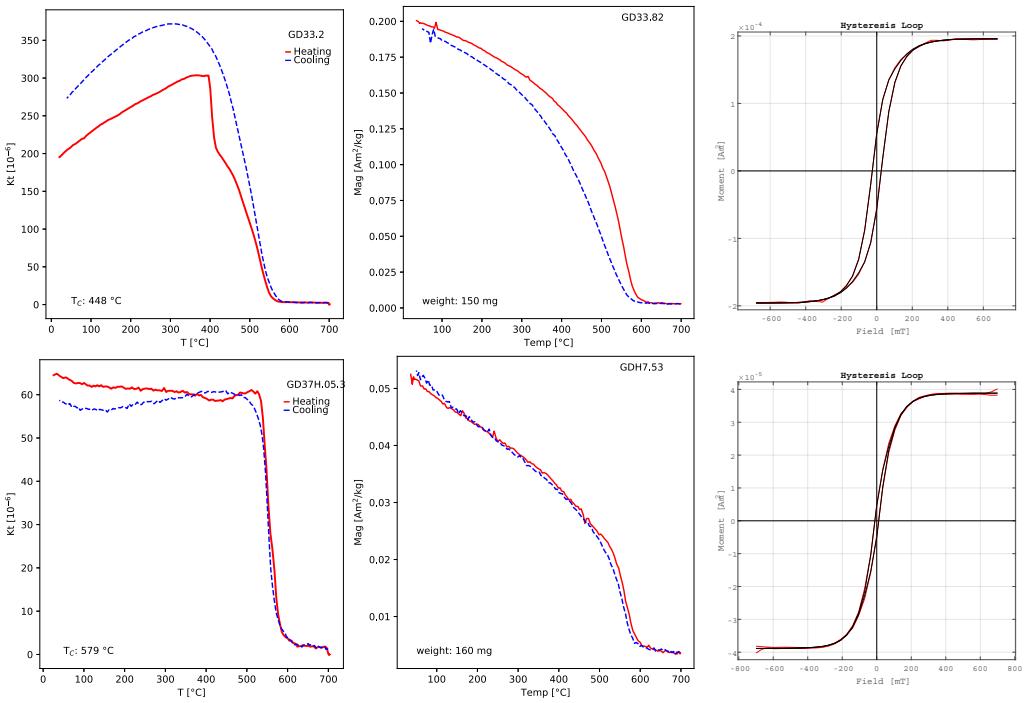

(D) Figure A.1 continued

FIGURE A.2: Elemental composition maps for Fe and Ti from BSE analysis: a) Site GD02 host rock at Augusta Lake dyke; b) Site GD33 Augusta Lake Dyke; c) GD29, Sand Bay Dyke, d) Site GD23; French River Dyke

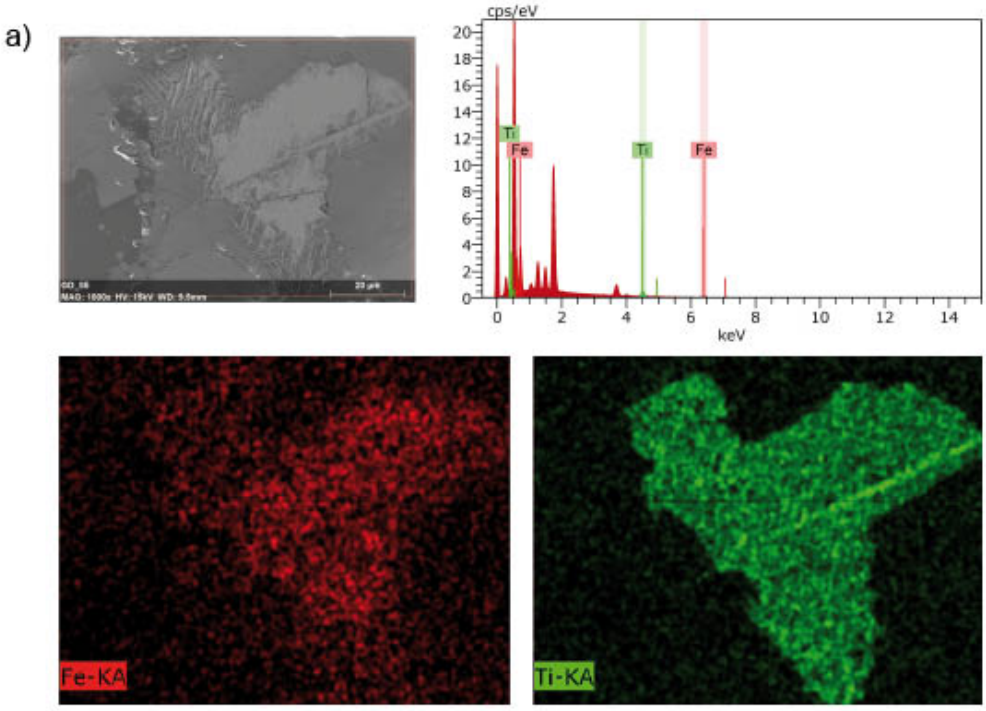

b)

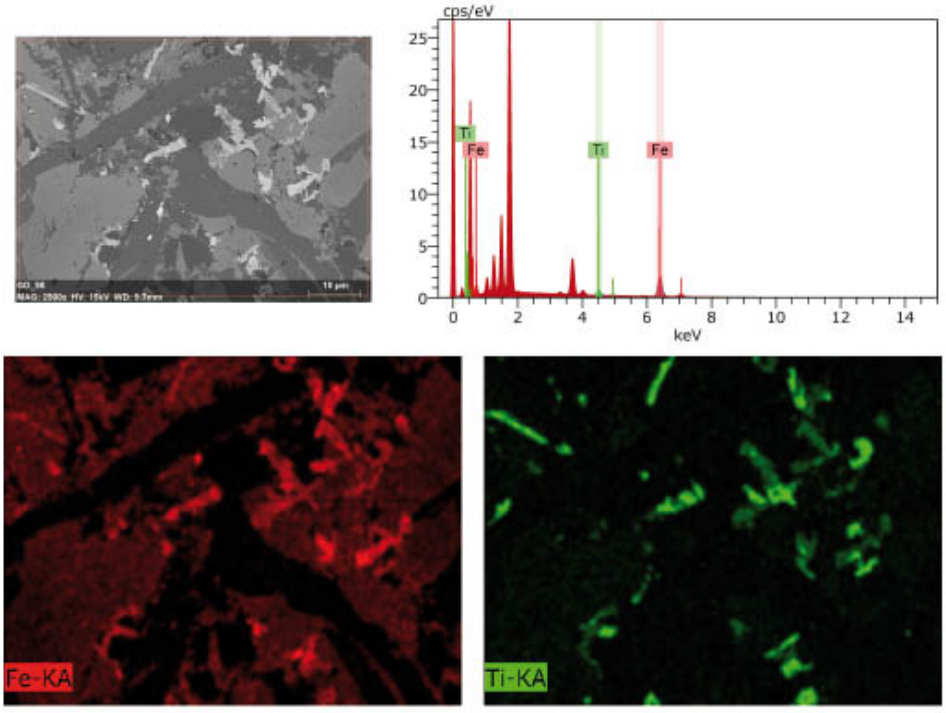
cps/eV
25
20
15
10
5
0
Ti
Fe
Ti
Fe
0
2
4
6
8
10
12
14
keV
Fe-KA
Ti-KA

c)

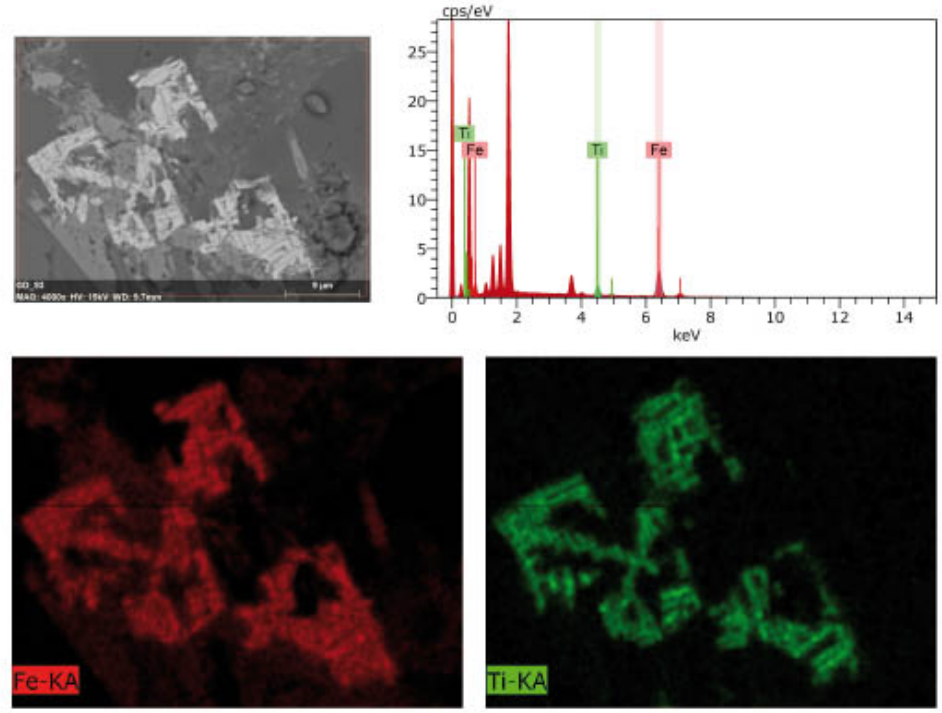
cps/eV
25
20
15
10
5
0
Ti
Fe
Ti
Fe
0
2
4
6
8
10
12
14
keV
Fe-KA
Ti-KA

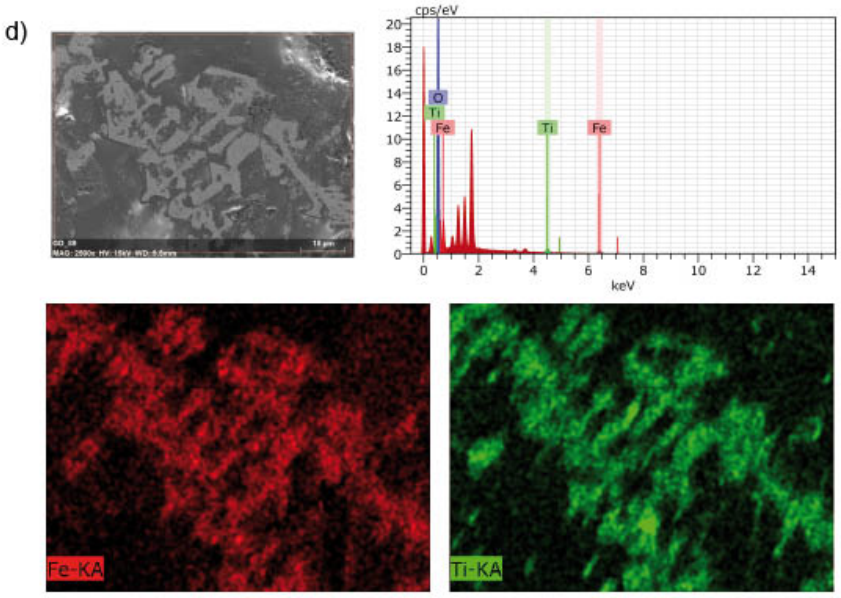

(A) Figure A.2 continued

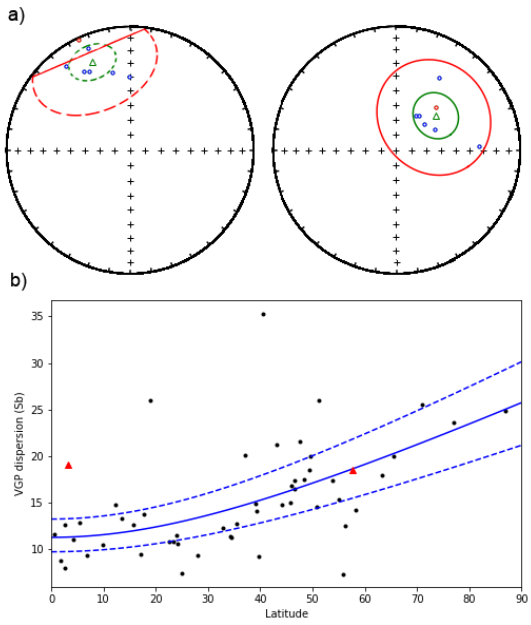

FIGURE A.3: Palaeosecular variation. (a) Filtered VGPs (nn $\geq$ 5, k $\geq$ 30) of shallow (right) and steep (left) directional component from Halls et al. (2015). Open circles indicate negative inclination. Red markers show VGPs with flipped polarity. Green triangles and circles show mean VGP and 95% confidence intervals. Variable cutoff values (Vandamme, 1994) are plotted as red circles. (b) angular dispersion of the Grenville dyke components (green triangles) compared to dispersion values from PSV10 and model G fit (blue line) with 95% bootstrap uncertainty interval (dashed lines) (Cromwell et al., 2018).

Appendix B

Skinner Cove supplementary data

The data included in Appendix B is intended to complement the examples presented in the main text of Chapter 3 and show rock magnetic and paleomagnetic data (figures) as well as paleointensity results and paleomagnetic site mean directions (tables). Figure B.1 gives examples of rock magnetic results for each of the studied sites. Figure B.2 shows BSE maps for the SEM images presented in the main text. Figure B.3 illustrates the previously published Skinner Cove Formation site mean directions (McCausland & Hodych, 1998) with a reinterpretation of site SC07 as a reversed direction.

Tables B.1 – B.4 give paleointensity results for each of the measured specimens with their critical values according to the Standard Paleointensity Definitions v1.2.0 (SPD, Paterson et al., 2014). Here, each table represents a different paleointensity method. Experiments in Tables B.1, B.2 and B.3 were analysed using paleointensity.org (Béguin et al., 2020). Table B.5 reproduces the published site mean direction results for the Skinner Cove Formation (McCausland & Hodych, 1998) including the reinterpretation of bedding correction for site SC07.

Raw measurement data can be accessed on the MagIC database, where it is published as Daniele Thallner, Andrew J. Biggin, Phil J. A. McCausland, Roger R. Fu (2021) "New paleointensities of the Skinner Cove Formation suggest a changing state of the geomagnetic field at the Ediacaran-Cambrian transition." Magnetics Information Consortium (MagIC). doi:10.7288/V4/MAGIC/16971

B.1 Supplementary Tables

TABLE B.1: Microwave Thellier results and critical SPD (v1.2.0, Paterson et al., 2014) values. Critical values are color-coded in the online version.

Specimen	B_{anc}	B_{lab}	Int_{min}	Int_{max}	n	f	β	q	k′	MAD_{Anc}	α	DRAT	CDRAT	$DRAT_{tail}$	type
SC0101B2	9.7	5	3	12	10	0.926	0.098	7.7	0.386	5	2.6	9.7	6.8		IZZI
SC0101B3	13.8	5	67.16	135.38	4	0.621	0.095	3.5	0.183	5.8	7	2.7	2.1		IZZI
SC0101B4	6.7	10	82.65	308.13	7	0.699	0.058	8.9	0	3	4.3	14.2	13		IZZI
SC0101B5	4.5	15	83.17	276.07	7	0.839	0.058	11	0.309	3	1.2	15.5	8.9		IZZI
SC0101B6	4.5	10	102.12	241.33	6	0.61	0.071	6.7	0.024	4.1	9.6	16.9	43.7		IZZI
SC0101B7	4.8	10	90.64	411.53	10	0.654	0.03	19	-0.054	2.5	6.5	17.3	23.5		IZZI
SC0103B1	1.9	10	100.79	410.08	8	0.639	0.059	9.1	-0.393	6.2	10	16	31.5		IZZI
SC0103B2	0.7	5	104.12	237.97	6	0.47	0.149	2.4	0.244	14.2	44.3	14.8	25.3		IZZI
SC0103B3	2.5	5	139.41	432.18	6	0.564	0.081	5.4	-0.36	6	6.2	15.4	27.8		IZZI
SC0103B4	9.8	5	0	104.8	6	0.412	0.075	4.3	0.005	7.4	32.8	6.6	4.9		IZZI
SC0104B1	2.2	10	105.97	459.98	8	0.632	0.112	4.1	-0.185	8.5	14.1	31.3	17.9		IZZI
SC0104B2	1.7	5	107.35	248.69	6	0.61	0.108	4.5	-0.404	3.5	2.9	20.6	31.7		IZZI
SC0104B3	2.1	5	105.95	225.5	6	0.45	0.138	2.2	0.004	12.3	31.9	13.4	12.2		IZZI
SC0306B2	4.3	10	71.05	175.31	5	0.77	0.224	2.2	-0.922	0.8	1.1	44.3	74.5		IZZI
SC0306B3	7.5	10	106.52	297.65	6	0.803	0.027	21.4	0.022	2.2	2.3	22.2	42.1		IZZI
SC0306B4	6.2	5	110.68	259.42	6	0.524	0.17	2	0.573	24.5	38.6	48.7	76.5		IZZI
SC0306B5	7	10	80.78	285.15	7	0.738	0.031	19.3	-0.115	2	3.4	16.8	41		IZZI
SC0308B1	3	10	86.02	381.98	9	0.548	0.029	14.7	-0.055	1.8	2.6	17.2	32		IZZI
SC0308B2	70.5	5	0	44.13	4	0.687	0.308	0.9	1.243	28.1	16.1	2.2	2.2		IZZI
SC0308B3	4	5	84.78	226.22	7	0.471	0.05	7.6	0.273	3.1	11.2	14.1	25.2		IZZI
SC0308B4	1.3	5	84.14	230.84	7	0.712	0.054	10.7	0.291	5.6	8.5	29.1	52.3		IZZI
SC0309B1	0.7	10	66.78	132.12	6	0.251	0.213	0.9	-0.741	4.8	16	51.3	86.5		IZZI
SC0309B2	3.3	5	95.19	193.7	6	0.422	0.088	3.8	0.58	2.6	1.2	39.2	49.6		IZZI
SC0309B3	1.9	5	62.33	97.73	4	0.268	0.399	0.4	1.546	4.3	27.5	64.5	65.8		IZZI
SC0309B4	1.4	20	78.61	151.28	5	0.443	0.164	1.7	0.039	3.5	7.2	68.5	97.3		IZZI
SC0312A1	5.5	10	115.67	195	5	0.408	0.014	20.6	0.049	1.2	5	34.7	57.8		IZZI
SC0312A2	4.7	5	99.06	185.17	6	0.332	0.096	2.6	-0.347	0.7	4.2	22.7	58.2		IZZI
SC0312A3	6.2	5	94.8	199.45	6	0.479	0.067	5.5	-0.27	0.5	1.6	25.8	50.7		IZZI
SC0312B1	7.8	10	81.49	125.53	3	0.349	0.144	1.1	0.093	0.8	3	28.6	25.4		IZZI
SC0312B2	6.5	5	67.94	106.98	3	0.356	0.242	0.7	0.753	1.8	9.2	3.8	4.7		IZZI
SC0312B3	9.9	20	65.8	101.93	3	0.301	0.167	0.7	-0.158	2	8.7	1.4	0.7		IZZI
SC0312B4	3.7	15	79.47	232.33	7	0.693	0.056	10.1	-0.102	2.4	5	28.2	70.1		IZZI
SC0312B5	7.7	10	91.98	130.11	5	0.293	0.127	1.7	0.529	1	5.9	12.9	7.6		IZZI
SC0312B6	3.1	5	119.38	352.38	7	0.758	0.053	10.3	0.416	1.4	3.2	27.5	58.3	3.8	C
SC0513B2	7.7	10	43.73	109.72	4	0.359	0.05	3.8	0.181	0.8	3.9	0.8	0.9		IZZI
SC0513B4	9.2	10	67.92	138.44	4	0.438	0.058	4.9	0.211	1	4.1	8.1	8.6		IZZI
SC0513B5	9.9	10	86.61	310.98	7	0.826	0.018	36.4	-0.04	1.1	1.6	16.8	29.3		IZZI
SC0513B6	9.5	10	84.22	292.86	7	0.874	0.046	13.6	-0.264	1.6	1.7	25.1	20.4		IZZI
SC0515B1	4.7	10	65.56	200.35	7	0.475	0.025	15.2	-0.09	1.6	5.6	13.7	25.6		IZZI
SC0515B2	5	5	44.55	450	11	0.804	0.043	15.4	0.266	1.2	0.9	7	9.8		IZZI
SC0515B3	5.6	5	65.96	148.48	5	0.352	0.076	3.2	0.332	0.6	2.3	9.9	3.2		IZZI
SC0515B4	5.1	5	87.66	236.53	7	0.636	0.038	13.2	-0.147	1.6	3.4	9.3	7.9		IZZI
SC0515B5	4.7	20	103.27	390.14	8	0.729	0.029	20.3	-0.077	2.7	4.2	17.3	27.4		IZZI
SC0515B6	5.4	5	0	223.4	11	0.621	0.014	37.7	-0.032	3.4	10.2	6.5	24.7		IZZI
SC0515B7	5.9	5	68.28	151.35	5	0.431	0.033	8.9	-0.152	0.9	3.4	17	14.7	8.7	C
SC0516B1	5.4	10	44.42	208.81	8	0.616	0.052	9	-0.113	3.3	7.7	21.7	14.5		IZZI
SC0516B2	4.2	5	65.65	265.89	8	0.547	0.04	11.2	-0.14	4	9.9	18.6	8.4		IZZI
SC0516B3	5.1	20	43.58	110.06	4	0.374	0.027	4.2	0.116	1.3	4.5	0.3	0.3		IZZI
SC0516B4	5.3	15	64.29	276.52	8	0.692	0.057	10	-0.299	1.9	4.1	14.5	29.4		IZZI
SC0516B5	4	10	87.19	234.57	9	0.726	0.028	22.1	0.105	1.1	0.2	18	44.4		IZZI
SC0517A1	3.6	10	66.1	205.11	8	0.339	0.114	2.4	0.488	8.5	46.9	39.8	44.7		IZZI
SC0517A2	4.5	5	65.57	224.63	8	0.617	0.041	11.6	-0.023	10.4	31.9	9.2	7.8		IZZI
SC0517A3	1.8	5	86.51	138.77	5	0.218	0.19	0.5	0.72	7.7	54.9	59.8	55.9		IZZI
SC0517A4	4.1	5	66.1	142.36	6	0.313	0.055	3.9	-0.225	7	37.6	24.1	17.3		IZZI
SC0622B2	2.2	10	44.63	86.75	3	0.221	0.234	0.5	1.162	2.4	9.9	72.4	70.7		IZZI
SC0622B3	2.2	10	84.77	166.75	4	0.694	0.109	4.2	0.116	6	6.6	35.6	37.5		IZZI
SC0622B4	5.5	10	44.92	87.66	3	0.167	0.087	0.7	1.02	3.8	38.3	17.3	8.5		IZZI
SC0910B2	7.5	10	0	260.79	11	0.766	0.014	48	0.031	4	7.4	13.8	35.3		IZZI
SC0910B3	12	10	66.66	546.24	8	0.77	0.025	25.6	-0.025	1.5	1.4	9.2	8.6		IZZI
SC0910B4	6.7	5	84.77	157.15	4	0.38	0.106	1.9	-0.535	1.1	4.4	17.1	17.6		IZZI
SC0910B5	8.5	5	83.22	499.69	9	0.819	0.04	16.6	-0.258	1.2	0.9	9.4	1.5		IZZI
SC0911B1	3.2	10	84.95	140.37	4	0.617	0.226	1.7	0.98	4.9	7.4	9.2	4.2		IZZI
SC0911B2	0.5	10	64.42	188.63	6	0.461	0.466	0.4	1.866	13	105.6	47.2	49.1		IZZI
SC0911B3	2.4	15	65.96	187.45	6	0.503	0.18	2.1	0.522	11	34.7	29.2	53.2		IZZI
SC0911B4	0.8	15	68.41	256.06	7	0.773	0.225	2.4	-1.174	13.7	11.8	26.8	34.4		IZZI

Table B.1 continued

Specimen	B_{anc}	B_{lab}	Int_{min}	Int_{max}	n	f	β	q	k′	MAD_{Anc}	α	DRAT	CDRAT	$DRAT_{tail}$	type
SC0911B5	0.5	5	65.67	308.88	8	0.603	0.253	1.5	-1.5	16.5	33.5	39.4	55.5		IZZI
SC1107B2	0.9	10	61.9	122.21	6	0.117	0.676	0	1.848	6.4	62	18.8	20.3		IZZI
SC1107B3	12.3	10	65.55	109.93	5	0.357	0.074	3.6	0.517	9.4	24.1	28.9	63.5		IZZI
SC1107B4	1.7	5	82.41	148.76	7	0.18	0.469	0.3	2.652	10.1	65.1	29.2	66.6		IZZI
SC1107B5	51.2	10	21.41	92.39	7	0.836	0.074	8.4	0.226	3.8	6.1	4.4	7.7		IZZI
SC1108B1	1.1	10	79.97	155.88	5	0.332	0.414	0.4	1.441	8.9	43	33.8	25		IZZI
SC1108B2	2.9	5	98.7	197.13	5	0.589	0.26	1.4	1.194	8.6	18.9	8.5	1.4		IZZI
SC1111B1	1.5	10	84.45	229.04	7	0.479	0.123	3	0.238	9.4	29	22.4	26.2		IZZI
SC1111B2	1.4	5	108.47	276.47	7	0.543	0.046	9.2	-0.198	4	5.5	8.9	1.5		IZZI
SC1111B3	4.1	5	129.75	328.59	6	0.48	0.081	4.4	0.478	1.2	1.1	9.4	2.2		IZZI
SC1111B4	1.2	5	106.01	183.63	6	0.332	0.085	2.3	-0.29	2.2	4.9	23.3	15.2	4.4	C
SC1308B2	1.9	10	80.59	129.74	6	0.214	0.22	0.5	1.586	10.3	65.3	15.5	36.5		IZZI
SC1308B3	3.9	10	80.3	136.44	4	0.458	0.397	0.7	1.893	8.2	16.2	16.7	39.1		IZZI
SC1308B4	3.8	5	110.26	241.56	8	0.351	0.165	1.7	0.94	1.1	7.1	32.4	69.9		IZZI
SC1308B5	3.1	10	112.09	228.34	7	0.427	0.163	2.1	1.113	2.8	2.8	25.1	20.6		IZZI
SC1404B4	28.8	5	0	143.59	9	1.06	0.31	2.7	1.46	11.7	13.6	6.9	10.6		IZZI
SC1504B2	2.6	10	124.8	147.94	3	0.347	0.461	0.3	0.152	25.9	65.1	65.9	87.6		IZZI
SC1504B3	61.1	10	0	99.12	6	0.857	0.093	7.1	0.376	2.7	4.2	0.9	0.7		IZZI
SC1504B4	58	10	0	65.36	4	0.914	0.135	4.5	0.494	5	6.9	3	3		IZZI
SCTS01B1	75.6	5	0	85.65	6	1.001	0.476	0.9	1.486	3.2	4.6	3.3	3.7		IZZI
SCTS01B2	65.2	10	0	85.49	5	0.77	0.087	6.5	0.299	1	0.8	1.5	2.2		IZZI
SCTS01B3	5.5	10	83.62	143.16	3	0.685	0.178	1.9	-0.057	9.8	4	37.6	38.6		IZZI
SCTS01B4	34.8	20	0	108.27	7	0.776	0.189	3.2	-0.172	14.3	13.1	19.5	17.6		IZZI
SCTS01B5	12.1	20	21.62	86.48	4	0.407	0.16	1.5	0.713	10.2	27.2	20.3	13.6		IZZI
SCTS01B6	8.1	20	85.78	139.75	3	0.396	0.057	3.4	-0.11	8.9	25.3	61.6	64.6		IZZI
SCTS02B1	16.9	10	84.46	164.28	6	0.373	0.076	3.6	-0.244	5.1	25.7	14.1	10.8		IZZI
SCTS02B2	13.9	5	109.98	436.99	8	0.72	0.082	6.5	0.221	0.6	0.3	6.3	3.3		IZZI
SCTS02B3	10.3	5	109.47	321.74	7	0.526	0.026	16.4	-0.042	1.3	3.8	3.5	2.8		IZZI
SCTS02B4	11.7	20	101.52	186.16	5	0.677	0.053	8.6	0.217	2.9	5.1	2.4	2.8		IZZI
SCTS02B5	11.4	5	64.77	234.24	8	0.797	0.045	14.8	0.067	2.4	3.7	6.3	7.4		IZZI
SCTS02B6	12.5	5	106.23	228.78	6	0.558	0.066	5.9	-0.081	1.1	2.8	8.8	3.8		IZZI
SCTS02B7	12.9	5	81.62	212.61	7	0.382	0.087	2.8	0.424	2.4	9.1	9.5	6.4	4.4	C
SCTS04B1	26.1	10	0	64.18	4	0.813	0.068	7.3	0.203	7.8	11.1	0.3	0.3		IZZI
SCTS05A1	10.3	10	88.03	434.38	9	0.657	0.05	8.4	0.388	3.8	10.1	31.6	26.1		IZZI
SCTS05A2	7.8	5	105.36	427.14	8	0.666	0.048	10.1	0.224	2.8	6.7	8.1	14.4		IZZI
SCTS05A3	8.4	5	74.21	154.19	5	0.482	0.053	5.8	0.265	1.2	4.2	18	16.5	11.9	C
SCTS05B1	11.7	10	83.64	222.83	6	0.638	0.058	8.4	0.082	1.3	2.3	15.9	21.2		IZZI
SCTS05B2	14.9	5	43.8	321.14	9	0.803	0.062	10.5	0.073	2.4	2.7	8.8	4.5		IZZI
SCTS05B3	9.8	20	86.21	281.31	7	0.8	0.032	18.2	-0.149	5.1	5.8	29.8	13.8		IZZI
SCTS05B4	14.5	15	83.69	308.59	5	0.777	0.035	16.1	-0.12	1.6	1.8	15.6	16		IZZI
SCTS06B1	10.9	10	0	134.62	7	0.838	0.143	4.7	0.383	13	43.5	7.5	7.5		IZZI

Specimen	B_{anc}	B_{lab}	T_{min}	T_{max}	n	f	β	q	k′	MAD_{Anc}	α	DRAT	CDRAT	type
SC0103B	1	10	400	530	7	14.6	0.459	11.2	2.754	21.3	11.3	8	11	IZZI
SC0104B	1.1	10	400	530	7	66.911	0.54	27.2	2.749	10.7	1.6	10.4	1.5	IZZI
SC0308B	2	10	460	530	5	0.706	0.162	3.2	0.355	14.6	23.9	4.7	2.2	IZZI
SC0309B	0.6	10	460	530	5	0.472	0.325	0.9	1.309	33.2	57.6	32.6	56.9	IZZI
SC0312B	5.5	10	460	530	5	0.867	0.152	4.1	0.294	4.2	5.4	27	26.5	IZZI
SC0515B	4.5	10	460	530	5	0.834	0.174	3.5	0.632	11.1	15.6	13.6	14.7	IZZI
SC0517A	2.8	10	460	520	4	0.397	0.091	5.4	0.24	7.2	8.5	2.5	1.7	IZZI
SC1108B	0.7	10	400	530	7	1.406	0.538	0.1	2.802	34.5	56.4	9	9.9	IZZI
SC1111B	15.2	10	200	510	10	0.638	0.185	3	0.864	5.1	6.9	15.3	26.4	IZZI
SC1112B	0.8	10	360	510	6	0.34	0.654	0.2	2.663	30.5	84.1	17.4	12.5	IZZI
SC1404B	4.1	10	280	510	8	1.172	0.447	1.2	2.719	7.9	10.5	18.5	4.4	IZZI
SCTS02B	6.2	10	430	530	6	0.908	0.057	10.3	0.399	2.6	2	6.7	3.2	IZZI
SCTS05B	7.1	10	460	530	5	0.865	0.08	6	0.255	3.3	2.4	9.7	4.3	IZZI
SCTS06B	1.3	10	430	530	6	0.782	0.125	4.7	0.615	12.1	10.7	5.1	9.5	IZZI

TABLE B.2: Thermal Thellier results and critical SPD values. Critical values are color-coded in the online version.

Specimen	B_{anc}	std-error	H_{lab}	AF_{min}	AF_{max}	n	f	r_n^2	r_t^2	α	MAD_a	MAD_f	$Slope_T$
SC0101A	26.5	0.5	10	10	50	8	0.7	0.998	0.999	4.06	5.45	2.71	1.14
SC0103A	5.6	0.28	10	10	30	5	0.43	0.992	1	2.06	2.45	1.95	0.9
SC0104A	4.8	0.11	10	5	70	11	0.78	0.996	0.999	0.49	1.46	1.34	1.08
SC0131	2.8	0.06	20	9	30	8	0.67	0.997	0.999	3.3	1.9	0.75	0.96
SC0306A	5.5	0.1	20	12	100	21	0.98	0.994	1	0.71	1.33	1.81	0.92
SC0308A	3.6	0.09	10	15	50	7	0.53	0.991	1	1.53	1.36	0.64	1.06
SC0309A	9.4	0.11	10	10	100	13	0.55	0.999	0.999	1.75	2.49	1.07	0.99
SC03122A	74.5	2.12	10	18	60	7	0.48	0.996	0.985	1.13	1.07	0.89	0.32
SC03122B	5.8	0.2	20	21	60	10	0.62	0.991	0.999	0.54	0.71	0.94	0.91
SC0312A	6.2	0.23	10	15	40	6	0.67	0.995	1	2.05	1.36	1.26	1
SC0515A	6.0	0.04	10	5	30	6	0.79	1	1	5.07	2.98	3.41	1.05
SC0516A	33.0	2.69	10	20	60	7	0.95	0.967	0.992	2.75	2.13	2.72	1.18
SC0516B	6.2	0.27	20	18	35	6	0.45	0.992	0.997	2.1	0.65	1.21	0.9
SC0517B	7.1	0.14	10	5	100	14	0.83	0.995	1	0.31	1.79	1.94	0.97
SC0622A	13.1	1.78	10	20	60	7	0.36	0.91	0.997	50.56	3.74	9.45	1.07
SC0625A	1.7	0.1	10	10	40	7	0.72	0.984	1	20.99	9.22	3.23	0.99
SC0626A	1.6	0.13	10	10	30	5	0.63	0.979	1	18.88	6.94	1.14	0.97
SC0652B	1.5	0.02	20	15	40	8	0.54	0.998	0.999	39.48	14.19	2.72	1.18
SC0911B	1.2	0.09	20	15	50	10	0.29	0.959	0.999	22.6	26.45	15.79	0.91
SC1112A	3.0	0.07	10	20	100	11	0.73	0.995	0.999	13.04	4.86	3.43	1.01
SC1402	1.6	0.3	20	10	50	11	0.82	0.721	1	19.49	6.69	17.3	0.93
SC1404A	1.3	0.08	10	20	60	7	0.39	0.979	0.998	2.47	13.54	11.63	1.04
SC1413A	2.6	0.11	10	5	25	5	0.64	0.995	1	8.14	1.32	1.04	1.04
SC1413B	2.6	0.1	10	3	25	6	0.74	0.994	1	8.92	1.34	1.27	1.03
SC1501A	0.3	0.06	20	10	40	9	0.47	0.705	0.999	16.47	6.58	30.99	0.86
SC1502	1.0	0.04	20	18	60	11	0.61	0.989	0.999	18.78	8.56	9.86	0.94
SC1504A	7.0	0.4	10	3	20	5	0.73	0.99	0.995	2.17	2	1.72	0.94
SC1505A	4.8	0.29	10	3	20	5	0.78	0.99	0.999	3.14	2.64	1.54	1.14
SCTS02A	8.0	0.23	10	10	30	5	0.62	0.998	1	2.65	1.3	0.79	1.02
SCTS041	1.4	0.04	20	21	45	7	0.32	0.996	0.999	7.62	3.47	6.04	1.05
SCTS04A	0.8	0.03	10	25	60	6	0.32	0.994	0.999	12.27	11.9	9.66	1.09
SCTS04B	0.9	0.04	10	20	40	5	0.32	0.992	1	14.82	9.14	9.06	1.02
SCTS05B	15.7	0.3	10	5	40	8	0.86	0.998	0.999	1.84	2.32	2.06	0.95

TABLE B.3: DHT Shaw results and critical SPD values, analyzed in Python. Critical values are color-coded in the online version.

Specimen	B_{anc}	B_{lab}	b	σb	AF_{min}	AF_{max}	n	$B_{1/2ARM}$	f	β	k′	r^2	MAD_{Free}	α	k'_{AA}	k'_{DD}	R^2_{AA}
SC0131	1.6	40	-0.135	0.012	45	85	9	18.8	0.103	0.087	-0.152	0.947	9.1	8	0.111	0.605	0.946
SC0306A	6.1	40	-0.503	0.008	15	45	9	35.8	0.581	0.017	-0.056	0.998	1.4	2.2	-0.014	0.043	0.998
SC0307	3.4	20	-0.562	0.028	25	75	7	18.5	0.343	0.05	0.21	0.987	2.2	1.8	-0.029	0.301	1
SC03122B	6.3	40	-0.518	0.014	15	40	8	23.5	0.653	0.026	0.128	0.996	1.6	1.4	0.008	0.116	0.998
SC0513A	13.5	20	-2.214	0.078	5	60	10	29.1	0.965	0.035	0.197	0.99	2.5	1.9	-0.002	0.205	1
SC0516B	4.1	40	-0.34	0.009	9	50	12	28.8	0.753	0.025	0.007	0.994	2.1	4.3	0.006	0.001	0.998
SC0624	4.4	11.416	-1.276	0.051	10	30	5	13.1	0.53	0.04	0.145	0.995	0.6	4	-0.021	0.154	1
SC0652B	0.9	40	-0.075	0.005	24	100	17	20.3	0.371	0.061	-0.133	0.945	11.5	9.6	0.118	0.29	0.964
SC0911B	0.7	40	-0.059	0.004	15	27	5	11.1	0.258	0.075	-0.349	0.983	19.1	2.5	-0.13	0.291	0.998
SC1109	1.0	40	-0.086	0.003	30	100	15	56.7	0.794	0.035	-0.046	0.984	6.7	4.8	0.291	0.328	0.987
SC1110	1.0	20	-0.158	0.005	5	60	10	35.3	0.852	0.033	0.153	0.991	10.5	10.9	0.005	0.16	1
SC1402	3.9	40	-0.319	0.027	0	15	6	29.5	0.725	0.085	0.493	0.971	5.7	12.6	0.017	0.468	0.996
SC1418	0.6	11.416	-0.16	0.019	20	100	11	23.6	0.595	0.116	-0.085	0.883	19.3	14.7	0.057	0.049	0.99
SC1501A	0.3	40	-0.023	0.002	0	100	25	29	0.922	0.071	0.125	0.889	29.6	32.1	0.187	0.058	0.995
SC1502	0.9	40	-0.073	0.002	18	100	19	28	0.735	0.025	0.09	0.989	8.3	4.3	0.16	0.055	0.995
SC1503	2.0	11.416	-0.579	0.048	15	100	12	11.6	0.38	0.083	0.204	0.932	8.7	3.5	0.013	0.269	0.96
SCTS041	1.0	40	-0.086	0.004	24	70	11	22.2	0.372	0.042	0.047	0.984	6.4	7.6	0.082	0.018	0.99
SCTS051	5.9	20	-0.963	0.074	30	60	5	13.5	0.142	0.077	0.145	0.982	1.5	4.6	0.082	0.801	0.921

TABLE B.4: Pseudo-Thellier results and critical SPD values. Critical values are color-coded in the online version.

Site	lithology	cmp	N	Strike	Dip	Dec(g)	Inc(g)	α_{95}	k	Dec(t)	Inc(t)
SC01	[1]	A	5	57	70	98.3	89.3	12.0	41	146.4	19.5
SC03	[2]	A	6	62	67	341.3	56.3	9.2	54	142.8	56.0
SC04	[3]	A	5	62	67	7.4	71.4	5.6	188	138.5	37.6
SC05	[3]	A	6	44	69	310.6	51.0	13.9	24	138.3	59.9
SC06	[4]	A	6	73	80	17.2	78.2	14.0	23	156.0	19.7
SC09	[3]	A	6	44	69	314.8	72.7	10.7	40	133.7	38.3
SC10*	[5]	A	3	57	56	151.2	70.1	*30.2*	*17*	148.8	14.1
SC11	[6]	A	4	57	56	207.6	80.3	17.5	28	156.6	28.9
SC13	[6]	A	5	50	80	16.1	77.2	14.5	28	128.9	16.9
SC14	[5]	A	9	59	72	219.1	87.8	11.1	22	151.2	17.2
SC15	[2]	A	5	59	77	345.0	79.4	8.5	81	145.8	23.2
SC07	[3]	B	4	**58**	**71**	143.2	-38.2	12.7	53	339.3	-70.4
SC08*	[3]	C	5	44	69	153.5	18.4	*20.7*	*14*	161.2	-46.2

TABLE B.5: Paleomagnetic site mean results for the Skinner Cove Formation reported in McCausland and Hodych (1998), with recalculated tilt correction for site SC07. Site mean results sorted by remanence direction groups A,B,C recognized by McCausland and Hodych (1998). Lithologies: [1] ankaramite, [2] trachybasalt, [3] alkali basalt, [4] trachyte, [5] trachyte dyke, [6] mafic dyke. Abbreviations: N – number of samples contributing to site mean; Strike, Dip – bedding orientation in right-hand rule sense with strike azimuth 90 degrees less than dip direction; Dec(g), Inc(g) – site mean declination and inclination in geographic coordinates; α_{95} – circle of 95% confidence about the site mean direction; k – precision parameter estimate; Dec(t), Inc(t) – site mean declination and inclination in tilt-corrected coordinates. * - sites with α_{95} larger than 20 degrees are excluded from plotting in Figure S3. Site SC07, originally reported with a bedding correction of 020/78, is here tilt corrected using the average bedding correction for the rest of the Skinner Cove Formation sites (058/71). Please see main text for discussion.

B.2 Supplementary Figures

FIGURE B.1: Rock magnetic data of at least one specimen per site: top left: hysteresis loop, processed with HystLab (Paterson et al., 2018), grey: raw data, red: fitted loop, top right: thermomagnetic curve (20-700°C), bottom left: temperature dependent susceptibility (40-700°C), bottom right: cyclic thermomagnetic curves (50-150°C, 100°C increments)

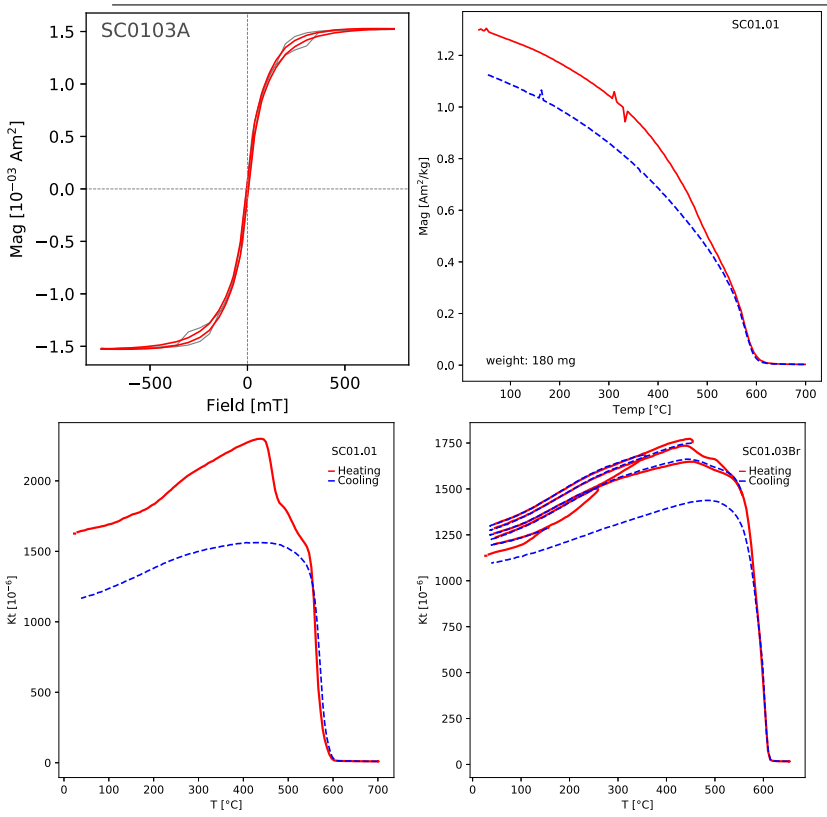

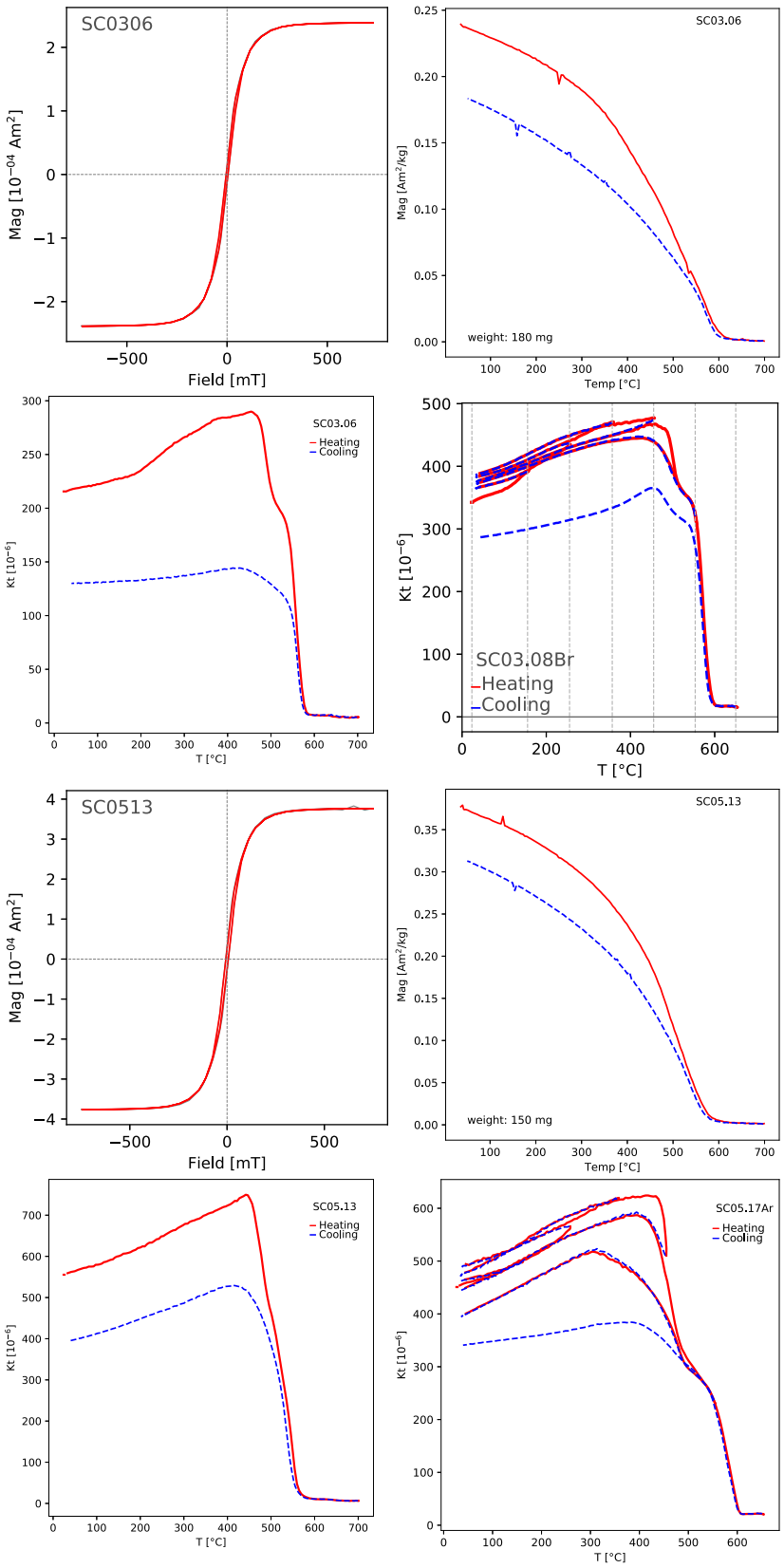

(A) Figure B.1 continued

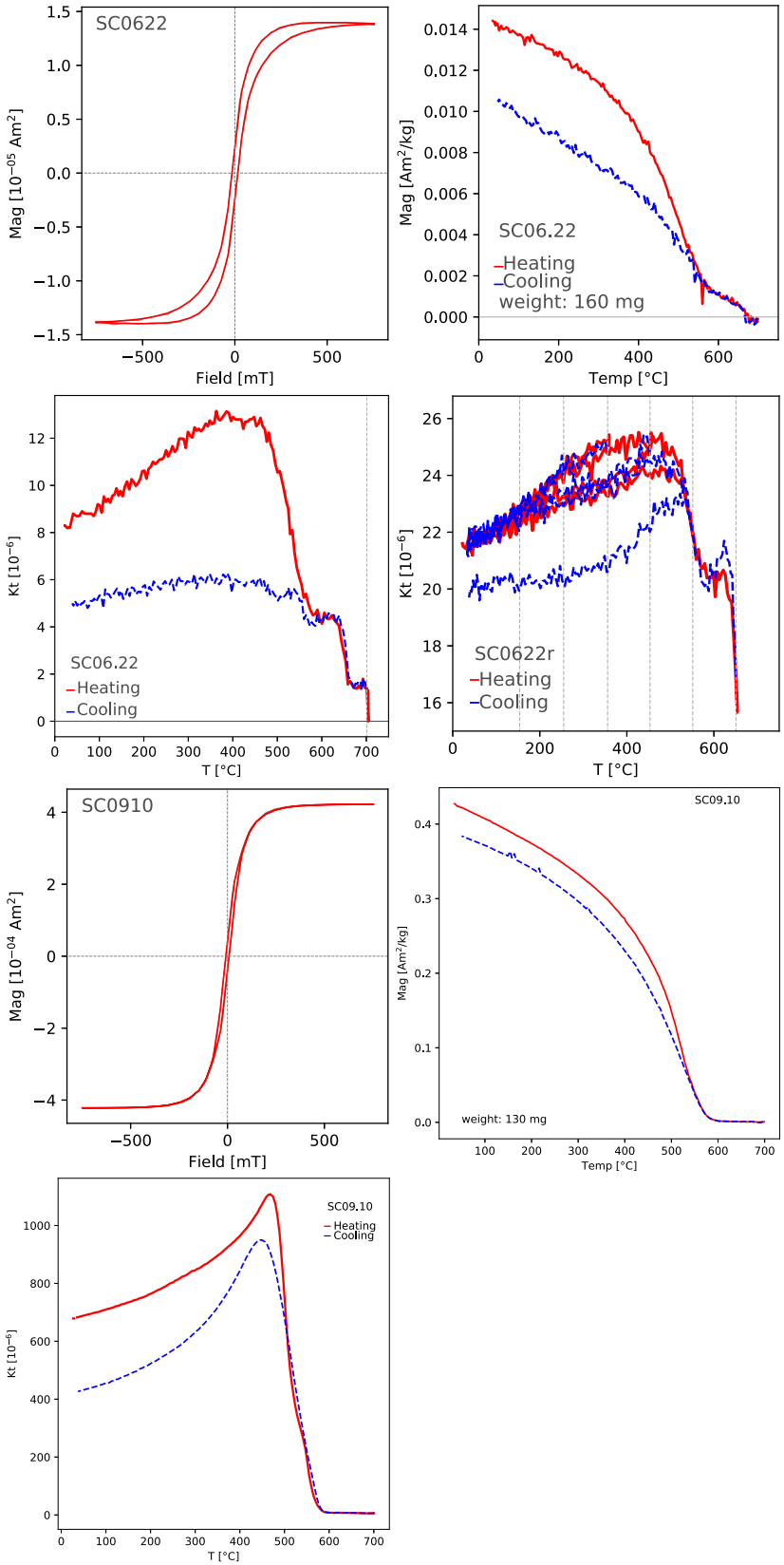

(B) Figure B.1 continued

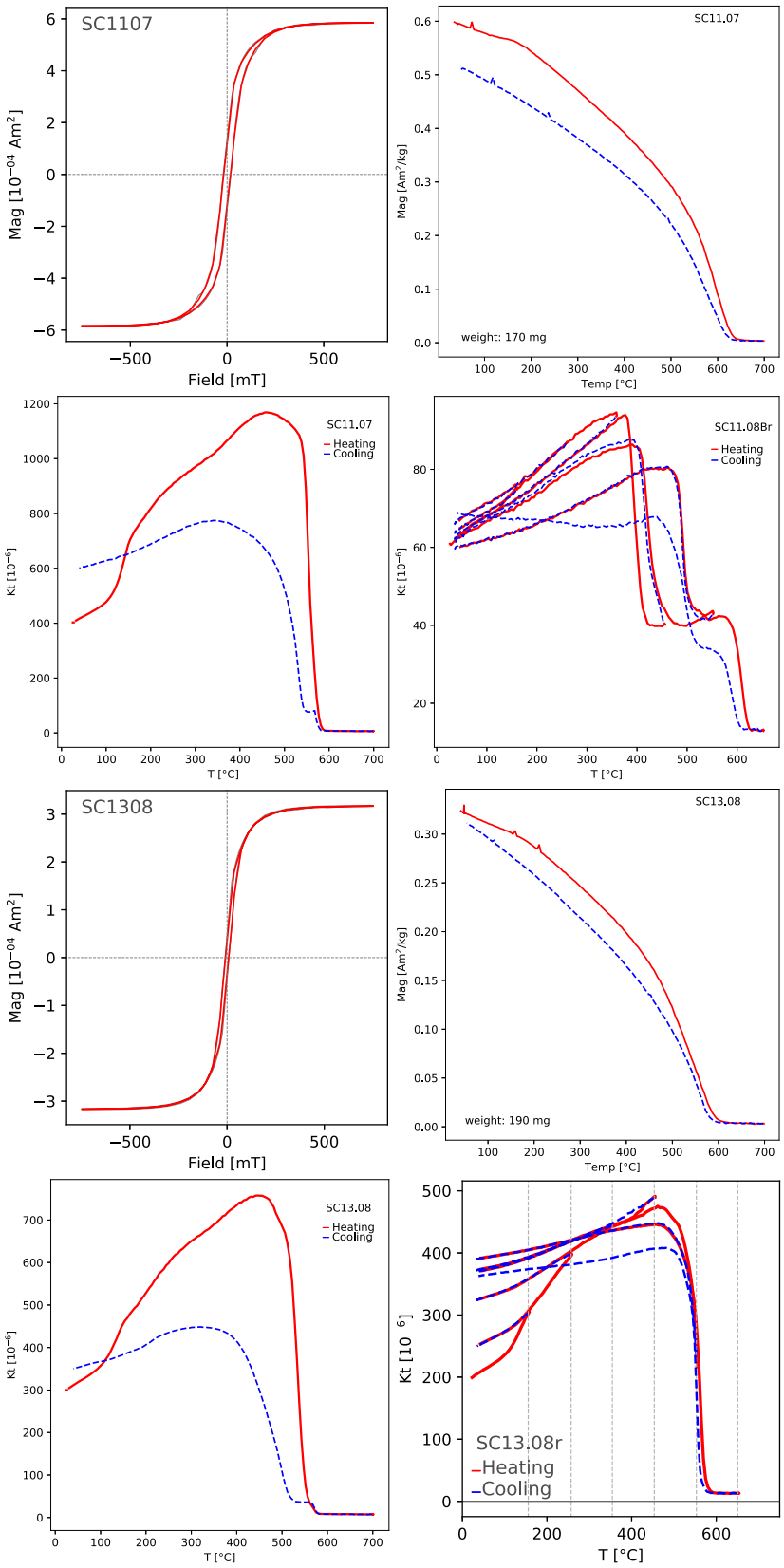

(C) Figure B.1 continued

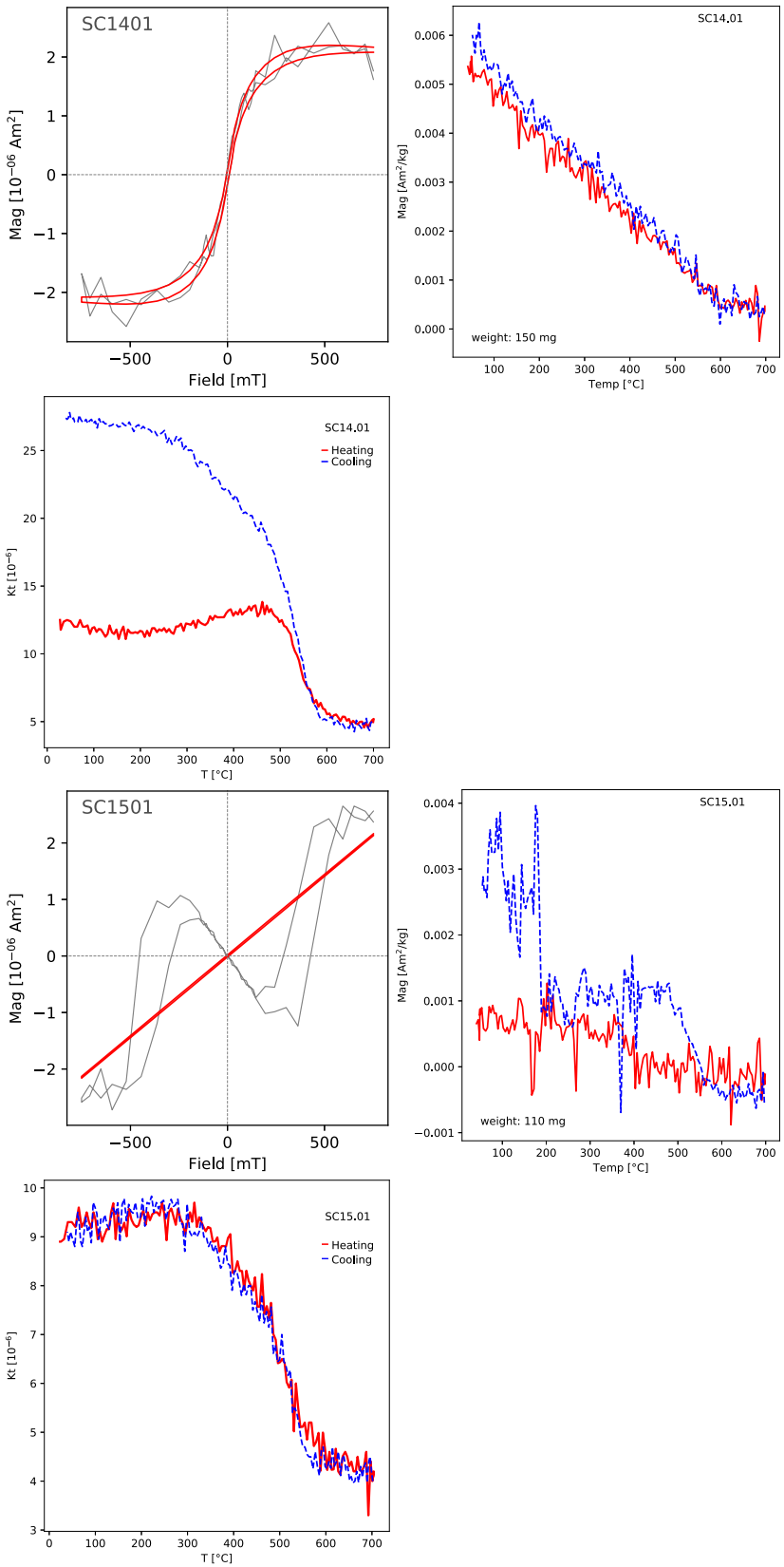

(D) Figure B.1 continued

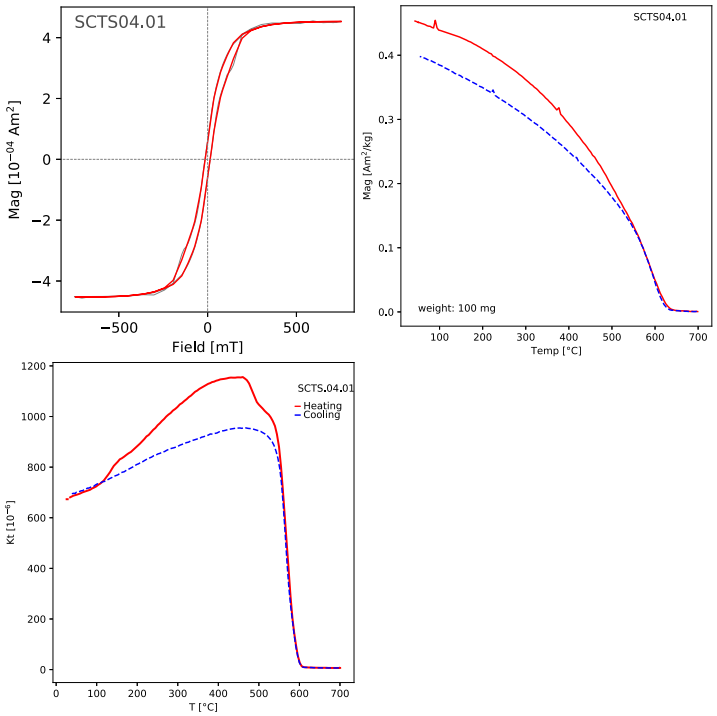

(E) Figure B.1 continued

FIGURE B.2: Elemental composition maps from BSE analysis for samples shown in figure 2.2 of the main text for specimens from sites SC05, SC09 and SC11.

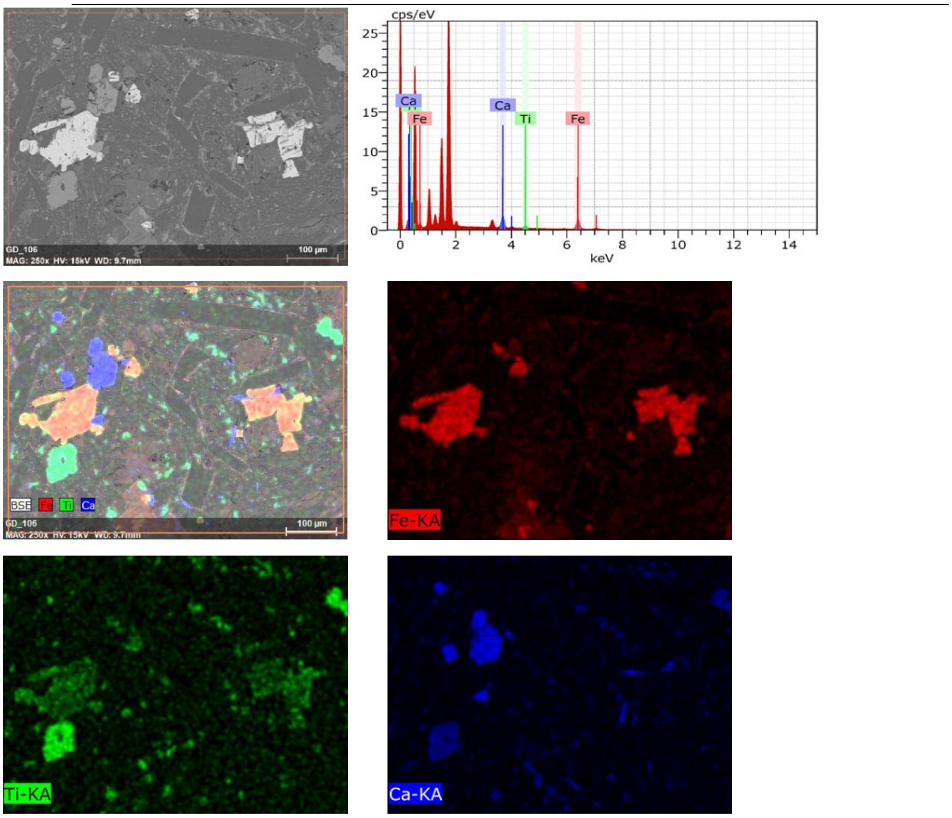

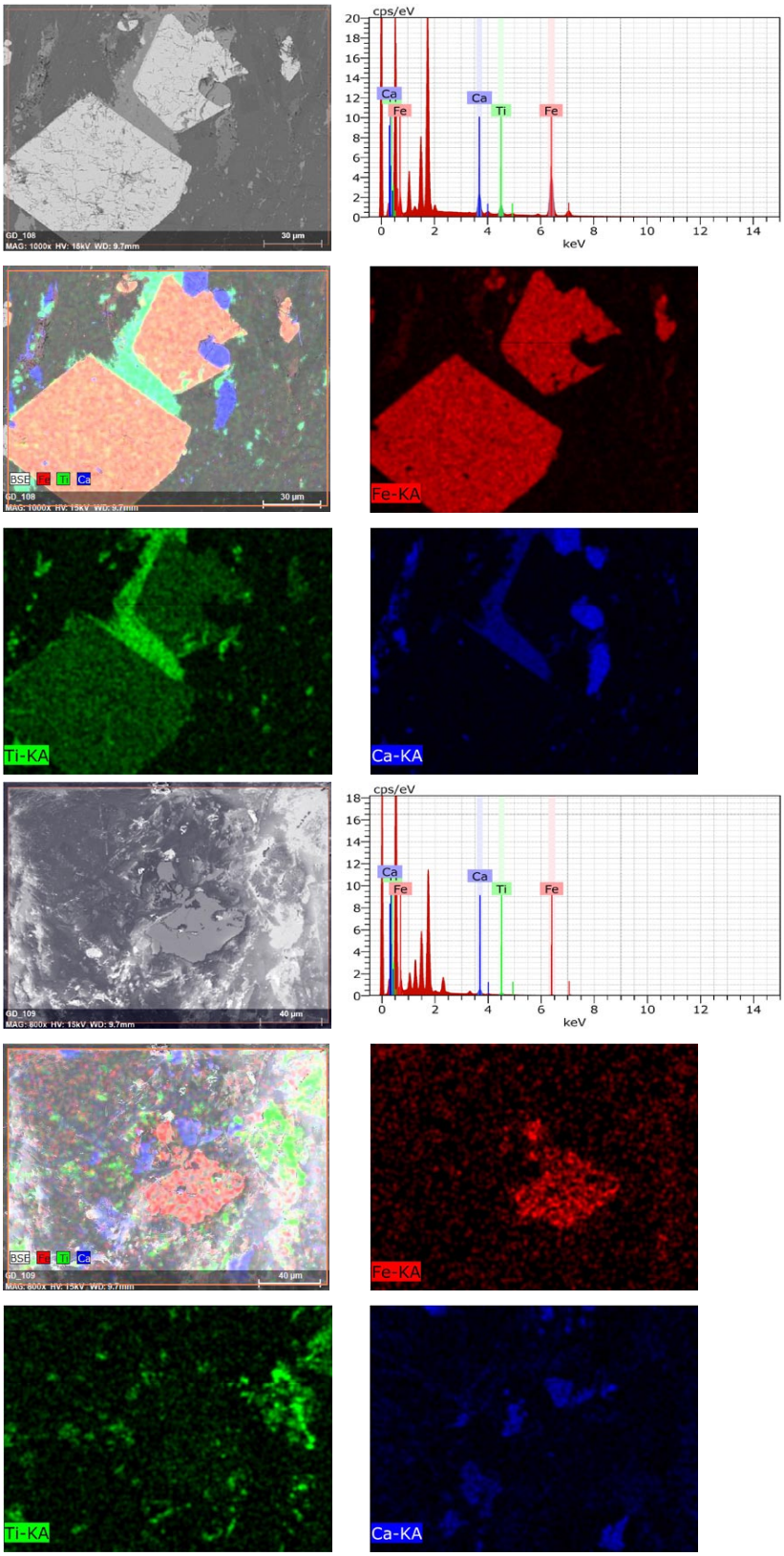

(A) Figure B.2 continued

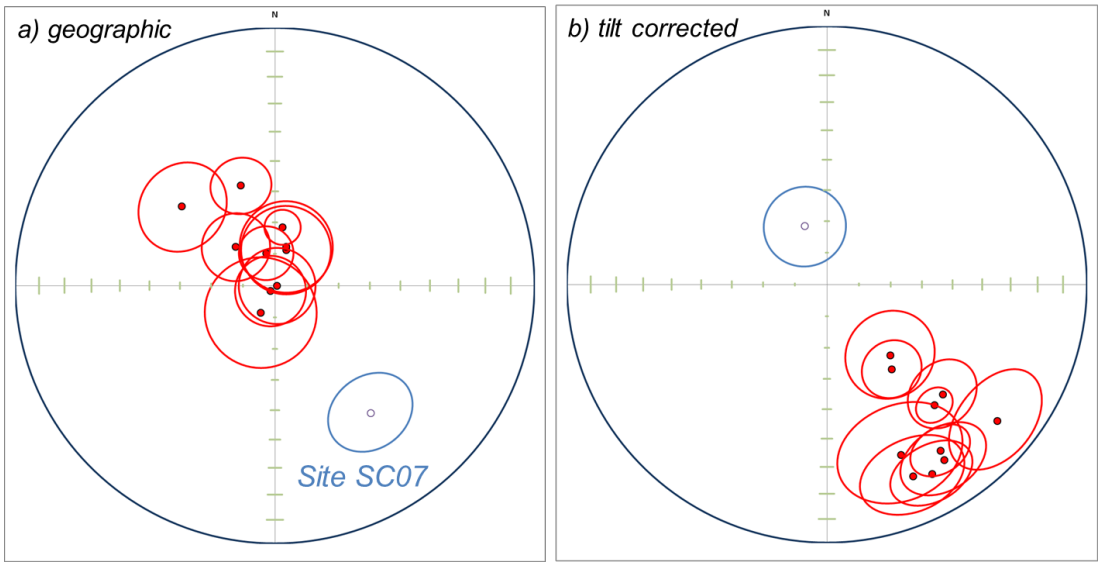

FIGURE B.3: Equal-area stereographic projection of Skinner Cove A and B site mean directions (Table B.5), drawn from McCausland and Hodych (1998) in a) geographic and b) tilt-corrected coordinates. Down (up) directions are shown as closed (open) circles, along with their α_{95} error ellipses. In geographic coordinates the B mean direction for site SC07 lies in the SE, up quadrant, opposite the down directions of the A sites. Tilt-correction of SC07 using the average bedding from all other Skinner Cove sites (058/71) suggests that the site carrying B remanence likely retains a reversed direction opposite the Skinner Cove A site mean directions. Directional data projected using DAIE software (Sagnotti, 2013).

Appendix C

Volyn Traps supplementary data

The data included in Appendix C is intended to complement the examples presented in the main text of Chapter 4 and show additional rock magnetic and paleomagnetic data as well as all paleointensity results and paleomagnetic site mean directions.

Figure C.1 shows a profile of rock- and palaeomagnetic data for the profile of the Rafalovka and Policy-2 quarries. Table C.1 gives additional information to the palaeomagnetic directions of the Basaltovoe and Berestovets sites, presented in Table 4.3 of Chapter 4. Tables C.2 to C.6 present paleointensity results for each of the measured specimens with their critical values according to the Standard Paleointensity Definitions v1.2.0 (SPD, Paterson et al., 2014), where each table represents a different paleointensity method. Experiments in Tables C.2, C.3 and C.6 were analysed using paleointensity.org (Béguin et al., 2020).

Raw measurement data is stored on the MagIC database, where it will be published as Thallner, D., Shcherbakova,V. V., Bakhmutov, V. G., Shcherbakov, V. P., Zhidkov, G. V., Poliachenko, I. B., Biggin, A. J.: "New palaeodirections and palaeointensity data from extensive profiles through the Ediacaran section of the Volyn Basalt Province (NW-Ukraine)" Magnetics Information Consortium (MagIC).
doi:10.7288/V4/MAGIC/19341

C.1 Supplementary Tables

TABLE C.1: Mean paleomagnetic directions calculated from samples of "high-Ti" basalts of the Volyn Series (Ratne Formation). Note: NRM is natural remanent magnetisation range and mean values; magnetic susceptibility range and mean values; n is number of samples which yielded the ChRM-component; Dec is declination; Inc is inclination; k is the precision parameter; α_{95} is half-angle of cone of 95 per cent confidence, in degrees. **bold** – insufficient data for statistics.

Site	Comp	Sample/ demagnetisation	NRM (A/m)	susceptibility SI	Q ratio	n	Dec	Inc	k	α_{95}
Berestovets quarry, 50.873ºN, 26.303ºE										
BE	1	BE01 - BE23 2 - 10mT	1.8 - 7.7 4.8	0.028 - 0.034 0.031	1.4 - 6.5 3.9	16	81.9	53.4	396.0	
	2	100 - 200°C				11	87.2	81.6	14	12.8
	3	200 - 420°C				22	76.0	53.6	58	4.1
Berestovets quarry, 50.863ºN, 26.307ºE										
BR	4	BR1 - BR13 5 - 15mT	1.9 - 6.4 3.5	0.039 - 0.06 0.048	0.8 - 3.4 1.9	7	63.1	49.9	18	14.7
	5	**great circle** **20 - 80mT**				**4**	**126.4**	**-17.9**		**(4.8)**
	6	200 - 400°C				10	83.0	54.7	27	9.5
Bazaltovoye quarry, 50.913ºN, 26.239ºE										
BAZ	7	BAZ1 - BAZ12 5-25mT	0.47 - 8.3 4.3	0.02 - 0.06 0.04	0.5 - 7.3 3.0	7	113.0	40.8	13	17.5
	8	**great circle** 15 - 80mT				**3**	**253.4**	**-11.7**		**(0.2)**
	9	100 - 300°C				6	140.2	62.4	7.6	26
	10	300 - 420°C				7	103.0	54.0	11	19.3
	11	400 - 560°C 'tail'				9	119.5	31.3	12	15.7
Bazaltovoye quarry, 50.923ºN, 26.237ºE										
BZ	12	BZ1 - BZ20 5-25mT	1.7 - 14.7 5.4	0.03 - 0.06 0.037	1.1 - 10.0 3.8	7	71.9	55.8	34	7.0
	13	**great circle** 20 - 70mT				**4**	**86.2**	**-28.1**		**(2.0)**
	14	**100 - 300°C**				**3**	**127.3**	**-25.0**	**49**	**17.9**
	15	300 - 420°C				12	127.3	47.4	36	7.3
	16	'tail' 360 - 500°C				13	95.9	16.2	9	14.8

TABLE C.2: thermal Thellier results and critical values (SPDv1.2.0, Paterson et al., 2014) analysed with paleointensity.org (Béguin et al., 2020). Experiment protocols (prot.): C: Coe, I: IZZI

Specimen	B_{anc}	B_{lab}	Min	Max	n	f	FRAC	β	g	q	k'	MAD_f	MAD_a	α	DRAT	CDRAT	prot.
BAZ-01U	0.9	10	450	580	5	0.336	0.14	0.24	0.102	0.1	1.78	30.8	17.2	74.5	7.6	15	C
BAZ-02U(1)	3.8	10	320	500	7	0.514	0.307	0.114	0.669	3	-0.722	9.6	10.9	32	45.5	29.7	C
BAZ-02U(2)	1.7	10	350	580	6	0.568	0.458	0.407	0.433	0.6	2.386	40.3	25.1	88.5	13.7	4.3	C
BAZ-03B	2.8	15	400	600	13	0.488	0.555	0.264	0.212	0.4	3.55	40.4	11.8	18.3	22.3	30.4	I
BAZ-03U(1)	3.1	10	320	500	7	0.614	0.27	0.2	0.338	1	1.492	8.7	40.2	32.6	34.7	31.7	C
BAZ-03U(2)	1.1	10	350	580	6	4.729	0.31	0.663	0.214	1.5	2.619	20.6	20.3	24	38	23.1	C
BAZ-04U(1)	3.1	10	320	500	7	0.676	0.394	0.187	0.684	2.5	0.616	17.7	16.2	26.9	41.1	63.9	C
BAZ-04U(2)	1.6	10	350	580	6	0.481	0.443	0.613	0.257	0.2	2.716	20.9	13.1	14.1	41.3	32.6	C
BAZ-05U(1)	2.6	10	260	500	10	0.584	0.411	0.087	0.799	5.4	-0.13	29	13.2	34.5	16	33.9	C
BAZ-05U(2)	1.5	10	250	580	7	3.138	0.642	0.575	0.08	0.4	2.359	30.6	24.8	156.3	41.1	31.9	C
BAZ-06U(1)	3.2	10	290	500	9	0.577	0.476	0.124	0.824	3.8	-0.788	33.6	16	51.6	21	28.4	C
BAZ-06U(2)	2.7	10	350	580	6	0.572	0.47	0.5	0.627	0.7	-1.701	35	16.9	12.1	22.2	0.1	C
BAZ-07U	54.2	10	200	410	9	0.944	0.663	0.197	0.605	2.9	1.25	3.4	7.2	5.9	7.6	20	C
BAZ-08U	3.9	10	290	500	9	0.941	0.402	0.142	-0.044	-0.3	0.903	11.4	27.2	7.2	31.9	51.3	C
BAZ-09U	1.5	10	140	410	11	0.606	0.429	0.217	0.656	1.8	0.47	10.8	21	68.8	10.3	24.8	C
BAZ-10B	6.5	15	360	600	14	0.681	0.377	0.157	0.506	2.2	0.157	34.7	26.3	50.9	61.8	79.9	I
BAZ-10U	6.5	10	290	500	9	0.922	0.353	0.212	0.233	1	1.405	6.3	22.9	9.6	31.4	58.1	C
BAZ-11U	3.1	10	290	500	9	0.913	0.408	0.352	0.139	0.4	1.798	7.5	22.5	2.4	33.5	17	C
BAZ-12U	1.1	10	260	500	10	0.4	0.452	0.367	0.413	0.5	1.748	42.5	10.7	23.8	52.2	63	C
BR-02B	3.2	15	490	600	10	0.547	0.248	0.18	0.726	2.2	0.631	8.4	3.9	2.4	42.2	43.9	I
BR-02U(1)	0.7	10	230	500	10	0.207	0.291	0.41	0.021	0	-0.789	23.4	13.6	85.4	31.3	66.8	C
BR-02U	0.6	10	400	570	5	0.202	0.16	0.758	-1.153	-0.3	-3.062	33.7	13.7	94.5	70.1	108.4	C
BR-03U(1)	4.2	10	350	500	6	0.742	0.246	0.565	0.138	0.2	3.337	39.8	11.3	113.5	101.7	154.7	C
BR-03U	1	10	400	570	5	0.624	0.234	0.238	0.225	0.6	1.261	17.1	17	27.7	25.2	30.5	C
BR-04U(1)	17.6	10	350	500	6	0.991	0.093	0.487	0.058	0.1	6.097	23.2	5.2	26.2	143.1	357.8	C
BR-04U	1.4	10	300	570	6	0.691	0.438	0.236	0.39	1.1	0.019	24.5	21.5	33	27.5	31.8	C
BR-05B	1.8	15	360	600	14	0.768	0.494	0.266	0.53	1.5	1.066	27.8	16	37.6	21.6	12.3	I
BR-05U(1)	7.7	10	260	500	9	1.34	0.429	0.171	0.588	4.6	0.116	7.2	21.8	35.2	49	76.2	C
BR-05U	1.2	10	200	570	7	0.676	0.505	0.395	0.194	0.3	2.044	24	26.5	27.7	18.4	21.4	C
BR-06U(1)	7.1	10	350	500	6	1.003	0.075	0.307	0.655	2.1	1.968	24.6	9.7	34.8	38.6	122.5	C
BR-06U	2.5	10	300	570	6	0.612	0.402	0.378	0.016	0	2.07	15.1	26.2	17.6	37.1	32	C
BR-07U(1)	7.4	10	380	500	5	0.261	0.12	0.231	0.733	0.8	0.041	12.5	10.1	54.7	34	35.5	C
BR-07U	1.9	10	300	570	6	0.787	0.481	0.442	0.044	0.1	1.971	19.5	16.4	4.5	29	17.6	C
BR-08U(1)	10.7	10	350	500	6	1.88	0.244	0.692	0.323	0.9	5.87	22.2	24	61.6	122.3	218.8	C
BR-08U	5.8	10	400	550	5	0.434	0.472	0.503	0.549	0.5	2.244	12.6	11.5	11.7	27.6	32.7	C
BR-09U(1)	169.5	10	170	410	9	0.499	0.464	0.092	0.799	4.3	-0.142	3.7	3.3	7.4	3.9	10	C
BR-09U	3.2	10	300	550	6	0.884	0.431	0.119	0.681	5	0.671	22.2	18.5	14.3	9.4	23.6	C
BR-10U	12.7	10	350	500	6	0.375	0.168	0.183	0.393	0.8	0.72	7.1	20.4	61.5	46	118.5	C
BR-10U-1	8.8	10	450	550	4	1.396	0.3	0.926	-1.35	-2	2.24	8.3	18.6	163	68.3	13.9	C
BR-11U	9.5	10	380	500	5	0.255	0.122	0.234	0.272	0.3	-0.739	39.4	10.2	38	45.2	124.2	C
BR-11U-1	6.2	10	400	550	5	0.462	0.453	0.79	0.443	0.3	2.324	13.5	25.2	23	39.8	45.9	C
BR-12U	21.5	10	380	500	5	0.813	0.075	0.806	-0.348	-0.4	4.464	9.3	14.5	56.8	127.8	507.7	C
BR-12U-1	5	10	400	550	5	0.522	0.466	0.752	0.339	0.2	2.235	8.8	10.6	12.4	16.5	9.5	C
BR-13U	5.5	10	380	500	5	0.191	0.089	0.582	0.593	0.2	-0.48	27.6	6	44	87.2	251	C
BR-13U-1	4.7	10	400	550	5	0.582	0.452	0.701	0.383	0.3	2.284	11.8	12.6	17.1	28.1	39.6	C
BZ-01U(1)	3.4	10	300	560	12	0.791	0.419	0.113	0.242	1.7	1.267	5.8	21.7	6.1	12.2	5.7	C
BZ-01U	10.2	10	300	530	5	0.859	0.625	0.259	0.499	1.7	0.117	5.7	6.1	4.8	28	31.3	C
BZ-02U(1)	0.7	10	400	620	11	6.197	0.123	0.243	0.488	12.5	3.799	24.8	5.8	30.2	74.2	165	C
BZ-02U	4.3	10	300	590	7	1.049	0.502	0.248	0.652	2.8	1.019	8.2	5.8	1.2	25.6	38.7	C
BZ-03U(1)	1.2	10	400	600	14	0.427	0.239	0.194	0.716	1.6	0.061	12.4	13.3	41	18.6	3.3	C
BZ-03U	3.6	10	300	590	7	0.929	0.644	0.192	0.736	3.6	0.933	18.1	15.5	13.5	29.7	31.8	C
BZ-04U(1)	0.6	10	400	570	12	0.822	0.223	0.431	0.389	0.7	4.26	38.5	12	48.5	65.2	86.5	C
BZ-04U	1.1	10	300	590	7	0.604	0.422	0.148	0.689	2.8	0.459	31.5	26.3	27.8	27.3	12.3	C
BZ-05	0.8	10	400	570	12	1.877	0.093	0.306	0.222	1.4	6.764	21.9	9.3	59.2	86.1	101.5	C
BZ-05U	12.4	10	300	530	5	0.339	0.33	0.374	0.514	0.5	2.01	3.6	12.3	5	5.2	2.8	C
BZ-06	1.5	10	400	570	12	0.183	0.079	0.376	-0.019	0	5.575	36.4	15.5	57.5	93.3	135.6	C
BZ-06U	1.4	10	400	530	4	0.224	0.06	0.337	0.201	0.1	-3.61	25.3	8.7	7	66.4	92.5	C
BZ-07	1.2	10	400	600	14	0.987	0.532	0.368	0.181	0.5	6.113	29.6	24.4	101.5	87.9	147.4	C
BZ-07U	20.1	10	350	500	4	0.293	0.303	0.99	0.616	0.2	2.974	14.7	21.8	26	124.4	123.4	C
BZ-08U	2.2	10	400	560	11	0.074	0.143	0.458	-0.329	-0.1	-3.433	28.2	16.9	94.2	162.5	491	C
BZ-08U-1	4.1	10	350	500	4	0.573	0.109	0.76	0.064	0	5.126	30.7	17.2	51.6	265.4	285.7	C
BZ-09U	5.9	10	260	500	9	0.91	0.394	0.178	0.664	3.4	1.197	5.7	15.9	10.1	27.8	64.2	C
BZ-09U-1	22	10	150	400	4	0.786	0.55	0.068	0.388	4.5	-0.056	5.6	4.2	2.4	5.2	5.2	C
BZ-10U	5.2	10	260	500	9	0.796	0.526	0.123	0.626	4.1	0.484	7.5	11	12.6	37.8	72.3	C
BZ-10U-1	8.3	10	150	550	7	0.955	0.746	0.157	0.527	3.2	0.926	11.5	16.7	8.9	37.6	41.2	C
BZ-11	5.1	10	300	585	14	0.704	0.421	0.073	0.164	1.6	1.638	6.6	27.8	16.8	27.2	46.7	C
BZ-11U	15.2	10	0	350	4	0.9	0.737	0.097	0.546	5.1	-0.068	15.9	9.1	8.7	3.4	3.4	C

Table C.2 continued

Specimen	B_{anc}	B_{lab}	Min	Max	n	f	FRAC	β	g	q	k'	MAD_f	MAD_a	α	DRAT	CDRAT	prot.
BZ-12U	10.7	10	150	450	5	0.735	0.561	0.064	0.439	5.1	-0.402	14	20.2	18.7	43.5	44.3	C
BZ-13U	7.4	10	200	400	4	0.788	0.492	0.039	0.587	11.9	0.12	3.7	2.8	2.4	1.4	1.4	C
BZ-13U-1	6.1	10	300	550	6	0.819	0.302	0.222	0.784	2.9	1.022	6.5	6	8.8	25.6	29.4	C
BZ-14U	0.7	10	320	620	13	5.963	0.278	0.379	0.504	7.9	-2.502	3.4	8.3	5.3	15	12.8	C
BZ-14U-1	7.9	10	350	500	4	0.458	0.215	0.19	0.661	1.6	0.84	7.6	20.1	21.6	27.8	29.9	C
BZ-15U	5.9	10	300	500	5	0.583	0.254	0.201	0.675	2	0.845	15.5	27.9	31.2	14.8	17.5	C
BZ-16U	1	10	300	570	11	0.596	0.364	0.286	0.52	1.1	1.801	15	26	60.2	42.7	86.6	C
BZ-16U-1	2	10	300	550	6	0.764	0.28	0.288	0.701	1.9	1.192	25	21.3	44.9	11.9	12.9	C
BZ-17U	0.7	10	300	550	6	0.452	0.361	0.398	0.359	0.4	1.842	27	38.2	56.2	10.3	13.3	C
BZ-18U	0.7	10	350	550	5	0.414	0.208	0.542	0.447	0.3	2.344	31	29.4	37.3	22.5	31.2	C
BZ-19	0.9	10	350	620	12	3.146	0.194	0.109	0.485	14	0.241	15	14	34.5	84.3	199.3	C
C4594-01(1)	2.5	10	400	600	14	0.895	0.69	0.016	0.879	47.8	0.13	13.7	10	3.4	6.2	0.5	C
C4594-01B	2.8	15	240	590	16	0.447	0.599	0.098	0.702	3.2	-0.036	15	3.2	10.9	3	1.8	I
C4594-02(1)	2.2	10	400	550	6	0.795	0.593	0.054	0.707	10.5	-0.018	4.4	3.4	2.4	5.6	7.5	C
C4594-02(2)	2.1	5	450	545	6	0.613	0.462	0.064	0.842	7.6	-0.356	4.7	4.1	6.2	6.4	3.7	C
C4594-03(2)	3.1	10	350	500	6	0.793	0.384	0.099	0.781	6.2	0.564	4.7	6	7.9	9	12.6	C
C4594-03(1)	2.3	10	300	510	7	0.864	0.333	0.125	0.808	5.6	0.747	7.5	7.3	8	12.8	11.4	C
C4594-04(1)	3.7	10	350	520	5	0.83	0.425	0.104	0.654	5.2	0.604	3.8	2.4	1	2.3	0.8	C
C4594-04(2)	5.4	20	250	510	6	0.942	0.524	0.121	0.737	5.7	0.475	17	15.5	14.6	0.6	0.1	C
C4594-05	1.4	10	400	540	5	0.726	0.421	0.039	0.665	12.5	-0.103	4.7	2.5	2	12.8	4.8	C
C4594-05(1)	2.2	20	350	510	5	0.929	0.541	0.089	0.735	7.7	-0.021	12.3	8.9	7.9	11.7	8.4	C
C4594-05(2)	1.8	3	350	500	7	0.604	0.383	0.104	0.82	4.8	0.62	4.8	1.6	1.6	9.4	3.3	C
C4594-06	1.5	10	400	540	5	0.716	0.367	0.044	0.7	11.4	-0.062	5.4	2.9	2.3	8.9	0.6	C
C4594-06(1)	1.6	10	400	545	8	0.734	0.395	0.031	0.852	19.9	-0.066	5.8	5.5	10.4	9.9	10.9	C
C4594-07(1)	3.4	10	300	470	4	0.661	0.306	0.074	0.649	5.8	0.353	5.9	5.6	10.3	1.6	1.6	C
C4594-07(2)	2.4	10	400	490	4	0.647	0.218	0.144	0.63	2.8	0.577	2.3	3.4	5.7	21.5	23.4	C
C4594-08(1)	1.9	1	350	500	4	0.825	0.446	0.032	0.693	16.1	0.145	1.5	1.5	0.6	3.6	5.9	C
C4596-01(1)	4.4	10	200	430	5	0.671	0.193	0.129	0.736	3.8	0.461	18.1	10.7	11.8	22.2	15	C
C4596-02(1)	3.1	10	200	450	6	0.646	0.188	0.225	0.743	2.1	1.274	14.9	17.4	16.8	3.3	4.9	C
C4596-05(1)	2.5	10	430	580	9	0.868	0.558	0.033	0.695	18.5	-0.266	3.8	2.3	1.6	7.9	14.5	C
C4596-06(1)	3.6	10	430	580	9	0.903	0.767	0.024	0.573	21.9	0.225	1	2.2	3.5	1.4	0.3	C
C4596-06B	12.5	15	490	600	10	0.29	0.327	0.118	0.904	2.1	0.257	6.8	1.9	13	4.4	3.7	I
C4596-07	3.8	10	485	580	6	0.86	0.739	0.014	0.498	29.9	0.078	0.6	0.5	0.3	1.3	1.4	C
C4596-08	3.2	10	500	600	6	0.824	0.619	0.027	0.512	15.5	-0.044	1	0.9	0.5	2.2	1.9	C
C4596-09(1)	2.6	10	430	545	7	0.708	0.432	0.021	0.743	24.8	0.042	3.8	1.7	2.1	13.7	8.3	C
C4596-10(1)	4.7	10	470	545	5	0.661	0.39	0.023	0.546	15.6	0.099	4	1.7	2.8	3.8	8.5	C
C4596-12(1)	3.5	10	485	600	8	0.838	0.557	0.015	0.818	46.9	-0.063	1.8	1.6	1.3	6.5	12.7	C
C4596-12B	15.9	15	320	580	12	0.433	0.503	0.104	0.905	3.7	0.401	4.1	1.6	6.8	4.3	14.7	I
C4596-13	3.5	10	430	580	10	0.897	0.218	0.027	0.836	27.6	0.12	4.5	2.7	1.2	8	10.6	C
C4596-14(1)	2	10	300	520	9	0.702	0.281	0.066	0.812	8.6	0.065	6.8	2.2	0.6	9.5	4.2	C
C4596-15(1)	1.5	10	430	520	6	0.777	0.221	0.098	0.783	6.2	0.468	6.4	6.5	7.4	5.6	2.1	C
C4596-17(1)	2.8	10	400	520	7	0.68	0.424	0.075	0.796	7.2	0.452	3.2	1.5	3.2	6.9	2.7	C
C4596-19(1)	3.2	10	400	520	7	0.737	0.306	0.039	0.779	14.9	0.059	5.4	5.7	8.6	6	7	C
C4596-20(1)	1.9	10	450	580	9	0.769	0.499	0.012	0.784	52	0.066	2.8	2	1.4	7.3	4.5	C
C4596-21	2.7	10	400	570	9	0.708	0.367	0.098	0.831	6	-0.451	13	7.5	1.2	21.2	6.4	C
C4596-21B	3.2	15	320	580	12	0.665	0.601	0.097	0.8	5.5	-0.295	16.1	6.4	11.2	8.5	9.6	I
C4596-22(1)	2.9	10	470	580	8	0.954	0.54	0.073	0.787	10.3	0.424	1.3	0.6	0.4	1.2	0.1	C
C4596-23(1)	2.7	10	460	570	6	0.768	0.483	0.047	0.775	12.7	-0.165	3.4	1.8	1.1	7	10.7	C
C4596-23B	3.6	15	320	600	15	0.866	0.66	0.108	0.852	6.8	1.057	4.9	12.1	11.7	11.1	23.8	I
C4596-24	0.7	10	520	580	5	0.428	0.05	0.016	0.609	15.9	0.017	4.4	2.2	0.2	13.1	15.2	C
C8262-01(1)	2.2	10	500	590	8	0.629	0.334	0.033	0.823	15.7	-0.037	5.7	2.3	2.2	6	0.8	C
C8262-02(1)	1.9	10	450	590	10	0.668	0.309	0.076	0.775	6.8	-0.042	12.2	4.6	9.8	4	10.5	C
C8262-03(1)	6.2	10	500	590	8	0.724	0.362	0.046	0.706	11.2	0.313	2.5	1	1.7	1.3	1.9	C
C8262-04(1)	3.8	10	400	555	9	0.82	0.525	0.054	0.864	13	0.246	4.3	2.6	0.7	17.4	3.9	C
C8262-05(1)	3.7	10	400	570	9	0.824	0.74	0.035	0.779	18.5	0.124	2.6	1	0.8	3.5	5	C
C8262-05(2)	4.6	10	450	610	7	0.631	0.516	0.063	0.781	7.8	-0.148	4.6	2.1	3.4	3.1	4.6	C
C8262-08(1)	2.6	10	400	560	8	0.664	0.476	0.09	0.682	5	-0.639	1.6	0.6	0.4	10.3	28.7	C
C8262-10(1)	2.2	10	480	560	4	0.618	0.194	0.097	0.517	3.3	0.309	5.9	3.6	3.2	6.9	20.2	C
C8262-12(1)	1.5	10	510	660	8	0.841	0.35	0.128	0.774	5.1	-0.09	19.5	11.6	9.7	6.7	10	C
C8262-13(1)	2.5	10	460	560	5	0.729	0.42	0.071	0.556	5.7	0.55	3.5	1.8	1	5.4	1	C
C8262-13(2)	2	10	480	600	7	0.709	0.386	0.093	0.757	5.8	0.341	16.8	8.7	12.8	11	13.2	C
C8262-15(1)	4	10	480	630	8	0.857	0.568	0.048	0.769	13.8	0.142	5	4.3	4.5	2.8	1.1	C
C8262-16(1)	1.4	10	400	540	8	0.763	0.237	0.082	0.806	7.5	0.314	11.4	4.7	4.8	8.8	11.8	C
C8262-16B	2.9	15	320	570	11	2.628	0.415	0.226	0.405	4.7	0.046	12	16.3	35.7	11.7	9.4	I
C8262-17(1)	2.6	10	400	600	7	0.819	0.633	0.061	0.75	10.1	-0.038	5.5	3.4	5.1	11.4	7.1	C
C8262-18(1)	4.3	10	300	540	8	0.864	0.613	0.036	0.732	17.4	0.009	4	1.5	1.2	11.3	6	C
C8262-19(2)	6	10	300	570	10	0.878	0.799	0.085	0.844	8.8	0.341	3.6	1.5	0.9	5.7	1.1	C
C8262-19(1)	5.5	10	440	540	6	0.658	0.483	0.035	0.789	14.7	0.079	2.1	0.8	0.4	10.3	3.4	C
C8262-19(3)	5.3	10	420	570	8	0.85	0.669	0.125	0.845	5.5	0.027	4.5	2.3	1.4	5.8	14	C
C8262-19(4)	5.2	10	400	580	6	0.874	0.618	0.073	0.71	9	0.032	1.8	2.3	2.7	11.5	19.7	C
C8262-19B	18.1	15	360	550	8	0.488	0.354	0.161	0.758	2.3	0.358	1.8	0.6	1.8	9.5	13.3	I

Table C.2 continued

Specimen	B_{anc}	B_{lab}	Min	Max	n	f	FRAC	β	g	q	k′	MAD_f	MAD_a	α	DRAT	CDRAT	prot.
C8262-20(1)	6.9	10	420	600	9	0.899	0.741	0.034	0.832	22.1	0.104	1.4	0.9	0.6	3	2.9	C
C8262-20(2)	6.9	10	400	560	5	0.822	0.625	0.037	0.726	16.1	0.049	2.6	1.6	1.5	2.7	1.8	C
C8262-21(1)	4.1	10	420	560	7	0.89	0.677	0.041	0.728	15.8	0.064	1.5	0.8	0.4	13.5	9.7	C
C8265-01(2)	3.9	10	400	540	7	0.746	0.471	0.072	0.508	5.3	-0.444	1.6	4.4	4.5	2.5	2	C
C8265-01(1)	3.8	10	400	540	9	0.793	0.492	0.044	0.833	15.1	0.162	3.4	3.5	4.3	2.4	3.1	C
C8265-02(1)	3.5	10	400	530	5	0.695	0.382	0.059	0.372	4.4	-0.449	2.4	2.9	3.2	2.8	5.1	C
C8265-02(2)	3.4	10	400	545	8	0.789	0.426	0.042	0.51	9.5	-0.012	2.2	3.5	3.3	2.5	5.9	C
C8265-02B	4.6	15	460	585	9	0.527	0.376	0.099	0.801	4.3	-0.051	7.5	3	6.2	9.3	5.6	I
C8265-03(1)	6.1	10	510	560	6	0.329	0.287	0.051	0.791	5.1	0.16	4.8	2.2	1.3	2.2	1	C
C8265-03(2)	7.9	10	400	510	5	0.513	0.317	0.126	0.738	3	0.205	5.9	3.4	9.8	4	1.5	C
C8265-04(1)	7.3	10	540	585	5	0.496	0.352	0.036	0.744	10.4	-0.023	1	0.5	1	5.9	14	C
C8265-04(2)	9.8	10	510	570	5	0.587	0.362	0.096	0.827	4.6	0.269	1.7	1.3	3.3	4.1	6.6	C
C8265-04(3)	9.5	10	500	560	7	0.649	0.472	0.036	0.824	15	0.266	0.7	0.6	1.1	4.5	10.6	C
C8265-07(1)	2.3	10	300	525	5	0.797	0.611	0.087	0.608	5.6	0.205	1.7	1.5	1.7	6.1	8.6	C
C8265-07(2)	1.5	10	400	540	7	0.681	0.386	0.042	0.801	12.9	-0.091	7.3	3.1	4.2	16.8	18.7	C
C8265-07B	1.9	15	320	590	14	0.513	0.55	0.095	0.769	4.1	-0.13	6	1.9	7	9.6	25.2	I
C8265-08	2.8	10	400	510	6	0.597	0.167	0.137	0.505	2.2	-0.776	9.2	22.3	14.5	14.6	24.8	C
C8265-09(1)	3.4	10	510	585	8	0.342	0.19	0.101	0.829	2.8	0.372	9.8	5.4	1	22.7	31	C
C8265-09(2)	4.1	10	400	520	6	0.709	0.269	0.091	0.715	5.6	0.441	6.3	8.1	10.2	5.6	12.1	C
C8265-10	2.1	10	300	540	8	0.89	0.511	0.033	0.5	13.3	-0.097	6.2	6.4	3.6	4.6	3.3	C
C8265-10(2)	1.9	10	420	540	6	0.687	0.353	0.029	0.779	18.2	0.175	8.9	5.2	6.1	9.7	6.9	C
CK3-01(1)	8.4	10	300	540	7	0.893	0.861	0.055	0.769	12.6	-0.203	0.6	0.4	0.3	1.3	2.4	C
CK3-03(1)	4.5	10	200	470	7	0.622	0.453	0.043	0.643	10.2	-0.025	2.2	2.3	7	0.7	0.4	C
CK3-03(2)	3	20	450	510	5	0.79	0.26	0.405	0.643	1.4	1.501	6.2	4.3	1.2	10.9	11.6	C
CK3-05(1)	1.1	10	440	585	12	1.059	0.202	0.079	0.891	11.9	0.686	5	3.6	2.5	9.6	4.4	C
CK3-05(2)	3.3	20	450	600	7	0.677	0.072	0.176	0.804	3.1	1.008	4	3.8	10.8	12.9	0.1	C
CK3-06(1)	4	10	400	570	12	0.975	0.691	0.013	0.888	69.1	0.057	1.5	1.2	0.8	2.6	10.5	C
CK3-06(2)	3.5	20	450	610	11	0.91	0.727	0.029	0.886	28	0.035	6.2	4.7	4.3	2.6	6.7	C
CK3-08(1)	2.3	10	300	550	8	0.781	0.758	0.034	0.752	17.3	-0.078	2.5	1.7	2.3	1.9	0.1	C
CK3-09(1)	2.2	20	450	650	9	0.643	0.413	0.084	0.771	5.9	0.234	6.5	2.2	4.2	3.5	2.7	C
CK3-09(2)	1.7	10	350	610	14	0.443	0.296	0.07	0.882	5.6	0.537	4.1	1.9	11.6	2.2	4	C
CK3-10(1)	1.9	10	400	470	3	0.563	0.241	0.11	0.485	2.5	-0.203	1.5	1.2	0.7	2.1	2.1	C
CK3-11(1)	10.5	10	470	600	12	0.395	0.479	0.051	0.896	6.9	0.295	1.4	0.8	0.7	14	13.5	C
CK3-12(1)	11.5	10	400	570	12	0.923	0.8	0.022	0.896	36.9	-0.013	1.2	1	0.7	4.1	9.9	C
CK3-12(2)	7.7	20	450	540	8	0.607	0.464	0.037	0.828	13.5	-0.121	5.4	2.1	2.3	9	11.2	C
CK3-12(3)	13.2	10	490	540	6	0.481	0.544	0.052	0.79	7.3	0.249	2.1	1.6	1	6.9	1.3	C
CK3-13(1)	8.5	10	400	570	12	0.847	0.565	0.043	0.878	17.4	-0.321	2.2	3.4	3.6	4.1	3.4	C
CK3-13(2)	7.3	20	350	580	7	0.845	0.744	0.063	0.827	11	-0.203	3.4	3.2	4.9	8.4	12.1	C
CK3-14(1)	6.8	10	300	520	8	0.877	0.442	0.043	0.482	9.8	0.275	3	3.9	2.2	13.4	23.3	C
CK3-14(3)	4.3	10	350	440	5	0.685	0.293	0.047	0.694	8.3	-0.33	2.1	1.8	1.4	7.6	1.9	C
CK3-15(1)	11.4	10	400	580	9	0.797	0.637	0.022	0.838	30.8	-0.158	1.7	1.2	1	2.3	6.7	C
CK3-15(2)	15.9	20	450	600	7	0.682	0.57	0.024	0.811	22.6	-0.125	1.8	1	1.5	5.6	14.3	C
CK3-16(1)	10.9	20	450	600	7	0.412	0.284	0.068	0.77	4.7	0.182	2.8	0.6	1.8	4.7	3.8	C
CK3-16(2)	2.1	10	540	600	6	0.568	0.241	0.046	0.767	9.4	0.241	2.7	1.9	0.7	5.4	3	C
CK3-17(2)	7.1	20	450	580	6	0.678	0.446	0.147	0.767	3.5	0.56	5.6	5.7	14.7	4.7	6.9	C
CK3-17(3)	5.5	10	485	580	6	0.611	0.37	0.019	0.734	24.1	0.052	5.1	3.8	4.8	5.4	0.5	C
CK3-17(4)	4.2	20	520	640	6	0.665	0.437	0.093	0.662	4.7	0.432	8.4	6.3	10.3	7.2	13	C
CK3-18	5.6	20	350	560	5	0.62	0.472	0.132	0.6	2.8	0.689	24.3	7.9	5.4	4.4	3.2	C
CK3-18(1)	7.2	10	400	520	5	0.632	0.429	0.048	0.685	9.1	-0.255	3.5	1.3	0.7	8.9	10.9	C
CK3-19	2.1	10	400	540	5	0.789	0.464	0.083	0.718	6.8	0.209	3.1	3	5.2	4.9	6.5	C
CK3-20(1)	13.2	20	450	620	8	0.385	0.311	0.073	0.837	4.4	-0.17	7.5	1.9	3	7.8	14	C
CK3-20(2)	11.2	12	450	685	15	0.641	0.728	0.045	0.701	9.9	-0.314	3.9	1.2	1.2	10.1	7.6	C
CK3-20B	30	15	100	600	20	0.44	0.451	0.088	0.92	4.6	-0.198	5.8	3.3	14.1	5.9	9.9	I
CK3-21(1)	16.6	20	450	650	9	0.571	0.465	0.048	0.705	8.4	0.018	5.1	1.7	2.2	6.6	8.5	C
CK3-21(2)	14.2	15	450	650	14	0.386	0.377	0.038	0.848	8.6	-0.201	5.9	1	1.2	10.2	11.2	C
CK3-23(1)	5.2	20	450	560	6	0.52	0.185	0.097	0.697	3.8	-0.625	19.1	5.6	5.7	6.8	4.5	C
CK3-23(2)	6.5	10	380	580	8	0.864	0.617	0.042	0.82	17	0.302	3	3.3	4.9	3.5	1.2	C
CK3-24(1)	8	10	350	570	9	0.918	0.798	0.026	0.687	24.5	0.277	0.8	0.5	0.2	5.1	4.5	C
CK3-24(2)	9.2	20	450	610	8	0.866	0.544	0.024	0.776	28.3	-0.063	4	2.1	1	3.7	5.7	C
CK3-27(2)	8.3	15	400	685	16	0.636	0.628	0.049	0.83	10.9	-0.295	4.8	1.6	0.6	7.1	3.4	C
CK3-27(1)	7.4	20	450	625	8	0.432	0.296	0.049	0.77	6.8	0.07	20.3	6.3	11.7	21.7	26.2	C
CK3-27(3)	9.5	10	300	680	11	0.685	0.719	0.091	0.77	6.2	0.371	4.7	2.2	1.2	9.9	7.7	C
CK3-28(1)	2.4	10	300	550	8	0.898	0.592	0.024	0.764	28.8	0.012	4.1	3.6	1.9	13.4	21.7	C
CK3-28(3)	2.3	10	275	520	11	0.89	0.499	0.042	0.865	18.2	0.284	2.7	2.5	2.4	9.4	7.1	C
CK3-29(1)	5.2	10	400	580	11	0.669	0.384	0.055	0.843	10.2	-0.201	3.1	2.6	2.7	6.2	8.1	C
CK3-29(3)	2.2	20	350	580	7	0.797	0.679	0.138	0.715	4.1	0.247	27	24	20.7	8.6	8.5	C
CK3-29B	2.1	15	400	600	13	0.799	0.52	0.111	0.796	5.7	0.845	9.1	22.3	16.4	12.5	24.9	I
CK3-31B	13	15	490	590	9	0.336	0.162	0.16	0.847	1.8	0.957	4.1	1.2	4.5	70.8	239.9	I
CK3-32(1)	3.8	10	350	540	6	0.677	0.203	0.114	0.78	4.6	0.632	4	2.3	1.9	7.8	5.1	C
PA-108B	3.9	15	460	600	11	0.737	0.474	0.039	0.868	16.2	0.162	5.6	2.5	3	20.6	31.9	I
PA-114B	4.6	15	490	600	10	0.48	0.42	0.032	0.846	12.9	0.181	13	3.9	14.4	11.8	13.6	I

Table C.2 continued

Specimen	B_{anc}	B_{lab}	Min	Max	n	f	FRAC	β	g	q	k'	MAD_f	MAD_a	α	DRAT	CDRAT	prot.
PA-116(1)	2.5	10	400	540	9	0.792	0.252	0.047	0.86	14.4	0.209	10.5	6.6	4.8	12	14.3	C
PA-117(1)	4.3	10	450	560	6	0.857	0.252	0.07	0.7	8.5	0.366	2.1	1.6	0.3	8	0.4	C
PA-119(1)	2.7	20	510	590	5	0.435	0.276	0.07	0.66	4.1	-0.147	15.3	4	5.7	21	28.5	C
PA-119(2)	2.8	10	400	580	9	0.914	0.582	0.02	0.777	35	0.092	2.6	2.4	1.4	11	5.2	C
PA-119B	3.3	15	460	600	11	0.648	0.494	0.04	0.882	14.3	0.099	8	4.8	11	19.6	23.1	I
PA-120(2)	3.2	10	400	540	9	0.926	0.593	0.033	0.869	24.7	0.141	6.4	4	3.2	13.3	6.5	C
PA-120(1)	4.4	20	350	530	6	0.646	0.432	0.102	0.728	4.6	0.535	11.9	4.7	9.9	5.2	7.1	C
PA-121(1)	3.3	10	400	540	9	0.867	0.563	0.019	0.857	38.4	0.014	6.6	3.8	3.9	12.4	12.8	C
PA-122(2)	3.7	10	300	530	9	0.918	0.656	0.056	0.844	13.8	0.3	9.7	6.8	7.3	16.3	0.6	C
PA-122(1)	3.4	20	350	510	5	0.528	0.348	0.15	0.735	2.6	0.78	13.2	5.8	13.2	10.3	12.1	C
PA-123(2)	2.9	10	440	540	8	0.772	0.295	0.124	0.852	5.3	0.766	5.5	4.4	4.4	14.9	2.5	C
PA-123(1)	3.3	20	350	530	6	0.819	0.377	0.204	0.773	3.1	0.917	0	0	0	6.2	2.6	C
PA-128(1)	4.3	5	400	600	11	0.97	0.732	0.022	0.88	39.1	0.161	1.9	1.4	1	2.6	1.4	C
PA-130	2.9	10	500	600	8	0.698	0.468	0.034	0.593	12.2	-0.139	1.7	2.8	2.3	14.2	2.5	C
PA-131	4.4	10	520	560	5	0.535	0.346	0.028	0.672	12.8	0.166	1.5	4.6	7.5	1.7	3.1	C
PA-132	2.5	10	440	550	9	0.756	0.271	0.06	0.867	11	0.211	11.4	6.8	5.6	14.1	19.6	C
PL-03(1)	7.8	10	445	600	11	0.779	0.589	0.054	0.71	10.2	-0.204	2.4	0.8	0.4	7.9	2.3	C
PL-03(3)	6.7	10	500	580	5	0.533	0.419	0.025	0.716	15.4	0.077	0.6	0.3	0.5	4.2	3.7	C
PL-03(2)	16.3	20	0	620	12	0.973	1	0.098	0.67	6.7	0.133	4.6	1.5	0.4	6.5	7.1	C
PL-04(2)	5.1	10	440	540	8	0.604	0.352	0.022	0.785	21.3	0.163	2.3	1.6	1.6	6.8	14.7	C
PL-05(1)	10.3	10	490	550	7	0.373	0.423	0.028	0.794	10.5	-0.138	2.8	2.1	2.3	5.6	7.2	C
PL-06(2)	6.7	10	400	540	5	0.766	0.664	0.073	0.724	7.6	-0.361	1.4	1.1	1.4	1.1	0.4	C
PL-10(1)	5.8	10	350	540	6	0.842	0.577	0.043	0.685	13.4	-0.072	2.9	3	3.4	3.4	5.3	C
PL-11(1)	11.1	10	490	540	6	0.374	0.413	0.061	0.781	4.8	0.08	2	1.4	0.5	11.7	7	C
PL-11(2)	10.2	20	450	540	4	0.709	0.665	0.086	0.654	5.4	-0.124	5.4	3.9	2.9	12.4	1.9	C
PL-12(1)	7.8	20	450	560	9	0.879	0.786	0.063	0.858	12	0.259	6.4	4.1	2.7	7.6	0.2	C
PL-12(2)	8	10	440	560	10	0.808	0.678	0.039	0.859	17.9	-0.222	0.9	1.3	1.5	3.9	2.9	C
PL-14(2)	3.4	10	300	520	8	0.769	0.224	0.094	0.827	6.7	-0.091	25.5	13.7	9.3	9.3	11.2	C
PL-15(1)	11.3	20	420	540	6	0.516	0.395	0.054	0.778	7.5	0.076	4.7	1.7	4.9	5.4	3.5	C
PL-15(2)	11.2	10	470	530	6	0.52	0.408	0.024	0.781	16.7	-0.11	0.6	0.4	1.2	5.4	7.4	C
PL-17B	7.1	15	360	560	9	0.499	0.479	0.099	0.768	3.9	-0.177	8.5	2	5	2.4	1.9	I
PL-22B	11.3	15	320	570	11	0.675	0.673	0.075	0.805	7.2	-0.184	3.7	1.9	4.7	4.3	0.7	I
PL-30B	11.3	15	490	600	10	0.389	0.305	0.025	0.879	13.8	0.189	7.2	2.4	9.5	7.1	9.2	I
PL-40B	7.2	15	530	600	8	0.587	0.484	0.016	0.803	29.7	-0.048	5.1	4.6	4.9	14.9	16.2	I

TABLE C.3: microwave Thellier results and critical values, analysed with paleointensity.org. (Béguin et al., 2020). Experiment protocols (prot.): C: Coe, I: IZZI

Specimen	B_{anc}	B_{lab}	Min	Max	n	f	FRAC	β	g	q	k'	MAD_a	α	DRAT	CDRAT	Tail	prot.
BAZ-021	5.3	15	83.84	291.43	7	0.713	0.458	0.091	0.785	6.2	0.324	6.5	13.2	19.3	34.1	-	I
BAZ-022	8.9	15	81.19	185.28	5	0.648	0.408	0.135	0.647	3.1	-0.658	4.5	8.2	36.1	32.9	3.8	C
BAZ-031	5	10	66.31	199.8	6	0.697	0.472	0.126	0.679	3.8	-0.586	10.5	16.7	7.7	9.1	-	I
BAZ-051	6.2	10	83.47	254.97	6	0.722	0.443	0.043	0.759	12.7	0.074	8.5	14.9	19	27.2	-	I
BAZ-052	3.6	10	84.47	318.67	7	0.741	0.372	0.155	0.769	3.7	0.369	10.9	19.3	17.2	30.4	2.3	C
BAZ-081	28.2	15	107.39	317.67	6	0.413	0.264	0.08	0.781	4	0.403	2.9	8.7	16.4	31.7	-	I
BAZ-082	85.4	10	61.69	318.72	8	0.268	0.237	0.216	0.656	0.8	1.484	1.7	11.8	5.3	9.5	4.4	C
BAZ-101	131.4	15	0	329.81	11	0.502	0.564	0.381	0.299	0.4	2.411	3.4	10.3	15.4	21.3	-	I
BR-02B1	2.9	10	66.47	111.09	3	0.531	0.32	0.054	0.403	4	0.05	7	12.6	2.7	3.3	-	I
BR-04B1	26.1	10	144.97	331.58	5	0.099	0.056	0.357	0.507	0.1	1.222	0.8	14.5	39	104.5	-	I
BR-05B1	6.7	10	66.42	209.13	6	0.78	0.434	0.05	0.708	11	0.272	7.3	10.7	14.6	8.6	-	I
BZ-02B1	5.5	10	66.65	238.75	6	0.738	0.583	0.101	0.712	5.2	0.04	9.5	17.9	15.4	12	-	I
BZ-04B1	6	10	112.86	213.19	4	0.546	0.36	0.101	0.637	3.5	0.369	5.3	11.3	9.1	4.1	-	I
BZ-04B2	73.9	5	0	337.07	11	0.528	0.522	0.283	0.548	1	0.491	6.3	24.1	5.8	14.2	-	I
C4594-011	3	10	108.85	365.88	6	0.869	0.588	0.067	0.735	9.6	-0.332	3.5	1.8	38	22.8	-	I
C4594-051	2.7	15	0	224.65	9	0.726	0.792	0.038	0.587	11.3	0.338	9.9	14.1	45.8	69.1	-	I
C4596-012	5.5	10	0	145.15	8	0.198	0.527	0.267	0.722	0.5	0.756	16.9	80.1	11.3	5.7	-	I
C4596-021	6.2	10	22.45	88.02	4	0.271	0.334	0.831	0.241	0.1	3.052	26.7	86.8	16.6	9.6	-	I
C4596-051	13.8	10	0	394.37	9	0.092	0.5	0.359	0.479	0.1	0.035	18.4	78.3	21.3	37.6	-	I
C4596-061	78.6	10	0	82.07	5	0.357	0.374	0.189	0.695	1.3	0.313	4.2	26.3	2.7	2.7	-	I
C4596-081	62.5	10	0	84.83	5	0.264	0.321	0.1	0.741	2	-0.14	4.5	33.9	1.4	2.4	-	I
C4596-121	5	15	0	87.22	6	0.565	0.8	0.542	0.393	0.4	1.76	41.9	82	84.9	105.5	-	I
C8262-091	42	15	0	61.86	5	0.75	0.743	0.081	0.619	5.7	0.107	20.1	29.6	0.7	0.7	-	I
C8262-111	40.5	15	20.23	78.22	4	0.532	0.462	0.146	0.618	2.2	0.432	10.7	25.1	3.9	3	-	I
C8262-141	37.9	10	0	80.84	5	0.602	0.345	0.127	0.626	3	0.628	5.4	25.9	0.6	0.6	-	I
C8262-191	32.4	10	0	84.2	5	0.488	0.283	0.04	0.736	9	0.068	4.3	26.1	3.9	5.1	-	I
C8262-201	5.6	15	0	79.38	5	0.045	0.173	0.492	0.587	0.1	0.248	3.8	83.8	6.2	8.8	-	I

Table C.3 continued

Specimen	B_{anc}	B_{lab}	Min	Max	n	f	FRAC	β	g	q	k′	MAD_a	α	DRAT	CDRAT	Tail	prot.
C8265-021	35.6	10	0	34.12	3	0.101	0.134	0.241	0.442	0.2	0.248	1.5	19.2	7.5	7.5	-	I
C8265-031	5.7	10	80.74	164.13	4	0.438	0.349	0.005	0.046	3.9	-0.039	1.4	2.7	2	3	-	I
C8265-051	5.5	15	43.26	210.34	7	0.673	0.365	0.026	0.686	17.5	0.009	2.8	3.8	6.5	9.4	-	I
C8265-071	2.9	15	0	169.93	8	0.854	0.798	0.1	0.673	5.7	-0.009	10.9	5.9	4.5	2.3	-	I
CK3-061	245.2	10	0	80.98	5	0.404	0.496	0.532	0.557	0.4	-1.597	1.5	5.5	3.1	4.7	-	I
CK3-081	12.2	10	67.38	188.83	6	0.68	0.559	0.056	0.633	7.7	0.346	3.5	4.7	20.2	18.3	-	I
CK3-082	6.9	15	86.62	179.58	5	0.56	0.404	0.101	0.549	3	-0.055	4.8	11.7	22.2	24.2	2	C
CK3-101	7.3	10	43.83	179.58	7	0.905	0.832	0.082	0.665	7.3	-0.453	5.4	5.3	1.2	33.2	-	I
CK3-102	1.4	15	64.44	112.27	3	0.301	0.165	0.074	0.17	0.7	-0.453	7.8	37.5	2.9	2	-	I
CK3-111	11.8	10	0	84.5	5	0.059	0.155	0.407	0.635	0.1	0.253	2.8	65.2	10.3	16.3	-	I
CK3-131	30.3	10	41.28	105.84	4	0.084	0.122	0.254	0.584	0.2	-0.221	2.5	48.5	19.6	15.7	-	I
CK3-141	78.5	10	0	64.77	4	0.401	0.457	0.248	0.567	0.9	0.01	4.4	18.9	0.9	0.9	-	I
CK3-171	9.8	15	112.55	261.81	5	0.603	0.372	0.061	0.721	7.1	0.268	4.3	9.4	18.6	19.4	-	I
CK3-172	5.9	10	145.44	360.98	5	0.677	0.291	0.16	0.734	3.1	0.765	5.1	11.4	37	41	2.9	C
CK3-181	11.3	10	0	75.23	5	0.109	0.184	0.154	0.715	0.5	0.033	3.3	57.7	5.3	1.3	-	I
CK3-201	39	10	81.09	164.75	4	0.523	0.486	0.032	0.653	10.8	0.148	2.1	2.6	4.3	7.2	-	I
CK3-211	57.7	10	0	97.39	6	0.491	0.502	0.084	0.782	4.6	-0.195	2	7.7	0.8	1.3	-	I
CK3-241	114.3	10	0	101.09	6	0.301	0.343	0.653	0.199	0.1	1.115	2.3	9.7	2.2	2.2	-	I
CK3-242	44.2	10	0	119.73	6	0.059	0.065	0.105	0.762	0.4	0.039	0.6	27.1	4	6.9	-	I
CK3-281	17.1	10	111.94	231.81	5	0.716	0.426	0.145	0.533	2.6	0.794	5.9	7.4	12.6	7.5	-	I
CK3-282	84	15	0	59.92	4	0.203	0.261	0.717	0.417	0.1	1.071	2.4	19.7	16	16	-	I
CK3-291	44.4	20	0	246.87	9	0.157	0.168	0.076	0.685	1.4	0.069	0.6	11.2	5.4	5.6	-	I
CK3-301	26.2	10	118.38	436.71	7	0.316	0.266	0.094	0.715	2.4	0.868	1.5	2.4	29.6	1.6	-	I
CK3-321	3.8	10	0	108.83	6	0.162	0.539	0.385	0.689	0.3	-0.591	13.5	93.3	13.6	7.3	-	I
PA-1021	5	10	143.88	329.62	5	0.618	0.295	0.06	0.677	6.9	0.209	4.4	6.1	32.1	45.6	-	I
PA-1041	5.8	10	140.44	345.07	5	0.667	0.378	0.044	0.732	11.1	0.215	3.4	4.5	21.4	39.4	-	I
PA-1051	9.9	10	82.67	190.12	5	0.722	0.413	0.16	0.698	3.2	0.541	4.8	7.7	4.7	5.7	-	I
PA-1072	33.8	15	0	62.25	4	0.158	0.195	0.128	0.66	0.8	-0.004	3.4	43	0.3	0.3	-	I
PA-1141	4	10	108.06	320.4	6	0.737	0.597	0.052	0.792	11.1	0.161	4.2	8.6	12.6	11.2	-	I
PA-1142	8.6	15	144.84	238.69	4	0.327	0.12	0.16	0.624	1.3	0.282	4.2	10.6	34.5	67.2	-	I
PA-1191	4.7	10	110.97	198.53	4	0.467	0.383	0.036	0.586	7.7	0.04	3.3	12.8	11.2	14.4	-	I
PL-171	7.4	10	113.19	209.85	5	0.441	0.349	0.05	0.74	6.5	-0.106	2.8	11.8	8.2	9.6	-	I
PL-211	3.5	10	0	113.45	6	0.026	0.066	0.427	-0.042	0	0.225	0.6	129.6	8.9	12.6	-	I
PL-221	12.2	10	111.3	464.13	8	0.678	0.701	0.04	0.766	13.1	-0.095	1.6	3.4	7.2	5.5	-	I
PL-241	5.5	10	0	63.55	4	0.036	0.101	0.818	0.367	0	0.175	1.3	63.9	2.6	2.6	-	I
PL-401	3.7	10	0	103.19	6	0.037	0.227	0.341	0.712	0.1	0.094	5.3	79.7	2.4	2.7	-	I

TABLE C.4: Wilson results and critical values, analysed at GO Borok

Specimen	B_{lab}	T1-T2	Han(1)	Han(2)	RS(Ha2)	Evaltn.	R2(Ha2)	Evaltn.	KS(Ha2)	Evaltn.	D(KS)	Dn(KS)
PL-03	10	38-560	20.5	15.23	0.01	YES	0.9044	YES	0.0508	YES	0.0333	0.0841
PL-04	15	170-560	7.35	7.26	0.003	YES	0.9963	YES	0.0912	YES	0.0061	0.0973
PL-05	10	370-561	8.2	7.83	0.0035	YES	0.988	YES	0.1126	YES	0.0262	0.1388
PL-06	15	400-564	8.4	7.92	0.005	YES	0.9895	YES	0.1161	YES	0.0337	0.1497
PL-10	15	400-565	9.9	10.06	0.0038	YES	0.9886	YES	0.1317	YES	0.0176	0.1493
PL-12	15	430-561	11.4	11.47	0.0038	YES	0.9941	YES	0.1568	YES	0.0106	0.1674
PL-14	15	400-565	8.4	8.49	0.0051	YES	0.989	YES	0.1145	YES	0.0348	0.1493
PL-15	10	420-561	12.6	11.83	0.0028	YES	0.994	YES	0.139	YES	0.0224	0.1614
PA-116	15	300-554	4.5	4.75	0.0072	YES	0.9793	YES	0.0925	YES	0.0279	0.1204
PA-117	15	300-563	4.35	4.83	0.004	YES	0.9876	YES	0.0892	YES	0.0291	0.1184
PA-119	15	330-572	2.85	3.24	0.0064	YES	0.9831	YES	0.0922	YES	0.0312	0.1234
PA-120	10	350-560	3.9	4.09	0.0036	YES	0.9898	YES	0.1243	YES	0.0081	0.1324
PA-121	10	300-561	3.9	4.14	0.0038	YES	0.9858	YES	0.1081	YES	0.0107	0.1188
PA-122	10	400-560	3.9	3.82	0.007	YES	0.9531	YES	0.1183	YES	0.0333	0.1516
PA-123	10	350-560	4.2	4.44	0.0041	YES	0.9835	YES	0.109	YES	0.0235	0.1324
PA-127-2d	15	280-610	3.3	3.39	0.0031	YES	0.9891	YES	0.0757	YES	0.03	0.1057
PA-128	15	240-570	3.6	3.92	0.0029	YES	0.9965	YES	0.0925	YES	0.0132	0.1057
PA-131	10	370-561	3.6	3.86	0.0021	YES	0.9956	YES	0.1175	YES	0.0213	0.1388
PA-132	10	370-561	4.1	4.63	0.0073	YES	0.9472	YES	0.0932	YES	0.0456	0.1388
CK-3-04	15	270-507	18	18.94	0.0126	YES	0.9431	YES	0.0765	YES	0.0481	0.1247
CK-3-04(2)	10	300-518	0.9	1.11	0.0181	NO	0.8806	YES	0.0276	YES	0.1024	0.13
CK-3-05	10	370-560	4	4.6	0.0137	YES	0.8245	NO	0.0664	YES	0.0728	0.1392
CK-3-06	10	39-511	-24	-21.89	0.0071	YES	0.9641	YES	0.0697	YES	0.0188	0.0884
CK-3-06(2)	10	450-550	8	8.7	0.0076	YES	0.9545	YES	0.1297	YES	0.0617	0.1914
CK-3-07	15	270-564	3.9	3.92	0.0036	YES	0.9871	YES	0.0975	YES	0.0145	0.112
CK-3-07	15	450-564	4.35	4.77	0.007	YES	0.9803	YES	0.1376	YES	0.0417	0.1794
CK-3-08	15	150-590	3.9	4.23	0.0037	YES	0.9941	YES	0.0681	YES	0.0235	0.0916

Table C.4 continued

Specimen	B_{lab}	T1-T2	Han(1)	Han(2)	RS(Ha2)	Evaltn.	R2(Ha2)	Evaltn.	KS(Ha2)	Evaltn.	D(KS)	Dn(KS)
CK-3-09-2d	15	100-609	2.85	2.6	0.0038	YES	0.984	YES	0.0615	YES	0.0237	0.0852
CK-3-10	10	250-560	1.8	1.66	0.0057	YES	0.9748	YES	0.0735	YES	0.0356	0.1091
CK-3-11-A	10	430-550	12.9	12.76	0.0039	YES	0.9881	YES	0.1534	YES	0.0215	0.1748
CK-3-11-B	10	250-538	7.6	6.79	0.0072	YES	0.9792	YES	0.0864	YES	0.0268	0.1131
CK-3-11-C	10	200-548	8.8	8.22	0.0063	YES	0.9839	YES	0.0807	YES	0.0222	0.103
CK-3-11-C2	10	350-550	9.8	9.15	0.0047	YES	0.9828	YES	0.0981	YES	0.0376	0.1357
CK-3-11(2)	10	400-576	8.8	8.17	0.0063	YES	0.9837	YES	0.1079	YES	0.0367	0.1446
CK-3-12	10	300-561	14.8	14.23	0.0025	YES	0.9951	YES	0.0989	YES	0.0199	0.1188
CK-3-13	10	170-560	13.8	13.52	0.002	YES	0.9962	YES	0.0895	YES	0.0077	0.0973
CK-3-14	10	400-560	5.8	5.29	0.0085	YES	0.9445	YES	0.1228	YES	0.0288	0.1516
CK-3-15(2)	10	100-540	15.6	16.17	0.0095	YES	0.9301	YES	0.0631	YES	0.0285	0.0916
CK-3-16(2)	10	300-538	16.9	16.22	0.0133	YES	0.931	YES	0.1095	YES	0.0149	0.1244
CK-3-17(2)	10	300-582	5.9	5.72	0.0084	YES	0.9709	YES	0.1008	YES	0.0135	0.1143
CK-3-19	15	300-567	3.15	2.87	0.0116	YES	0.9454	YES	0.0905	YES	0.027	0.1175
CK-3-20-2d	10	150-590	13.1	13.7	0.0053	YES	0.9683	YES	0.0783	YES	0.0133	0.0916
CK-3-21-2d	10	250-615	13.9	16.62	0.0066	YES	0.9516	YES	0.0757	YES	0.0248	0.1005
CK-3-22	15	250-470	4.35	4.2	0.0047	YES	0.9837	YES	0.0659	YES	0.0634	0.1294
CK-3-24	15	37-578	7.95	8.25	0.0018	YES	0.9975	YES	0.0768	YES	0.0058	0.0826
CK-3-25	15	300-592	5.25	4.89	0.0051	YES	0.9781	YES	0.0885	YES	0.0239	0.1124
CK-3-27-2d	10	150-630	6.5	5.96	0.0094	YES	0.8991	YES	0.0645	YES	0.0232	0.0877
CK-3-28	15	250-587	2.25	2.09	0.0077	YES	0.9508	YES	0.0669	YES	0.0377	0.1046
CK-3-29	10	270-573	2.5	2.12	0.0103	YES	0.9563	YES	0.0427	YES	0.0676	0.1103
CK-3-30	15	300-599	8.25	9.62	0.0093	YES	0.9285	YES	0.0886	YES	0.0225	0.111
CK-3-31	15	300-598	6.75	7.58	0.0123	YES	0.8768	YES	0.0784	YES	0.0329	0.1112
CK-3-32	15	300-593	2.25	2.76	0.0107	YES	0.9058	YES	0.0835	YES	0.0287	0.1122
8265-01	10	250-584	4	3.73	0.0049	YES	0.99	YES	0.0851	YES	0.02	0.1051
8265-02	10	150-558	5.2	5.26	0.0031	YES	0.9961	YES	0.0909	YES	0.0042	0.0951
8265-03	10	40-570	5.6	5.69	0.0031	YES	0.9904	YES	0.0732	YES	0.0103	0.0835
8265-04	10	39-570	12.6	12.89	0.0019	YES	0.9964	YES	0.0716	YES	0.0118	0.0834
8265-07	10	180-596	2.5	2.29	0.0039	YES	0.9935	YES	0.0668	YES	0.0274	0.0942
8265-08	10	100-571	3.5	3.26	0.0051	YES	0.9741	YES	0.0421	YES	0.0464	0.0885
8265-10	10	150-564	3.5	3.6	0.0069	YES	0.9807	YES	0.0832	YES	0.0112	0.0944
8265-11	10	240-598	3.2	3.52	0.0152	NO	0.9002	YES	0.0404	YES	0.0611	0.1015
8262-01	10	150-606	1.3	1.43	0.0156	NO	0.8956	YES	0.0498	YES	0.0401	0.09
8262-02	10	260-603	1.6	1.51	0.0156	NO	0.8955	YES	0.07	YES	0.0337	0.1037
8262-03	10	37-604	3.6	4.53	0.0095	YES	0.9608	YES	0.0367	YES	0.044	0.0807
8262-04	10	100-574	2.2	1.95	0.0085	YES	0.9704	YES	0.0568	YES	0.0314	0.0882
8262-05	10	310-609	5.5	5.68	0.0075	YES	0.975	YES	0.0931	YES	0.0179	0.111
8262-07	10	160-552	1.1	0.99	0.0136	YES	0.9284	YES	0.0449	YES	0.0521	0.097
8262-09	10	300-573	1.3	0.95	0.0246	NO	0.7672	NO	-0.031	NO	0.1472	0.1162
8262-10	10	100-609	2.6	2.47	0.0072	YES	0.9773	YES	0.0727	YES	0.0125	0.0852
8262-12	10	130-608	3.5	3.63	0.0084	YES	0.9688	YES	0.0708	YES	0.017	0.0879
8262-13	10	37-608	3.7	4.02	0.0114	YES	0.9428	YES	0.0614	YES	0.019	0.0804
8262-14	10	150-608	2.6	2.62	0.0224	NO	0.7893	NO	0.0429	YES	0.0469	0.0898
8262-15	10	230-588	3.1	3.24	0.0046	YES	0.9911	YES	0.0826	YES	0.0189	0.1015
8262-17	10	50-574	7.2	6.97	0.0051	YES	0.989	YES	0.0754	YES	0.0085	0.0839
8262-18	10	260-563	6.2	6.02	0.0066	YES	0.9823	YES	0.0949	YES	0.0155	0.1103
8262-19	10	370-573	8.2	8.07	0.0068	YES	0.9812	YES	0.1179	YES	0.0167	0.1347
8262-20	10	300-578	7.9	7.82	0.0036	YES	0.9944	YES	0.1088	YES	0.0063	0.1151
8262-21	10	260-565	7.5	7.41	0.0047	YES	0.991	YES	0.0957	YES	0.0143	0.1099
C4596-01	10	150-501	1.3	0.85	0.0262	NO	0.7671	NO	0.0138	YES	0.0887	0.1025
C4596-02	10	150-526	0.5	0.39	0.0441	NO	0.3996	NO	-0.0295	NO	0.1286	0.0991
C4596-03	10	150-342	8.5	9.2	0.0246	NO	0.7539	NO	0.0782	YES	0.0602	0.1384
4594-01	20	200-550	3.8	4.06	0.0041	YES	0.9866	YES	0.0809	YES	0.0218	0.1027
4594-02	15	250-574	2.7	3.1	0.0058	YES	0.9723	YES	0.0614	YES	0.0453	0.1067
4594-03	20	350-581	2	1.84	0.0104	YES	0.9157	YES	0.0522	YES	0.0744	0.1265
4594-05	15	39-599	2.25	2.06	0.0097	YES	0.9591	YES	0.0438	YES	0.0374	0.0812
4594-06	15	170-595	2.55	2.53	0.0044	YES	0.9837	YES	0.0791	YES	0.0141	0.0932
4594-07	10	200-530	2.3	2.45	0.0042	YES	0.9826	YES	0.0769	YES	0.0288	0.1057
4594-08	15	150-487	3.9	4.07	0.0037	YES	0.9906	YES	0.097	YES	0.0076	0.1046
4594-09	15	50-526	1.2	4.12	0.0195	NO	0.8599	YES	-0.0627	NO	0.1508	0.0881
4594-10	15	250-550	1.65	2.08	0.0112	YES	0.948	YES	0.072	YES	0.0389	0.1109

TABLE C.5: DHT-Shaw results and critical values. Specimens that broke during the first or second heating and count as failed for success rates are listed with the pseudo-Thellier data in Supplementary table C.6

Specimen	B_{anc}	B_{err}	N	B_{lab}	AF_{min}	AF_{max}	FRAC	f	α	DANG	MAD_a	$Slope_T$	β	k'_n	r_n^2	r_t^2
BZ-01A	4.55	0.47	10	10	25	100	0.06	0.13	21.11	153.5	13.45	0.82	0.103	0.408	0.917	0.999
BZ-02A	2.51	0.27	10	10	25	100	0.03	0.11	11.76	165.5	10.69	0.96	0.109	0.244	0.907	0.983
BZ-04A	2.92	0.38	10	10	25	100	0.03	0.07	14.76	162	15.58	1.03	0.13	0.071	0.87	0.998
BZ-05A	7.81	0.84	10	10	25	100	0.05	0.14	9.41	165.7	8.9	0.63	0.107	0.286	0.91	0.996
BZ-06A	5.46	0.32	10	10	25	100	0.07	0.15	16.36	157.8	11.45	0.62	0.059	0.103	0.973	0.988
BZ-07A	5.12	0.37	10	10	25	100	0.08	0.13	8.64	168.7	7.91	0.79	0.071	0.054	0.96	0.99
BZ-08A	6.51	0.92	10	10	25	100	0.05	0.13	1.33	178.3	6.44	0.59	0.142	0.848	0.846	0.987
BZ-09A	6.95	1.06	10	10	25	100	0.05	0.12	11.19	14.4	10.31	0.62	0.152	0.772	0.824	0.972
BZ-10A	5.46	0.61	10	10	25	100	0.06	0.12	2.15	177.2	8.94	0.76	0.112	0.179	0.902	0.997
BZ-11A	6.16	0.79	10	10	25	100	0.07	0.12	7.11	171	7.07	0.77	0.127	0.509	0.874	0.988
BZ-12A	2.1	0.17	10	10	25	100	0.07	0.15	18.04	157.5	11.43	0.99	0.08	0.051	0.949	0.998
BZ-13A	1.27	0.15	10	10	25	100	0.05	0.13	29.45	146.5	14.05	0.95	0.12	0.215	0.888	0.998
BZ-14A	2.85	0.11	10	10	25	100	0.06	0.15	32.11	139.7	17.7	0.93	0.038	0.105	0.989	0.998
BZ-15A	1.28	0.13	10	10	25	100	0.07	0.16	18.64	158.2	10.79	0.87	0.102	0.356	0.918	0.998
BZ-16A	2.58	0.3	10	10	25	100	0.06	0.15	19.11	153.7	15.09	0.94	0.116	0.53	0.895	0.989
BZ-17A	3.43	0.31	10	10	25	100	0.07	0.12	7.66	167.3	7.75	0.83	0.089	0.486	0.938	0.997
BZ-18A	4.39	0.22	10	10	25	100	0.12	0.19	3.23	175.3	4.54	0.91	0.049	0.13	0.981	0.996
BZ-19A	5.21	0.21	10	10	25	100	0.29	0.32	1.92	177.4	1.6	0.89	0.04	0.224	0.987	0.997
BZ-20A	5.49	0.14	10	10	25	100	0.24	0.2	4.88	173.5	3.38	0.88	0.026	0.118	0.995	0.999
BR-01A	3.4	0.3	10	10	25	100	0.03	0.08	18.03	20.2	10.11	0.87	0.087	0.086	0.94	0.999
BR-02A	5.35	0.63	10	10	25	100	0.05	0.08	33.02	35.7	10.79	0.9	0.117	0.487	0.893	0.995
BR-03A	2.72	0.18	10	10	25	100	0.04	0.15	34.96	116.8	28.07	0.86	0.066	0.188	0.966	0.999
BR-04A	3.26	0.42	10	10	25	100	0.02	0.08	30.54	31.8	8.35	0.95	0.128	0.133	0.872	0.995
BR-05A	2.46	0.12	10	10	25	100	0.04	0.15	41.6	49.3	20.28	0.93	0.048	0.23	0.982	0.998
BR-06A	3.7	0.36	10	10	25	100	0.03	0.12	43.09	53.5	23.85	0.85	0.097	0.479	0.926	0.994
BR-07A	3.22	0.26	10	10	25	100	0.1	0.13	22.41	118.4	25.96	0.72	0.082	0.31	0.947	0.999
BR-08A	3.54	0.18	10	10	25	100	0.15	0.2	2.73	175.5	6.86	0.96	0.051	0.095	0.979	0.996
BR-09A	4.68	0.35	10	10	25	100	0.07	0.11	0.94	178.3	8.2	0.76	0.075	0.061	0.956	0.991
BR-11A	2.39	0.39	10	10	25	100	0.02	0.08	8.87	94.2	29.5	1.02	0.162	0.214	0.802	0.995
BR-12A	3.87	0.65	10	10	25	100	0.02	0.07	6.33	172.7	14.24	0.93	0.168	0.085	0.787	0.994
BR-13A	3.45	0.71	10	10	25	100	0.03	0.1	22.51	94.5	32.42	0.92	0.207	0.657	0.687	0.997
BAZ-01A	3.54	0.26	10	10	25	100	0.09	0.2	22.04	29.1	13.07	0.78	0.073	0.472	0.957	0.994
BAZ-02A	2.63	0.27	10	10	25	100	0.05	0.12	37.2	46.6	20.83	0.79	0.101	0.616	0.919	0.994
BAZ-03A	4.7	0.68	10	10	25	100	0.05	0.07	24.83	27.3	10.04	1.01	0.145	0.236	0.839	0.997
BAZ-05A	3.25	0.18	10	10	25	100	0.07	0.11	32.41	37.2	13.53	0.92	0.056	0.253	0.975	0.986
BAZ-06A	5.96	0.52	11	10	20	100	0.14	0.15	16.81	26	13.46	0.96	0.087	0.459	0.932	0.995
BAZ-08A	10.29	1.27	11	10	20	100	0.08	0.12	4.45	6.8	6.89	0.68	0.124	0.728	0.867	0.999
BAZ-09A	6.08	1.3	11	10	20	100	0.08	0.11	23.18	30.1	16.84	0.68	0.214	0.939	0.629	0.998
BAZ-10A	6.81	0.6	11	10	20	100	0.05	0.14	29.42	37.9	18.61	0.82	0.087	0.169	0.932	0.994
BAZ-11A	7.22	1.76	11	10	20	100	0.05	0.11	29.24	38.8	18.07	0.75	0.244	1.179	0.536	0.996
BAZ-12A	1.88	0.1	10	10	25	100	0.1	0.23	27.47	31.1	11.66	0.94	0.051	0.214	0.979	0.995
PA-102	9.6	0.48	8	10	20	70	0.19	0.17	1.53	2.1	2.4	0.93	0.05	0.138	0.985	0.999
PA-104	9.4	0.25	8	10	20	70	0.23	0.18	2.88	3.9	2.61	0.9	0.027	0.064	0.996	0.998
PA-105	10.71	0.42	8	10	20	70	0.17	0.14	1.62	2.1	1.94	0.88	0.04	0.002	0.991	0.999
PA-107	10.3	0.21	8	10	20	70	0.28	0.25	2.01	2.5	1.39	0.8	0.02	0.04	0.998	0.996
PA-108	9.87	0.44	8	15	20	70	0.26	0.19	2.31	3	1.67	0.95	0.045	0.204	0.988	0.998
PA-109	8.99	0.29	8	15	20	70	0.19	0.16	2.27	3.1	2.52	0.93	0.032	0.071	0.994	0.998
PA-110	8.66	0.27	8	15	20	70	0.35	0.24	1.54	2	1.38	0.94	0.031	0.059	0.994	0.996
PA-111	8.14	0.2	8	15	20	70	0.33	0.26	0.15	0.2	1.2	1.02	0.025	0.067	0.996	0.999
PA-112	6.38	0.86	7	15	25	70	0.06	0.09	17.54	23.4	11.88	1.1	0.134	0.384	0.912	0.996
PA-114	5.13	0.15	8	15	20	70	0.61	0.65	1.1	1.4	1.01	1.02	0.03	0.187	0.995	0.998
PA-115	7.07	0.46	8	15	20	70	0.17	0.15	3.44	4.4	2.57	0.96	0.065	0.379	0.975	0.997
PA-116A	7.1	0.53	8	15	20	70	0.21	0.16	12.72	18	8.47	1	0.075	0.009	0.966	0.997
PA-117A	7.04	0.2	8	15	20	70	0.3	0.36	5.18	7.1	3.4	0.94	0.029	0.011	0.995	0.996
PA-118A	7.62	0.38	8	15	20	70	0.2	0.17	6.91	161	8.81	1.14	0.05	0.163	0.985	0.996
PA-119A	5.57	0.1	8	15	20	70	0.5	0.44	3.06	3.7	1.46	1.03	0.018	0.03	0.998	0.999
PA-120A	6.4	0.22	8	15	20	70	0.28	0.3	6.06	7.7	3.28	0.97	0.034	0.009	0.993	0.996
PA-121A	7.35	0.5	8	15	20	70	0.26	0.25	5.54	6.8	2.87	1.07	0.068	0.383	0.973	0.993
PA-123A	6.86	0.35	8	15	20	70	0.24	0.28	5.01	7	3.62	1.09	0.051	0.201	0.984	0.996
PA-124A	5.72	0.21	8	15	20	70	0.33	0.36	4.03	4.9	2.11	1.05	0.037	0.192	0.992	0.995
PA-125A	6.94	0.45	8	15	20	70	0.16	0.14	10.75	14.3	6.56	1.14	0.064	0.089	0.975	0.98
PA-126A	5.48	0.15	8	15	20	70	0.5	0.56	2.33	3	1.38	0.97	0.028	0.171	0.995	0.999
PA-127A	5.38	0.21	8	15	20	70	0.33	0.36	2	2.4	1.2	1.02	0.038	0.228	0.991	0.994
PA-128A	5.07	0.19	6	15	30	70	0.37	0.35	3.1	3.9	1.74	0.9	0.037	0.173	0.994	0.998
PL-03A	12.33	0.44	6	15	35	80	0.64	0.4	0.83	178.9	0.73	1	0.036	0.209	0.995	1
PL-09A	10.3	4.69	8	15	25	80	0.04	0.01	52.54	123.1	11.65	0.15	0.455	3.161	0.143	0.724
PL-10A	18.85	1.32	8	15	25	80	0.59	0.14	5.41	7.7	3.7	0.85	0.07	0.028	0.971	0.999

Table C.5 continued

Specimen	B_{anc}	B_{err}	N	B_{lab}	AF_{min}	AF_{max}	FRAC	f	α	DANG	MAD_a	$Slope_T$	β	k'_n	r^2_n	r^2_t
PL-13A	-6.89	3.95	8	15	25	80	0.05	-0.01	31.09	129.3	15.56	0.88	-0.574	-2.823	0	0.996
PL-16A	11.36	0.66	8	15	25	80	0.73	0.23	2.64	176.9	1.41	0.94	0.058	0.336	0.98	0.996
PL-17A	23.47	1.01	8	15	25	80	0.72	0.28	0.82	179.1	0.4	1	0.043	0.234	0.989	0.997
PL-18A	16.53	0.54	12	15	15	100	1.13	0.65	0.83	1	0.5	0.97	0.033	0.209	0.989	0.998
PL-19A	15.45	0.55	12	15	15	100	1.02	0.83	1.21	1.6	0.97	0.95	0.036	0.292	0.987	1
PL-21A	19.06	0.8	11	15	20	100	0.88	0.67	0.23	0.4	0.72	0.91	0.042	0.288	0.984	0.998
PL-22A	17.59	0.68	12	15	15	100	0.99	0.6	1.25	1.7	0.89	1.01	0.038	0.276	0.985	0.999
PL-24A	12.65	0.23	12	15	15	100	0.85	0.64	1.51	2.2	1.18	0.97	0.018	0.123	0.997	0.998
PL-25A	12.15	0.51	12	15	15	100	1.09	0.65	1.59	2.6	1.52	0.95	0.042	0.331	0.982	1
PL-27A	10.73	0.29	6	15	35	80	0.54	0.44	1.26	1.5	0.67	1	0.027	0.161	0.997	0.993
PL-28A	28.67	2.13	6	15	35	80	0.39	0.19	1.5	1.8	0.74	0.75	0.074	0.41	0.978	0.982
PL-30A	1.22	0.11	6	15	35	80	0.22	0.37	64.1	65.4	12.31	1.01	0.094	0.292	0.965	0.998
PL-32A	1.81	0.11	6	15	35	80	0.33	0.42	11.3	13.1	4.74	1.03	0.06	0.233	0.986	0.999
PL-40A	7.98	0.08	10	15	20	90	0.89	0.58	2.13	2.9	1.39	1.16	0.009	0.011	0.999	0.98
PL-41A	8.97	0.25	10	15	20	90	0.72	0.37	3.77	5.1	2.38	1.04	0.028	0.16	0.994	0.998
CK3-06A	191.75	52.17	10	10	25	100	0.43	0.31	2.82	3.8	1.89	0.11	0.272	1.351	0.495	0.171
CK3-08A	62.73	19.56	10	10	25	100	0.18	0.24	7.67	10.2	4.49	0.17	0.312	1.223	0.373	0.791
CK3-10A	87.42	23.45	10	10	25	100	0.46	0.1	5.07	8.1	3.99	0.14	0.268	0.705	0.507	0.837
CK3-11A	462.17	100.53	10	10	25	100	0.57	0.07	0.91	1.2	0.68	0.05	0.218	1.456	0.657	0.502
CK3-13A	471.44	100.67	10	10	25	100	0.45	0.15	0.88	1.4	0.8	0.07	0.214	0.831	0.669	0.521
CK3-20A	7.65	0.21	6	10	50	100	0.69	0.49	11.39	168.6	0.62	0.94	0.028	0.008	0.997	0.995
CK3-21A	9.5	0.23	10	10	25	100	0.94	0.74	24.55	155.4	1.62	0.91	0.024	0.098	0.995	0.989
CK3-28A	8.44	0.32	10	10	25	100	0.07	0.12	4.38	157	9.56	0.45	0.038	0.183	0.988	0.937
CK3-31A	7.49	0.12	10	10	25	100	0.13	0.2	9.59	11.1	4.04	0.51	0.016	0.093	0.998	0.994
C8262-01A	6.23	0.5	10	10	25	100	0.59	0.33	4.48	4.9	1.74	0.45	0.08	0.553	0.949	0.999
C4596-02A	4.35	0.87	10	10	25	100	0.06	0.6	19.94	19.2	4.63	0.13	0.2	0.805	0.705	0.921
C4596-05A	124.06	11.42	10	10	25	100	0.18	0.2	13.5	151.7	14.3	0.12	0.092	0.565	0.933	0.821
C4596-11A	6.46	0.44	10	10	25	100	0.61	0.97	21.26	100.4	3.85	0.47	0.068	0.247	0.963	0.989
C4596-15A	39.48	3.68	10	10	25	100	0.27	0.12	1.66	2.1	1.73	0.75	0.093	0.221	0.932	0.95
C4596-16A	23.8	3.69	10	10	25	100	0.05	0.06	26.72	28.2	8.01	1.49	0.155	0.748	0.817	0.676
C4596-17A	140.35	25.33	10	10	25	100	0.61	0.14	1.66	177.2	1.86	3.4	0.181	0.814	0.756	0.449
C4596-18A	42.34	4.47	10	10	25	100	0.05	0.06	5.65	5.9	4.49	0.76	0.106	0.242	0.913	0.283
C4596-20A	87.73	9.85	10	10	25	100	0.2	0.2	4.58	172.4	4.05	0.18	0.112	0.727	0.902	0.86
C4596-21A	21.58	1.61	10	10	25	100	0.22	0.18	12.78	16.5	7.15	0.41	0.074	0.498	0.956	0.93
C4596-22A	453.12	66.26	10	10	25	100	0.59	0.22	2.2	176.8	1.53	0.99	0.146	0.097	0.836	0.663
C4596-24A	20.79	0.64	10	10	25	100	0.24	0.18	12.64	16.8	7.42	1.14	0.031	0.129	0.992	0.955
C4596-25A	21.46	2.35	10	10	25	100	0.4	0.14	8.8	10.7	4.28	0.1	0.109	0.139	0.907	0.86

TABLE C.6: pseudo-Thellier results and critical values from combined pseudo-Thellier-Shaw experiments, analysed on paleointensity.org

Specimen	b	σ_b	AF_{min}	AF_{max}	n	$B_{1/2ARM}$	f	β	k'	r^2	MADf	α	DANG	k'_{AA}	k'_{DD}	r^2_{AA}
BAZ-01A	-0.89	0.057	25	100	10	10.5	0.227	0.064	0.027	0.967	6.8	3.8	8.2	0.533	0.963	0.851
BAZ-02A	-0.851	0.078	20	100	11	10.5	0.212	0.091	0.023	0.927	11.7	6.3	16.4	1.116	0.717	0.858
BAZ-03A	-1.369	0.14	15	100	12	8.4	0.227	0.102	0.291	0.899	14.8	8.6	19.8	0.971	0.207	0.895
BAZ-05A	-1.276	0.064	10	30	5	9.4	0.368	0.05	-0.028	0.992	5.7	9	13.5	-0.026	0.005	0.993
BAZ-06A	-1.467	0.161	20	100	11	9.4	0.193	0.11	0.159	0.894	8.4	5.4	11.9	-0.045	0.43	0.937
BAZ-08A	-1.567	0.288	20	100	11	7.7	0.177	0.183	0.102	0.72	10.2	7.6	12.1	2.788	0.111	0.672
BAZ-09A	-2.185	0.06	2	20	5	7.5	0.88	0.028	0.086	0.998	3.9	3.9	6.3	-0.033	0.13	0.997
BAZ-10A	-1.777	0.209	15	100	12	7.1	0.197	0.118	-0.151	0.867	11.2	6.5	17.5	1.218	0.114	0.8
BAZ-11A	-1.73	0.163	15	100	12	7.2	0.193	0.094	0.249	0.913	9.3	6.8	20	1.302	0.143	0.729
BAZ-12A	-0.594	0.065	25	100	10	12.1	0.248	0.109	-0.112	0.907	14.7	6.3	10.4	0.957	-0.013	0.969
BR-01A	-0.958	0.063	15	100	12	9.4	0.235	0.066	-0.024	0.957	20.2	17.1	32.8	0.266	0.091	0.963
BR-02A	-1.135	0.13	15	100	12	9.6	0.332	0.115	0.173	0.872	10.3	3.8	9.7	0.116	0.136	0.848
BR-03A	-0.692	0.067	20	100	11	8.7	0.235	0.096	0.157	0.918	12.7	6.8	14.1	-0.163	0.367	0.89
BR-04A	-1.332	0.154	15	100	12	7.8	0.202	0.116	0.153	0.871	8.8	2.9	7	-0.233	0.688	0.798
BR-05A	-0.822	0.042	20	100	11	9.6	0.21	0.051	0.127	0.977	18.4	9.5	17.6	-0.04	0.338	0.973
BR-06A	-1.181	0.099	15	100	12	8.8	0.251	0.084	0.353	0.931	11.6	6	17.7	-0.06	0.617	0.982
BR-07A	-1.027	0.09	15	100	12	8.5	0.22	0.087	0.152	0.925	8.7	2.9	6.2	-0.033	0.376	0.939
BR-08A	-1.022	0.06	20	100	11	13.4	0.272	0.058	-0.088	0.97	9.1	3.7	6.6	-0.051	0.065	0.956
BR-09A	-1.043	0.076	20	100	11	9.7	0.188	0.073	-0.1	0.953	10.8	6.9	12	-0.162	0.134	0.948
BR-11A	-0.861	0.12	20	100	11	7.7	0.127	0.14	0.027	0.832	24.3	1.5	3.7	-0.198	0.558	0.713
BR-12A	-1.365	0.21	15	100	12	7	0.153	0.154	-0.048	0.777	19.2	18.1	34.4	-0.298	0.74	0.819
BR-13A	-1.135	0.182	15	100	12	7.9	0.239	0.161	0.404	0.758	17.1	4.2	13.7	-0.008	0.721	0.813
BZ-01A	-1.153	0.096	20	100	11	8.9	0.19	0.083	-0.155	0.939	16.4	9.3	16.3	0.921	0.075	0.918
BZ-02A	-1.016	0.064	15	100	12	8.9	0.275	0.063	0.228	0.96	15.8	10.9	23.7	5.06	1.005	0.48

Table C.6 continued

Specimen	b	σ_b	AF_{min}	AF_{max}	n	$B_{1/2ARM}$	f	β	k′	r^2	MADf	α	DANG	k'_{AA}	k'_{DD}	r^2_{AA}
BZ-04A	-0.763	0.053	15	80	10	9.1	0.279	0.069	0.22	0.962	15	15.2	52.7	-0.136	0.418	0.974
BZ-05A	-1.87	0.105	10	80	11	8.8	0.411	0.056	0.065	0.972	11.1	7.7	17.3	-0.011	0.092	0.979
BZ-06A	-1.41	0.124	15	80	10	9.3	0.284	0.088	0.273	0.939	7.3	6.6	11	0.029	0.331	0.974
BZ-07A	-0.977	0.066	15	100	12	9.6	0.321	0.067	0.004	0.955	12.2	5.8	11.5	0.158	0.175	0.953
BZ-08A	-1.384	0.069	15	100	12	8.1	0.269	0.05	0.033	0.975	12.2	5.1	11.1	-0.124	0.187	0.936
BZ-09A	-1.388	0.064	15	100	12	8.3	0.27	0.046	0.12	0.979	12.6	5.2	10.3	-0.092	0.248	0.954
BZ-10A	-1.344	0.232	20	100	11	9	0.187	0.173	0.267	0.749	15	6.4	13.1	0.191	0.21	0.76
BZ-11A	-1.432	0.194	20	100	11	9.2	0.185	0.135	0.334	0.842	12.4	5.5	9.8	0.243	0.096	0.828
BZ-12A	-0.635	0.051	20	100	11	10.7	0.235	0.08	0.026	0.944	19.9	8.4	12.9	0.071	0.03	0.972
BZ-13A	-0.318	0.034	15	100	12	12.4	0.371	0.108	-0.025	0.887	27.4	5.1	11.6	0.308	0.447	0.89
BZ-14A	-0.779	0.063	20	100	11	9.5	0.23	0.081	-0.1	0.942	12.7	10.3	17.7	-0.069	0.038	0.945
BZ-15A	-0.409	0.092	30	100	9	13.6	0.132	0.226	-0.415	0.675	17.8	13.3	18.1	-0.179	0.476	0.886
BZ-16A	-0.792	0.024	15	80	10	11.7	0.345	0.03	0.039	0.993	13.6	15.1	33	0.003	0.025	0.984
BZ-17A	-0.928	0.059	15	80	10	11.4	0.343	0.063	-0.054	0.968	8.1	6.8	13.5	-0.077	0.096	0.989
BZ-18A	-1.551	0.053	15	70	9	9.3	0.307	0.034	0.008	0.992	8	4.6	6.9	-0.063	0.107	0.994
BZ-19A	-1.907	0.041	20	90	10	16.1	0.366	0.022	0.058	0.996	3.5	0.4	0.7	0.049	0.009	0.991
BZ-20A	-1.92	0.107	20	90	10	10.9	0.23	0.056	0.098	0.975	3.5	2.5	3.9	0.009	0.135	0.97
C4594-01A	-1.224	0.03	10	35	6	13.3	0.459	0.024	-0.019	0.998	1.3	1.1	1.3	0.066	0.078	0.998
C4594-05A	-0.945	0.027	15	35	5	18.4	0.375	0.029	0.005	0.998	1.5	0.3	0.4	0.135	0.132	0.997
C4596-01A	-0.266	0.051	30	100	9	9.5	0.186	0.192	-0.304	0.759	17.1	9.7	17.5	-0.277	0.548	0.636
C4596-02A	-0.103	0.023	30	100	9	16.8	0.307	0.226	-0.471	0.674	30.3	61.8	72.8	0.426	0.718	0.861
C4596-05A	-1.265	0.123	15	80	10	13.1	0.421	0.097	0.014	0.925	4.8	3.7	6.2	0.109	0.095	0.927
C4596-06A	-1.665	0.101	30	90	8	20	0.398	0.061	0.005	0.978	0.8	1	1.7	-0.108	0.175	0.978
C4596-07A	-2.818	0.214	20	80	9	20.1	0.48	0.076	-0.108	0.96	1.3	0.7	1.1	-0.148	0.058	0.965
C4596-08A	-2.612	0.12	15	100	12	20.7	0.607	0.046	0.032	0.979	1.6	0.2	0.4	0.073	0.037	0.986
C4596-11A	-0.141	0.011	35	100	8	50.5	0.696	0.076	-0.061	0.966	13.9	4.9	6.5	0.085	0.121	0.999
C4596-12A	-2.572	0.098	25	80	8	21.6	0.405	0.038	0.114	0.991	0.9	0.2	0.3	0.097	0.019	0.993
C4596-15A	-1.421	0.051	10	100	13	9	0.448	0.036	-0.007	0.986	2.8	0.7	1.7	0.125	0.148	0.992
C4596-16A	-0.71	0.114	25	100	10	7.7	0.095	0.161	0.072	0.804	17.1	5.4	10.4	0.078	0.47	0.726
C4596-17A	-2.835	0.328	10	80	11	8.5	0.393	0.116	-0.135	0.883	1.1	0.5	0.9	0.159	0.341	0.895
C4596-18A	-0.395	0.119	25	80	8	4.7	0.133	0.301	-0.386	0.53	18.9	15.5	20.8	0.45	0.799	0.492
C4596-19A	-0.501	0.021	10	100	13	9.7	0.484	0.043	-0.008	0.98	6.7	1.5	3.4	-0.004	0.019	0.991
C4596-20A	-0.954	0.079	25	100	10	20.2	0.42	0.083	0.079	0.946	2.6	1.4	2.5	-0.076	0.159	0.942
C4596-21A	-0.834	0.021	15	50	7	16	0.467	0.025	-0.002	0.997	2	4	5.9	-0.156	0.155	0.995
C4596-22A	-2.241	0.102	25	90	9	23.4	0.469	0.045	0.022	0.986	0.9	0.5	0.8	-0.088	0.11	0.986
C4596-23A	-0.888	0.054	20	100	11	19.6	0.487	0.06	0.038	0.968	1.9	1.1	2	-0.061	0.112	0.97
C4596-24A	-0.976	0.03	15	100	12	15.8	0.53	0.03	0.077	0.991	3.8	1.7	3.5	0.106	0.027	0.99
C4596-25A	-0.437	0.014	25	70	7	26.5	0.44	0.032	0.161	0.995	3.4	1.8	2.4	-0.034	0.189	0.998
C8262-01A	-0.601	0.045	20	90	10	19.4	0.496	0.075	-0.078	0.955	3.4	2.3	3	0.291	0.424	0.936
C8262-09A	-1.329	0.422	25	80	8	9	0.185	0.318	-0.463	0.485	4.3	2.6	3.4	-0.275	0.618	0.57
C8262-11A	-0.543	0.076	30	100	9	16.6	0.21	0.14	0.134	0.867	4	1.6	3.2	0.233	0.216	0.861
C8262-14A	-1.429	0.134	25	80	8	14.6	0.316	0.094	-0.133	0.948	2.5	3.6	5.6	-0.003	0.132	0.956
C8262-16A	-0.859	0.174	20	100	11	8.1	0.298	0.203	-0.243	0.665	4.3	2.2	4.4	-0.114	0.299	0.711
C8262-19A	-3.502	0.413	20	100	11	15.5	0.389	0.118	-0.052	0.878	1	0.8	1.4	0.072	0.184	0.891
C8265-02A	-1.708	0.095	10	90	12	15	0.642	0.056	0.148	0.969	2.8	1.2	2.4	0.085	0.048	0.966
C8265-03A	-2.112	0.115	15	90	11	19.1	0.547	0.054	-0.02	0.974	0.9	0.8	1.4	0.174	0.159	0.973
C8265-05A	-2.669	0.206	30	100	9	17.1	0.268	0.077	-0.078	0.959	0.9	0.5	0.9	0.087	0.188	0.974
C8265-07A	-0.996	0.083	20	80	9	16.5	0.39	0.084	-0.247	0.952	2.6	1.8	2.7	0.147	0.39	0.963
C8265-08A	-2.563	0.087	15	100	12	17.1	0.534	0.034	-0.13	0.988	1.1	0.2	0.3	0.195	0.307	0.989
CK3-06A	-1.435	0.087	20	100	11	22.4	0.547	0.061	0.092	0.967	3.5	1.4	2.3	-0.038	0.106	0.965
CK3-08A	-1.164	0.098	40	100	7	15.5	0.168	0.084	0.139	0.965	2.3	2.1	4.8	-0.008	0.224	0.951
CK3-10A	-2.769	0.095	20	70	8	11.7	0.285	0.034	0.055	0.993	0.9	0.9	1.1	0.187	0.186	0.984
CK3-11A	-4.188	0.339	25	100	10	19.5	0.397	0.081	-0.095	0.948	0.8	0.6	1	0.107	0.169	0.946
CK3-13A	-6.326	0.177	15	60	8	17.5	0.447	0.028	-0.114	0.995	2	1.8	2.3	-0.064	0.047	0.996
CK3-14A	-1.574	0.035	5	40	8	12	0.62	0.022	0.081	0.997	1.2	0.4	0.6	-0.057	0.119	0.995
CK3-17A	-2.418	0.071	0	35	9	16.2	0.857	0.029	0.068	0.994	6.1	7.3	9.7	0.067	0.003	0.995
CK3-18A	-3.129	0.194	10	100	13	11.1	0.527	0.062	-0.141	0.958	1.6	0.7	1.4	-0.132	0.007	0.96
CK3-20A	-0.31	0.023	40	100	7	56.1	0.658	0.073	-0.038	0.974	1.6	0.9	1.3	0.234	0.264	0.968
CK3-21A	-0.619	0.081	50	100	6	46.1	0.421	0.131	-0.309	0.933	5.6	3.3	4.9	-0.071	0.201	0.956
CK3-24A	-3.822	0.207	20	80	9	30.7	0.636	0.054	0.149	0.98	0.9	0.7	1	0.159	0.012	0.977
CK3-28A	-0.885	0.173	20	90	10	10.1	0.303	0.196	0.311	0.717	2.1	2.2	4.7	0.125	0.305	0.718
CK3-29A	-1.098	0.074	10	80	11	9.5	0.467	0.068	0.181	0.959	2.7	0.5	1.1	-0.205	0.298	0.944
CK3-30A	-1.643	0.065	20	90	10	28.3	0.741	0.04	0.091	0.987	1.3	1.1	1.9	-0.068	0.139	0.987
CK3-31A	-0.997	0.066	15	80	10	18.2	0.603	0.066	0.182	0.965	2.9	2.4	5	-0.073	0.225	0.968
CK3-32A	-0.72	0.016	10	90	12	14	0.648	0.023	0.108	0.995	2.1	2	4.2	0.01	0.091	0.996
PA-102A	-2.151	0.111	15	100	12	9.9	0.354	0.052	-0.101	0.974	4.1	1.6	3.4	-0.032	0.12	0.964
PA-104A	-2.097	0.105	15	100	12	9.7	0.341	0.05	0.054	0.975	4.8	1.7	3.7	0.169	0.127	0.964
PA-105A	-2.093	0.083	15	80	10	9.4	0.317	0.04	0.04	0.987	4.3	2.8	5.3	0.04	0.037	0.974
PA-107A	-2.286	0.062	10	80	11	12.2	0.583	0.027	0.031	0.993	3.1	1.8	3.7	0.15	0.115	0.993
PA-108A	-2.157	0.039	10	90	12	10.9	0.53	0.018	0.021	0.997	4.3	1.4	3.2	0.171	0.149	0.992
PA-109A	-2.262	0.111	15	90	11	9.5	0.318	0.049	0.098	0.978	4.6	1.8	4	0.05	0.044	0.969

Table C.6 continued

Specimen	b	σ_b	AF_{min}	AF_{max}	n	$B_{1/2ARM}$	f	β	k′	r^2	MADf	α	DANG	k'_{AA}	k'_{DD}	r^2_{AA}
PA-110A	-2.056	0.061	20	80	9	13.6	0.321	0.03	0.02	0.994	2.5	2.4	4.2	0.113	0.133	0.99
PA-111A	-2.154	0.052	15	90	11	13.2	0.445	0.024	0.05	0.995	3.6	2.4	4.9	0.175	0.138	0.986
PA-112A	-0.87	0.182	30	100	9	7.6	0.092	0.209	0.039	0.718	16.3	3	6.9	-0.078	0.312	0.533
PA-114A	-2.984	0.075	20	100	11	24.5	0.586	0.025	0.026	0.994	1.7	1.1	2	0.029	0.003	0.998
PA-115A	-1.76	0.107	15	90	11	9	0.3	0.061	0.013	0.967	5	2.8	6.1	-0.094	0.131	0.96
PA-116A	-1.854	0.093	15	80	10	9.4	0.301	0.05	0.139	0.98	4.5	0.6	1.2	0.195	0.065	0.978
PA-117A	-1.89	0.095	25	90	9	17.6	0.314	0.05	0.181	0.982	2	1.1	2.2	0.055	0.159	0.988
PA-118A	-2.162	0.132	15	90	11	9.6	0.306	0.061	-0.065	0.967	4.1	1.6	3.1	-0.136	0.101	0.968
PA-119A	-2.012	0.196	10	80	11	18.7	0.718	0.097	0.01	0.917	1.2	0.5	0.7	0.185	0.174	0.92
PA-120A	-2.026	0.089	20	90	10	14.5	0.345	0.044	0.028	0.985	2.5	0.5	1	0.074	0.049	0.988
PA-121A	-2.196	0.057	20	50	6	13.3	0.252	0.026	0.071	0.997	1.4	1.8	2.4	-0.081	0.172	0.996
PA-123A	-2.211	0.071	15	70	9	12.1	0.396	0.032	0.155	0.993	3.3	3	5.6	0.125	0.017	0.986
PA-124A	-1.895	0.024	25	90	9	15.5	0.301	0.013	0.002	0.999	2.1	0.7	1.2	-0.026	0.032	0.998
PA-125A	-1.867	0.14	15	90	11	9.3	0.314	0.075	0.059	0.95	3.3	2.7	5.9	-0.099	0.159	0.928
PA-126A	-2.387	0.09	20	90	10	20.6	0.504	0.038	0.143	0.989	1.6	0.5	0.9	0.174	0.033	0.989
PA-127A	-2.03	0.092	20	90	10	17.3	0.393	0.045	0.157	0.984	2.6	2.3	3.7	0.159	0.002	0.985
PA-128A	-2.519	0.07	20	90	10	23.6	0.572	0.028	0.014	0.994	1.2	0.9	1.6	0.041	0.022	0.997
PA-130A	-2.627	0.078	15	80	10	19.7	0.597	0.03	0.134	0.993	0.6	0.9	1.6	0.071	0.059	0.998
PA-132A	-1.933	0.147	15	90	11	12.1	0.373	0.076	-0.101	0.949	2.4	2	4.1	-0.132	0.03	0.96
PL-03A	-2.73	0.222	50	100	6	33.2	0.286	0.081	0.097	0.974	3.1	2.8	6.1	0.084	0.017	0.974
PL-04A	-2.626	0.102	25	90	9	21.5	0.433	0.039	0.138	0.989	1.1	0.9	1.6	0.044	0.107	0.992
PL-08A	-0.325	0.031	10	100	13	8.3	0.372	0.097	-0.353	0.9	35	26.7	39.8	0.124	0.706	0.917
PL-09A	-0.335	0.066	15	100	12	7.8	0.215	0.197	-0.524	0.648	36.7	67.8	75.3	-0.209	0.428	0.874
PL-10A	-3.96	0.233	20	90	10	11.6	0.279	0.059	-0.012	0.972	2	1.7	3.7	-0.044	0.029	0.952
PL-13A	-0.465	0.094	10	100	13	6.7	0.275	0.203	-0.383	0.599	29.5	52.2	86.2	-0.046	0.572	0.824
PL-16A	-3.687	0.156	20	90	10	14.8	0.333	0.042	0.041	0.986	1.9	0.3	0.4	-0.027	0.102	0.992
PL-17A	-7.737	0.232	25	90	9	17.8	0.329	0.03	0.123	0.994	0.6	0	0	-0.048	0.189	0.994
PL-18A	-7.476	0.412	25	80	8	22	0.36	0.055	-0.098	0.982	0.6	0.5	0.7	-0.038	0.084	0.98
PL-19A	-12.291	0.642	50	100	6	29	0.152	0.052	-0.053	0.989	0.5	0.4	0.7	-0.201	0.348	0.941
PL-21A	-11.494	0.36	35	100	8	24.2	0.282	0.031	0.064	0.994	0.8	0.6	1.2	0.108	0.104	0.981
PL-22A	-7.988	0.288	25	90	9	19.3	0.348	0.036	-0.046	0.991	1	0.4	0.6	0.04	0.092	0.995
PL-24A	-3.772	0.18	20	90	10	19.9	0.491	0.048	0.023	0.982	1.1	0.3	0.5	0.085	0.059	0.979
PL-25A	-3.854	0.059	20	90	10	23.9	0.569	0.015	-0.005	0.998	1	1	1.7	0.11	0.114	0.997
PL-27A	-5.782	0.385	40	100	7	25.9	0.296	0.067	-0.102	0.978	0.6	0.4	0.8	-0.083	0.043	0.967
PL-28A	-4.367	0.11	15	90	11	22.6	0.648	0.025	0.029	0.994	0.9	0.3	0.5	0.018	0.01	0.994
PL-30A	-0.182	0.005	40	80	5	52.9	0.557	0.026	0.092	0.998	11.3	11.4	16.8	0.214	0.093	0.996
PL-32A	-0.374	0.02	35	70	5	39.1	0.475	0.055	0.249	0.991	2.9	4.3	6.7	0.04	0.231	0.999
PL-37A	-1.609	0.061	25	80	8	15.2	0.283	0.038	0.102	0.991	2.4	3.3	5.3	0.099	0.008	0.987
PL-40A	-3.39	0.174	25	90	9	21.6	0.417	0.051	0.083	0.982	1.2	0.3	0.5	0.171	0.104	0.979
PL-41A	-2.357	0.053	20	90	10	17.2	0.407	0.022	0.011	0.996	1.5	1.1	1.9	0.038	0.027	0.994
PL-42A	-2.101	0.065	25	90	9	27.6	0.527	0.031	0.103	0.993	0.9	1.1	1.8	0.084	0.02	0.996
PL-43A	-1.678	0.044	20	90	10	16.9	0.452	0.026	0.082	0.995	1.7	1	1.6	0.199	0.127	0.991
PL-44A	-2.357	0.067	15	90	11	19.9	0.602	0.029	0.158	0.993	2.3	1.8	3.1	0.025	0.121	0.997
PL-47A	-1.78	0.068	30	100	9	20.7	0.345	0.038	0.121	0.99	1.4	1.2	2.2	0.002	0.141	0.993

C.2 Supplementary Figures

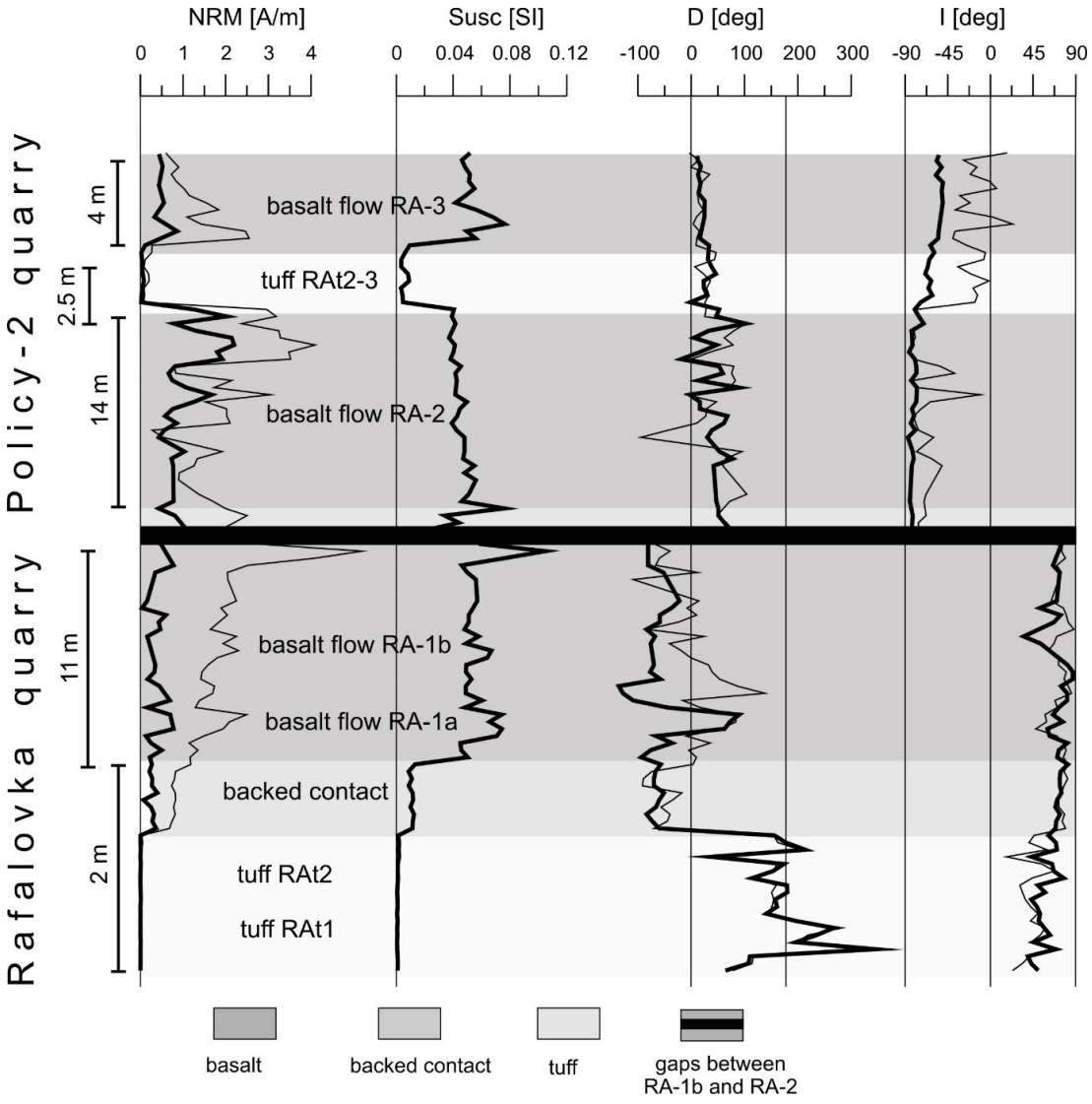

FIGURE C.1: Rock magnetic parameters and palaeomagnetic directions from the Rafalovka and Policy-2 quarries. The thin and thick lines in the left column represent initial NRM values and values after heating to 500°C, respectively. Declinations (D) and inclinations (I) are shown for the initial NRM (thin line) and the ChRM component (thick line) throughout the section.

Appendix D

PSV analysis supplementary data

The data included in Appendix D is intended to complement the analysis done in Chapter 5. Table D.1 presents the directional data used for the determination of VGP scatter. Table D.2 lists the numerical geodynamo simulations and their parameters that were used in the comparison to the Ediacaran observational data.

D.1 Supplementary Tables

TABLE D.1: Palaeomagnetic data from the Paleomagia (Veikkolainen et al., 2014b) database, showing all localities included in the PSV analysis. Sites and directions are shown before application of quality filters. ID: reference number in the Paleomagia database, slat, slon: site location

ID	dec	inc	nn	α_{95}	k	age	site	slat	slon
Fajjoud-Tadoughast formation					Robert et al. (2017)				
13380	290.2	-83.2	6	5.8	135.4	562	282	30.223	352.175
13380	318.6	63.2	5	9.1	72.2	562	283	30.825	353.213
13380	229.5	-54	6	4.3	244.3	562	284	30.235	352.195
13380	63.2	68.2	6	8.2	67.6	562	285	30.235	352.195
13380	130.5	55.1	5	7	121.9	562	286	30.227	352.164
13380	320.7	-77.1	4	10.1	83.5	562	287	30.236	352.195
13380	93.5	39.5	4	14.8	21.6	562	288	30.236	352.195
13380	112.7	52.8	5	12.3	39.7	562	289	30.313	352.225
13380	84.7	39.5	4	19.7	22.8	562	290	30.313	352.225
13380	201.7	74	3	13.8	81.3	562	291	30.258	352.193
13380	358.4	69.2	5	10.8	50.9	562	292	30.222	352.174
13380	93.9	59.9	4	23.7	16	562	293	30.224	352.174
13380	119.4	55.3	7	10.6	33.5	562	294	30.215	352.191
13380	70.8	35.5	4	16.6	42.2	562	295	30.257	352.19
13380	125.2	85.3	6	6.9	110.3	562	296	30.285	352.384
13380	110.8	54.6	6	5.6	142.6	562	297	30.282	352.228
13380	98.7	52.7	5	13.7	32	562	298	30.282	352.227
13380	112.8	75.4	4	10.7	75.2	562	299	30.282	352.227
13380	132	-85.4	4	7.8	139.9	562	300	30.545	353.002
13380	104.4	33.2	4	15	38.4	562	301	30.225	352.17

Table D.1 continued

ID	dec	inc	nn	α_{95}	k	age	site	slat	slon
Djebel Boho formation					Robert et al. (2017)				
13381	71.7	36.8	4	12.1	59	535	302	30.387	353.336
13381	76	56.3	6	11.5	34.8	535	303	30.386	353.336
13381	15.1	67.2	7	7.9	58.8	535	304	30.386	353.336
13381	315.3	-51.9	4	8.1	129.7	535	305	30.401	353.34
13381	112.9	57.6	6	13.1	21.1	535	306	30.409	353.335
13381	41.6	83	4	5.3	306.9	535	307	30.521	353.177
13381	19.3	88.4	4	14.9	39.1	535	308	30.411	353.346
13381	151.6	81.9	4	12.2	57.3	535	309	30.4	353.3
13381	327.4	-54.7	4	3.3	764.5	535	310	30.404	353.343
13381	190.2	78.6	5	18.8	17.5	535	311	30.399	353.339
13381	60.6	43.9	5	6.5	141.2	535	312	30.397	353.341
13381	85.3	76.1	5	5.2	213.9	535	313	30.39	353.342
13381	64.9	65.6	5	12.1	41.3	535	314	30.386	353.336
Lynn-Mattapan volcanics					Thompson et al. (2007)				
100012	127	-35.4	7	3.8	193	597	1	42.3	288.805
100012	144.2	-54.4	8	7.5	43	597	2	42.3	288.805
100012	324.8	61	6	13.9	16	597	3	42.301	288.804
100012	153.1	-53.5	8	10.2	23	597	4	42.268	288.725
100012	313.4	55.2	7	5.4	96	597	5	42.217	288.765
100012	138.8	-67.6	4	1.9	1357	597	6	42.267	289.129
100012	301	70.4	4	9.2	57	597	7	42.266	288.131
100012	327.5	59.9	7	8.1	42	597	8	42.489	288.954
100012	326.8	52.2	8	8.9	30	597	9	42.489	288.954
Bull Arm Argentia					Pisarevsky et al. (2012)				
10240	229.7	37.7	6	18	14.9	593	79	47.269	306.02
10240	258.4	58.6	5	10.5	54	593	80	47.269	306.02
10240	66.9	-39.3	4	9.5	95.1	593	81	47.269	306.02
10240	53.4	-57.9	8	7.5	55.8	593	82	47.269	306.071
10240	43.5	-31.2	5	14	30.8	593	83	47.269	306.071
10240	54.9	-29.5	5	8.9	74.8	593	84	47.269	306.071
10240	55.2	-31.8	8	6.2	80.1	593	85	47.269	306.072
10270	205.6	16.5	8	14.6	15.3	570	86	48.451	306.459
10270	194.7	54.2	6	14.1	23.5	570	87	48.468	306.459
10270	208.8	21.6	5	12.5	36.1	570	88	48.468	306.459
10270	207.6	-6	6	7.4	82.9	570	89	48.468	306.459
10270	50.3	-28.4	3	29.2	18.9	570	90	48.394	306.445
10270	54	-42.8	5	14.8	27.9	570	91	48.459	306.472
10270	18.4	-54.9	3	14.2	76.5	570	92	48.463	306.472
10270	17.9	-67.7	3	11.7	111.9	570	93	48.463	306.472
10270	201.2	25.5	5	3.4	507.2	570	94	48.463	306.472
Alno carbonatite complex					Meert et al. (2007)				
10067	43	72	6	4.9	187	584	64	62.5	17.5
10067	22	73	2	16.5	231	584	65	62.5	17.5
10067	97	82	4	23.4	16	584	66	62.5	17.5
10067	37	51	6	10.8	39	584	67	62.5	17.5
10067	53	54	3	22.7	30	584	68	62.5	17.5
10067	30	84	8	6	87	584	69	62.5	17.5
10067	33	75	7	6.4	90	584	70	62.5	17.5

Table D.1 continued

ID	dec	inc	nn	α_{95}	k	age	site	slat	slon
10067	76	58	7	8.9	47	584	71	62.5	17.5
10067	82	60	1			584	72	62.5	17.5
10067	340	73	2	29.1	76	584	73	62.5	17.5
10067	86	63	6	17.4	16	584	74	62.5	17.5
10067	64	62	2	64.1	17	584	75	62.5	17.5
10067	18	57	4	10	85	584	76	62.5	17.5
10067	327	71	4	19.2	24	584	77	62.5	17.5
10067	102	58	11	14.6	11	584	78	62.5	17.5
Skinner Cove volcanics					McCausland and Hodych (1998)				
8321	155.9	19.7	6	14	23.7	551	588	49.51	301.91
8321	146.5	19.5	5	12	41.9	551	589	49.51	301.91
8321	142.7	56	6	9.2	54.4	551	590	49.51	301.91
8321	138.5	37.6	5	5.6	188.9	551	591	49.51	301.91
8321	133.6	38.3	6	10.7	40.4	551	592	49.51	301.91
8321	137.3	59.8	6	13.9	24.1	551	593	49.51	301.91
8321	156.7	28.8	4	17.5	28.6	551	594	49.51	301.91
8321	145.8	23.2	5	8.5	81.9	551	595	49.51	301.91
8321	151.1	17.2	9	11.1	22.4	551	596	49.51	301.91
8321	128.9	16.9	5	14.5	28.7	551	597	49.51	301.91
Grenville dykes - steep					Halls et al. (2015)				
10836	137.7	-75.8	9	6.7	61	588	155	45.946	280.635
10836	140.9	-66.8	5	6.7	130	588	156	45.961	278.809
10836	163.8	-76.7	6	14.4	22	588	157	45.961	278.827
10836	100.6	-56.2	5	11.9	42	588	158	45.843	279.459
10836	143.1	-71.7	7	5.1	141	588	159	45.898	279.101
10836	139	-67.3	6	8.4	64	588	160	45.991	279.423
10836	118.2	-76.4	3	9.9	155	588	161	45.943	280.635
10836	40	-82	8	8.7	41	588	162	45.898	279.101
10836	299.2	69.6	6	10.6	41	588	179	46.018	279.409
10836	294	74.1	3	14.5	73	588	180	46.001	279.999
Grenville dykes - shallow					Halls et al. (2015)				
10836	120.7	23.1	8	6.7	69	588	163	46.237	278.401
10836	135.6	31.2	6	8.4	64	588	164	46.236	278.681
10836	140.9	25.8	4	6.1	232	588	165	45.943	280.635
10836	134.8	1.2	6	11.2	37	588	166	46.232	278.724
10836	132.7	32.6	3	8.7	202	588	167	46.006	279.183
10836	136.5	9.6	9	8.8	36	588	168	45.581	279.507
10836	120.5	27.7	6	5.9	130	588	169	45.898	279.101
10836	297	-40.1	9	5.2	97	588	170	45.458	279.652
10836	299	-42.8	4	21	20	588	171	45.423	279.651
10836	284.3	-30.2	6	9.3	53	588	172	45.423	279.651
10836	115.5	-17.1	3	32.4	16	588	173	46.496	279.159
10836	125.9	-39.6	13	6.5	42	588	174	46.487	279.199
10836	117.5	-39.8	6	9.9	47	588	175	46.487	279.193
10836	100	-20.3	5	31.5	9	588	176	46.488	279.195
10836	95.9	-23.8	3	26.3	23	588	177	46.489	279.235
10836	130.1	-23.8	6	10.1	45	588	178	46.61	279.645

Table D.1 continued

ID	dec	inc	nn	α_{95}	k	age	site	slat	slon
Long Range dykes					Murthy et al. (1992)				
6934	111.2	50.9	9	8	31	615	497	53.7	303.3
6934	106.2	49.9	8	7.9	45	615	498	53.7	303.3
6934	131.7	39.7	5	8.5	66	615	499	53.7	303.3
6934	114.2	52.4	6	9.5	60	615	500	53.7	303.3
6934	158	53.2	5	22.3	32	615	501	53.7	303.3
6934	129	48.6	6	18.8	44	615	502	53.7	303.3
6934	120.5	51.7	5	15.6	16	615	503	53.7	303.3
6934	136.5	64.3	5	10.4	32	615	504	53.7	303.3
6934	137.1	40	5	6.6	104	615	505	53.7	303.3
6934	136.8	43.3	5	20.1	11	615	506	53.7	303.3
6934	117	66	5	5.8	79	615	507	53.7	303.3
6934	132.6	68.6	5	3.1	257	615	508	53.7	303.3

TABLE D.2: Model: model name, MAG (LED) simulation run on the MagIC (Leeds) code; Ref: studies where the models were published, 1: Wicht and Meduri (2016), 2: Sprain et al. (2019), 3: Biggin et al. (2020), 4: Meduri et al. (2021); ar: aspect ratio of inner to outer core radii. Control parameters are: Ek: Ekman number, Ra: Rayleigh number and Pm: magnetic Prandtl mumber. the Prandtl number was 1 in all runs; TBC: thermal boundary conditions were either fixed flux (FF) or fixed temperature (FT), the first (second) two characters refer to the inner (outer) boundary; MBC: magnetic boundary condition of conducting inner core (CI) or insulating inner core (II); eps: amplitude of lateral heat flux variations on the outer boundary. HP: heat flux heterigeneity patterns: none - homogeneous heat flux, r-y20: recumbent spherical harmonic of l=2 and m=0, tomo: variation following a tomographic model of Masters et al. (1996); Regine: dynamo regime (D: stable dipole dominated, R: Earth-like reversing, M: multipolar), defined by τT: relative transitional time; Rm: magnetic Reynolds number, tsim: total simulation time in units of outer core magnetic diffusion time

Model	Ref	ar	Ek	Ra	Pm	TBC	MBC	HP	eps	Regime	τT	Rm	tsim
LEDA001	2,3,4	0.35	0.0005	250	5	FFFF	II	0	None	R	0.1496	217.5	10.175
LEDA002	2,3,4	0.35	0.0005	350	10	FFFF	II	0	None	M	0.16	479.4	4.667
LEDA003	2,3,4	0.35	0.0005	350	10	FFFF	II	0.3	r-Y20	M	0.2201	474.6	3.11
LEDA004	2,3,4	0.35	0.0005	350	10	FFFF	II	0.75	r-Y20	M	0.4023	474.4	3.35
LEDA006	2,3,4	0.35	0.0005	300	5	FTFF	II	0	None	M	0.2533	226.7	7.061
LEDA007	2,3,4	0.35	0.0005	350	5	FFFF	II	0	None	R	0.111	226	12.801
LEDA008	2,3,4	0.35	0.0005	400	5	FFFF	II	0	None	R	0.1149	226.7	13.732
LEDA009	2;3,4	0.35	0.0005	250	10	FFFF	II	0	None	D	0.0021	326.8	4.979
LEDA010	2,3,4	0.35	0.0005	200	10	FTFF	II	0	None	D	0.0278	326.8	9.012
LEDA011	3	0.35	0.0005	200	10	FTFF	II	0	None	R	0.0611	5.7	4.595
LEDA012	3	0.35	0.0005	200	10	FTFF	II	0	None	M	0.1901	5.4	4.494
LEDA013	3	0.35	0.0005	200	10	FTFF	II	0	None	M	0.302	5.5	4.355
LEDA015t	3	0.35	0.0005	200	10	FTFF	II	0	None	D	0	244.1	4.45
LEDA016	3	0.35	0.0005	200	10	FTFF	II	0	None	D	0	211.2	3.668
LEDA017	3	0.35	0.0005	200	10	FTFF	II	0	None	D	0	191.5	4.452
LEDA018	2,3,4	0.35	0.0005	200	10	FTFF	II	0.3	r-Y20	M	0.3223	348.8	5.342
LEDA019	2,4	0.35	0.0005	200	10	FTFF	II	0.75	r-Y20	M	0.4356	361.7	6.739
LEDA021	2,3;4	0.35	0.0005	400	10	FTFF	II	0	None	D	0	240.7	1.559
LEDA022	2,3;4	0.35	0.0005	450	5	FFFF	II	0	None	R	0.15	289.4	6.999

Table D.2 continued

Model	Ref	ar	Ek	Ra	Pm	ThBC	MBC	HP	eps	Regime	τT	Rm	tsim
LEDA023	2,3;4	0.35	0.0005	250	5	FTFF	II	0	None	M	0.2755	208.2	29.502
LEDA024	2,3;4	0.35	0.0005	400	5	FTFF	II	0	None	R	0.0556	258.2	6.121
LEDA025	2,3;4	0.35	0.0005	450	10	FFFF	II	0	None	M	0.2723	537.4	4.918
LEDA026	2,3	0.35	0.00012	34.9	10	FTFF	CI	0.3	tomo	D	0	110.7	10.183
LEDA027	2,3	0.35	0.00012	57.5	10	FTFF	CI	0.6	tomo	D	0	191.2	0.726
LEDA028	2,3	0.35	0.00012	34.9	10	FTFF	CI	0.9	tomo	D	0	135.2	9.301
LEDA029	2,3	0.35	0.0005	100	10	FTFF	II	1.5	r-Y20	D	0	214.1	4.333
LEDA030	2,3	0.35	0.0005	100	10	FFFF	II	1.5	r-Y20	D	0	209.8	4.141
LEDA032	2,3	0.35	0.0005	150	10	FFFF	II	1.5	r-Y20	M	0.26	336.9	11.97
LEDA033	2,3	0.35	0.00012	20	2	FTFF	CI	0	None	D	0	126.1	8.981
LEDA034	2,3	0.35	0.00012	50	2	FTFF	CI	0	None	D	0	188.7	9.035
LEDA035	2,3	0.35	0.00012	100	2	FTFF	CI	0	None	D	0	264.4	4.14
LEDA036	2,3	0.35	0.00012	20	2	FTFF	CI	0	None	D	0	78.4	9.998
LEDA037	2,3	0.35	0.00012	50	2	FTFF	CI	0	None	D	0	104.7	2.683
LEDA038	2,3	0.35	0.00012	20	2	FTFF	CI	0	None	D	0	71.9	5.456
LEDA039	2,3	0.35	0.00012	50	2	FTFF	CI	0	None	D	0	102.5	10
LEDA040	2,3,4	0.35	0.001	60	10	FTFF	II	0	None	D	0	118.8	19.265
LEDA041	2,3,4	0.35	0.001	70	10	FTFF	II	0	None	D	0	134.1	14.178
LEDA042	2,3,4	0.35	0.001	90	10	FTFF	II	0	None	D	0	160.6	13.407
LEDA045	2,4	0.35	0.001	150	10	FTFF	II	0	None	M	0.4313	261.3	6.571
LEDA046	2,3,4	0.35	0.001	200	10	FTFF	II	0	None	M	0.3672	299.6	0.711
LEDA047	3	0.35	0.0005	400	10	FTFF	II	0	None	D	0	1	3.641
LEDA048	3	0.35	0.0005	250	10	FTFF	II	0	None	D	0	274.6	5.714
LEDA049	3	0.35	0.0005	400	10	FTFF	II	0	None	D	0	373.6	4.728
LEDA051	3	0.2	0.0005	350	5	FFFF	II	0	None	D	0	330.8	4.33
LEDA052	3	0.1	0.001	90	10	FTFF	II	0	None	D	0	367.8	9.763
LEDA053	3	0.2	0.001	90	10	FTFF	II	0	None	D	0	460.2	10.713
LEDA054	3	0.35	0.0005	300	5	FTFF	II	0	None	M	0.1808	272.8	5.76
LEDA055	3	0.35	0.0005	300	5	FTFF	II	0	None	R	0.1427	285.0	3.992
LEDA056	3	0.35	0.0005	300	5	FTFF	II	0	None	M	0.2673	298.4	7.483
LEDA057	3	0.35	0.0005	250	5	FTFF	II	0	None	D	0.015	246.7	4.974
LEDA058	3	0.35	0.0005	250	5	FTFF	II	0	None	M	0.2547	264.5	6.182
LEDA059	2,3	0.35	0.0005	100	20	FTFF	II	0	None	D	0	330.8	3.967
LEDA060	2,3	0.35	0.001	120	20	FTFF	II	0	None	D	0	367.8	3.149
LEDA061	2,3	0.35	0.001	200	20	FTFF	II	0	None	M	0.25	460.2	2.89
LEDA062	2,3	0.35	0.001	120	20	FFFF	II	0	None	M	0.25	442	5.347
LEDA063	2,3	0.35	0.001	150	20	FFFF	II	0	None	M	0.2	495.2	4.074
LEDA065	3,4	0.35	0.001	105	10	FFFF	II	0	None	M	0.3896	225.4	6.632
LEDA066	4	0.35	0.001	120	10	FFFF	II	0	None	M	0.443	243.6	6.231
LEDA067	3,4	0.35	0.0005	100	10	FFFF	II	0	r-Y20	D	0	199.0	5.481
LEDA068	3	0.35	0.0005	400	10	FTFF	II	0	None	D	0	332.9	4.681
LEDA069	3	0.35	0.0005	400	10	FTFF	II	0	None	D	0	286.0	5.033
LEDA070	3,4	0.35	0.0005	100	10	FFFF	II	0	None	D	0	204.6	4.843
LEDA071	3,4	0.35	0.0005	100	10	FFFF	II	1	r-Y20	D	0	204.6	3.468
LEDA072	3	0.35	0.0005	400	10	FTFF	II	2	r-Y20	D	0	329.7	3.084
LEDM001	4	0.35	0.0005	150	10	FFFF	II	0	None	D	0	281	31.03
LEDM003	4	0.35	0.00015	200	3	FFFF	II	0	None	D	0	121	28.442
LEDM007	4	0.35	0.00015	300	3	FFFF	II	0	None	D	0	148	25.548
LEDM008	4	0.35	0.00015	400	3	FFFF	II	0	None	D	0	176	21.726
LEDM010	4	0.35	0.00015	800	3	FFFF	II	0	None	D	0	262	20.036
LEDM011	4	0.35	0.00015	1200	3	FFFF	II	0	None	D	0	333	15.778
MAGA001	1,4	0.35	0.0003	4800	3	FTFF	CI	0	None	D	0	264	10.661

Table D.2 continued

Model	Ref	ar	Ek	Ra	Pm	ThBC	MBC	HP	eps	Regime	τT	Rm	tsim
MAGA002	1,4	0.35	0.0003	5100	3	FTFF	CI	0	None	D	0	340	36.639
MAGA003	1,4	0.35	0.0003	3000	3	FTFF	CI	0	None	R	0.0653	408	86.764
MAGA004	1,4	0.35	0.0003	6000	3	FTFF	CI	0	None	M	0.2025	497	7.847
MAGA007	1,4	0.35	0.001	5400	10	FTFF	CI	0	None	R	0.0784	442	431.365
MAGA008	1,4	0.35	0.001	4950	10	FTFF	CI	0	None	M	0.1597	491	9.345
MAGA009	1,4	0.35	0.001	500	10	FTFF	CI	0	None	M	0.3834	564	24.974
MAGB001	4	0.35	0.0003	800	3	FFFF	CI	0	None	D	0.0177	365	36.571
MAGB002	4	0.35	0.0003	4500	3	FFFF	CI	0	None	R	0.0536	380	31.077
MAGB003	4	0.35	0.0003	1000	3	FFFF	CI	0	None	D	0	281	60.807
MAGM001	4	0.35	0.0003	1100	3	FFFF	CI	0	None	R	0.1335	418	11.024
MAGM003	4	0.35	0.0003	3000	3	FFFF	CI	0	None	R	0.0966	395	40.644
MAGM007	4	0.35	0.0003	4500	3	FFFF	CI	0	None	R	0.0459	376	22.422
MAGM009	4	0.35	0.001	6000	10	FTFF	CI	0	None	D	0	229	58.064
MAGM012	4	0.35	0.001	9000	10	FTFF	CI	0	None	D	0	312	60.368
MAGS002	4	0.35	0.0003	1250	3	FFFF	CI	0	None	D	0.0083	350	35.569
MAGS004	4	0.35	0.001	1500	10	FTFF	CI	0	None	D	0.0001	372	35.775
MAGS005	4	0.35	0.001	2000	10	FTFF	CI	0	None	D	0.0102	401	58.333